MEASUREMENTS OF TROPOSPHERIC SCATTER WITH A NEW MULTI-BEAM, MULTI-RECEIVER VHF DOPPLER RADAR

By

Bridget Hobbs, B.Sc. (Hons)

Thesis

submitted for the degree of

DOCTOR OF PHILOSOPHY

at the

UNIVERSITY OF ADELAIDE

(Department of Physics and Mathematical Physics)

September 1998

Contents

Abstract

This thesis discusses the work done by the author to upgrade the Buckland Park (BP) VHF stratosphere-troposphere (ST) radar, verify the data from the new system, plan and run new experiments, and analyse the resultant data in order to study the scattering and aspect sensitivity of the troposphere.

Between 1995-1998 the system was upgraded to enable Doppler beam-swinging (DBS) measurements at a wide range of angles, and spaced antenna (SA) measurements in a variety of antenna configurations. The upgraded system is discussed, with emphasis on the tests that were conducted in order to estimate the various phase errors in the system, including the antenna arrays, the new beam steering hardware and receivers, and tests to ensure the correct operation of the system as a whole in both multiple beam DBS and SA modes

The new DBS capabilities of the system, in particular, required that new data analysis algorithms be developed. These algorithms were necessary to perform the analysis in the frequency domain and to cope with various new contaminants observed with the new system due to the increased number of pointing directions relative to the old system. These algorithms are discussed in detail with various examples of the resultant improvement in data quality.

The primary aims of the work in this thesis were to use SA and DBS techniques together and to examine DBS data at many off-zenith angles, in order to study the scattering and aspect sensitivity of the troposphere. Two joint DBS/SA experiments were run, an approach which for the most part is not taken in VHF ST studies. The first deals with a comparison between SA full correlation analysis (FCA) and DBS data. The main result of this experiment was that in aspect sensitive conditions, θ_s values using DBS beams at 3.6° off-zenith and 0.0° were in excellent agreement with FCA estimates of θ_s, suggesting that the same scattering structures were affecting both angles.

The second DBS/SA experiment deals with a comparison between SA angle of arrival (AOA) measurements and DBS data. The main results of this experiment indicated that the aspect sensitive structures at small off-zenith angles were tilted

layers. This was seen in a comparison of the AOA on a vertical beam with power differences in off-zenith beams at 3.6°.

With respect to multiple off-zenith beam DBS measurements, most of the similar studies have their emphasis on examining the behaviour at small, aspect sensitive off-zenith angles, in relatively short data sets. Instead of this approach, the emphasis of the multiple off-zenith beam experiments discussed in this thesis was to examine the scattering over the full angle range from 0.0° to 22.0° over a large period of time to quantify the variation in the decrease in power as a function of off-zenith angle, and to identify the isotropic scattering level. The main result of this experiment was that the isotropic scattering level occurred at a minimum off-zenith angle of approximately 14.5°.

This thesis represents the first use of the upgraded system for atmospheric studies in the ST region. As such it is a study of the new capabilities of the radar. In addition, the experiments now possible with the system have provided new information on the nature of the aspect sensitivity and scattering of the troposphere.

Preface

This work contains no material which has been accepted for the award of any other degree or diploma in any university or other tertiary institution and, to the best of my knowledge and belief, contains no material previously published or written by another person, except where due reference has been made in the text. I give consent to this thesis, when deposited in the University Library, being available for loan and photocopying.

Signed: dated: 2/9/98

Bridget Hobbs, B.Sc. (Hons)

Acknowledgements

This thesis would have been impossible without the assistance, encouragement, counselling and distractions provided by a number of people. First among those that I would like to thank is my husband Chris whose love, understanding and friendship have been my foundation throughout my PhD candidature.

I would like to thank my supervisors Iain Reid and Bob Vincent for their advice and assistance during my candidature, David Holdsworth for his help in dealing with the vagaries of multiple receiver data and Andrew Taylor for his guidance and support during the dark days when the BP VHF ST radar was in many not-working pieces.

I would like to thank the technical staff of the Atmospheric Physics Group, Simon Ludborzs for designing the new beam-steering unit, and Lesley Rutherford and Alex Didenko for their help building it. Thanks must also go to Lesley and Alex, along with Malcolm Kirby for installing the new North-South CoCo array, and to the those two third year students, Brenton and Michael, who soldered the 1408 antenna elements of the new array. Still on the technical side, I would like to thank Mike Shorthose, the staff of Tomco Electronics, Genesis Software and ATRAD (Atmospheric Radar Systems) for their help during my candidature, and the Bureau of Meteorology Research Centre (BMRC) for the radiosonde data from Adelaide Airport.

The past and present students of the Atmospheric Physics Group, Brenton Vandepeer, David Holdsworth, Manuel Cervera, David Low, Simon Allen, Dorothy Gibson-Wilde, Karen Berkefeld, Ali Kazempour, Scott Dullaway, Sujata Kovalam, Stephen Grant, Andrew Mackinnon, Jonathan Woithe, Rupa Vuthaluru, Florian Zink, Minh Nguyen and Daniel Badger, along with Group staff Dallas Kirby, Lyn Birchby, Laurence Campbell and Graham Elford, have been great to laugh, whinge, work and eat cake with over the years. Thank you.

Outside physics, I would like to thank my most excellent friends, Christina, Fiona, Sandra, Seana and the "story", for more laughs than I can count, the Tuesday night group in its various forms, the violin group, and Troy and Claire. Finally, I would like to thank my fantastic family Mum, Dad, David, Justine, Michael and Simba, and family in-law Dick, Lee, Susan, Philip, Peter and Allison. The constant encouragement

and support I have received from you all throughout my PhD has meant a great deal to me, and I am extremely grateful for it. I would also like to thank my extended family, for their interest and support throughout my studies.

This work was supported through receipt of an Australian Postgraduate Award.

Chapter 1

Introduction and background

1.1 Introduction

The use of VHF (very high frequency) radars to study the MST (mesosphere-stratosphere-troposphere) region of the atmosphere, began in the 1970s with *Woodman & Guillén* [1974]. Their work proved the usefulness of the technique for the measurement of winds and the study of the nature of the scattering medium, and was quickly followed by other authors reporting results from VHF radars around the world. These radars receive backscatter from irregularities in the radio refractive index, the exact nature of which has been the subject of extensive debate since the first experiments were conducted. The dominant mechanism responsible for backscatter at VHF is turbulent scattering. However, early work by *Röttger & Liu* [1978] and *Gage & Green* [1978] reported what has come to be known as aspect sensitive scatter, that is, a decrease in the power of the backscatter with increasing off-zenith angle.

The mechanisms that are assumed to be responsible for the aspect sensitive nature of the atmosphere are backscatter from horizontally stratified layers, which may be tilted, and anisotropic turbulence, both of which exist alongside the turbulent scattering structures. The exact mechanism which produces the thin specular layers responsible for the aspect sensitivity is not fully understood, but numerous VHF radar observations of the atmosphere over the last 20 years have shed light on some interesting features of the aspect sensitivity of the atmosphere, and the layers believed to be at

least partly responsible. These studies include work on the effects of various weather events on the degree of aspect sensitivity (e.g. *Yoe et al.* [1994], *Hooper & Thomas* [1995]), the effects of the tilting of the specular layers on VHF radar on vertical velocity measurements (e.g. *Röttger et al.* [1990], *Larsen & Röttger* [1991]) and the possible manifestation of these layer tilts in power measurements made in off-zenith Doppler beams (*Worthington & Thomas* [1996], *Tsuda et al.* [1997a], *Tsuda et al.* [1997b].

In general, fixed frequency VHF radars operating in the MST region have been used to study the winds and backscatter of the atmosphere via two distinct techniques. One centres on Doppler beam-swinging (DBS) using only a single receiver and a narrow Doppler beam (e.g. *Gage & Green* [1978], *Röttger et al.* [1981]), and the other is based around the use of multiple spaced antennas (SA) for reception, and includes the commonly used full correlation analysis (FCA) and spatial domain interferometry (SDI) techniques (e.g. *Röttger & Vincent* [1978], *Vincent & Röttger* [1980]).

This thesis is based on the results of experiments conducted with the upgraded Buckland Park (BP) VHF ST (stratosphere-troposphere) radar. Between 1995-1998 the system was upgraded such that it is now capable of both DBS measurements at a wide range of angles, and SA measurements in a variety of antenna configurations. The thesis covers the construction and testing of the new hardware, the implementation of software to ensure the reliability of the new DBS results, and the results of experiments designed to study the scattering characteristics and aspect sensitivity of the atmosphere, using both DBS and SA techniques. The increased flexibility and variety of experiments made possible with the new hardware in the BP VHF ST radar allows for new combinations of experiments that were previously not possible at this location. In addition, the upgrade brings the BP VHF ST radar up to date with the increasing number of new VHF radars around the world that are capable of both multiple direction DBS and SA measurements.

This chapter will describe the general mechanisms and characteristics of radar backscattering, and the techniques that are used to obtain information about the atmosphere in general, and radar backscatter in particular. It will provide the background necessary for the data collection and analysis methods used in this thesis, as well as the theory behind the results that are presented in later chapters.

1.2 Radar backscattering

Various radars have been used to measure atmospheric parameters in the ST region, utilising various backscattering mechanisms. Weather radars operate in the 1-10 *cm* band and receive backscatter from hydrometeors, while VHF and UHF (ultra high frequency) radars, which operate in the 1-10 *m* and 10 *cm* - 1 *m* wavelength bands respectively, receive backscatter from the clear air. VHF and UHF radars are able to measure wind velocity by receiving backscatter from irregularities in the radio refractive index, which are assumed to be tracers of the wind motion.

These radars have been termed MST or ST radars in reference to the regions of atmosphere that they are able to observe; *clear-air* radars, in reference to the mode of backscatter; or *wind-profiling* radars in reference to their most common mode of operation. The term *clear-air* radars can be misleading because backscatter with VHF and UHF radars can also be obtained from hydrometeors, while the term *wind-profiling* radars refers to only one measurement capablility of these radars, which is not an adequate description of their application in this thesis. This thesis is concerned with the operation of VHF radars in the ST region. Consequently, for the remainder of this thesis, these radars will be referred to as VHF or VHF ST radars, which denote the frequency and atmospheric height range of interest.

There are various mechanisms by which backscatter is received from the clear air, all of which originate from irregularities in the radio refractive index, n, which can be written (*Balsley & Gage* [1980])

$$n - 1 = \frac{3.73 \times 10^{-1} e}{T^2} + \frac{77.6 \times 10^{-6} p}{T} + \frac{N_e}{f_0^2}, \tag{1.1}$$

where p *(mb)* is atmospheric pressure, e *(mb)* is the partial pressure of water vapour, T *(K)* is the absolute temperature, $N_e(m^{-3})$ is the number density of electrons, and f_0 is the operating frequency of the radar. The three components of the refractive index are commonly called the wet, dry and ionization terms respectively. The wet term is the contribution due to water vapour, and is dominant in the lower troposphere, up to about 5 *km*. The dry term is due to dry air and dominates from mid-troposphere up to about 50 *km*, or the approximate height of the stratopause. The ionization term is

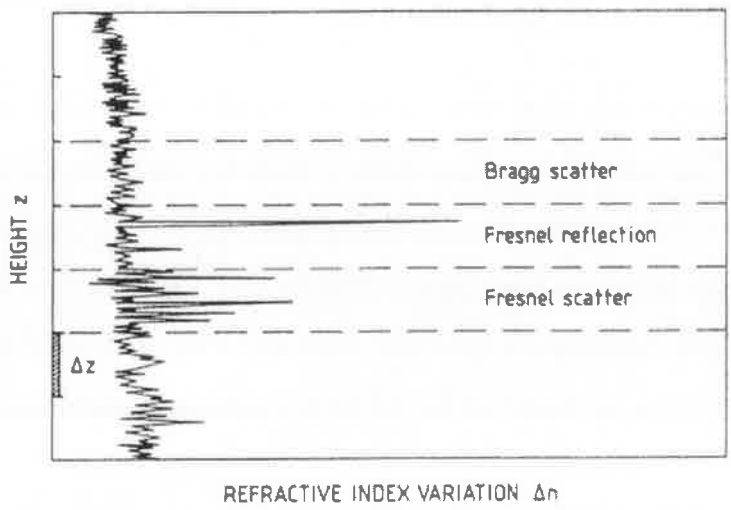

Figure 1.1: Schematic of the nature of the scattering processes of Bragg scatter, Fresnel scatter and Fresnel reflection within a radar range gate of size Δz, after *Rottger* [1989].

the contribution from free electrons and dominates above the stratopause.

The principal scattering mechanism of VHF radars is called Bragg or turbulent scatter. This type of scatter occurs preferentially from irregularities of size equal to one half of the wavelength of the radar. Bragg scatter can be isotropic or anisotropic, depending on whether or not the irregularities of the refractive index are homogeneous and statistically similar in all radar beam pointing directions.

Other types of scatter result from stratification in the structure of the radio refractive index. Fresnel reflection is caused by backscatter from a single discontinuity of refractive index of large horizontal extent, while Fresnel scatter is caused by backscatter from many such discontinuities within the radar beam volume. Figure 1.1 is a schematic of these scattering mechanisms. The strong horizontal stratification of these Fresnel structures make them aspect sensitive in the same manner as anisotropic turbulent scatter. Backscatter from a radar beam pointed to the zenith is enhanced by the presence of these layers, whereas scatter from off zenith beams is not. Early in the debate over the nature of the echoes which caused aspect sensitivity, the issue whether anisotropic turbulence or thin specular layers were the cause. It is now generally accepted that the two mechanisms co-exist, although the task of attributing a given case of strong aspect sensitivity to one mechanism or another is difficult.

The measurements of *Gage & Green* [1978] and *Green & Gage* [1980] showed

that enhanced backscatter from radar beams directed vertically was accompanied by enhanced atmospheric stability as shown in temperature measurements made with radiosondes. Observations of layered structures in the temperature field of the atmosphere have been made by *Lane* [1964], *Lane* [1968], *Bufton* [1973] and *Dalaudier et al.* [1994]. The results of *Dalaudier et al.* [1994] in particular, which were made at a resolution of 20 *cm*, using balloon borne sensors, showed the existence of strong temperature gradients or "sheets" associated with regions of high static stability, which accords well with the findings of *Gage & Green* [1978] and *Green & Gage* [1980]. *Dalaudier et al.* [1994] have not only proven the existence of layered structures in the temperature field, but also that these layers are capable of causing enhanced vertical radar backscatter. Following the modelling work of *Gage & Balsley* [1980], which provides the reflectivity of an individual sheet in the atmosphere, *Dalaudier et al.* [1994] used their balloon data to construct a refractivity profile which they compared with backscatter profiles from a nearby VHF radar. Their results indicated that scatter from the temperature gradients accounted for a significant fraction of the vertical radar echoes. In addition, the authors reported evidence that the sheets were not flat and horizontal. Other evidence that the specular layers are not exactly horizontal has come from spaced antenna measurements of the angle of arrival of the scatter in a vertical beam (e.g. *Vincent & Röttger* [1980], *Palmer et al.* [1991]) and, recently, from Doppler beam swinging experiments with the highly flexible MU radar in Japan. These beam swinging experiments, by *Tsuda et al.* [1997a] and *Palmer et al.* [1998] have revealed that measurements of power at a range of angles close to zenith sometimes show that the maximum power comes from some small off-zenith angle.

The exact production mechanism of these specular layers is the subject of ongoing debate. *Luce et al.* [1995] discussed the mechanisms proposed by *Gossard et al.* [1985] and *Hocking et al.* [1991] and their applicability to the measurements of *Dalaudier et al.* [1994]. The model of *Gossard et al.* [1985] is based on "sheet and layer" generation associated with turbulence, while the model of *Hocking et al.* [1991] proposes that viscosity and/or thermal conduction could be responsible for layer formation above the tropopause. *Luce et al.* [1995] concluded that neither of these models in their present forms were capable of accounting for the balloon borne observations.

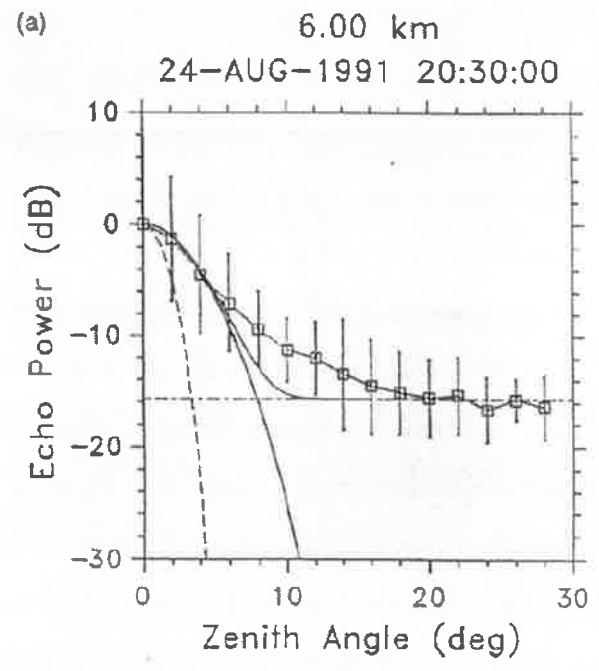

Figure 1.2: Backscattered power as a function of off-zenith angle from 0° - 28° after *Tsuda et.al.* [1997a]. The dashed line is the radar antenna gain squared, the dash-dot line is the turbulent scattering level, and the solid lines respresent a model function calculated by *Tsuda et.al.* [1997a].

The aspect sensitive nature of the atmosphere is best viewed by directing radar beams to a number of off-zenith angles. Early measurements of this nature have been made by *Gage & Green* [1978], *Green & Gage* [1980], *Röttger et al.* [1981], *Waterman et al.* [1985], *Tsuda et al.* [1986]. From these measurements, it is generally held that radar beams directed at angles greater than about 10° will be unaffected by aspect sensitive scatter. Independant evidence of this fact comes from the balloon studies of *Luce et al.* [1996], who, in a similar vein to *Luce et al.* [1995], have compared the radar backscatter at an off-zenith angle of 15° with an isotropic scattering model which utilises the balloon data of *Dalaudier et al.* [1994]. Their results indicated that isotropic scattering is the dominant scattering mechanism at 15° off-zenith.

The dominance of isotropic scattering at off-zenith angles larger than 10° means that less aspect sensitive scatter is observed at these angles. However, the recent work by *Tsuda et al.* [1997a] has shown that there are times when off-zenith beam angles greater than 18° are required to consistently observe purely isotropic scattering.

Figure 1.2, from *Tsuda et al.* [1997a] shows the fall off of power as a function of off-zenith between the vertical and about 18°, indicative of aspect sensitive scatter, while the independance of power as a function of off-zenith angle between 18° and 28° is indicative of isotropic scatter. The almost constant power in this latter range of angles is called the isotropic scattering level.

In recent years, many measurements of the scattering and aspect sensitivity of the ST region of the atmosphere have been conducted. Some of these studies have concentrated on investigations of the nature of the specular layers which are believed to cause the aspect sensitivity. These measurements have focussed on calculating the angle of arrival of the scatter in the beam of the radar, to investigate the possibility that the layers may be tilted with respect to the vertical direction. Other work has focussed on studying the nature of the polar diagram of the backscatter, either by simply viewing multiple beam scatter, as shown in Figure 1.2, or by using a mathematical parameterisation of the polar diagram of the scatterers in order to quantify the scattering conditions.

Before a discussion of the methods of these studies can be presented, it is first necessary to discuss the techniques used by VHF radars to measure various atmospheric parameters. The remainder of this chapter will deal with methods and analysis, rather then specific results as discussed in the literature, which will instead be presented in later chapters where relevant to the presentation of the work in this thesis.

1.3 The Doppler beam swinging method

VHF studies have their roots in DBS measurements, as the first investigations by *Woodman & Guillén* [1974] were conducted with a Doppler radar. As such, the DBS technique is the most common VHF radar technique in the ST region, partly due to the ease with which the requisite narrow beams can be created at VHF wavelengths, and partly due to the fact that the technique and associated analysis are easily understood. *Hocking* [1997*a*] has recently compiled a comprehensive list of radars operating in the MST region. It shows that of the 24 radars listed as being capable of ST or MST observations, all are capable of DBS measurements while only eight are capable of

utilising spaced antenna techniques.

The most common application of VHF radars in the ST region is to measure the wind velocity. This is achieved in a Doppler radar by directing a beam at off-zenith angle θ, and azimuth angle ϕ, to measure the radial velocity V_r

$$V_r(\theta, \phi) = u \sin\theta \sin\phi + v \sin\theta \cos\phi + w \cos\theta, \tag{1.2}$$

where u, v and w are the zonal, meridional and vertical velocities respectively.

Under the assumption that the atmosphere is statistically homogeneous on horizontal scales larger than the separation of the radar beams, two off-zenith Doppler beams directed at off-zenith angles θ and -θ in a single plane can be used to measure the horizontal wind velocity V_h in the plane

$$V_h = \frac{1}{2\sin\theta}(V_\theta - V_{-\theta}), \tag{1.3}$$

where V_θ and $V_{-\theta}$ are the radial velocities in the plane at the relevant off-zenith angles. As such, normal DBS operation involves directing narrow beams vertically to measure the vertical velocity, and off-zenith to the north and south to measure V_h in the meridional direction, and to the east and west to measure V_h in the zonal direction. The transmission and reception beams are identical in the DBS method, usually formed by a large array of individual antenna elements to form a single aperture. DBS experiments require a single receiver to collect the data, although the same effect can be achieved by summing the phase coherent output of multiple receivers.

There are two basic ways to analyse DBS time series to obtain atmospheric parameters; correlation analysis in the time domain, and spectral analysis in the frequency domain. The radial velocity V_r measured by a Doppler beam can be calculated in the frequency domain by using the equation

$$V_r = \frac{\lambda(f_D - f)}{2}, \tag{1.4}$$

where λ is the radar wavelength, f is the transmitting frequency of the radar and f_D is the frequency of the signal returned by the atmosphere, which has been Doppler shifted by the motion of the scatterers, which are assumed to be tracers of the wind

motion. While in the time domain the radial velocity can be calculated by using the equation

$$V_r = \frac{\lambda}{2}\frac{1}{\pi}\frac{d\phi}{d\tau}, \tag{1.5}$$

where λ and V_r have their usual meaning and $\frac{d\phi}{d\tau}$ is the rate of change of phase of the returned signal. Including the radial velocity, there are three main parameters that are measured in either analysis method. These parameters are calculated from the power spectrum in the frequency domain and the auto-correlation function in the time domain. Figure 1.3 shows these functions in the two domains and the parameters that are measured in each of them.

In the frequency domain, the three parameters of interest are directly associated with the moments of the spectrum, which are a set of variables related to the Gaussian shape of the spectrum, as can be seen from Figure 1.3. The zeroth moment m_0 is equal to the signal power P, which is commonly used in conjunction with the noise level N, to calculate the SNR (signal-to-noise ratio) of the echo. The zeroth moment is equal to the area under the peak in the power spectrum, which corresponds to the peak amplitude of the auto-correlation function in the time domain, and is written

$$m_0 = \int S(f)df, \tag{1.6}$$

where $S(f)$ denotes the power spectrum as shown in Figure 1.3. It should be noted here that the spectrum $S(f)$ used in this equation has first had the noise level N subtracted.

The first moment m_1 is written

$$m_1 = \int 2\pi f S(f)df, \tag{1.7}$$

and is used to calculate the frequency shift f_D of the peak in the power spectrum. This is equivalent to $\frac{d\phi}{d\tau}$, the slope of the phase of the auto-correlation function in the time domain. The frequency shift is calculated from the moments via the equation

$$f_D = \frac{m_0}{m_1}, \tag{1.8}$$

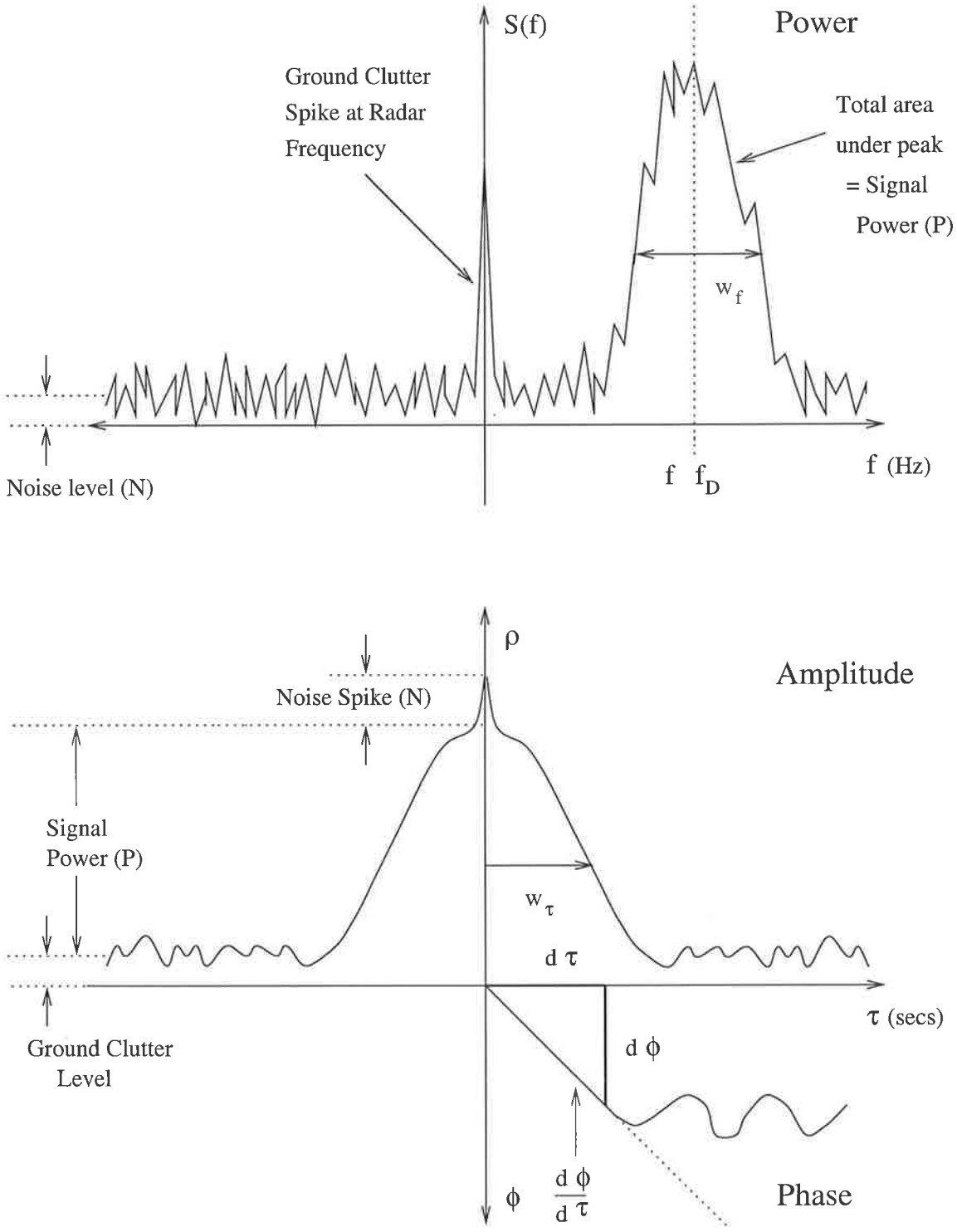

Figure 1.3: Functions used to calculate the atmospheric parameters using the DBS method. A power spectrum is shown at the top of the figure and an autocorrelation function at the bottom.

which can then be used to calculate the wind velocity.

Finally, the second moment m_2 is written

$$m_2 = \int (2\pi f)^2 S(f) df, \tag{1.9}$$

and is used to calculate w_f, the width of the peak of the power spectrum which is a measure of the degree of turbulence in the volume sampled by the beam. The spectral width is calculated from the moments via the equation

$$w_f = \sqrt{\frac{m_2}{m_0} - (\frac{m_1}{m_0})^2}. \tag{1.10}$$

In the time domain this measurement is related to w_τ, the width of the amplitude of the auto-correlation function, which is a measure of the lifetime of the echo. Atmospheric parameters can be calculated from spectra by simply calculating the moments, or by fitting a Gaussian function to the atmospheric peak to obtain the position, width and area below the peak.

There are advantages and disadvantages inherent in either domain. In the frequency domain, contaminating scatter from precipitation, ground clutter and the like are visible as spectral peaks which makes them relatively easy to identify and remove, compared to the same task in the time domain. But analysis in the time domain has the advantage of efficiency; if none of the afore-mentioned contaminants exist, analysis via the auto-correlation function is faster and less computer-intensive. All of the DBS analysis in this thesis was performed in the frequency domain using power spectra, by fitting a Gaussian function to the atmospheric peak.

1.4 Spaced antenna methods

Spaced antenna (SA) methods refers to those techniques which use the signals recorded at a number of spatially separated receiving antennas. Figure 1.4, from *Holdsworth* [1995], (adapted from *Vandepeer* [1993]) summarises the full family of techniques. Of these analyses, the work presented in this thesis is concerned with the use of full correlation analysis (FCA), to determine the degree of aspect sensitivity, and spatial

domain interferometry, to determine the angle of arrival (AOA) (sometimes called the mean angle of arrival MAOA), from data collected with the upgraded BP VHF ST radar.

Spaced antenna techniques were first applied to VHF data from the ST region by *Röttger & Vincent* [1978], and *Vincent & Röttger* [1980] who made both the FCA and layer tilt measurements. Both of these techniques utilise a single transmit beam, usually formed by a large array of individual antennas, and a number of broader reception beams, usually formed by subgroups of the original transmission array.

The essential idea of the spaced antenna methods is to sample the diffraction pattern produced by the transmit beam, on a number of receivers. For both the FCA and AOA analysis, the output of the receivers is cross-correlated to provide information on the time and phase delays between antennas. This information can then be used to calculate the motion of the ground diffraction pattern, the so-called "apparent" velocity between pairs of antennas, or the AOA of the signal between any two antennas. FCA is applied to data from a minimum of three non-colinear antenna groups to correct for the effects of the non-stationarity of the scatters in the diffraction pattern (turbulence). The resulting velocity is called the "true" velocity.

1.4.1 Full correlation analysis

The basis of the FCA is that the spatio-temporal correlation function of the ground diffraction pattern can by described by a family of ellipsoids (e.g. *Briggs et al.* [1950]). The temporal characteristics of the spatio-temporal correlation function are parameterised by the "correlation parameters" which are determined from the amplitudes of the auto- and cross-correlation functions, as shown in Figure 1.5.

The determination of these correlation parameters for a given data set, results in atmospheric parameters such as the "true" wind velocity, the direction of the prevailing wind, and the orientation and elongation of the scatterers. The mathematical details of the determination of the atmospheric parameters from the correlation parameters are beyond the scope of this thesis, but are described in full by *Holdsworth* [1995]. Despite this, in order to understand the information that the FCA can provide about

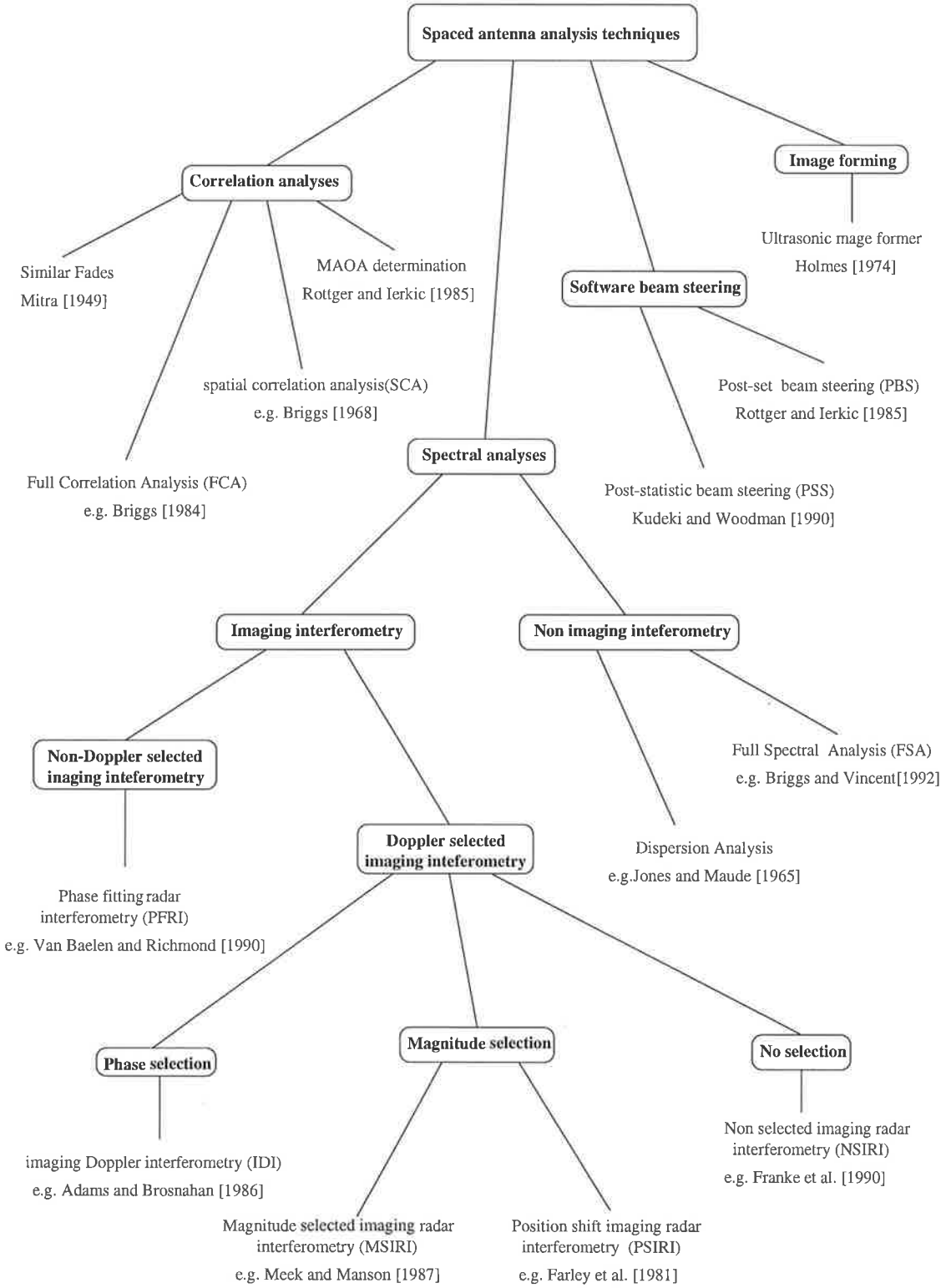

Figure 1.4: Taxonomy of spaced antenna techniques, after *Holdsworth* [1995], adapted from *Vandepeer* [1993].

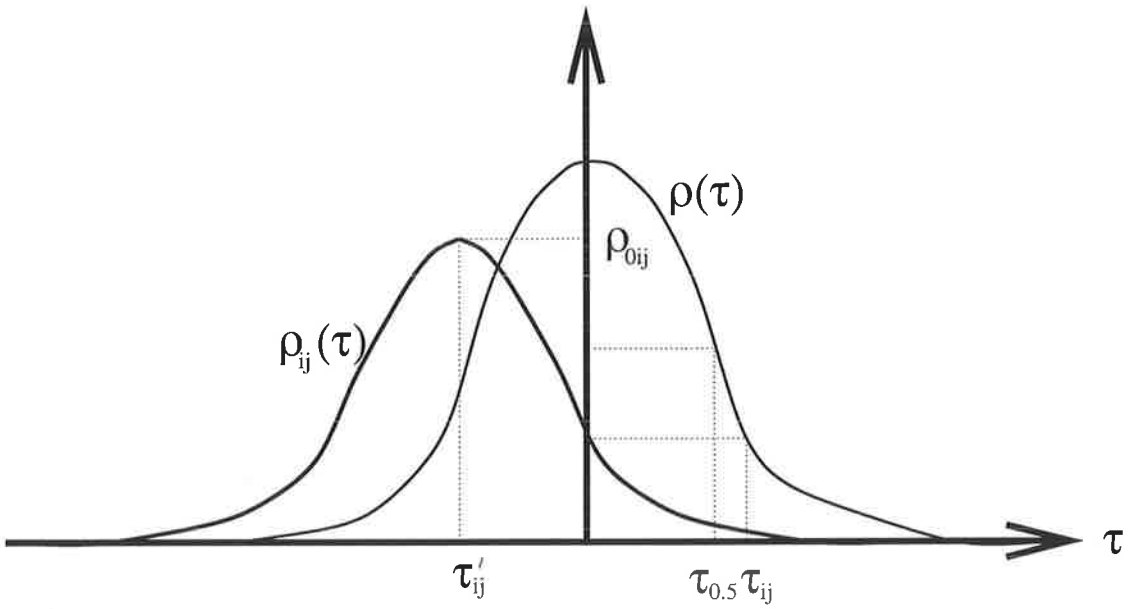

Figure 1.5: Schematic of the auto- and cross- correlation functions, $\rho(\tau)$ and $\rho_{ij}(\tau)$ respectively, showing the correlation parameters used by the FCA. The parameters are the fading time $\tau_{0.5}$ which is the lag where the auto correlation function equals 0.5, the cross-correlation maximum ρ_{0ij} and corresponding lag τ'_{ij}, and the lag τ_{ij} where the auto-correlation function equals the zero lag cross-correlation function, after *Holdsworth* [1995].

the radar backscatter, it is useful to describe the atmospheric parameters that are determined from the various correlation parameters. The description provided by *Holdsworth* [1995] is utilised for this purpose.

The horizontal velocity or true velocity is determined from the cross correlation function maximum delay times, τ'_{ij}, once the effects of random changes in the ground diffraction pattern have been accounted for. The elongation of the characteristic ellipse is parameterised by the axial-ratio, R_{ax}, and is calculated from τ_{ij}, which is the lag at which the auto-correlation function equals the zero-lag cross-correlation functions, and τ'_{ij}. The pattern scale, $S_{0.5}$, is usually defined by the "geometric mean" of the major and minor axes of the ellipse. It is, however, sometimes defined by the "geometric mean" of the major and minor axes so that

$$S_{0.5} = \frac{r_{maj}}{\sqrt{R_{ax}}}. \tag{1.11}$$

This method of calculating $S_{0.5}$ provides an indication of the average "radius" of the characteristic ellipse. Another useful parameter from the FCA is the fading time,

$\tau_{0.5}$, which is the lag where the auto-correlation function equals 0.5. The fading time is directly related to the spectral width of the Doppler technique.

There have been a number of comparisons of the horizontal velocities produced by both the Doppler and FCA techniques with other techniques throughout the MST region. These comparisons, with rockets (e.g. *Vincent et al.* [1977]), balloons (e.g. *Hocking* [1997*b*]) and meteor drifts (e.g. *Cervera & Reid* [1995]) have in general shown good agreement, at least below 90 *km*. However, there have been only a few direct comparisons of FCA and DBS velocities in the ST region; including the studies by *Vincent et al.* [1987] and *Van Baelen et al.* [1990], which both showed good general agreement between the two techniques. Similar comparisons at MF (medium frequency) in the mesosphere have also shown good agreement (e.g. *Reid* [1988]).

1.4.2 Angle of arrival analysis

The first AOA measurements in the ST region were made by *Vincent & Röttger* [1980], followed by *Röttger & Ierkic* [1985], who proposed the method that is most commonly used. The AOA is a measure of the power-weighted mean position of the radiowave backscatter, calculated from the cross-correlation phase difference between pairs of receivers. Figure 1.7 shows the manner in which this information is retrieved from the cross-correlation function.

Using a simple geometric calculation, if the distance and phase difference between two receiving antennas i and j are denoted d_{ij} and ϕ_{ij} respectively, then the incidence angle, or AOA, in the plane defined by the vertical direction and a line joining the two receiving antennas is given by

$$\delta_{ij} = sin^{-1}(\frac{\lambda\phi_{ij}}{2\pi d_{ij}}). \tag{1.12}$$

This method works entirely in the time domain. The AOA can also be calculated in the frequency domain using cross-spectra, although this method is more susceptible to the effects of outliers (e.g. *Chau & Balsley* [1998]) and is not as commonly used as the time domain method that has been described here. The time domain method is used to calculate the AOA values in this thesis.

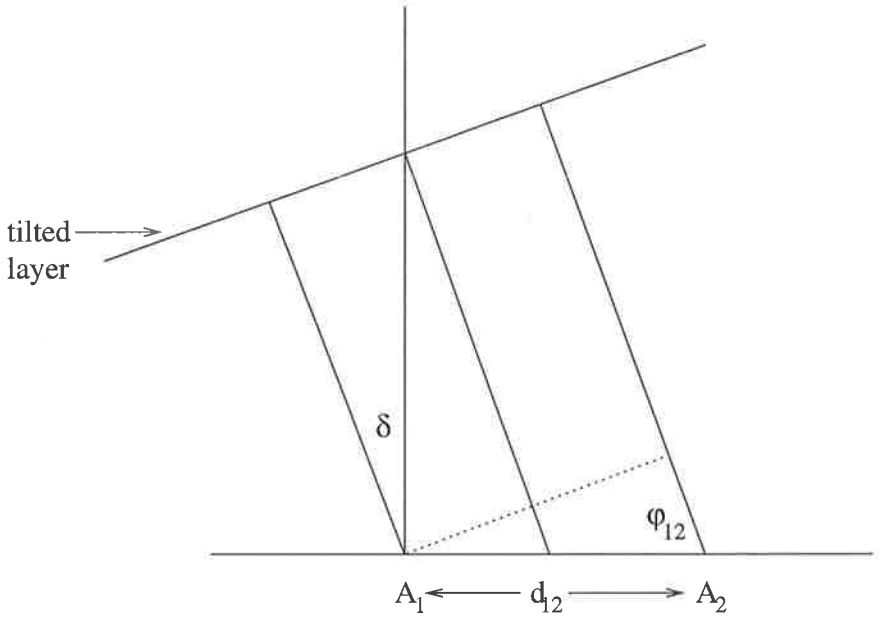

Figure 1.6: Schematic of the phase difference induced between antennas 1 and 2, by the tilting of a refractivity layer, adapted from *Rottger & Ierkic* [1985].

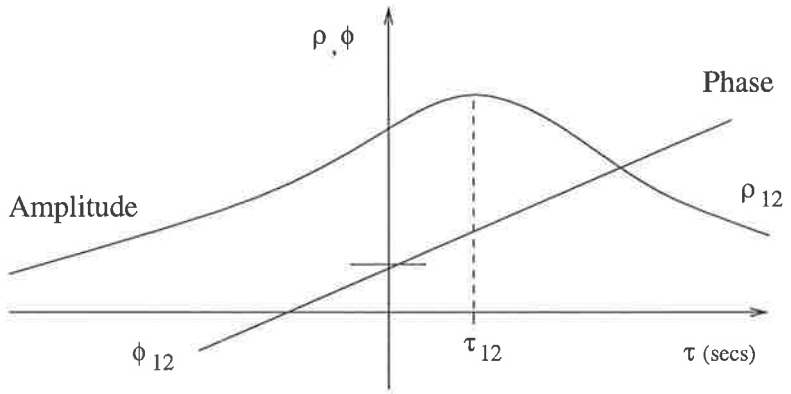

Figure 1.7: Schematic of an ideal cross-correlation function for the signals received in two spatially seperated antennas, 1 and 2. The slope of the phase of the cross-correlation function is a measure of the angle of arrival of the signal between antennas 1 and 2, adapted from *Rottger & Ierkic* [1985].

A number of AOA studies have been carried out in the ST region since the first efforts by *Vincent & Röttger* [1980] and *Röttger & Ierkic* [1985]. These studies include *Röttger et al.* [1990], *Palmer et al.* [1991], *Larsen & Röttger* [1991], *VanBaelen et al.* [1991b] and *Palmer et al.* [1998]. With the exception of the last of these studies, the determination of the AOA was with the aim of examining and/or correcting the effect of the tilted layers on vertical velocities. The last of these studies, that by *Palmer et al.* [1998], extended this aim by examining the relationship between the AOA observed on spaced receivers, and the power distribution in beams directed at small off-zenith angles. The assumption with AOA measurements is that the measured incidence angle is equivalent to the location of the peak in the backscattered power distribution as a function of off-zenith angle. *Palmer et al.* [1998] showed that this assumption is reasonably accurate, and were able to calculate an incidence angle from the off-zenith power which agreed well with that from the spaced antenna measurements.

1.5 Techniques to measure aspect sensitivity

Various modelling studies have attempted to relate the behaviour of the scatter as seen in Figure 1.2 to the behaviour of scattering structures in the atmosphere. Studies include those by *Gage & Balsley* [1980], *Doviak & Zrnić* [1984], *Waterman et al.* [1985] and *Tsuda et al.* [1997a]. In terms of characterising the general form of the scatter as seen in Figure 1.2, the most commonly used parameterisation is to assume that the polar diagram of the scatterers has the form

$$exp(-sin^2\theta/sin^2\theta_s), \tag{1.13}$$

where θ_s is the $1/e$ half width of the backscatter polar diagram, often termed the aspect sensitivity parameter or factor. For highly aspect sensitive scatter, θ_s approaches 0°, while purely isotropic scatter is characterised by larger values of θ_s. In practice, θ_s values in excess of about 10° to 20° can be regarded as almost isotropic. *Hocking & Hamza* [1997] have made use of the parameterisation to distinguish between scattering from anisotropic turbulence and reflection from specular layers. The authors concluded that the minimum θ_s value that can be expected if observed aspect

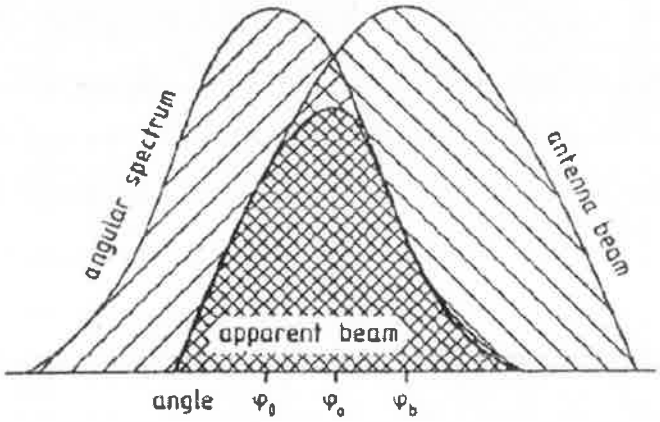

Figure 1.8: Schematic of the effect of aspect sensitive scatter on the effective angle of an off-zenith beam. The antenna beam is biased back towards zenith, resulting in an under-estimation in the horizontal wind velocity measured in the beam, after *Rottger* [1981].

sensitivity is the result of anisotropic turbulence is 5°, while they assert that θ_s values less then this limit are probably the result of specular reflection from layers.

Both DBS and SA methods have been used to calculate θ_s in the MST region using both MF and VHF radars. This thesis is concerned with measurements made in the ST region using VHF radars only, but it should be noted that measurements of θ_s in the mesosphere at MF, using a variety of techniques have been made by, for example, *Lindner* [1975a], *Lindner* [1975b], *Hocking* [1979], *Fritts & Vincent* [1987], *Reid* [1988] and *Lesicar & Hocking* [1992].

1.5.1 Doppler beam swinging methods

Figure 1.8 from *Röttger* [1981] shows the effect of aspect sensitive scatter on off-zenith Doppler beams. It can be seen that the finite width of the angular spectrum causes the off-zenith beam to be biased towards the vertical direction, which would result in an under-estimation of the horizontal velocity in that Doppler beam. The fact that the aspect sensitivity alters the measurement of parameters in off-zenith beams is utilised by most of the DBS methods of calculating θ_s. Assuming that the two-way polar diagram of a vertically pointing radar beam can be written

$$exp(-sin^2\theta/sin^2\theta_0), \tag{1.14}$$

where θ_0 is the beam width, *Hocking et al.* [1986] has derived relationships that enable the calculation of the aspect sensitivity parameter, θ_s, as well as the bias induced in an off-zenith beam.

Measurements of the signal power, $P(\theta)$, as seen on a vertical beam and an off-zenith beam directed at angle θ_A, where the subscript A denotes the apparent beam direction, can be used to form the ratio $r = P(0)/P(\theta_A)$. From this ratio of powers, θ_s can be determined

$$\theta_s = arcsin[(-sin^2\theta_A/lnr - sin^2\theta_0)^{\frac{1}{2}}], \tag{1.15}$$

and the effective beam direction, θ_E, resulting from this measured aspect sensitivity can be calculated

$$\theta_E = arcsin[sin\theta_A/(1 + sin^2\theta_0/sin^2\theta_s)]. \tag{1.16}$$

Another method of calculating θ_s from powers in Doppler beams that has been used in the ST region is a slight variation on the *Hocking et al.* [1986] technique. The method of *Hooper & Thomas* [1995], avoids the use of power observed on a vertical beam in favour of that measured on two off-vertical beams at off-zenith angles θ_1 and θ_2

$$\theta_s = arcsin[((sin^2\theta_2 - sin^2\theta_1)/lnr - sin^2\theta_0)^{\frac{1}{2}}], \tag{1.17}$$

where r=$P(\theta_1)/P(\theta_2)$.

These two methods are used to calculate θ_s in this thesis. Other DBS methods of measuring θ_s in the ST region are described by *Hocking et al.* [1990]. These alternative θ_s calculation methods involve attempting to estimate the degree to which the radial velocity (in an off-zenith beam) or spectral width (in a vertical beam) are underestimated due to the presence of specular scatterers. However, these methods are not in common use.

DBS measurements of θ_s in the ST region have been made by a number of authors, mainly using the technique of *Hocking et al.* [1986], but also by the method described by *Hooper & Thomas* [1995]. Studies include those by *Hocking et al.* [1990], *Yoe et al.* [1994], *Thomas et al.* [1997] and *Jain et al.* [1997].

1.5.2 Spaced antenna methods

One method of calculating θ_s from SA data is from the FCA output parameters. This method is called the spatial correlation method. The spatial correlation method relates the pattern scale, $S_{0.5}$, and axial ratio, R_{ax}, to the $1/e$ half width of the effective polar diagram of the scatter, θ_{sb}, by the equation

$$\theta_{sb} = \frac{15.2\lambda\sqrt{R_{ax}}}{S_{0.5}}, \tag{1.18}$$

where λ has its usual meaning. The aspect sensitivity can then be calculated from θ_{sb} by using the equation

$$sin^{-2}\theta_s = sin^{-2}\theta_{sb} - sin^{-2}\theta_b, \tag{1.19}$$

where θ_b is the beam width.

Another SA method of calculating θ_s utilises the post-set beam steering technique of *Röttger & Ierkic* [1985] to determine the effective beam direction. The principle is described in *Vandepeer & Reid* [1995]. The FCA spatial correlation method is used in this thesis to calculate θ_s values from SA data.

The fact that the DBS technique is by far the most popular method used on VHF ST systems has meant that there have been few studies of θ_s made using the SA methods in the ST region. Studies include the work of *Vincent & Röttger* [1980] and *Vincent et al.* [1987].

1.6 Motivation and scope

The motivation for the work presented in this thesis was to examine the nature of the scattering and aspect sensitivity of the lower atmosphere with a variety of techniques,

made possible with the upgrade of the BP VHF ST radar.

One aim was to use SA and DBS techniques together, an approach which has for the most part not been taken in earlier studies. In particular, there has been only one comparison of the relationship between the distribution of power as a function of off-zenith angle and the AOA measured in a spaced antenna arrangement; there have been few experiments comparing the wind velocity as measured by the spaced antenna FCA and DBS techniques in the ST region; and, there have not been any experiments which compare θ_s as measured using both DBS and FCA methods in the ST region. It is worth noting here that *Lesicar & Hocking* [1992] have made such a comparison in the mesosphere.

Another aim was to study the scattering of the atmosphere over a large range of off-zenith beam angles, over an extended period of time. In section 1.2, it was noted that a number of authors have investigated the distribution of power as a function of off-zenith angle. For the most part, however, the data for these studies were collected over very short time periods, ranging from one hour, up to 25 hours in duration. As such, one aim in the present work was to observe the nature of the distribution of power at many off-zenith angles in an extended data set, in order to gain a quantitative understanding of both the variability as a function of angle, and the angular ranges where aspect sensitivity and isotropic scatter dominate.

A substantial part of this project was to actually build and test the hardware added to the system in the upgrade, and to develop analysis routines to handle the new data. This thesis is therefore organised as follows.

Chapter 2 describes the radar with emphasis on the new capablilites of the system, and the author's contribution to the construction and testing. These new capabilities meant that this project was the first implementation of many-beam DBS measurements with the system. In addition, prior to the upgrade on the radar, all DBS analysis on the BP VHF system was performed in the time domain where contaminants could not be easily identified and removed. For these reasons, new analysis routines were developed by the author to analyse the DBS data in the frequency domain using spectra, and cleaning algorithms were developed to remove the various contaminants from the data. These procedures are described in Chapter 3.

The BP VHF ST radar is a relatively low power radar. As a result, it was only possible to consistently obtain radar data with high time resolution and good time coverage from tropospheric heights. As a result of this limitation, the results in this thesis have their emphasis on time coverage rather than height coverage. The details and results of these experiments are discussed in Chapters 4, 5 and 6. In Chapter 4, a comparison of FCA and DBS data collected with the new system is presented. In Chapter 5, a comparison of DBS and AOA data is presented. While Chapter 6 discusses a study of DBS data collected in many beam directions, in data sets comprising several days.

Chapter 2

The new VHF Doppler beam-swinging radar

2.1 Introduction

The Buckland Park (BP) VHF ST radar operates at a frequency of 54.1 MHz (approximate wavelength 5.5 m), a peak power of 32 kW and is located about 35 km north of Adelaide, at the Buckland Park field station (34°37′S, 138°29′E). The field site also houses an MF radar (1.98 MHz), a VHF boundary layer radar (54.1 MHz) and a three-field photometer, and is situated on a flat plain, approximately 3 km at the closest point from the coast of the Gulf of St. Vincent. The nearest orography is Adelaide Hills, some 50 km to the east, making the site essentially free from topographic effects, as westerlies dominate the local prevailing wind conditions.

The original BP VHF ST system was commissioned in 1984 and was designed for bistatic spaced antenna (SA) measurements and east-west monostatic Doppler beam swinging (DBS) measurements. First results appear in *Vincent et al.* [1987]. Since that time, the system has been used for the study of cold fronts (*May* [1986], *Low* [1996]), and associated gravity wave activity (*Eckermann & Vincent* [1993]), turbulence (*Hocking & Mu* [1997]), meteor wind measurements (*Cervera & Reid* [1995]), meteor shower observations (*Cervera* [1996]) and Faraday rotation measurements of

meteor echoes (*Elford & Taylor* [1997]). Beam-swinging on the system was only available in the east-west plane, and was enabled via a series of phasing cables which were changed manually. This meant that beam-steering at multiple angles was only possible by physically replacing the phasing cables after each data run. The system was capable of steering the beam to angles of 4°, 7° and 11° for atmospheric work, and 30° for meteor work. For atmospheric work, the system has been mainly run in SA mode, due in part to the fact that DBS was only obtainable in the east-west plane.

In 1995 work was begun to upgrade the radar to a flexible, electronically steered system, capable of DBS measurements at a variety of angles between data sets [1] in both the east-west and north-south planes, and SA measurements on multiple receivers. A new, antenna array was constructed and installed on top of the original transmission array. Both arrays can be split into groups allowing SA measurements to be made in a variety of configurations. A new receiver and data acquisition system (RDAS) capable of multiple gain settings and equipped with six receivers was installed, as well as a personal computer (PC) with on-line data analysis software, enabling instant fault diagnosis and correction at the field site. Beam steering on this new system is now possible with a resolution comparable to the beam-width of the radar via relay switched phasing cables under computer control. The new facilities of the radar for fast, multiple beam DBS measurements within a data collection period, and SA measurements on multiple receivers, make the system ideal for interesting combinations of these techniques.

The author's role in this upgrade was in the construction, testing and installation of the beam steering hardware. As such, this chapter will focus on the tests conducted by the author on various aspects of the new hardware including the new antenna array, the circuit boards and phasing cables that comprise the beam steering system, and the full radar in both DBS mode at a variety of off-zenith angles, and SA mode on multiple receivers. Also included in this chapter are details of the debugging and fault-finding that was applied to the radar as a whole when the new beam steering hardware was being installed.

[1] The system is not designed for inter-pulse beam steering.

2.2 Antenna arrays

The new system consists of two orthogonal arrays of coaxial-colinear (CoCo) dipole rows (see *Balsley & Ecklund* [1972], *Judasz* [1983]), as shown in Figure 2.1. The two sets of antennas are arranged such that the dipole rows in the North-South array[2] are orthogonal to the dipole rows in the East-West array. Note from Figure 2.1 that the arrays are actually aligned along a north-south axis that is 4° west of north, and parallel with the MF radar array at the BP field site. This alignment of the arrays from true north was set so that the array is aligned with the site boundaries. The area covered by the coincident arrays is approximately square, being almost 7900 m^2 with sides of length close to 89 m each.

The original East-West array consists of 32 CoCo rows [3] which are split into two groups, separated by one wavelength (λ), to accommodate the transmitter caravan between them. The new North-South array consists of 64 CoCo dipole rows, 32 on either side of the caravan. The rows in each array are centre fed, separated by $\lambda/2$ and raised $\lambda/4$ above the ground. Each row in the East-West array consists of 48 half-wave dipoles; 1536 dipoles in all. The rows in the North-South array consist of two strings of 22 half-wave dipoles each; 1408 dipoles in all. Each dipole has a physical length of 0.67λ to account for the velocity propagation of the signal within the cable. In order to improve the efficiency of the array, there is a ground plane beneath the antennas which consists of individual copper wires, spaced $\lambda/4$ apart in both directions. Both arrays are weatherproof. This was achieved by applying a silastic coating applied to the joins between pairs of antenna elements, and then wrapping the joint with ultra-violet resistant covering tape. The antennas in the existing East-West array were weatherproofed in this manner over a period in 1995, while the new North-South array was weatherproofed as it was being constructed in 1996.

These CoCo arrays can be used for both transmission and reception in DBS or SA modes. In addition to the CoCo arrays, the system also contains three sets of 16 Yagi antennas each which can be used for reception only. In the original SA radar system

[2]North-South refers to the array that produces northward and southward pointing beams, while East-West refers to the array that produces eastward and westward pointing beams.

[3]Note that the beam is swung in the east-west plane so antenna rows are aligned in the north-south direction.

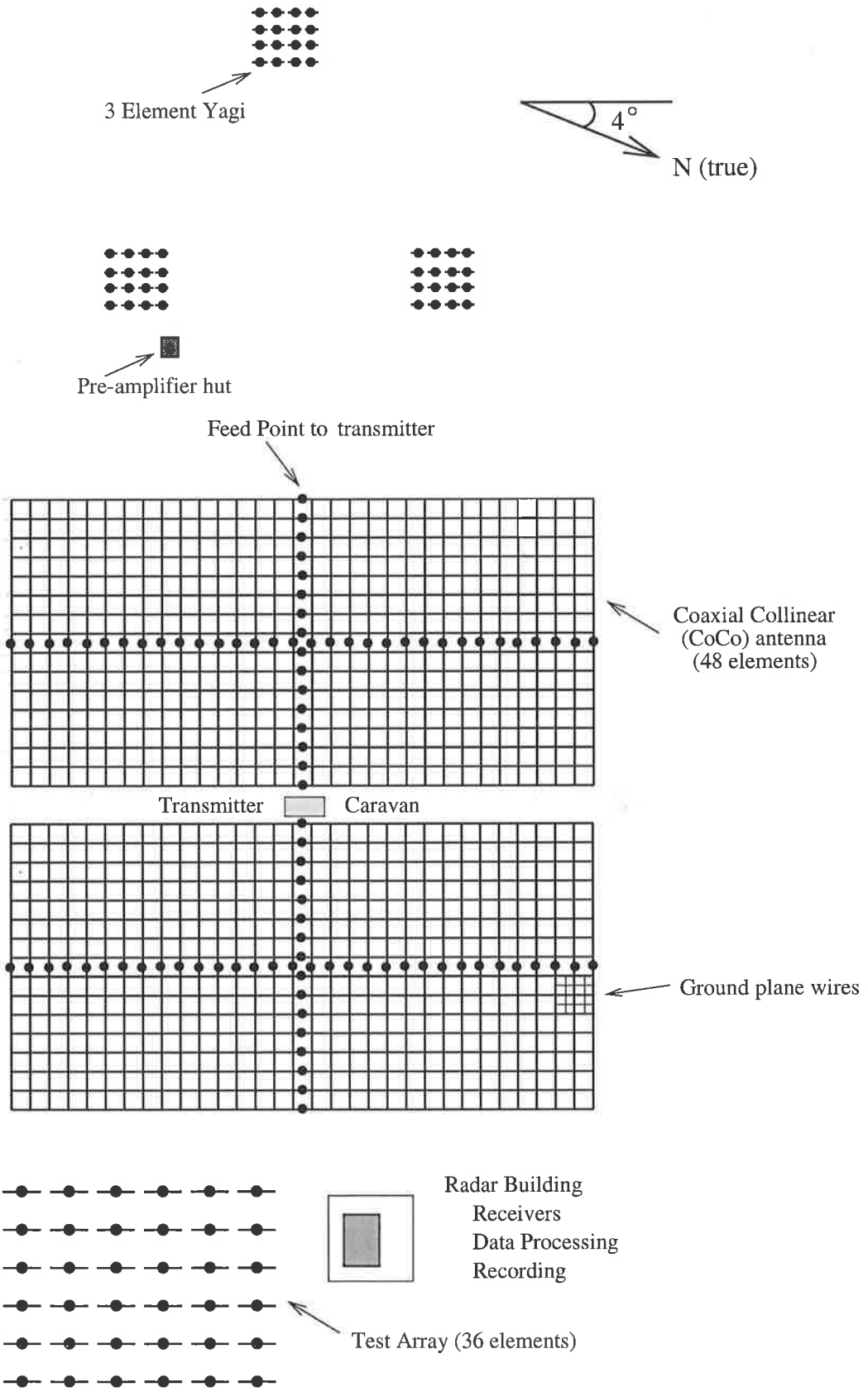

Figure 2.1: The Buckland Park VHF radar array and associated buildings.

described by *Vincent et al.* [1987] the East-West CoCo array was used for transmission while the three sets of Yagi antennas were used for reception, thus comprising a bi-static radar system. The BP VHF ST system is shown in Figure 2.1. Also shown in this diagram is a general purpose VHF test array.

2.2.1 Antenna array phase checks

DBS on transmission is achieved by inserting phase delays between antennas, in hardware. A basic assumption therefore, is that a vertically directed antenna array should have equal values of phase at each of the elements of the array. In early 1997, measurements of the phase at each of the centre feeds for a vertically pointing beam on the new North-South array were carried out. These measurements were made using a current probe (or current detector) identical to the one constructed by *Cervera* [1996], and used by *Cervera* [1996] and *Low* [1996] for measurements of the phase on the existing East-West CoCo array in 1992. For the measurements on the new array, the probe was reconstructed owing to its deteoriation since the 1992 measurements. Figure 2.2 shows a diagram of this device.

The phases at the centre feeds of each row were measured by first feeding a test signal at 54.1 MHz into the row from the transmitter caravan. The current probe was then placed a fixed distance from the centre feed and used to measure the amplitude and phase of the signal appearing on the antenna from the caravan. Finally, this phase measurement was compared with a phase reference which was taken from the test signal, prior to it entering the row antenna. In initial current probe measurements, it was found that the position of the cable back to the caravan from the current probe had a large affect on the results. When the cable lay on the ground directly above buried feeder cables from the caravan to the antennas, the amplitude and phase measurements were quite different to measurements on the same antennas when the cable was remote from any buried cables. In order to avoid this 'pick-up' of current in underground cables, the cable back to the caravan was kept away from the centre of the array where the underground cables are buried.

The current probe itself consists of a double loop of coaxial cable, through which

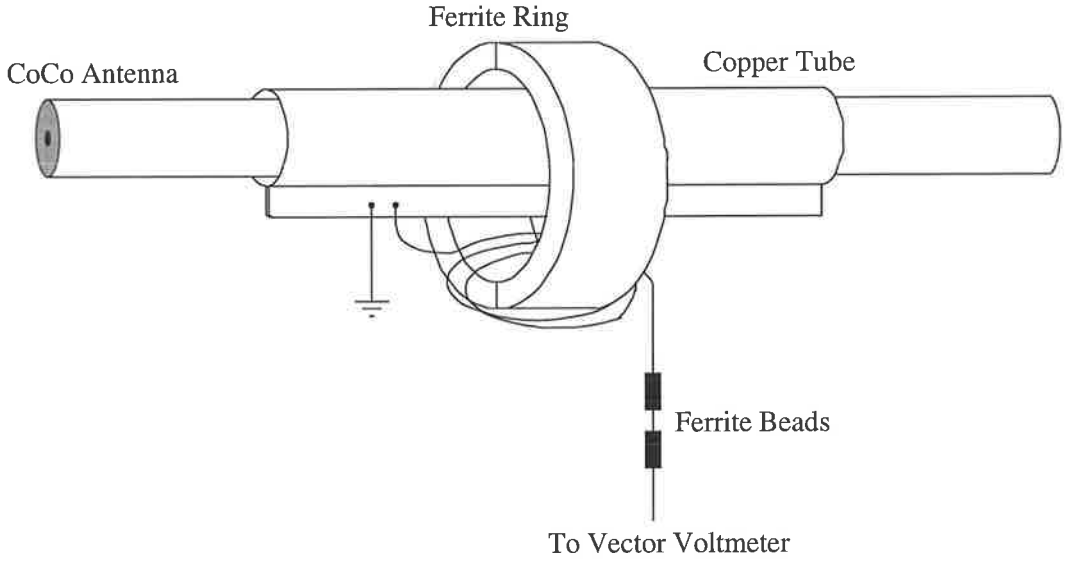

a)

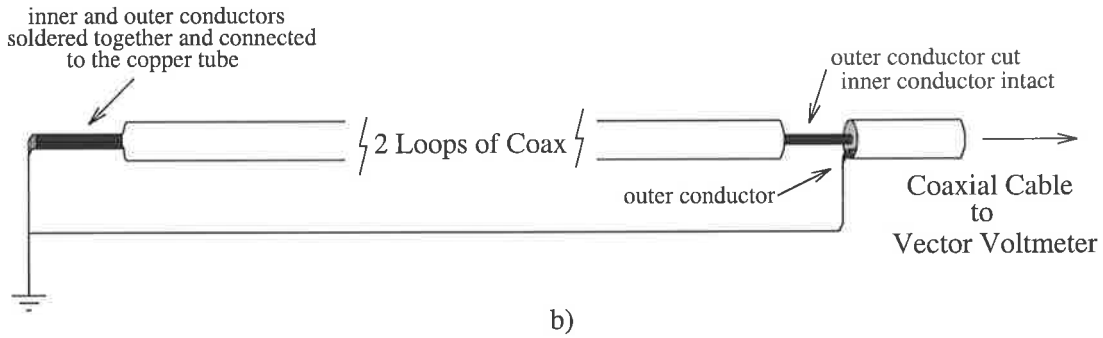

b)

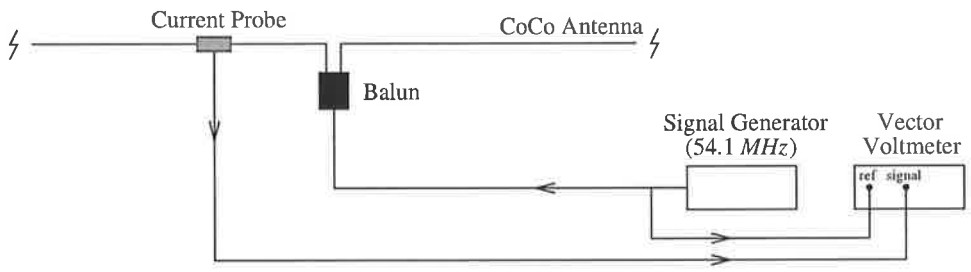

c)

Figure 2.2: (a) A schematic of current probe on a row antenna of the CoCo array, (b) a close up of the coaxial cable component of the loop antenna and (c) a schematic of the current probe in action. After *Cervera* [1996].

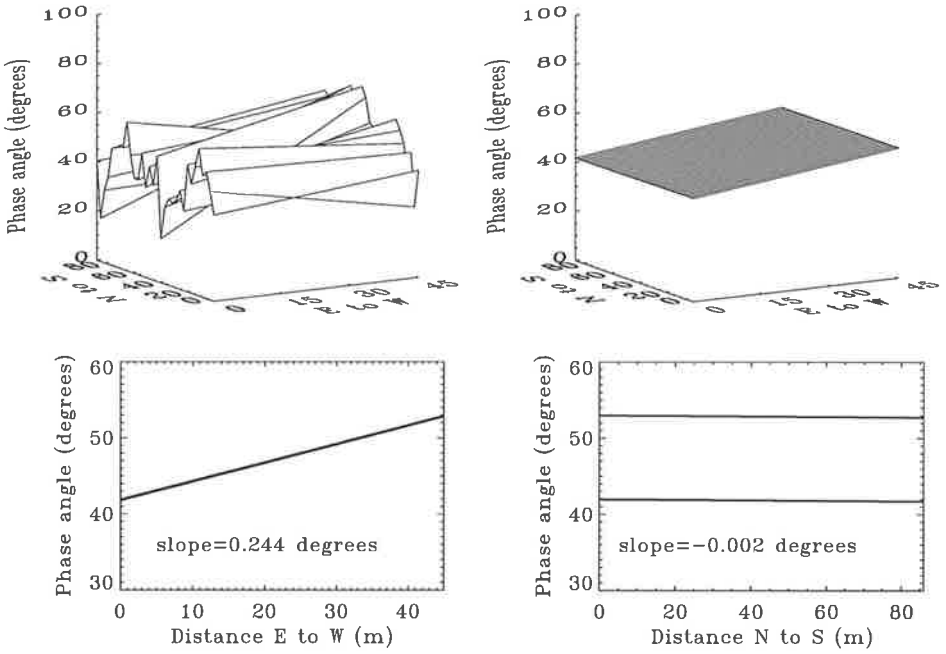

Figure 2.3: Top left: Phase surface of the North-South CoCo array from measurements made with the current probe. Top right: Plane surface fitted to phase slope. Bottom left: east-west cross-section of the plane surface. Bottom right: north-south cross-section of the plane surface. Note that the east-west axes on all of the plots correspond to the distance between the centre feeds of the two parallel rows of dipoles in the North-South array, while the north-south axes correspond to the full distance covered by the 32 paired dipole rows of the North-South array.

any current fed into the centre feed of the row antenna is detected. A grounded copper tube placed over the row antenna shields the loop antenna from electrical radiation of the CoCo antenna so that any current measured in the loop antenna is induced by the radiated magnetic field only. In order to increase the coupling between this loop antenna and the CoCo row antenna, a ferrite core is placed around the copper shield and through the double loop of the loop antenna. Ferrite beads were also placed on the cable back to the vector voltmeter to help in shielding the signal from stray 'pickup'. A more in depth description of the original design and construction of the current probe can be found in *Cervera* [1996].

Figure 2.3 shows the results of these measurements. The top left plot is the actual phase measurements made at the centre feeds of the two halves of the North-South array, while the top right plot shows a surface fitted to the measurements. The bottom two plots show the two orthogonal cross-sections of the fitted surface. It can be

seen that there is a net phase slope of the array of approximately 0.24° from east to west; the slope in the north-south direction is insignificant in comparison. This means that a nominally vertical beam will actually point at an off-zenith angle of approximately 0.24°, in the westward direction, assuming that the physical slope of the ground beneath the array is zero. This 0.24° off-zenith angle measurement is of the same order of magnitude as the 0.13° eastward value resulting from the slightly tilted East-West array, as seen in the results of *Low* [1996] for the 1992 phase test measurements. In addition to these electrical phase slopes, Kazempour[4] has measured the slope of the ground under the Buckland Park CoCo arrays with a high degree of precision. These measurements reveal a marginal slope beneath the array which results in a net beam pointing direction of 0.18° from the zenith, at an azimuth angle 30° west of south.

As well as providing useful information on the electrical phase tilt of the antenna array, the use of the current probe to check the phasing of the array turned out to be a useful tool in the identification of a balun that was incorrectly wired when the antenna array was constructed. The balun at the centre of each row of antennas is constructed by connecting the underground coaxial cable from the transmitter caravan firstly to one side of the centre, then via a $\lambda/2$ loop of coaxial cable, to the other side of the centre. This introduces a 180° phase difference across the centre feed of each of the antenna rows. Initial testing of the phasing of the antenna array using the current probe revealed an approximately 180° phase difference between a measurement on one antenna that and that on all of the others. A simple check of the construction of the offending balun revealed that the 180° phase delay across the centre feed had been introduced from the wrong side of the centre feed. This was corrected, bringing the phase value as measured by the current probe back in line with those on the other antenna centre feeds.

[4]Private communication, 1996.

Cable length (mm)	Ideal phase delay ($degrees$)
112	11.25
248	22.5
484	45.0
1038	90.0
1932	180.0

Table 2.1: Phasing cable lengths and corresponding ideal phase delays.

2.3 New beam steering hardware

The main design criteria of the new beam steering hardware was to be able to swing the beam of the radar with a resolution of the same order of magnitude as the full beam width; approximately 3.6°. This requirement set the minimum phase difference, $\Delta\phi$, between antennas separated by distance d, equal to 11.25° via the equation

$$\Delta\phi = \frac{2\pi d}{\lambda} sin\theta, \tag{2.1}$$

where θ is the off-zenith angle and λ is the wavelength of the radar. Other phase differences are then integer multiples of this minimum phase difference, such that the full range from 11.25° up to 360° between antennas can be achieved. These phase differences correspond to the cable lengths that must be inserted between antennas to achieve the desired delays. For example, the minimum phase difference of 11.25° corresponds to $\lambda/32$ where λ is approximately 5.5 m. Five cables of lengths: $\lambda/32$, $\lambda/16$, $\lambda/8$, $\lambda/4$ and $\lambda/2$ are needed to produce the full range of phase differences.

In practice, coupling between cables in close proximity to one another, meant that these cable lengths did not produce the exact phase differences required. As such, some effort was spent trying to optimise the cable lengths to get the maximum number of angles as close to their ideal value as possible. The phasing cables were optimised in order of decreasing length, due to the fact that the largest cable lengths make the greatest contribution to any phase delay that they are required for. Table 2.1 shows the final lengths of the five phase delay cables and the corresponding ideal phase delays.

Once the optimum lengths of the five individual cables had been selected, 64 sets of cables were measured, cut and stripped, prior to installation on to the printed circuit

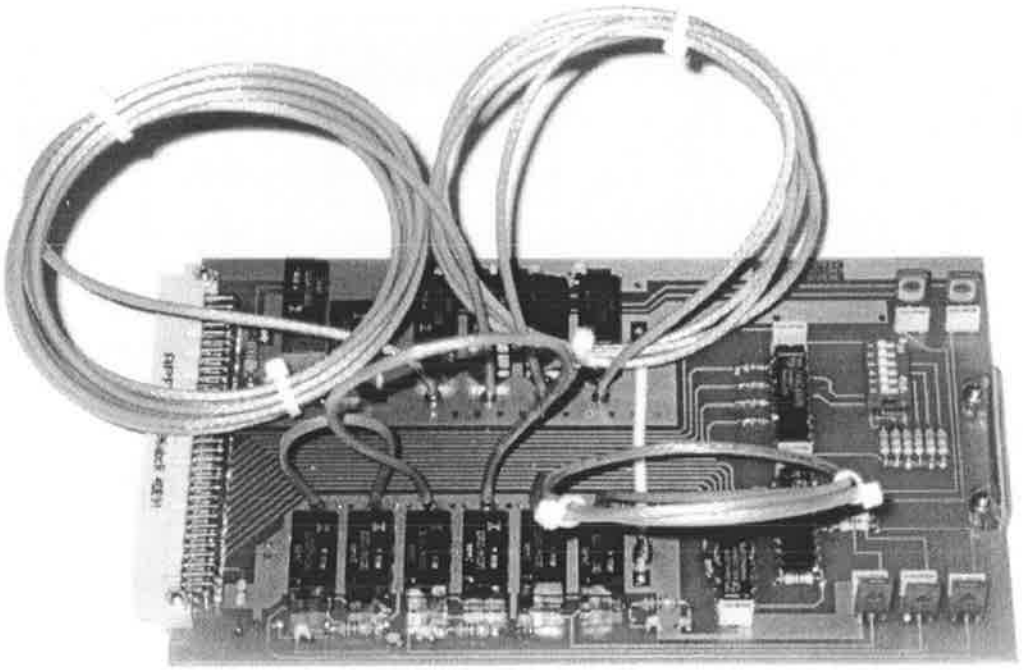

Figure 2.4: Top face of a beam steering card, note the five phasing cables.

boards which enable the selection of the phasing cables to be computer controlled. One set of five cables is required for each of the 64 antenna rows in the North-South array, and two sets of five cables, combined into 32 pairs, are required for each of the 32 antenna rows in the East-West array. The beam swinging unit was designed to swing a beam either on either the North-South array, or the East-West array, so that the 64 sets of phasing cables are inserted into one array or the other. Both arrays are connected to the beam swinging rack, but only one of the two arrays is phased, transmitted into and received from at any given time. The phasing cables were then installed along with relays on to printed circuit boards (or cards), thereby enabling electronic switching between various cable combinations for a given antenna row.

Sets of eight beam steering cards were combined into one rack, along with an additional circuit board, called a driver card through which communication between the interface unit and the phasing cables on the beam steering cards is facilitated. These eight racks were then stacked into a large chassis, along with a power supply and an interface card to enable communication with the PC in the receiver hut. Photographs of a single beam steering card appear in Figure 2.4 and Figure 2.5, while Figure 2.6 is a

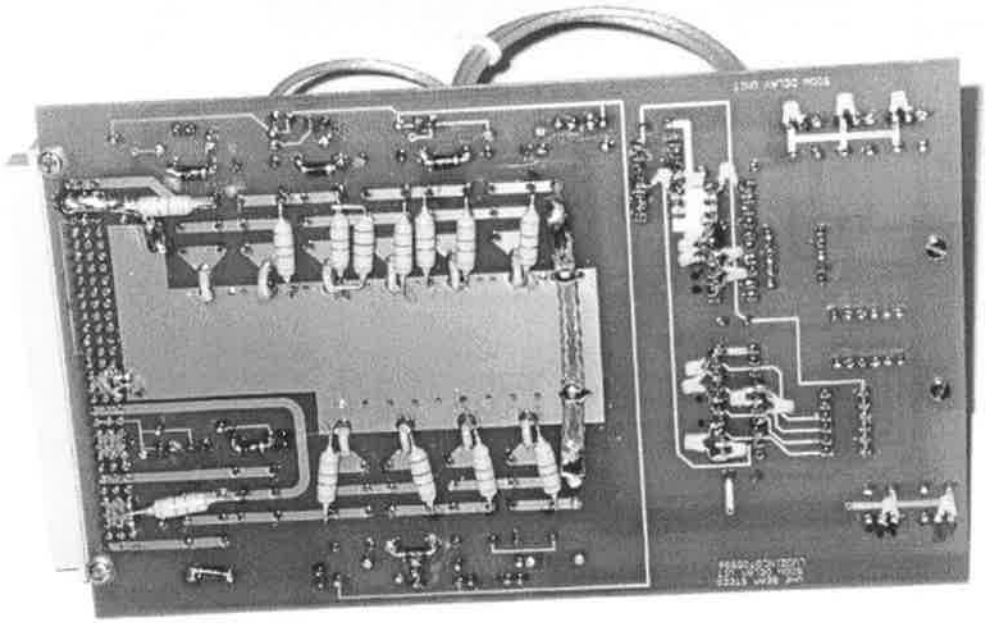

Figure 2.5: Bottom face of a beam steering card.

schematic of the beam steering hardware as it appears in the chassis in the transmitter caravan. Appendix A contains a circuit diagram of a beam steering card.

2.3.1 Testing of phase steering cards and error implications

As each rack of eight beam steering cards was built, the phase delays of each of the cards were tested in a variety of ways. For the first rack built, the phase delays on each card were checked for every possible combination of cables on the card. Initially, the phase delay was measured on a single card where only that card had the relevant cables switched in. Then, the phase delay was measured on the same card, where all of the eight cards in the rack had the relevant cables switched in. Figure 2.7 shows the difference between the average phase delays as measured on the eight individually switched cards, and the average phase delays as measured on the eight cards switched in unison, as a function of ideal phase delay. It can be seen that this difference is positive for all but one of the angles, which implies that the effect of switching in phasing cables on many cards at once is to slightly decrease the measured phase delay on any one card.

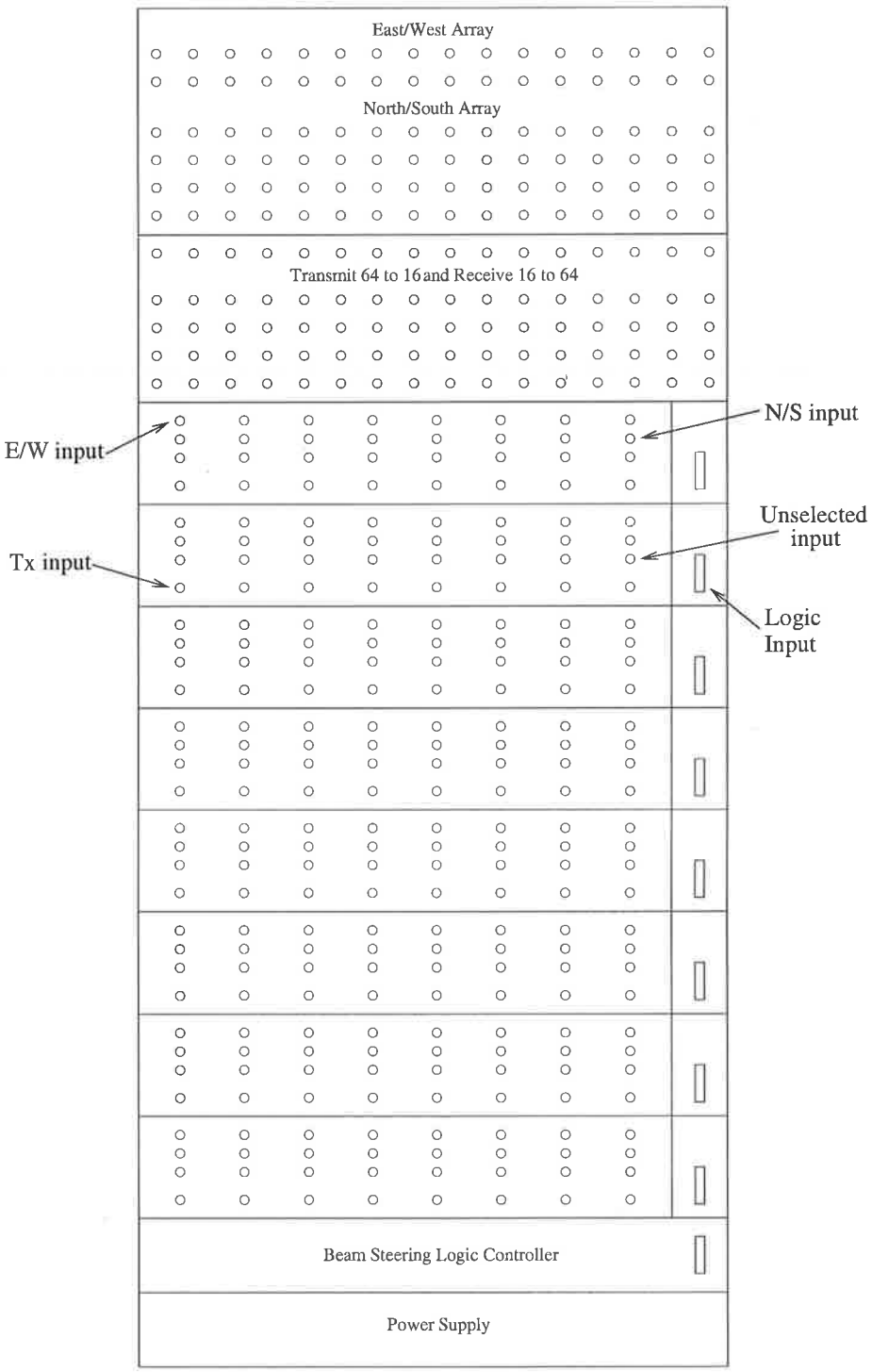

Figure 2.6: Schematic of the eight beam steering racks in the chassis with the other associated beam swinging hardware, in the transmitter caravan at the Buckland Park field site. Each circle on the rack is a BNC connection. The racks in the chassis are, from top to bottom, the antenna patchboard, the 64 to 16 combiner (or 16 to 64 splitter), the eight beam steering racks, each containing eight beam steering cards, the rack containing the PC interface card which controls the beam steering logic, and the power supply which provides 5 V and 24 V to the beam steering cards.

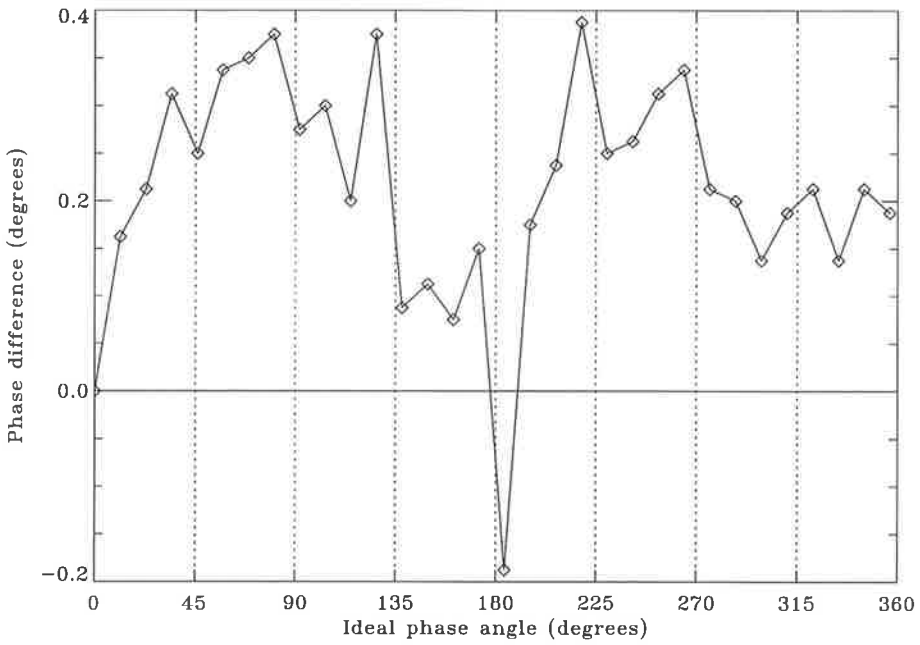

Figure 2.7: Differences between phase delay measurements made on each of eight cards with only a single card switched at a time, and phase delay measurements made on cards with all eight cards switched at once.

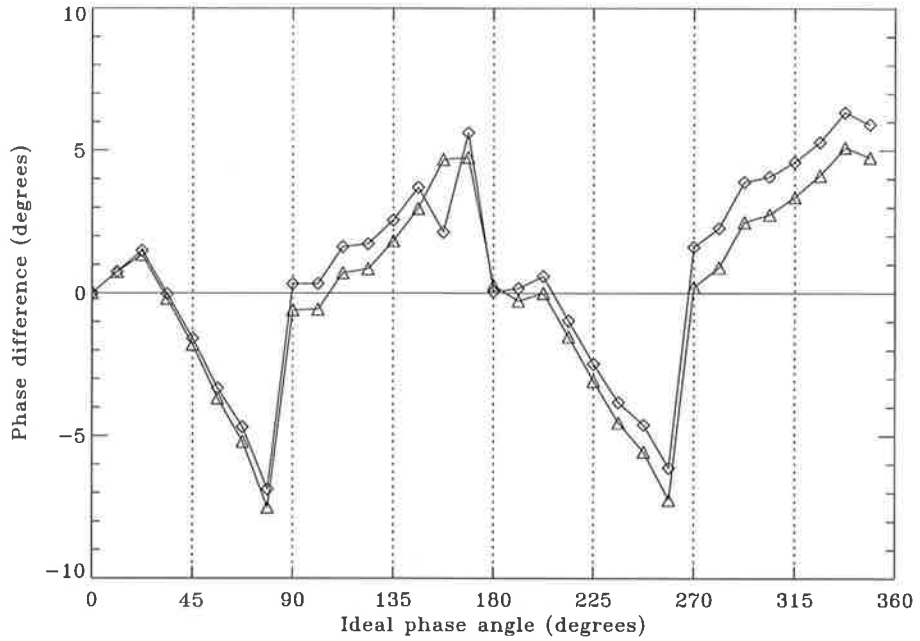

Figure 2.8: Differences between the average phase delays of the first two beam steering racks and the corresponding ideal phase measurements. Triangles represent results from the first rack and diamonds represent results of the second.

Ideal phase delay (deg)					# cables	Mean abs. difference (deg)
0					0	0
11.25	22.5	45.0	90.0	180.0	1	0.93
33.75	56.25	67.5	101.25	112.5	2	1.75
135.0	191.25	202.5	225.0	270.0		
78.75	123.75	146.25	157.5	213.75	3	3.73
236.25	247.5	281.25	292.5	315.0		
168.75	258.75	303.75	326.25	337.5	4	5.14
348.75					5	5.33

Table 2.2: Ideal phase delays for all possible combinations of cables. Also shown are the number of cables required to produce a given phase delay, and the mean absolute differences between phase delay measurements made on the 16 cards of the first two beam steering racks and their corresponding ideal values.

Measurements of the phase delays on each of the eight cards for all possible cable combinations, with the relevant cables on all of the eight cards switched in at once, were also made for the second of the eight racks. The average of these eight measurements in each rack, represents the average phase delay for each combination of phasing cables, for the rack as a whole. Figure 2.8 shows the difference between these average values and the ideal phase delays for a given combination of cables, as a function of ideal phase delay, for the the two beam steering racks measured.

The shape of the curves in Figure 2.8 is explained by the number of cables that are required to produce the desired phase delay on a card. Table 2.2 lists the values of the ideal phase delays and the total number of delay cables required to produce them. Also shown in Table 2.2 is the mean absolute difference between the phase delay measurements on the 16 cards in the first two racks and the corresponding ideal phase delay values. It can be seen that the deviation of a given phase delay measurement from the ideal value increases as the number of phasing cables that are switched in, increases. These results reveal that for any combination of phasing cables, the resultant phase delay produced on the beam-steering card is within just over 5° of the ideal value.

In practice, this small error in the absolute phase delay applied to a given beam steering card is insignificant. This is in part due to the cyclic nature of the difference

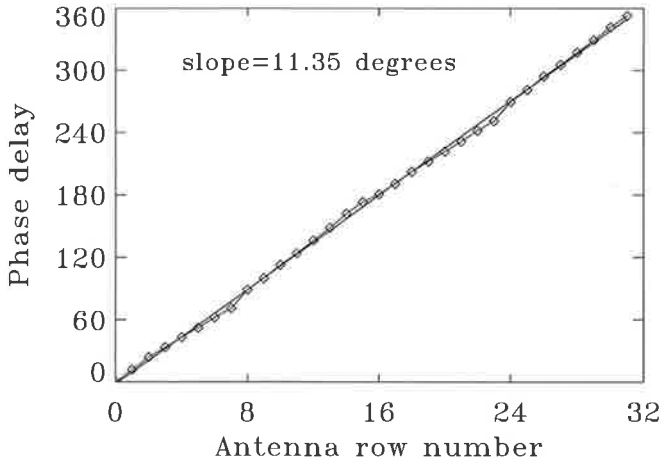

Figure 2.9: Phase slope across the North-South CoCo array to produce an off-zenith angle of 3.6°. Also shown is the linear fit and slope to the measured values.

between the measured and ideal values, as seen in Figure 2.8. Over the full 32 rows of antennas, the differences between the measured and ideal values almost completely cancels out, leaving a phase slope across the array, or an off-zenith angle, within a fraction of the ideal value. Figure 2.9 shows the phase slope across the North-South array for an off-zenith angle of 3.6°, measured on a single card from the second beam steering rack. It can be seen that the slope is only fractionally different from the ideal value of 11.25°. This difference produces an angle on the sky 0.03° different from the ideal value. The phase slopes averaged over all 16 cards for the first eight off-zenith angles, from 3.6° to 30°, differ from the ideal for a given zenith angle by less than 0.05° (not shown). This value is small compared to both the beam width of the full CoCo arrays, and the error introduced into the beam pointing direction caused by the antenna phase slopes, as discussed in Section 2.2.1.

For the remaining six beam-steering racks, phase delay measurements were made on each of the eight constituent cards for the case where only the same single cable was switched in on each card. In this way only the primary phase delay angles of 11.25°, 22.5°, 45°, 90° and 180° on each card were measured. By combining these measurements with the same from the first two racks, an indication of the variation in these primary phase delay values can be obtained, as well as the consistency that can be expected in the phase delays for all of the 64 beam steering cards. These results

Ideal phase delay (deg)	Actual mean phase delay (deg)	Stand. dev. (deg)
11.25	12.1	0.2
22.5	23.8	0.3
45.0	43.5	0.4
90.0	90.7	0.7
180.0	180.1	0.4

Table 2.3: Ideal phase delays for single cables and the corresponding mean measured phase delay values, as well as their standard deviations, for all 64 cards of the beam steering unit.

are presented in Table 2.3. Because of the fact that the cable lengths were optimised from the largest length to the shortest, the mean phase delays are closer to ideal for the larger lengths.

These results show that the beam steering unit can provide the required antenna phase delays with an accuracy and precision that will place the beam of the radar at the desired off-zenith angle, to within a fraction of the ideal value. Later in this chapter preliminary tests of the radar at the Buckland Park field site over the full range of angles will further verify the correct operation of the beam-steering unit.

2.3.2 Polar diagrams of the arrays

The antenna beam pattern, or polar diagram of the radar antenna array is a useful guide of the characteristics of the array, such as the width of the main lobe and the position of the sidelobes. Figure 2.10 and Figure 2.11 show the model one-way polar diagrams of the East-West and North-South arrays respectively, for vertically pointing beams. It can be seen that the two are very similar, the only minor difference being a slight increase in the power of the primary sidelobes of the North-South array relative to the East-West array. The half-power-half-widths of the one way (transmission or reception) polar patterns of the full arrays are 1.6° and 1.5° for the east-west direction and north-south directions of the East-West array respectively, and 1.6° for the east-west and north-south directions of the North-South array respectively.

The calculations of the parameters of the model polar diagrams depicted in Figure 2.10 and Figure 2.11 do not include the effects of factors such as an imperfect

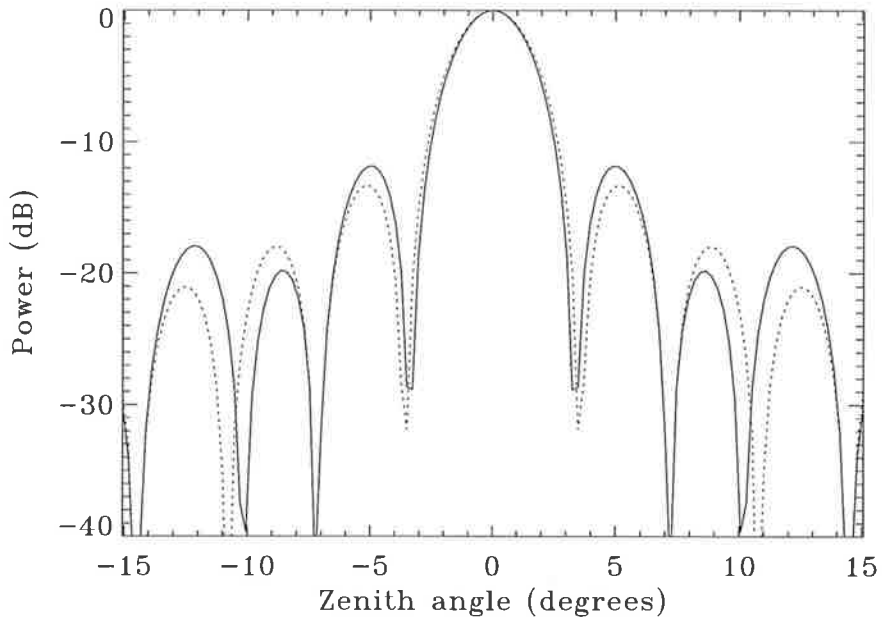

Figure 2.10: Cross-sections through the one way polar diagram of the East-West array for a vertically pointing beam. Solid lines denote the east-west cross-section and dashed lines denote the north-south cross-section.

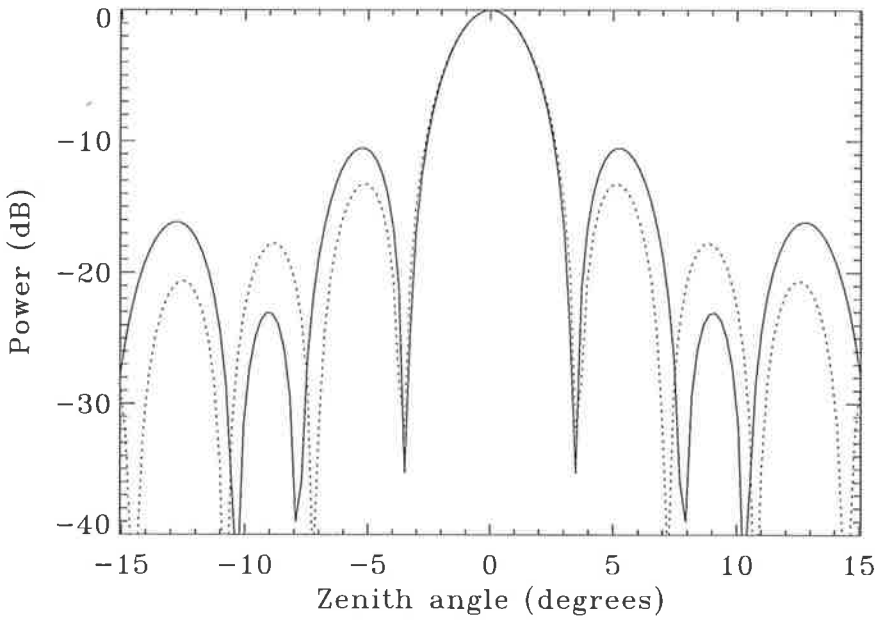

Figure 2.11: Cross-sections through the one way polar diagram of the North-South array for a vertically pointing beam. Solid lines denote the east-west cross-section and dashed lines denote the north-south cross-section.

ground plane, random errors in the phase and amplitude and phase of the current supplied to the elements, and attenuation of the signal along the CoCo rows. *Cervera* [1996] has included these factors in his polar diagram calculations. His results of show that these factors lead to polar diagram half-power-half-widths approximately 0.1° greater than those quoted above.

2.4 Transmitting and receiving systems

The placement of the beam steering unit in the transmit/receive (T/R) path of the radar is shown in Figure 2.12. This diagram shows that 64 cables from the 64 beam steering cards are connected to each of the 64 North-South array antenna rows, while another 64 cables from the cards are combined into 32 pairs, which are in turn connected to each of the 32 East-West array antenna rows. The beam steering cards have been set up so that pairs of adjacent cards are switched to the same angle. Pairs of cards are then connected to one antenna row in the East-West array, and to a pair of rows either side of the transmitter caravan that makes up one antenna row in the North-South array.

From the beam-steering rack the 64 beam-steering cards are then connected to a 64 to 16 combiner. The 16 outputs of this combiner are connected to the 16 T/R switches. In transmit mode, these switches pass 500 W of power from the 16 power amplification (PA) modules, through each beam steering card, to the antennas. In receive mode, the 16 outputs of the T/R switches are combined via a 16 to 4 combiner, to four ouputs. These outputs can be combined in a variety of ways depending on the experiment. Figure 2.12 shows each of these four ouputs connected to an individual preamp and then to each of four receivers in the receiver and data acquisition system (RDAS) which is housed in the receiver hut. Other options, not shown in Figure 2.12, include combining the four outputs of the 16 to 4 combiner into two receivers, each being connected to half of the appropriate array, or combining all four outputs of the 16 to 4 combiner to one receiver in the RDAS.

The RDAS houses six receivers. Data can be collected with variable gain settings over the range from 0-42 dB. Although the CoCo arrays can be split into as many

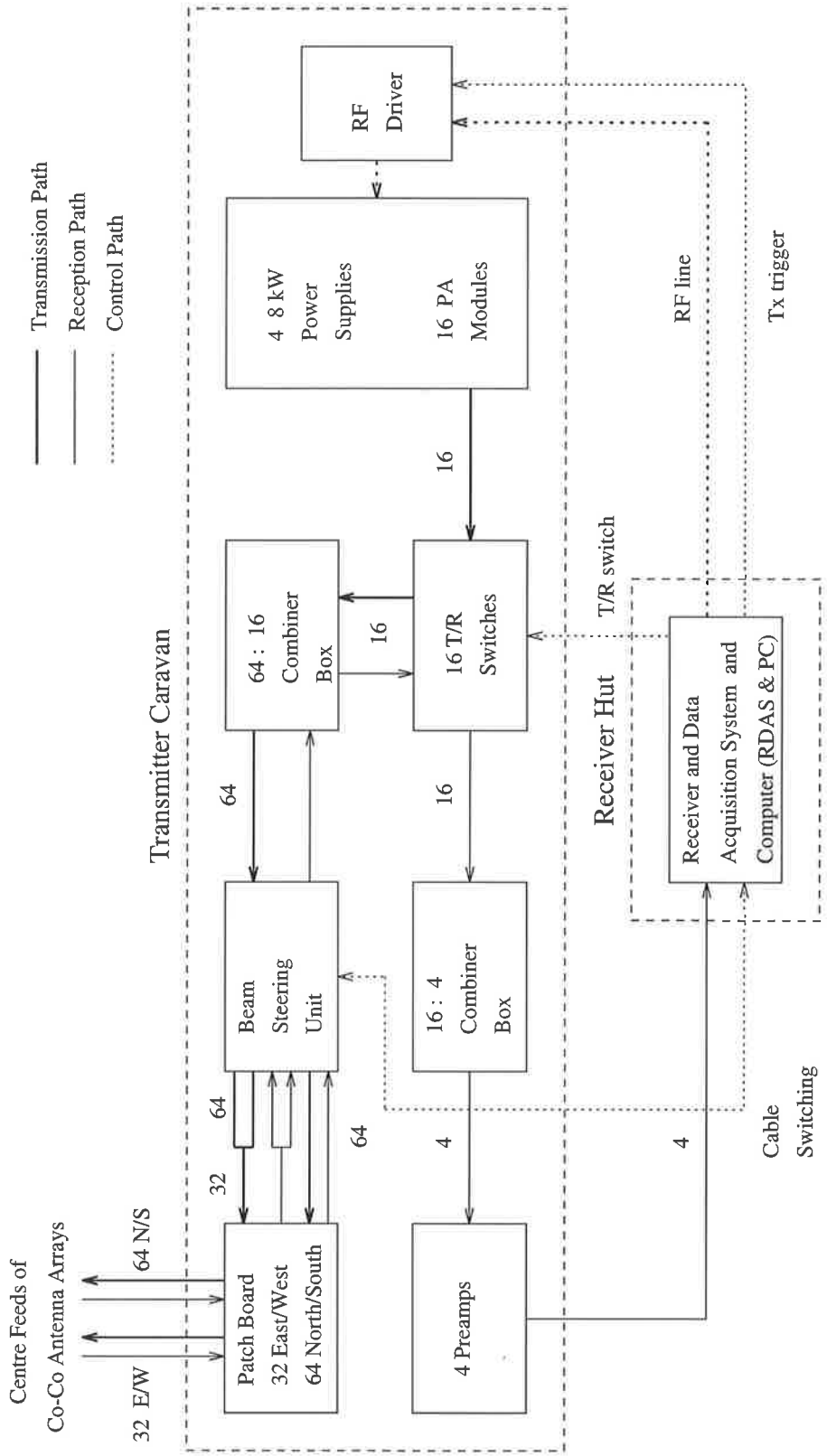

Figure 2.12: Schematic of the VHF radar hardware showing the transmission and reception paths from the CoCo arrays, as well as the control lines between the RDAS and the various transmitter hardware.

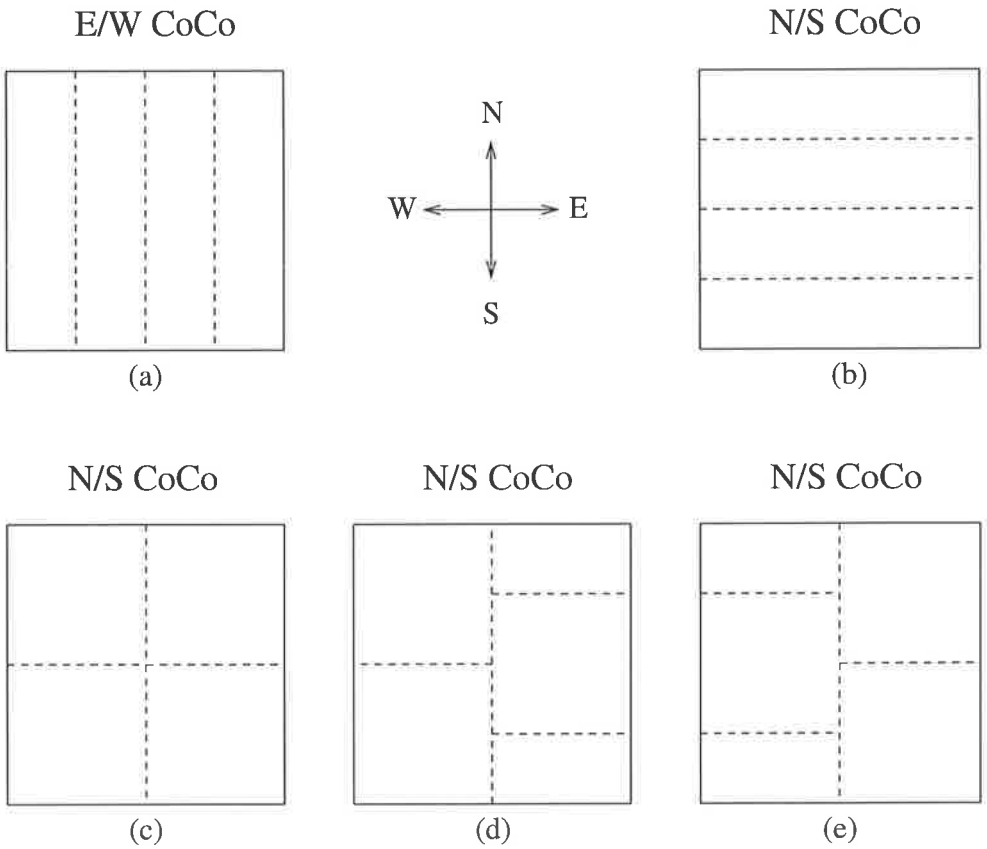

Figure 2.13: Schematic of some possible antenna configurations of the two orthogonal CoCo arrays.

sections as there are receivers, four receivers are adequate to carry out the analysis discussed in Chapter 1. Figure 2.13 shows the antenna combinations that are now possible with the new radar hardware. For the North-South array, a combination of configurations (b) and (c) is also possible. SA experiments presented in this thesis were conducted in each of these combinations (except for (d) which is just the reverse of (e)). DBS experiments were run by either combining the output of multiple receivers to form a single Doppler beam in later analysis, or by combining the array groups in hardware, to collect data on a single receiver.

The installation of the new RDAS and beam swinging hardware into the system revealed a number of potentially damaging features of the interaction between these two new pieces of hardware and the existing transmitter hardware. In order to ensure the safety of the system as a whole, it was necessary to implement a number of hardware adjustments. For the benefit of future users of the system, and in order to

document the changes that were made, these modifications will be described.

2.4.1 Transmitter lockouts

Two new hardware lockouts were installed in the system to prevent the transmitter becoming operational in the event that the T/R switches were in receive mode, and in the event that the beam swinging hardware was swinging to a new beam direction. Logic gates were installed in the transmitter caravan where the T/R, Tx trigger, (where Tx here means transmit) and beam swinging signals enter from the receiver hut. Figure 2.14 shows the signals involved in these lockouts.

The first stage of Figure 2.14 prevents the Tx trigger signal, which provides information about the pulse length of the transmit beam, from triggering the transmitter in the event that the T/R switches are not in transmit mode. Only if the T/R switch signal is high (transmit mode) and the Tx trigger is high (on) will the Tx trigger signal be allowed to pass this gate. If the T/R switch signal is low (receive mode) the Tx trigger signal is sent low (off) also.

The second stage of Figure 2.14 is an extra stage made necessary by the introduction of the new beam swinging hardware. The relays on the cards in the beam swinging rack are not designed to be transmitted through while they are switching. The RDAS software does not attempt to switch the beam while the transmitter is operational, but the second logic gate shown in Figure 2.14 was added as an extra safety measure. This gate will only allow the Tx trigger signal to remain high (on) if the beam swinging signal is not high (beam not swinging). In the event that the beam swinging signal is high (beam swinging) the Tx trigger signal is sent low (off).

2.4.2 Preamp protection

Extra preamps were required to run the system in the split array modes now possible, as shown in Figure 2.13. The system now has four new preamps which have approximately 25 dB gain and are powered by 12 V from the receivers in the RDAS. Initial attempts to install the preamps and conduct sky noise runs with the system failed when the preamps were damaged by unexpected voltages entering from the antennas,

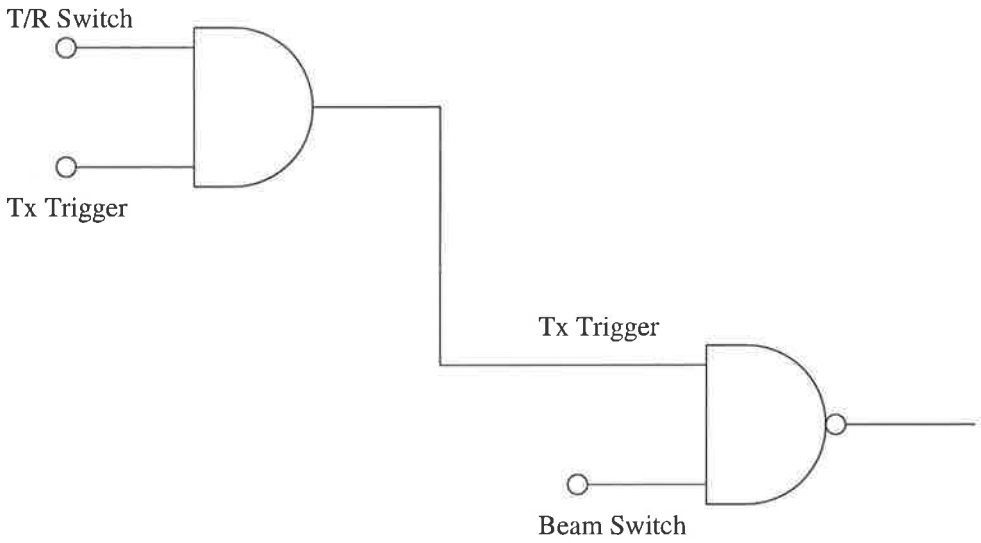

Figure 2.14: Logic gates controlling the transmitter. In the first stage the Tx trigger signal is kept high (on) only if the T/R signal is also high (on). In the second stage the Tx trigger is kept high (on) only if the beam swinging signal is not also high (on). If the beam swinging signal is high, the Tx trigger signal is sent low (off) and no transmission occurs.

which pass through the T/R switches to the preamps, as shown in Figure 2.12. This voltage was found to be the result of inadequate grounding of the backplane on the existing T/R switch rack. Up to 60 V peak-to-peak enters the preamp from the T/R switches when an entire CoCo array is combined and connected into one preamp, and then one receiver. A redesign of the back plane of the T/R rack is the ideal way around this problem, but for simplicity, an alternative solution was implemented in which diodes were connected across the antenna inputs to each of the preamps. This solution protected the preamps from the 60 V from the T/R rack such that they can now operate within the system as required.

2.4.3 RF interference with beam-steering logic

Initial tests incorporating one of the eight beam steering racks into the transmit path of the radar were unsuccessful. The layout of the electronics on the beam steering cards has logic circuitry and RF (radio frequency) lines in close proximity to one another. This design led to the RF actually triggering the beam steering unit into changing the phase delays on the beam steering cards. A solution involving a series of RC filters

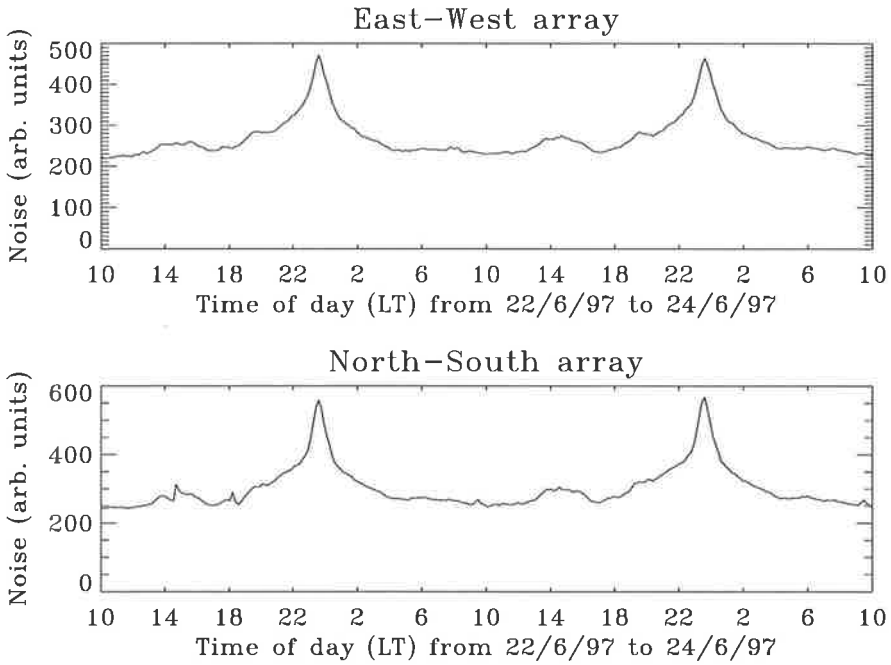

Figure 2.15: Sky noise as seen on the two orthogonal CoCo arrays of the radar over a two day period. The peaks on each day are due to the passage of the galactic centre through the beam of the radar. The units on the y-axis are arbitrary.

was implemented which protected the logic lines from the RF passing through the cards. The single beam steering card shown in Figure 2.4 and Figure 2.5 has this extra circuitry in place. The final switching time of the beam swinging rack in the system is of the order of 1-2 seconds, after the addition of the filters and the delays designed to prevent the beam position changing when the radar is transmitting.

2.5 Doppler beam-swinging tests

As a first test of the operation of the new North-South CoCo array, a noise run was conducted on the radar, with a vertical beam only. The North-South array was used for transmission, while both the North-South and the East-West arrays were used for reception on single receiver each. This test verified the use of the North-South array for transmission as well as the similarity of the response of the two arrays to sky noise. Figure 2.15 shows the results. It can be seen that the sky noise profile obtained from the North-South array is slightly more variable. This could be due to a variety of factors which include greater noise and interference generated by traffic on

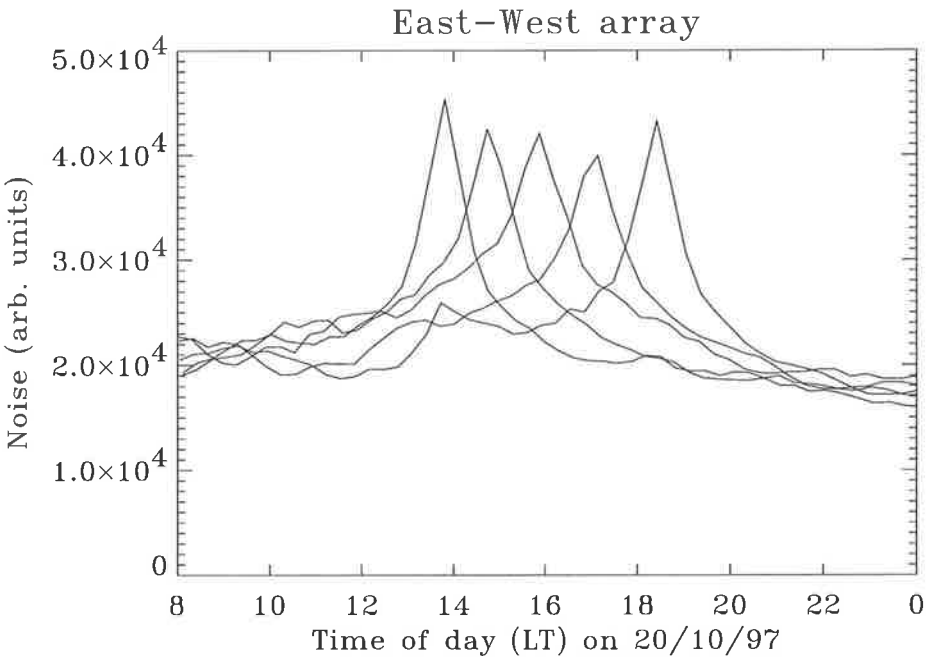

Figure 2.16: The galactic centre in five beams on the East-West array. The beam off-zenith angles are, from left to right, 30° east, 14.5° east, 0°, 14.5° west and 30° west.

the local main road, due east of the Buckland Park field site. This noise is more likely to affect the returns on the North-South array which was used for transmission as well as reception. The orthogonal polarisation of the East-West array with respect to the transmission of the radar in this experiment, means that backscatter will be received with relatively less power on this array than on the North-South array, which could explain the relative lack of noise on the East-West array.

Once the beam swinging hardware was installed, a noise run was carried out on all 62 possible beam directions. The beam of the radar was swung from vertical on the North-South array, through all the 15 off-zenith directions to the south and then to the north, followed by a vertical beam on the East-West array, and then all 15 off-zenith directions to the west and then to the east. Figure 2.16 shows the results for the off-zenith angles east 30°, east 14.5°, 0°, west 14.5° and west 30° on the East-West array only, while Figure 2.17 shows the results of this noise run, for all angles to which the beam was pointed.

The position of the peak that represents noise from the galactic centre can be used to verify that the beam of the radar is pointing in the right direction. The rotation

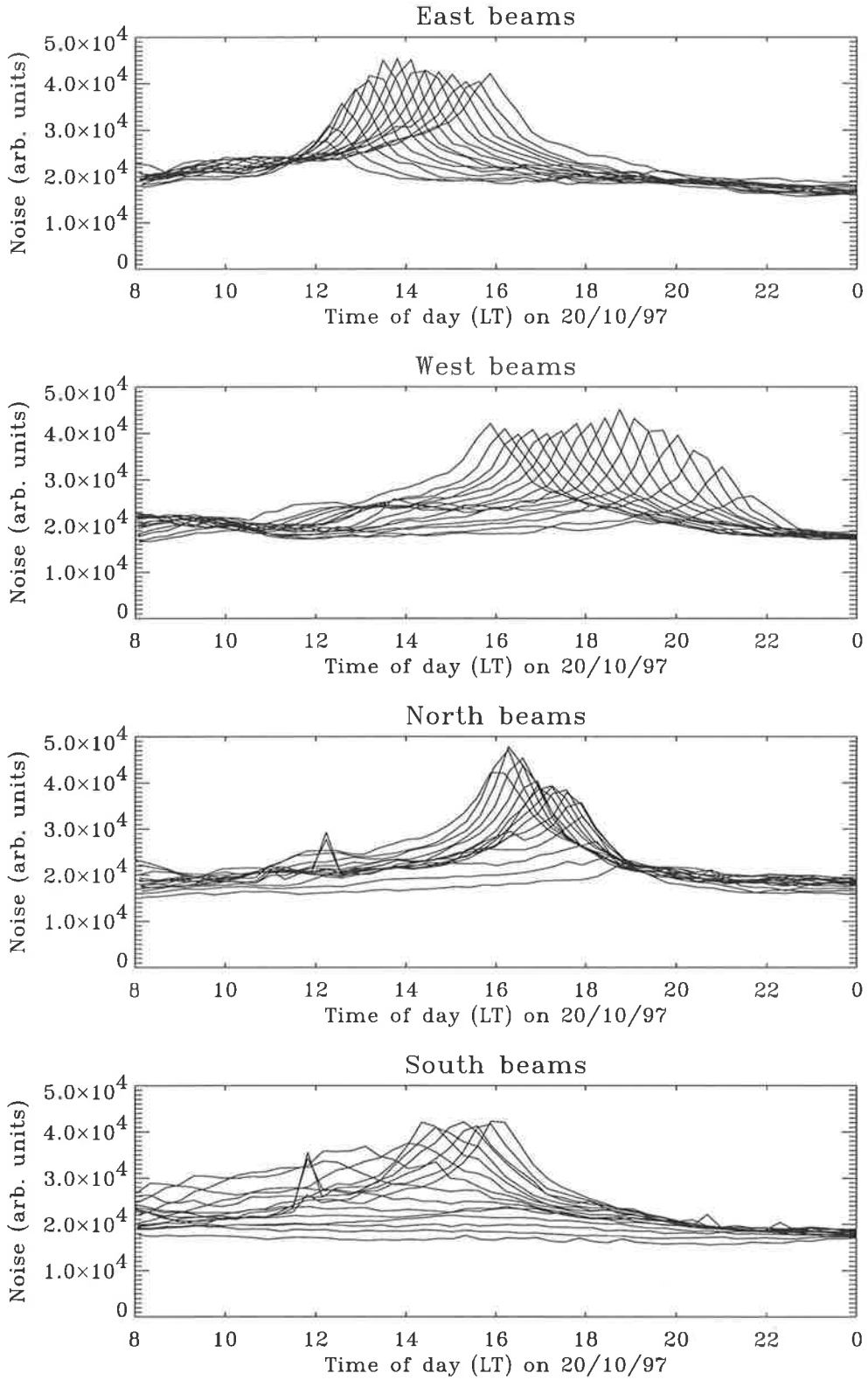

Figure 2.17: Sky noise as seen on North-South CoCo array of the radar over a one day period, at all possible off-zenith angles, in all four cardinal directions. The peaks on each day are due to the passage of the galactic centre through the beam of the radar.

of the earth relative to the galactic centre means that the galactic centre appears to move from east to west at a rate of approximately 15° an hour. This means that the five beams shown in Figure 2.16 should observe the peak approximately an hour apart from one another. It can be see from Figure 2.16 that this is the case, within the time resolution of the data set, which was limited to 20 minutes between successive points in a given direction, and accounting for the fact that the radar is not aligned exactly east-west (see Figure 2.1).

Figure 2.17 shows the behaviour of the galactic centre in all 62 beam directions. The top diagram shows the peak representing the galactic centre as seen in the range of eastward pointing beams from 69.6° east to vertical, from left to right. The galactic centre enters the eastern-most beam first, 69.6° off-zenith to the east, and appears later in each successively smaller off-zenith eastward beam, as expected. The second diagram from the top shows the galactic centre as seen in the range of westward beams from vertical to 69.6° off-zenith to the west. The galactic centre is seen in the vertical beam first before appearing in each successively larger off-zenith westward beam, as expected. Note that the galactic centre takes relatively less time to pass through the full range of eastward beams than it takes to travel through the corresponding range of westward beams. This is a geometrical effect of the fact that the array is not aligned exactly along the east-west plane, combined with the effects of the irregular shape of the galactic centre. The galactic centre is an elongated shape rather than a point source, which means that the beam of the radar beam samples different slices of the centre in the eastward and westward directions leading to this time slewing effect when comparing the times for symmetrical off-zenith angles in the two directions.

The third diagram from the top and the bottom diagram show the behaviour of the galactic centre in the northward and southward pointing beams respectively. The galactic centre passes to the north of Adelaide and, as such, it is expected that the peak will be seen in more northward pointing beams than southward pointing beams. It can be seen from these two bottom plots that this is the case. The combination of the results presented in Figure 2.16 and Figure 2.17 show that the beam-swinging unit is operating as required.

2.6 Receiver tests

As discussed in Chapter 1, the phase of the cross-correlation function at zero lag between time series received on a pair of channels, or, equivalently, the phase difference between a pair of channels, can be related to the angle of arrival (AOA) of the backscatter seen by the radar. The time variation of the AOA of the backscatter is an interesting and important measurement for the purposes of studying the changing orientation of tilted layers that may be present in the atmosphere. In order to take this measurement accurately, it is necessary to know what the base variation of the phase difference between receivers is, independant of any atmospheric variation. This will give an indication of the minimum AOA measurement that can be accurately made with the system.

An experiment was set up to combine all of the antennas into one output, but instead of putting this one antenna into one receiver, in the normal DBS configuration, the output was split into four and connected to four receivers. In this manner each of the four receivers were seeing exactly the same antenna and any variations in the phase of the cross-correlation function at zero lag as a function of time were due to the receivers, cables, and other hardware. The beam was directed at a range of angles from 0.0° on both the North-South and East-West arrays, to 3.6° and 10.8° off-zenith in all four directions. Figure 2.18 shows a time series of the phase difference between pairs of receivers for the times when the beam was directed vertically on the East-West array. The data in this figure have had the mean removed and are shown averaged over the range gates from 4 - 8 km, where the atmospheric signal is strong.

It can be seen from Figure 2.18 that there is a slight diurnal variation as a function of time in all but the data for receiver pairs 1 and 3 and 2 and 4. The data from these two pairs have less variation then the other pairs and show no systematic time variation. The diurnal variation is probably due to changing temperature in the VHF hut housing the RDAS. *Vandepeer* [1993] saw a diurnal variation in the phase differences between receivers in the RDAS of the BP MF system, which were initially housed in a hut without airconditioning. The variations shown in Figure 2.18 are significantly smaller than the ±10° seen in the work of *Vandepeer* [1993], which is probably due to

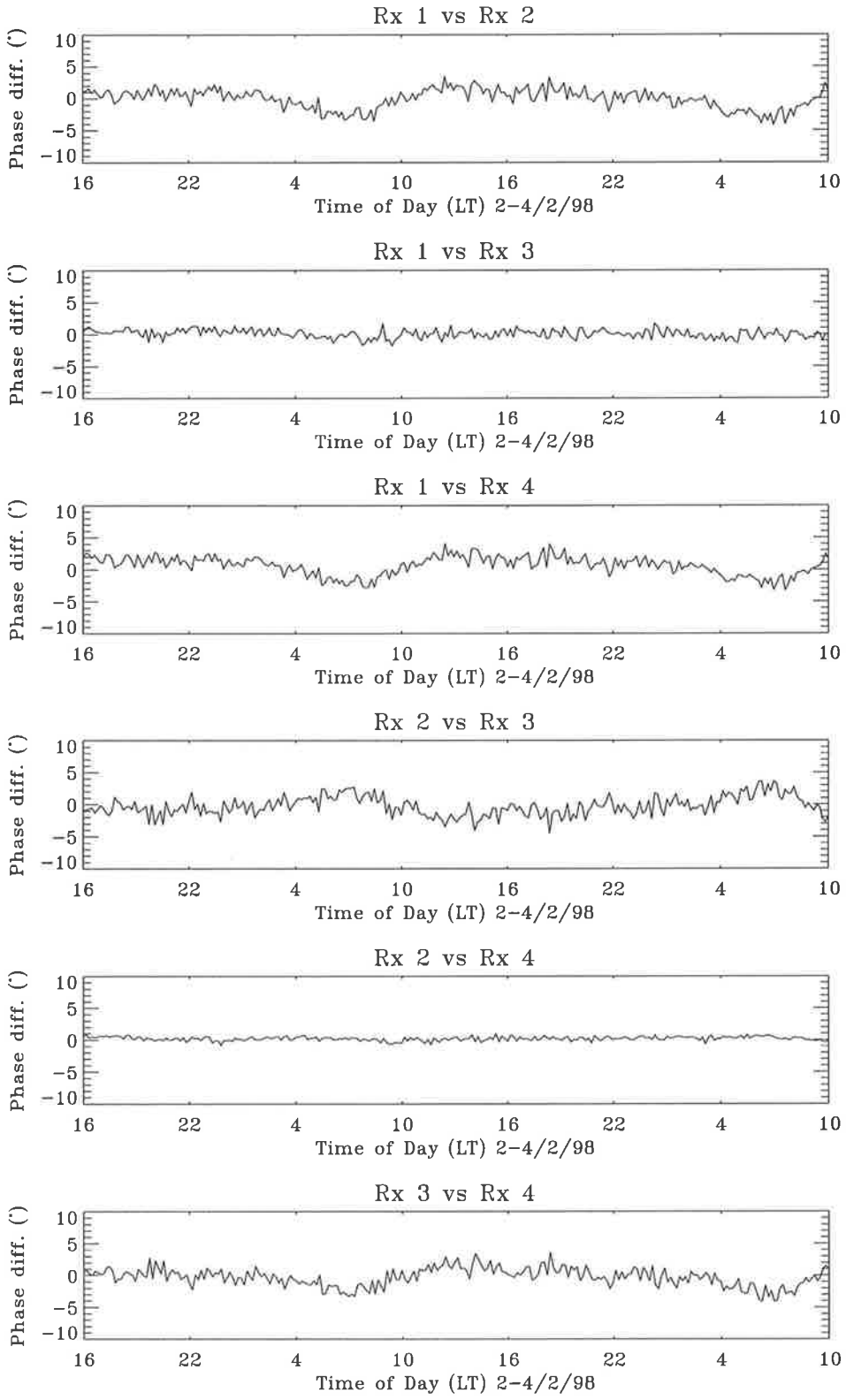

Figure 2.18: Residual phase difference between pairs of receivers, over a 2 day period. Rx here refers to receiver number, so Rx 1 vs Rx 2 refers to the phase difference between receivers 1 and 2.

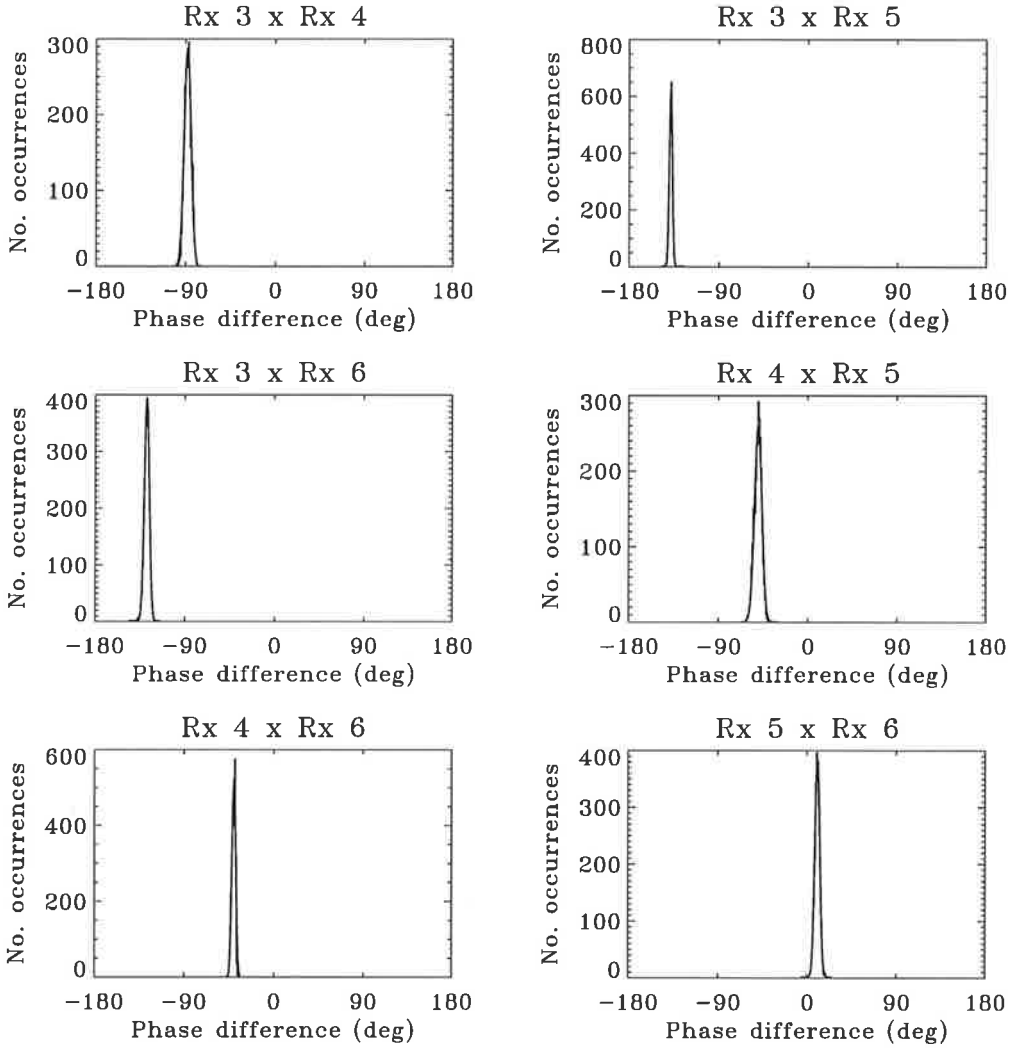

Figure 2.19: Histograms of the phase differences between pairs of receivers, over the full two day period. Note the phase offsets of the histograms, these offsets must be removed before data from different receivers can be combined to provide a single Doppler beam.

the higher quality of the new receivers in the VHF system, as well as the fact that the VHF hut is airconditioned. It is of interest to note from Figure 2.18 that the smallest variations over time are between receivers which are physically separated from one another by one receiver. It appears that there may be some "cross-talk" between receivers which are physically next to one another in the RDAS; receiver pairs 1 and 2, 2 and 3, and 3 and 4, which may result in the relatively larger variance seen in the time series for these pairs. The only pair which doesn't follow this trend is the pair which are physically separated by the greatest amount; receiver pair 1 and 4. It is not clear why the variation for this pair is not as small as that for the other separated pairs.

Figure 2.19 shows histograms of the phase differences between receivers for the test data set. Data from the vertical beam on the North-South array are shown, where the histograms were formed using data from range gates between 4 - 8 km. The standard deviation over these range gates, over all beam directions, was calculated to be less than $\pm 5°$. It can be seen from Figure 2.19 that the half-widths of the histograms, assuming a Gaussian form, are consistent with this value. By using Equation 2.1, an estimate of the "wobble" in the beam direction as seen by the four receivers can be gained. This is the lower limit in the time variation of the AOA that can be observed with the system, a limitation imposed by the radar hardware. Using the minimum separation between the antenna groups, as shown in Figure 2.13, of 4λ, Equation 2.1 gives an off-zenith angle variation, due to the system, of $\pm 0.2°$. For larger antenna group separations this figure becomes even smaller, and by using the receiver pairs which have the smallest time variation, this "wobble" reduces to less than $\pm 0.1°$. Note that this variation is of the same order of magnitude as the tilt of the antenna arrays introduced by phase errors on individual antenna rows, as discussed in Section 2.2.1.

2.7 Summary

In this chapter the Buckland Park VHF ST radar has been described, with particular emphasis on the new beam swinging and multiple receiver capabilities of the system. The radar has been upgraded to a flexible system, capable of DBS measurements at a variety of off-zenith angles in all four cardinal directions, and SA measurements

with a variety of antenna configurations. The majority of this chapter discusses the tests that were conducted on the system to ensure the correct operation of the new hardware. These tests covered antenna phase checks, beam steering hardware phase tests, receiver phase tests, tests of the operation of the new North-South array, and final tests of the full system, using the beam-steering hardware to point in all possible off-zenith beam directions, and using multiple receivers.

The beam-swinging tests on the system indicate that beam-swinging on the system is working as expected, as seen through various combinations of beams viewing the galactic centre. The phase errors in the system, which have implications for the accuracy of the beam pointing direction and the validity of AOA measurements were estimated. The error in the pointing direction of the new North-South array due to the phasing of the antennas was measured at 0.24°, while the same on the East-West array as measured by *Cervera* [1996] was 0.13°. The phase errors on the individual beam steering cards was estimated to result in a 0.05° error in the direction of a given off-zenith beam. While the minimum AOA that can be measured with the BP VHF ST system as a whole was estimated at approximately 0.2°, depending on the distance separating the reception antenna groups. This lower limit is due to small phase variations inherent in the system as a whole.

Chapter 3

Analysis of DBS radar data

3.1 Introduction

In Chapter 1 the manner in which information about the atmosphere can be extracted from Doppler beam steering (DBS) power spectra was discussed. Ideally the power spectrum will look as it is depicted in Figure 1.3. In practice, however, the spectra often contain many contaminants which complicate the information retrieval process. The majority of data in this thesis were collected using the DBS technique, it was therefore an important task to ensure that any contaminants that might degrade the DBS results were properly accounted for.

The identification of the true atmospheric peak in VHF spectra has been the subject of much literature over the last 10-15 years, due to the fact that VHF radars have become increasingly common over this period. As such, this chapter will begin with a discussion of some of the main contaminants that have been seen in the literature and some of the attempts that have been made to measure the true wind velocity in contaminated data. The remainder of this chapter will then focus on the algorithm developed by the author to reduce the effects of contaminants in the data, identify and measure the true atmospheric peak in the spectra, and ensure that the resultant atmospheric parameters are consistent with their neighbours in both time and height.

3.2 Problems in the analysis of VHF radar data

One of the big advantages that VHF radars, in the lower frequency band, have over their higher frequency VHF and UHF counterparts is that their longer operating wavelength means that they are not as sensitive to some of the contaminations that seriously affect UHF and high frequency VHF radars. The Bragg scattering mechanism, through which most atmospheric radar backscatter takes place, displays the following relationship between radar wavelength λ and radar reflectivity η;

$$\eta = \lambda^{-\frac{1}{3}}. \tag{3.1}$$

By comparison, Rayleigh scattering from hard targets exhibits the following relationship;

$$\eta = \lambda^{-4}. \tag{3.2}$$

On comparing these two equations it can be seen that Rayleigh scattering dominates Bragg scattering at shorter wavelengths. This means that the low wavelength of UHF radars makes them particularly prone to contamination from small hard targets such as birds, (e.g. *Wilczak et al.* [1995], *Merritt* [1995]) and precipitation (e.g. *Ralph* [1995], *Ralph et al.* [1996]). Precipitation can also be a problem for lower frequency VHF radars, but it is not nearly so serious in the sense that the atmospheric backscatter echo can usually be detected in the data, whereas the precipitation echo in data from higher frequency radars often completely dominates the atmospheric echo. *Ralph* [1995] has shown that only heavy rain is likely to appear regularly in lower frequency VHF radar data; whereas Rayleigh scattering from hydrometeors is likely to exceed the atmospheric scatter under conditions of light rain or even drizzle with higher frequency radars.

Another hard target contaminant that affects both UHF and VHF data is aircraft echoes. The size of aircraft relative to the wavelength of VHF radars makes them very effective scatterers. The big difference between the contamination observed from precipitation or bird backscatter and aircraft backscatter is the duration of the contamination. Bird migrations and precipitation events are often observed to last for

hours or even days at a time, while airplanes are usually only present in the beam of the radar for a short time. The CLOVAR radar system,[1] described by *Hocking* [1997*b*], is situated beneath major flight paths out of Detroit and Chicago. As discussed in *Hocking* [1997*b*], approximately several hundred aircraft pass close to CLOVAR every day, with a resultant average contamination period in affected time series of about 10 seconds. *Hocking* [1997*b*] describes the use of an algorithm which identifies aircraft contamination in time series by searching for strong rising and falling signals which persist for about 10 seconds. In addition to this check on the time series, the data collection procedure outlined in *Hocking* [1997*b*] involves using a minimal number of coherent integrations. This means that backscatter signals from aircraft retain their characteristic high velocity, relative to the atmospheric signal, rather than being frequency aliased into the velocity range normally occupied by atmospheric peaks. This process makes it relatively easy to identify and account for aircraft contamination in the spectra.

Non-stationary ground clutter is another problem that can be encountered in any radar data set. The power spectrum in Figure 1.3 shows a ground clutter peak at essentially one frequency, which can easily be removed by simply interpolating over the affected region. However, real ground clutter is often present in spectra as a peak of significant width which is not quite so easily removed. *Sato & Woodman* [1982] attribute the width of fading ground clutter in the spectra to variations in the air refractivity along the ray path between the radar and the stationary target. Compounding this problem, as discussed in *Sato & Woodman* [1982], is the fact that there is an intrisic spreading of frequencies in the power spectra caused by the finite length of the radar time series. A finite time series is effectively sampled by a boxcar window which has significant sidelobes in the corresponding frequency sampling function. This means that any ground clutter returns are spread in frequency; making the clutter peak wider, as well as folding noise across the whole spectrum. Ground clutter peaks therefore not only represent a contaminating peak, but also a source of general spectral noise. *Sato & Woodman* [1982] use a method where the shape of clutter and atmospheric returns are both parameterised. Sampling distortion is then applied

[1] Canadian (London Ontario) VHF atmospheric radar.

to the parameters, and the parameter set is compared with the data and adjusted in order to obtain the best fit and therefore provide the most accurate estimates of the atmospheric backscatter moments. In contrast to this work by *Sato & Woodman* [1982], *May & Strauch* [1998] discuss a relatively simple method of reducing the effects of fading ground clutter based on detrending of the radar time series.

The problem of reducing the effects of various contaminants in a set of atmospheric parameters has been tackled in many ways and at many different levels of the analysis process. Some methods work on raw time series or power spectra prior to the calculation of atmospheric parameters, such as the methods used by *Sato & Woodman* [1982], *Hocking* [1997*b*] and *May & Strauch* [1998]. Other methods aim to identify outliers at the level of the atmospheric parameters that are derived from the data, that is, they aim to remove outliers from profiles of velocity or spectral width which have already been calculated from raw time series.

A method which identifies outliers in atmospheric parameters has been used on the NOAA[2] demonstration network in the U.S.A., and is called the consensus averaging method (*Fischler & Bolles* [1981]). This method works by essentially calculating the average of those points in a data set of velocities that have the closest values, the assumption being that the number of contaminanted velocities in the data set will be less than the number of true wind velocity values. The consensus averaging method works by requiring that the data points are consistent in time.

Another method of removing outliers at the atmospheric parameter level, called the continuity method (*Weber et al.* [1993]), also requires that data points are consistent in time, but has the added restriction that data points must also be consistent in height. Data points are checked for continuity in time and height by comparing the value of a data point with the value interpolated from neighbouring data points. A pattern recognition algorithm is used to decide which points are good or bad by placing data points in various subsets depending on how similar the velocities are. The algorithm then places greater confidence on the branch with the most data points in it as representing the correct velocity value.

Miller et al. [1994] compared the performance of the *Weber et al.* [1993] continuity

[2]National Oceanic and Atmospheric Administration.

algorithm with an earlier algorithm called the Brewster/Schlatter method (*Brewster & Schlatter* [1986], *Brewster & Schlatter* [1988]) which rejects data on the basis of time-height inconsistencies, as well as a vertical shear test. The Brewster/Schlatter method was the quality control algorithm already in place on the NOAA Wind Profiler Demonstration Network data in the U.S.A.. The comparison discussed in *Miller et al.* [1994] showed that the *Weber et al.* [1993] method labelled less winds as inconclusive than the Brewster/Schlatter method, and as such, was considered to be a preferable quality control algorithm.

In contrast to these methods which act on atmospheric parameters, the algorithm of *Merritt* [1995] tests the statistical distribution of the power in each spectral bin before power spectra are averaged, thus removing the contribution of outliers before a velocity is calculated. The *Merritt* [1995] algorithm was designed to find the atmospheric echo in data that was heavily contaminated with migrating bird echoes. He therefore could not rely on the assumption that the contaminated velocities would be in the minority. Instead, he assumed only that the radar dwelt on a particular volume of atmosphere for long enough that the atmospheric return would be observed at some point in the absence of bird contamination. In general, atmospheric backscatter is weaker than backscatter from birds. *Merritt* [1995] made use of this general characteristic by sorting the spectral estimates for a given spectral bin in ascending order of strength. He then identified only the weakest signals, those below some threshold, as being from the atmospheric backscatter and only these values were averaged together to get the resultant power spectra.

Another algorithm that was born out of a need to find the atmospheric backscatter return in raw data dominated by bird echoes is that of *Ralph et al.* [1996]. In this study *Ralph et al.* [1996] investigated the characterics of bird echoes at each stage of the analysis; time series, spectra and moment calculations. From this, they discovered that by simply thresholding high values of power and spectral width, they were able to remove the effects of the bird contamination from the radar spectra and calculate the moments of the atmospheric peaks more reliably. This is a very simple but effective method. Other methods often use more complex techniques.

The method of *Clothiaux et al.* [1994] uses an analyst trained neural network to

find the correct velocity profile in the presence of noise. Spectra which have low peak power densities are averaged, smoothed and normalised. All local power density maxima are then identified and linked through height by forming chains which connect each maxima to a corresponding maxima in the range gates immediately above and below. An analyst then inspected a subset of the whole data set and identified the atmospheric peak in each one. In this way, the neural network was trained to look for features that identify the correct return. The back-propagating neural network then searched through the data to find the velocity profiles that most closely resembled the sorts of profiles chosen by the analyst.

Another technique which has recently been applied to radar time series in an effort to remove contaminants involves the use of wavelet transforms. *Jordan et al.* [1997] report the use of wavelet transforms to "filter" ground and intermittent clutter, caused by objects such as birds, from radar time series. The use of the wavelet transform, as discussed in *Jordan et al.* [1997], results in obvious improvements in the detectability of the true atmospheric echo in power spectra which was previously unuseable due to the dominant clutter contribution.

The algorithm developed by the author and discussed in this chapter acts initially on time series and power spectra prior to the calculation of atmospheric parameters, and then on power spectra and velocity profiles in tandem. As such, it is a blend of the approaches of many of the investigators discussed above. The algorithm will be discussed in order of analysis, from the treatment of the time series, to the treatment of the spectra, to the search for outliers in the velocity profiles and the methods used to extract alternative, correct values from the spectra associated with a given spurious velocity.

3.3 Contaminant removal in time series and power spectra

The main identifiable contaminants encountered in data from the Buckland Park VHF ST radar, during rain-free periods[3], were non-stationary ground clutter, aircraft echoes[4] and sea scatter from the Gulf of St. Vincent. Sea scatter as a contaminant in VHF data was not discussed in the previous section as it is a rarely studied contaminant in the literature on VHF data. However, there is some discussion of sea scatter removal from HF radar data (e.g. *Headrick & Skolnik* [1974], *Martin & Kearney* [1997]). Another contaminant which appeared regularly in certain beam directions was an interference spike from an unknown source. The interference spikes occurred in the general frequency range where sea scatter spikes were often present, the only difference being that in theory, sea scatter spikes occur at a fixed frequency, while the interference spikes that often occurred in the data had a certain range of frequencies which is suggestive of interference rather than sea scatter. For the purposes of the algorithm discussed here, it is not important whether the spikes in frequency were caused by sea scatter or by some unknown source of interference. As such, it is assumed that both sea scatter and interference are the cause of the observed frequency spikes.

Sea scatter echoes are caused by back-scatter from prevailing ocean surface currents, and are present as narrow spikes at a fixed frequency, in a given power spectrum. The frequency at which a sea scatter spike appears in a power spectrum is dependant on the wavelength of the radar, and partially dependant on the depth of the water. VHF radars have been used to study ocean surface currents by directing beams towards the ocean at low elevation angles (e.g. *Balsley et al.* [1987], *Broche et al.* [1987]). However, for the off-zenith angles typically utilised by a Doppler radar in atmospheric measurements, side lobes may be present at sufficiently low elevation angles that sea scatter is detected as an unwanted contaminant.

The next two sub-sections cover the measures taken to account for aircraft and

[3]The data presented in this thesis were all collected during rain-free periods.

[4]Aircraft echoes are quite common at the Buckland Park field site as the area encompassing the field site is a designated low flying test area for the nearby Parafield airport.

ground clutter contamination of the data, first in the time series, and then in the spectra, prior to the calculation of atmospheric parameters from the spectra.

3.3.1 Treatment of the time series

The in-phase and quadrature time series from the radar are the raw data from the system; they therefore represent the first opportunity to remove any unwanted echoes. Hard targets, like aircraft, backscatter transmitted radar power more efficiently than the atmosphere. This makes aircraft echoes identifiable as regions within the time series with higher amplitudes and variances than the surrounding data.

The first step in the analysis procedure was to split the in-phase and quadrature components of the time series into a number of sections, and calculate the standard deviation in each of these sections. The maximum standard deviation over all sections of each component of the time series was then calculated; if this value occurred in the same section of both the in-phase and quadrature components of the time series, and was four times greater than the average standard deviation of the remaining sections, then the offending time series was discarded. This figure of four was chosen on the basis of experience. It was found to be the best compromise between detecting an aircraft and not detecting generally noisy data which was not affected by an aircraft. The figure of four was generous and allowed aircraft to remain undetected rather than reject unaffected time series. Figure 3.1 shows five consecutive time series in the same beam direction, the first of which has aircraft contamination.

The number of sections that the time series were split into was dependant on the length of the time series. Aircraft echoes were observed in a given time series for up to 20 seconds at a time, so the number of sections that were chosen was set such that an aircraft-affected region would dominate a section of the time series, and trigger the detection test. For most of the data discussed in this thesis, the time series were split into four sections for this aircraft detection test.

The effects of ground clutter with a non-zero spectral width can be seen in time series as a slowly varying mean. Ground clutter is caused by backscatter from stationary objects, which can be detected in the sidelobes of the radar beam in much the

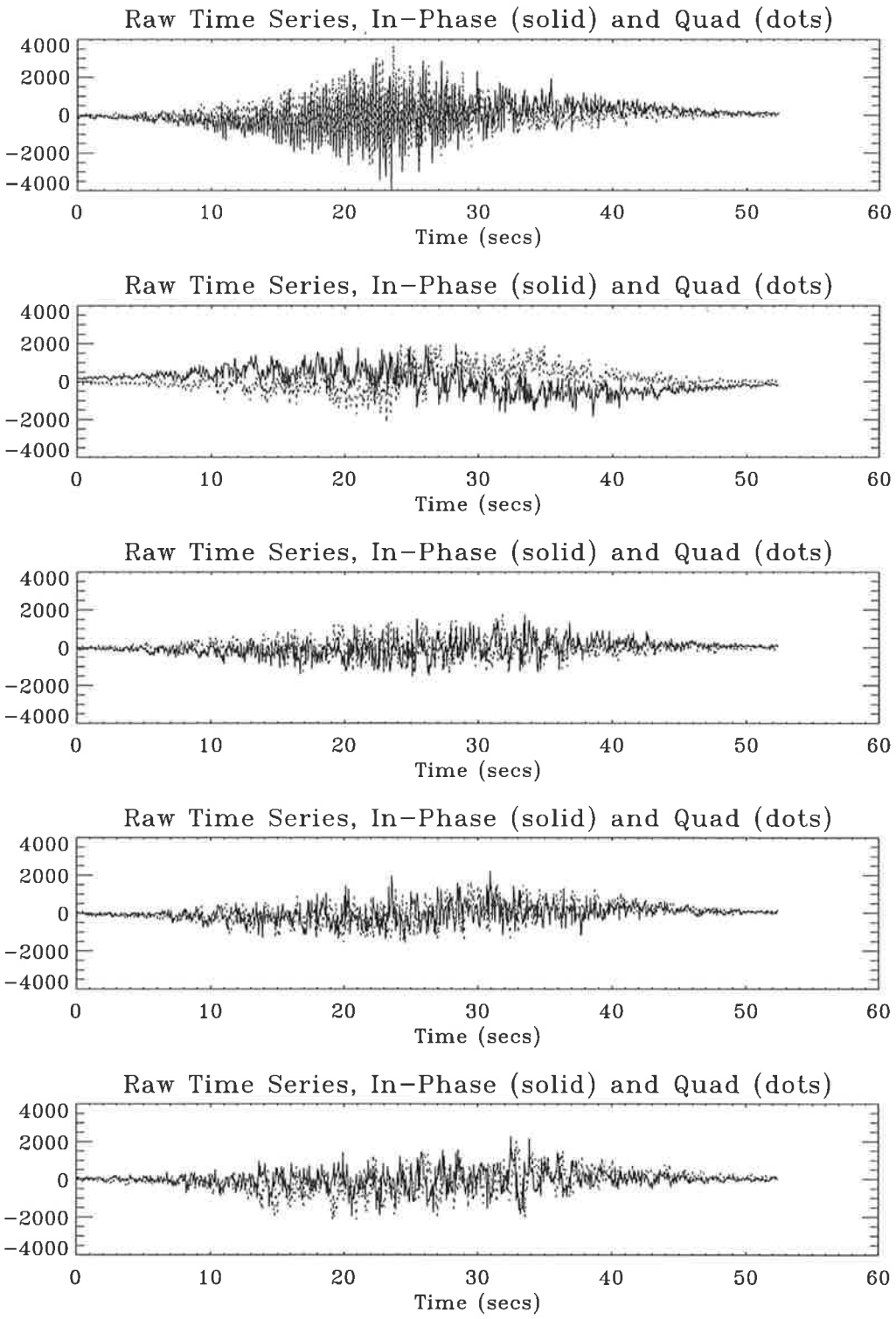

Figure 3.1: Five consecutive time series in the same beam direction. The topmost time series is affected by aircraft contamination. This contamination can be seen in the higher amplitude and variance in this first time series. Note that the tapered shape of the time series is due to the use of a filter window. The aircraft rejection is actually carried out prior to filtering of the time series.

same manner as sea scatter. As discussed in the previous section, the finite length of the time series leads to spreading of the frequency components of the power spectrum across adjacent frequency bins which results in widening of any features in the spectrum, including ground clutter. In an effort to reduce the presence of the ground clutter peaks in the spectra, the time series were filtered with a Hamming window (*Harris* [1978]). This has the effect of reducing the sidelobes of the frequency sampling function caused by the boxcar shape of the time series sampling function. The time series shown in Figure 3.1 are shown with Hamming filter applied. Filtering the time series in this manner reduced the amplitude and width of the ground clutter peak.

3.3.2 Treatment of the power spectra

Time series which passed through the algorithm, without being rejected on the basis of an aircraft detection, were then Fourier transformed, and fitted with a Gaussian function. Depending on the desired time and frequency resolution required of the data set, power spectra could be averaged together at this point. This had the effect of smoothing the power spectrum which made it easier to obtain a good Gaussian fit to the spectrum. In a situation where an aircraft was detected, a power spectrum was not calculated for that time series, which meant that a data gap resulted. Therefore, the other benefit of averaging sets of spectra was that a data gap was less likely to result as the duration of the aircraft contamination rarely extended across the time taken to collect all of the spectra being averaged. The data in this thesis, as discussed in Chapters 4, 5 and 6, were collected at a relatively high time resolution, which required that a maximum of two spectra were averaged together, and in some data sets atmospheric parameters were calculated from individual spectra.

Once the spectra were calculated, and averaged together if appropriate, the frequency bins prone to ground clutter contamination were interpolated over. The number of frequency bins that were interpolated across depended on the frequency resolution of the spectrum, and the pointing direction of the radar beam. A discernible ground clutter peak in the power spectra was only obvious in data from off-zenith

beams. As such, only the middle frequency bin was interpolated over in vertical beam data, in order to smooth over the null left by the subtraction of the mean from the time series. In off-zenith data the middle three or five points were interpolated over. A five point linear interpolation was performed on data with a spectral resolution of approximately 0.02 Hz and a three point interpolation was performed on data with half this resolution.

3.4 Calculation of atmospheric parameters

This project was the first implementation of DBS analysis in the frequency domain on the BP VHF ST radar. Previous DBS measurements with the system were analysed in the time domain using the so-called "pulse-pair" technique. It was therefore necessary to develop methods to obtain atmospheric parameters from power spectra. As noted in Chapter 1, atmospheric parameters can be calculated from power spectra by fitting a Gaussian function to the peak corresponding to the atmospheric backscatter in the spectra. The fitted Gaussian function provides the velocity and width of the atmospheric peak and can be used to calculate the SNR of the backscatter. Due to the aspect-sensitive nature of the scatterers in the atmosphere, less power is received in a radar beam directed at a large off-zenith angle then is received in a radar beam directed at a relatively smaller off-zenith angle. It is therefore necessary to be able to detect atmospheric peaks in low SNR data in order to consistently obtain profiles of atmospheric parameters at a given height, over as large a time period and range of off-zenith angles as possible. The BP VHF ST radar is a relatively low power system, at peak power of 32 kW, which makes this task more important then it would be for a high power system such as the MU radar in Japan which operates at a peak power of 1 MW.

The data analysis routines that were used or developed by the author to analyse the data presented in this thesis were written in IDL (Interactive Data Language). This language has many built in functions and procedures, including a Gaussian function fitting routine. However, low power peaks in the data proved to be impossible to fit reliably with the existing Gaussian function fitting routine, so considerable time was

spent developing a new one. The main reason that the original Gaussian function fitting routine was unreliable was that it used moment calculations, calculated over the entire spectrum, as the initial estimates of the parameters of the spectra. In the case of low SNR these moment estimations of the atmospheric parameters were not accurate[5]. These initial bad estimates meant that the routine was often not able to calculate an initial function to fit to the data, or, if it did manage to calculate an initial function, the parameters it started with were so far from the parameters of the real peak in the data that it was not able to converge to it. This called for a new approach to calculating these initial estimates so that the Gaussian function would have a better chance of achieving a good fit to the data.

At this point in the analysis, spectra were assumed to contain only the atmospheric peak. The first step in locating the peak in each spectrum was to split each spectrum into 16 equal sections in frequency. Then, for all but the end two sections, the maximum value within each section was calculated. Finally, the maximum of the maximum values over the 14 sections was divided by the minimum of the maximum values over the 14 sections. If the resultant number was greater than 2.0, that is, if the maximum value was double the minimum value, then the maximum value was classified as a peak. The maximum value of the peak and the location of the peak were then used as the first estimates of the amplitude and velocity in the Gaussian fitting process.

The initial estimate of the width of the spectrum used by the Gaussian fitting function was estimated less directly. Each data set contained a power spectrum for each of the ranges observed, and the fitting process started at the lowest range and iterated upwards. Radar backscatter at lower ranges was generally strong and the peaks within these spectra were well defined. Any changes to the spectra as a function of range were also generally smooth, so the parameters of a peak at one height were not much different from that of the range above or below. This fact was utilised in making a first estimate of the width of the spectra. The first width estimate for the lowest range was set at a value of 1 ms^{-1}. This value was then updated with the value returned from the Gaussian fit to the data and used as the estimate of the width

[5]Limiting the width of the spectrum that the moments are calculated over, to the region containing the peak only, would have produced more accurate results.

for the next range. This process provided good initial estimates of the width for less distinct peaks at upper ranges in the data set.

Calculating all of the initial estimates of the peak characteristics in the manner described above led to far superior estimates of these parameters to those which could be obtained with the existing Gaussian fitting function. This in turn led to more reliable Gaussian fits to the data, and subsequently, better values of the atmospheric parameters themselves over time and height. Figure 3.2 shows the flow of data as discussed in Section 3.3 and Section 3.4.

The goal of the sensitive peak detection and Gaussian fitting was to improve the height and time coverage of the radar parameters. Figure 3.3 shows the height coverage that is possible using this process, for all three basic atmospheric parameters; radial velocity, spectral width and SNR. The data shown in Figure 3.3 were actually taken with the BP VHF ST system prior to the installation of the new beam-steering hardware, and are shown in their final form, free from outliers. The data were collected with beams directed to the east at 11° off-zenith, using manually inserted phasing cables on the East-West array only. The atmospheric parameters shown in Figure 3.3 were calculated from averaged spectra which were compiled from five one minute data sets. Each data point in Figure 3.3 therefore took five minutes to collect, but approximately 20 minutes were required for an entire beam cycle, using east and west 11° off-zenith beams and vertical beams. Figure 3.3 shows data covering three hours, at the minimum 20 minute resolution.

It can be seen from Figure 3.3 that atmospheric parameters were measured up to approximately 17 km in some profiles. However, 20 minutes is a relatively low time resolution and the experiments described in this thesis, using the fully upgraded radar, required high time resolution and good time coverage. These requirements meant that atmospheric parameters were calculated on a single minute of data in a given beam direction, and that only those heights where data was reliably obtained were useful. It can be see in Figure 3.3 that there are gaps in the last two profiles of radial velocity above about 8 km, and that there are gaps in all of the profiles above approximately 13 km, just above the common tropopause height at Adelaide. Data gaps above these two height ranges were a common feature of the data collected with the BP VHF ST

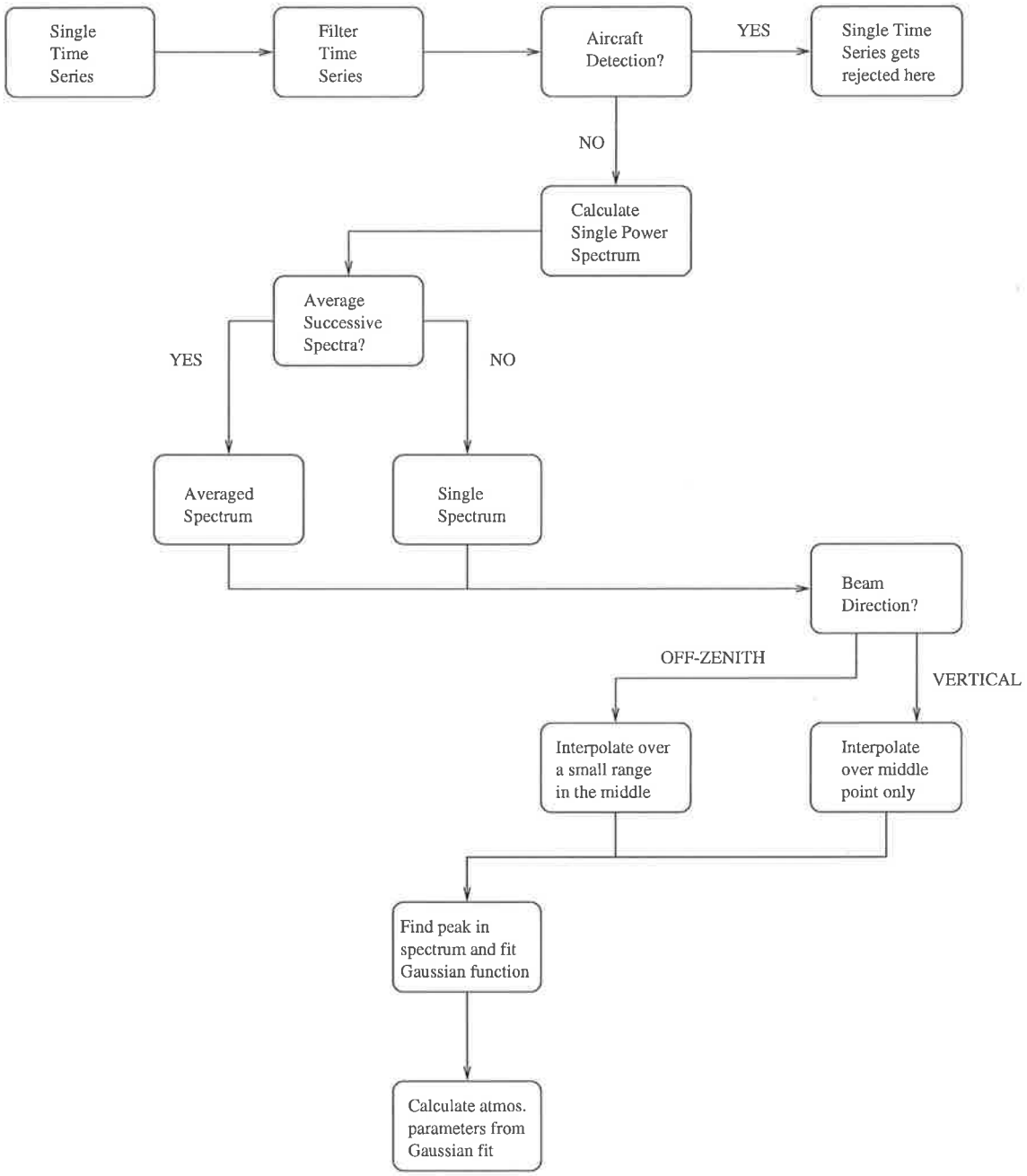

Figure 3.2: Flow chart showing the analysis process from single time series, to atmospheric parameters calculated from a Gaussian fit to the corresponding power spectrum. This diagram covers the analysis discussed in Sections 3.3 and 3.4 to minimise the effects of ground clutter and aircraft backscatter in the time series and power spectra.

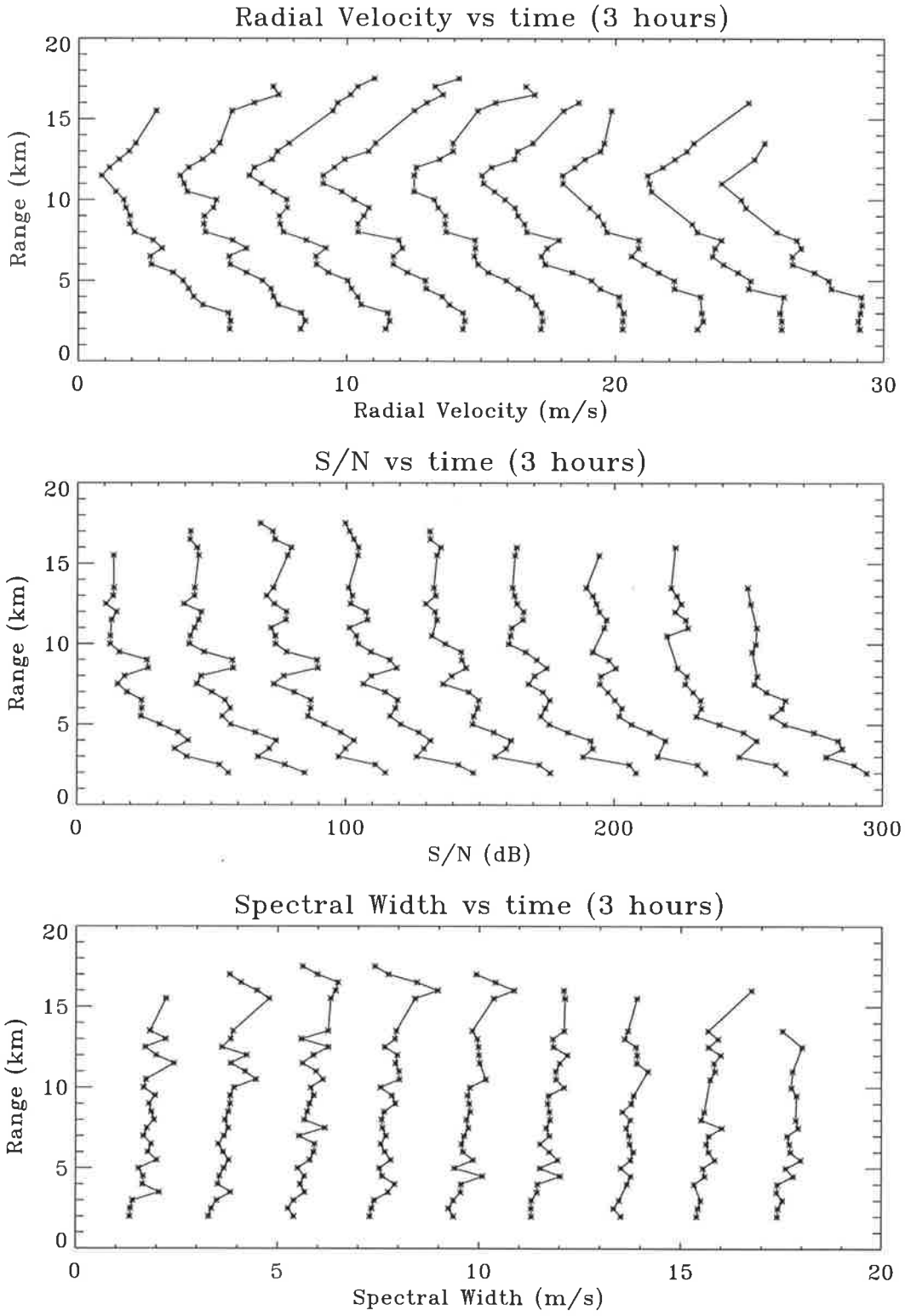

Figure 3.3: Profiles of the radial velocity, spectral width and SNR measured in an 11° off-zenith east beam. The data in this figure were collected with the old BP VHF ST system, using manually inserted phasing cables on the East-West array only. Each parameter was calculated from five minutes of data.

radar, and often the range in between these two heights contained only patchy data, as in the last profile in Figure 3.3. As a result, in order to obtain the best possible time resolution and time coverage for the data collected with the upgraded BP ST radar that is discussed in this thesis, all atmospheric parameters were calculated over the reduced range from 3 - 8 km.

3.5 Quality control of atmospheric parameters

The measures discussed in Section 3.3 to combat the effects of aircraft and fading ground clutter in the data were observed to work in the majority of cases. However, they were designed to be reasonably relaxed so that good data would not be adversely affected. This meant that there were cases where aircraft were not detected and spectra were calculated from affected time series, or where a significant ground clutter peak remained in the data after filtering and interpolating. In addition to these error sources, which have already been partially addressed at the time series and power spectra level, outliers caused by sea scatter and interference spikes and other, unidentified sources existed in the atmospheric parameter data set calculated from the power spectra. As such, the algorithm relies on being able to pick up these contaminants when they have propagated through to become outliers in atmospheric parameters such as radial velocity.

The manner in which the algorithm presented here identifies an outlier can be broken down into two sections based on whether or not the contaminant in the spectrum, which caused a given data point to be an outlier, can be easily characterised or not. If a strong ground clutter, sea scatter or interference spike dominated a given spectrum, and was therefore incorrectly fitted with a Gaussian function in preference to the true atmospheric peak somewhere else in the spectrum, then it was usually easy to characterize as it had a certain small range of widths and was within a certain known range of frequency bins. If, however, an aircraft echo or some other unidentified backscatter peak was fitted instead of the true atmospheric peak, then it had a random shape and position within the spectrum, thus making it harder to characterise.

The outlier detection and correction algorithm acts on a time series of atmopsheric

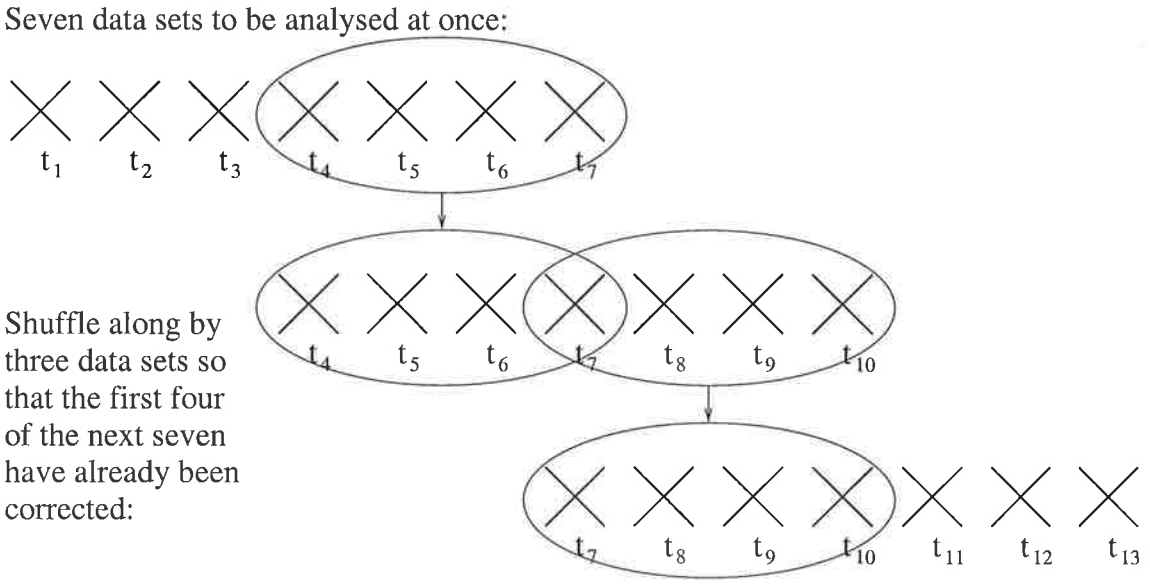

Figure 3.4: Data file progression through the algorithm. The last four data points of one set of seven are used as the first four of the next set of seven data points to be analysed. This helps to increase the chance that random outliers will be detected as they should always be in the minority due to the fact that over half of the data in the seven points has already been corrected and should not contain any outliers.

parameters, over a range of heights where the signal power is great enough for data to be consistently collected. Profiles of spectral width, radial velocity and SNR for seven successive data sets in a given beam direction were analysed together. These seven data sets were shuffled through the algorithm by sliding along three files after every iteration, as shown in Figure 3.4. In this manner, files which had already been corrected were used as reference points to correct files which contained possible outliers. In the first instance these seven data sets were scrutinised for well-characterised contaminants. The algorithm then attempted to correct for random outliers in the data set. The following sub-sections will cover the manner in which the algorithm detects and corrects both types of outliers in the atmospheric parameter data set.

3.5.1 Correcting well-characterised outliers

In the data presented here, ground clutter peaks in the spectra were sometimes observed with enough power to be incorrectly identified as atmospheric peaks. This occurred in eastward beams only, when the width of the ground clutter spike was such that the narrow range of frequencies that were interpolated over in the central bins

of the power spectra was not sufficient to remove the spike entirely. The fact that significant ground clutter was only seen in eastward beams was probably due to the fact that most of the buildings and towers close to the radar are east of the radar. In addition, most of the suburbs and main roads close to Buckland Park are to the east. The top figure in Figure 3.5 shows a power spectrum in which a strong ground clutter peak has been incorrectly identified as the atmospheric peak and fitted with a Gaussian function. The bottom figure shows the same spectrum, but in this case the correct atmospheric peak has been identified and fitted. Note that all the data shown in this chapter were collected with a maximum unaliased radial velocity of over 22 ms^{-1}, and that the plots which show spectra are shown over the range ± 10 ms^{-1} for clarity.

Gaussian fits that were made to ground clutter in preference to true atmospheric peaks were observed to have spectral widths less than 0.3 ms^{-1} and radial velocities less than 0.3 ms^{-1}. The other feature of a fit to ground clutter at a given range in a given data set, was that other data points at the same range in other data sets among the seven being analysed together were observed to have the true velocity and width, which were usually both higher and wider respectively. A fit to ground clutter was therefore identified as a point in a data set collected with an eastward pointing beam, where the spectral width and radial velocity were less than 0.3 ms^{-1}, in a range bin where at least one other point in the other data sets had a velocity three times this value; 0.9 ms^{-1}. This extra criterion prevented points in data sets where the spectral width and velocity of the data points were correct, but small, in all seven data sets from triggering the ground clutter detection. This extra criterion was used for all but the first seven data sets from a given data run. The reason for this was that in the first iteration of the algorithm there were no corrected profiles from the previous run. This meant that all seven files could in fact contain outliers. This is the case shown in Figure 3.6. It shows the velocity profiles from the first seven data sets of a data run to be passed through the algorithm. The topmost plot shows the contamination of ground clutter, as shown in Figure 3.5, affecting every profile, over a range of heights. The bottom profile shows the result after correcting for this contamination.

Sea scatter and interference spikes in the data presented in this thesis were only

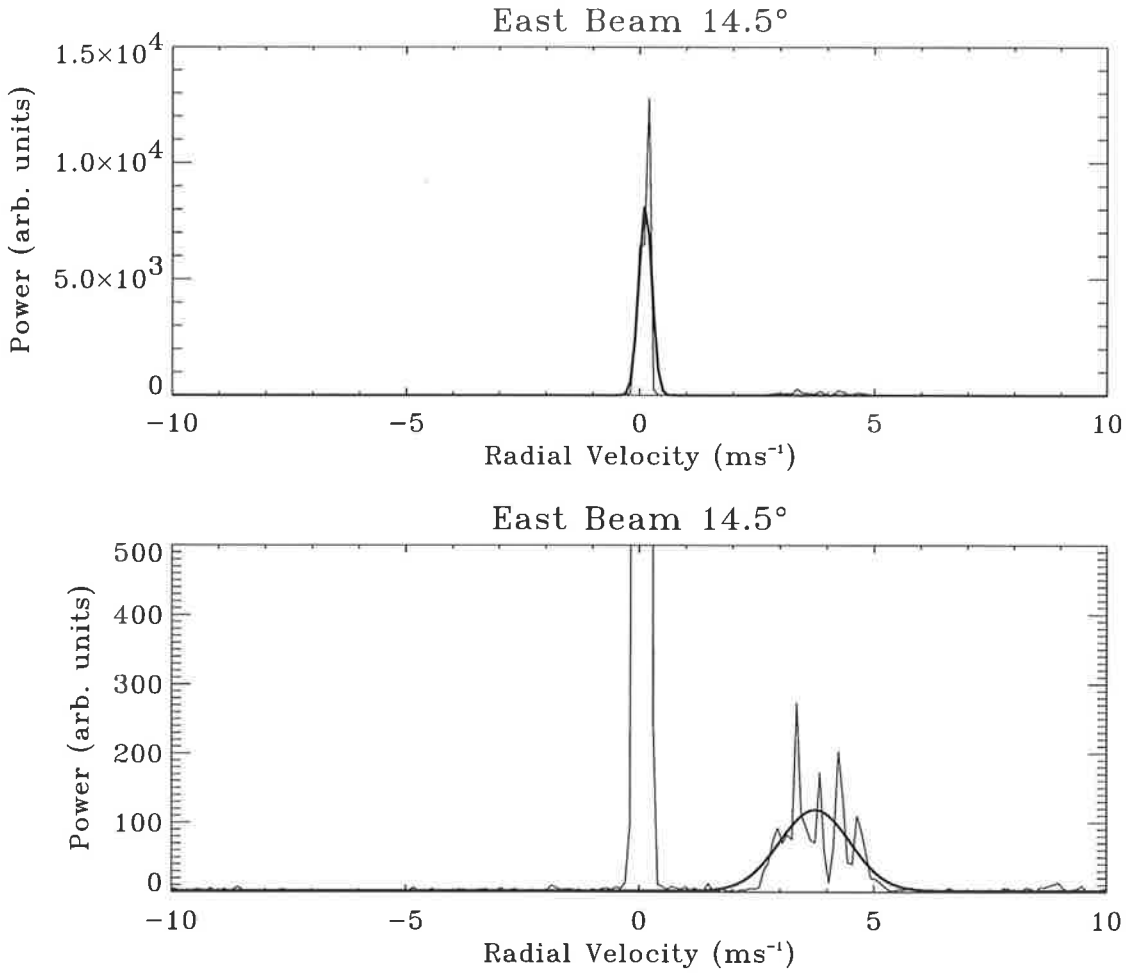

Figure 3.5: Top: Single power spectrum collected with a 14.5° off-zenith east beam. The ground clutter in this diagram is sufficiently wide to escape the interpolation discussed in 3.3.2, and has enough power that it is incorrectly identified as the atmospheric peak and fitted with a Gaussian function, which is shown plotted over the spectrum. Bottom: The same power spectrum, but with the correct atmospheric peak identified and fitted. Note the different y-axis scales; the amplitude of the ground clutter peak is such that the true atmospheric peak is barely visible in the top plot.

observed with enough power to be incorrectly identified as the atmospheric peak in radar beams directed to the south. They were observed to have spectral widths less than 0.25 ms^{-1} and radial velocities between 1.6 ms^{-1} and 2.4 ms^{-1}. Unlike ground clutter peaks which could dominate at any range, the sea scatter or interference spikes were only seen to be dominant above a range of 6 km. The fact that the position of the spikes varied within this velocity range is the main reason that they were not simply interpolated over in the power spectra in the same manner as ground clutter. The only

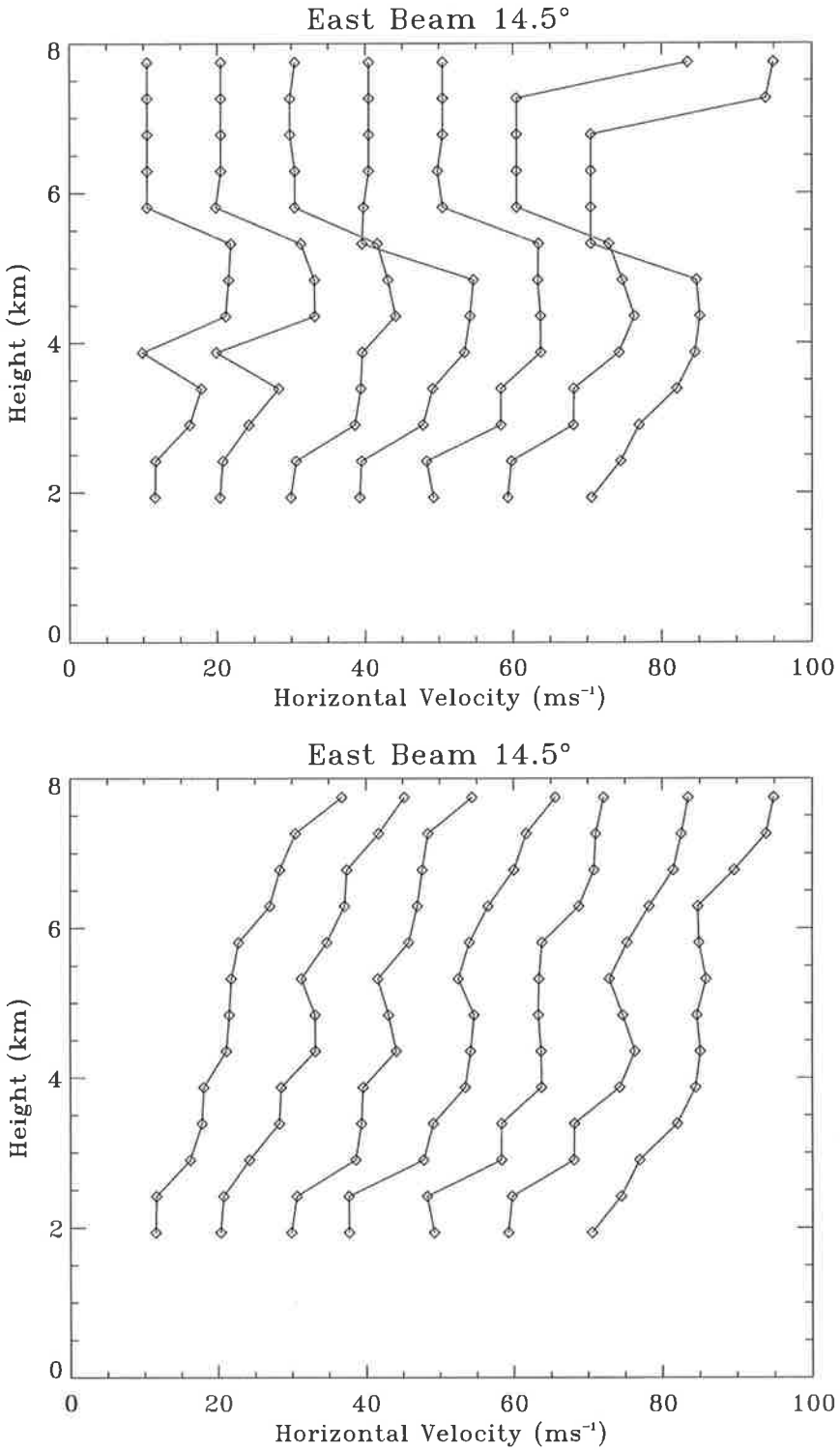

Figure 3.6: Top: Seven successive profiles of horizontal velocity through time at beam direction of 14.5° off-zenith to the east. This plot shows many outliers due to incorrect identification of ground clutter peaks as atmospheric peaks. Bottom: The same seven profiles - here corrected for ground clutter contamination. Each successive profile is shifted by 10 ms^{-1}.

way to only act on the very narrow range of velocities actually containing the spike, within the wider range where the peak was generally observed to occur, was to allow it to be incorrectly identified as an atmospheric peak, and then search for "atmospheric" peaks which fitted the characteristics of sea scatter/interference spike contamination. The top plot in Figure 3.7 shows a power spectrum in which a high amplitude frequency spike has has been incorrectly identified as the atmospheric peak and fitted with a Gaussian function. The bottom figure shows the same spectrum, but in this case the correct atmospheric peak has been identified and fitted. Figure 3.8 shows a set of seven velocity profiles affected by frequency spikes. The topmost plot shows the affected profiles, while the bottom plot shows the same profiles after correction.

Data points which triggered either the ground clutter or sea scatter/ interference spike detection tests were flagged. The next step was to find the correct peak in the spectra affected by ground clutter or sea scatter. For data affected by sea scatter and interference spikes this was done by interpolating over a small range of frequency bins centred on the spike; four frequency bins in data collected with a frequency resolution of approximately 0.04 Hz. For ground clutter affected data this was done by interpolating over a range of frequency points greater than the three or five already carried out and discussed in Section 3.3.2; nine frequency bins in data collected with a frequency resolution of approximately 0.04 Hz.

Spectra at ranges where sea scatter or ground clutter were detected were then passed to a procedure which located a peak, and then calculated new atmospheric parameters as discussed in Section 3.4. Without the contaminating spike in these spectra the true atmospheric peak had a much better chance of being correctly fitted. Figure 3.9 shows the flow of data as discussed in this section.

The advantage of looking for and correcting outliers in this manner is two-fold. Firstly, it means that in most of the data, where frequency spikes and ground clutter are not a problem, wide interpolations in the spectra are not carried out in the first instance. Instead, in the first analysis of the data as discussed in Section 3.3.2, a conservative interpolation over the ground-clutter affected regions of the spectra is performed, and no attempt to account for sea scatter is made. Wide interpolations over suspected ground clutter and frequency spikes at this point could adversely affect

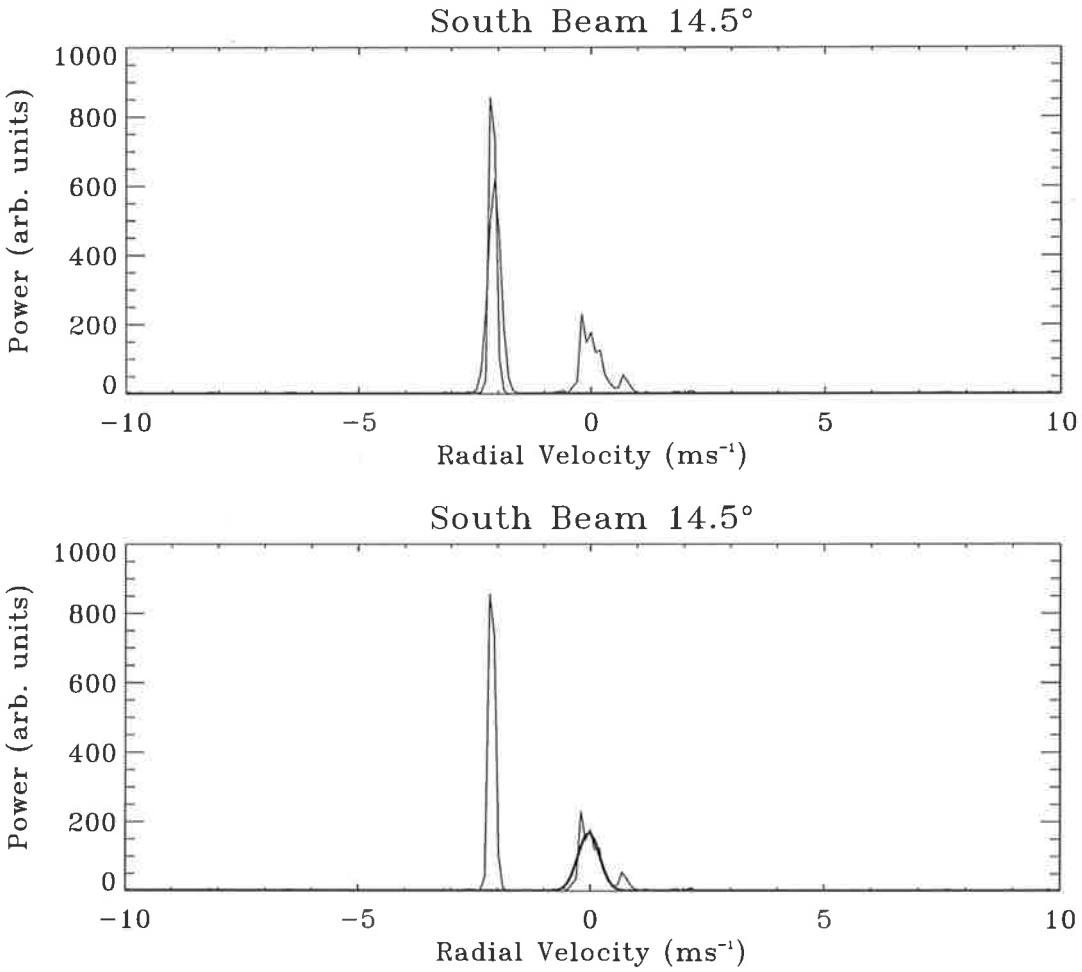

Figure 3.7: Top: Single power spectrum collected with a 14.5° off-zenith south beam. The narrow sea scatter/interference spike has been incorrectly identified as the atmospheric peak and fitted with a Gaussian function, which is shown plotted over the spectrum. Bottom: The same power spectrum, but with the correct atmospheric peak identified and fitted.

good data. Instead, extra interpolations are only carried out on spectra which have already resulted in outliers; spectra which could only produce a better result by having these extra interpolations made. Secondly, by identifying and removing the contaminant in the spectra, the true atmospheric peak can be fitted and reliable atmospheric parameters calculated. This means that once an outlier is detected, the data set was not rejected - which would result in a data gap. Instead a new value is found which is not simply the average of the values above and below, or the average of values before and after, but a new value which actually corresponds to the true atmospheric peak in the data. In this manner the maximum amount of information which can be

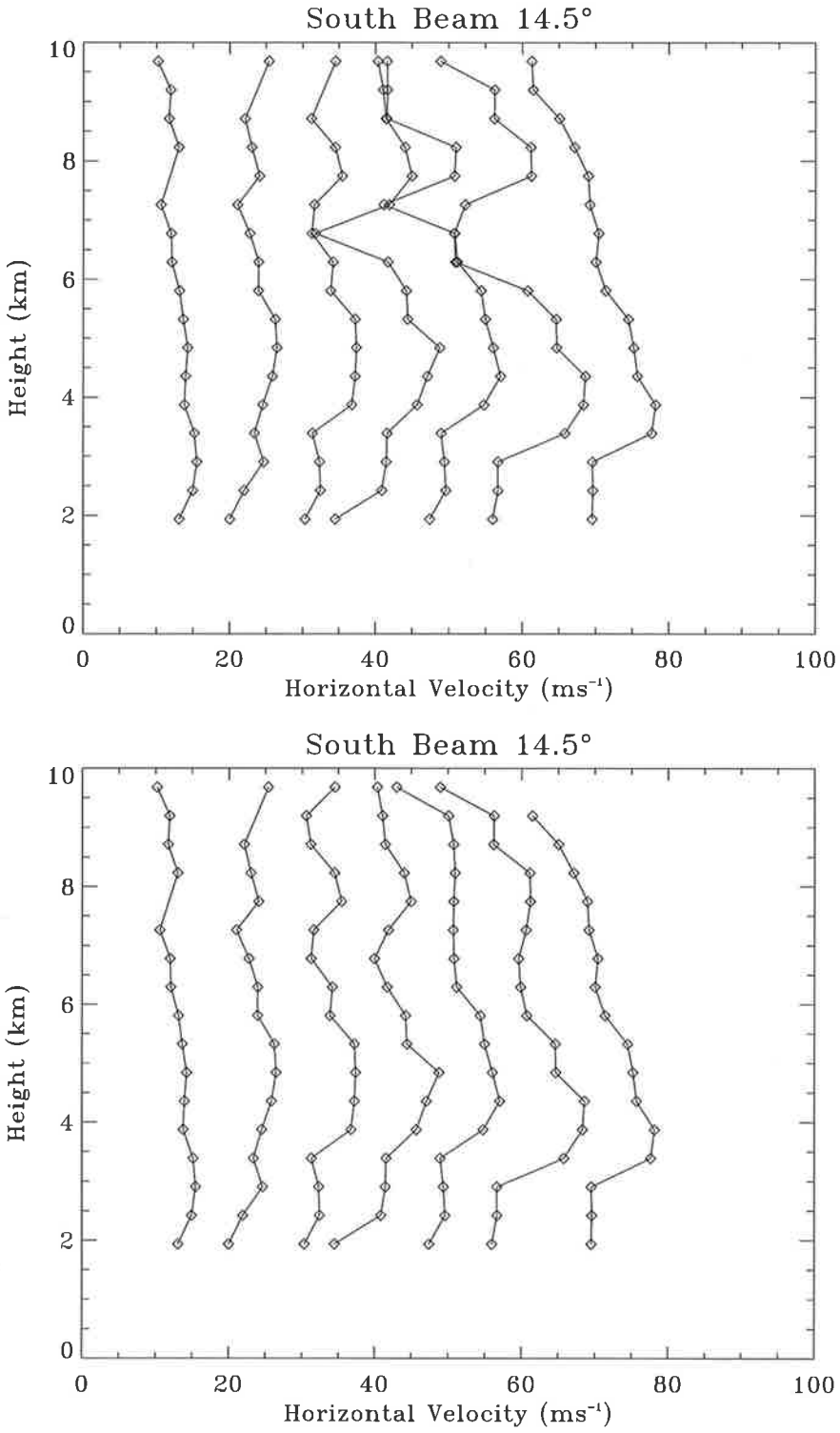

Figure 3.8: Top: Seven successive profiles of horizontal velocity through time with a 14.5° off-zenith south beam. This plot shows outliers due to incorrect identification of sea scatter/interference spikes as atmospheric peaks. Bottom: The same seven profiles - here corrected for the spikes. Each successive profile is shifted by 10 ms^{-1}.

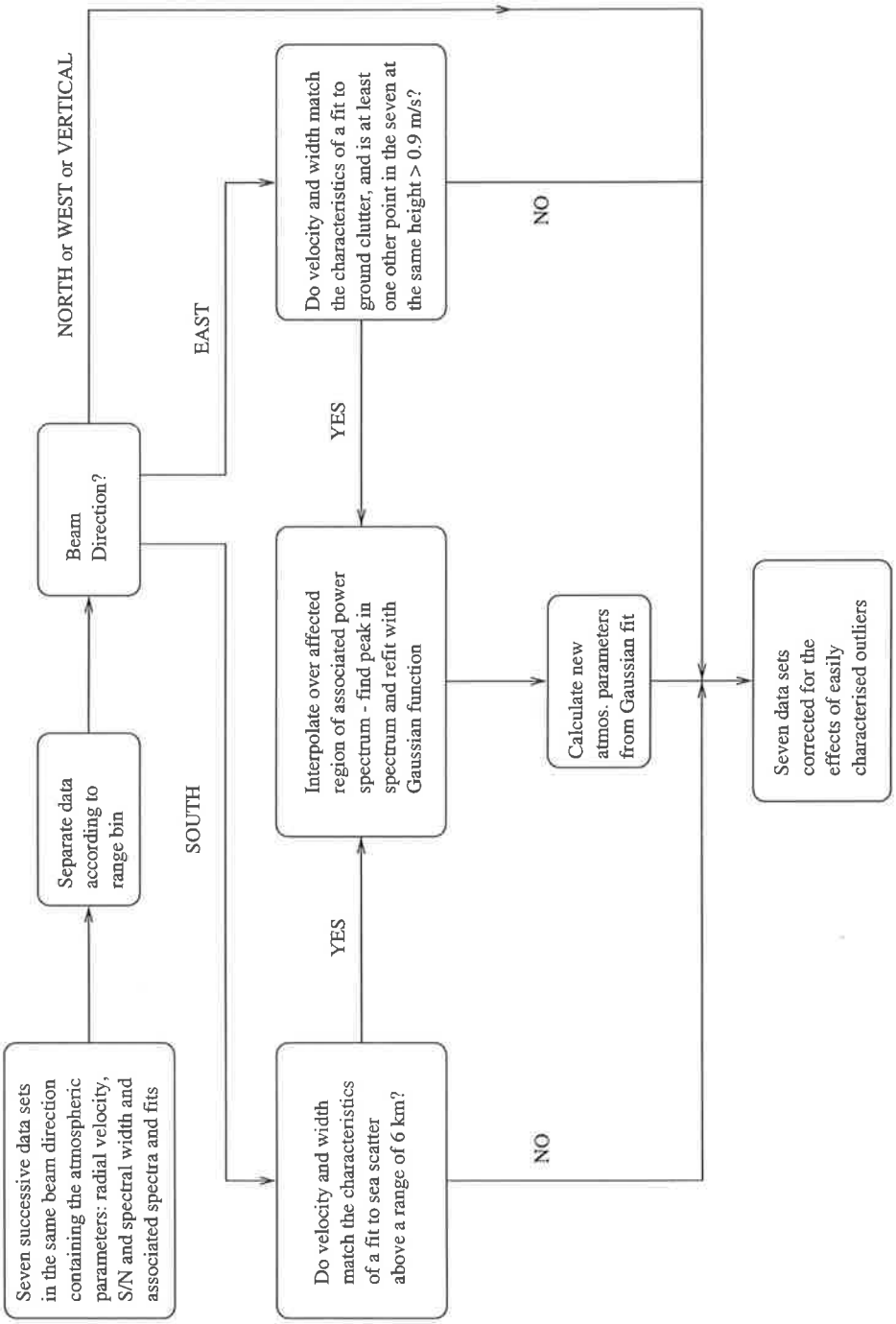

Figure 3.9: Flow chart showing the method of detecting well characterised outliers and correcting for them in the atmospheric parameter data set. This diagram covers the analysis discussed in Section 3.5.1.

extracted from a spectrum is extracted. This is of paramount importance when good time coverage is required of the data.

3.5.2 Correcting random outliers

The search for random outliers centres on detecting and correcting radial velocity values. Prior to the algorithm acting on any data at all, it was necessary to build up criteria of what constituted an outlier in data for a given off-zenith direction. This was done by collecting statistics on the radial velocity values in all the data sets in a given beam direction for the duration of the data run. The data collected for this thesis and presented in Chapters 4, 5 and 6, were collected over periods ranging from two to five days in length, with anything up to 26 different beam directions.

The statistics for a given data run were gathered on data before ground clutter and sea scatter spikes were accounted for, as discussed in 3.5.1. For an off-zenith beam, the upper limit on what constituted a good radial velocity value for a given off-zenith angle was set at the integer velocity value greater than 95.5% of the velocity values in the data set - the 2σ level. This level was calculated for north-south azimuths together, and for east-west azimuths together. The maximum value of these two pairs was then used as the maximum velocity level. In theory, different limits could have been used for different azimuths, but using one level for all azimuths at a given off-zenith direction was observed to produce good results, and was therefore adopted. The minimum velocity level for a good velocity was set at 0.5 ms^{-1}, just above the ground clutter limit discussed in Section 3.5.1 of 0.3 ms^{-1}.

For data collected with a vertical beam, most random outliers were points with velocities that were too large. As such, the velocity range that constituted a good velocity in a vertical beam data set was set at all points below the 2σ limit for the data run. In general, the vertical beam data presented in this thesis were not as affected by outliers as data from off-zenith beams. This meant that strict limits on what constituted a good atmospheric data point were not as crucial. The probable reason for the relatively clean nature of the vertical beam data relative to off-zenith data is the fact that sidelobes in a vertically directed beam are better behaved than

in an off-zenith beam, which makes the data less susceptible to spurious backscatter.

In this part of the algorithm, where persistent ground clutter and sea scatter have already been taken care of, the assumption that more good values than bad values exist at a given range gate in the data set is made. This assumption was observed to be true for the overwhelming majority of data as the outliers that this part of the algorithm detects are due mainly to aircraft and spurious, unidentified returns which do not have the persistency to overwhelm data over a large period of time. The odds are also pushed in favour of this assumption being true by cycling through the seven data sets analysed at any one time in the manner shown in Figure 3.4. The diagram in Figure 3.4 shows that of the seven files that are analysed in any one cycle of the algorithm, the last four are passed in their updated, possibly corrected form to be the first four of the next seven files to be analysed. By shuffling through the files in this manner, the odds are in favour of there being more good points than bad in a given range gate, simply because over half of the seven data sets have already been corrected, if necessary.

The seven data sets were split up according to range, into time series of seven data points at each range gate. Each radial velocity in the time series was then tested against the upper and lower velocity limits calculated earlier. If more points in an off-zenith beam data set were less than 0.5 ms^{-1}, then were between 0.5 ms^{-1} and the 2σ limit for the appropriate off-zenith direction, then the points less than 0.5 ms^{-1} were labelled as being true atmospheric points. If more points were between 0.5 ms^{-1} and the 2σ limit, than below 0.5 ms^{-1} then the points between 0.5 ms^{-1} and the 2σ limit were labelled as being true atmospheric data points. All points greater than the 2σ limit were excluded from being labelled true atmospheric data points. Figure 3.10 shows a set of seven profiles, one of which contains outliers outside the 2σ limit for the relevant beam direction and data run. The topmost figure shows the profile containing the outliers, while the bottom plot shows the same profile corrected for the outliers.

Points which were excluded from the true atmospheric data point set were then tested against the mean and standard deviation of the points in the true atmospheric data point set. If these excluded points were more than two standard deviations away

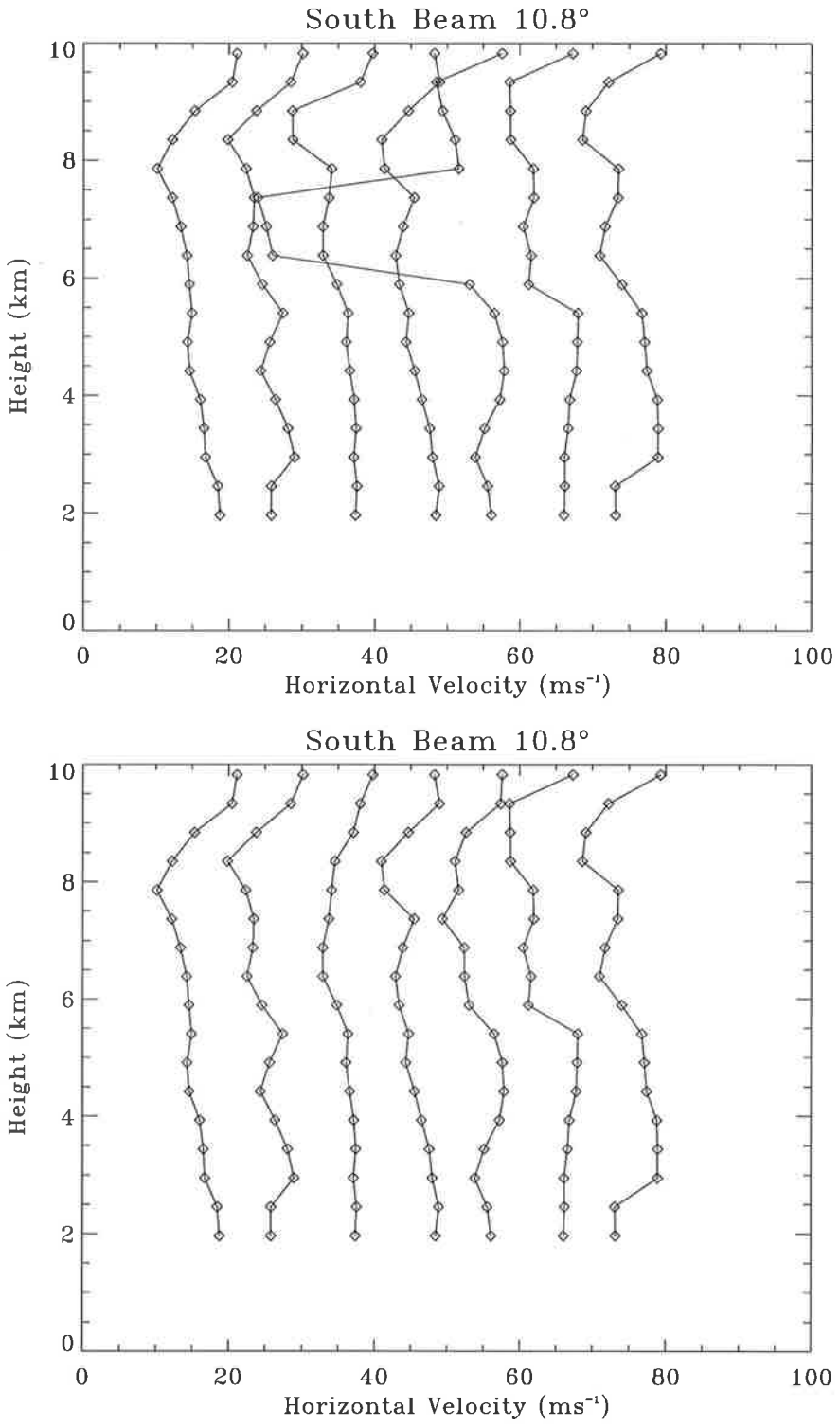

Figure 3.10: Top: Seven successive profiles of horizontal velocity through time with a 10.8° off-zenith south beam. This plot shows outliers due to random peaks in the spectra of one of the profiles. These outliers are probably as a result of aircraft backscatter which was not detected in Section 3.3.1. Bottom: The same seven profiles - here corrected for these random outliers. Each successive profile is shifted by 10 ms^{-1}.

from the mean of the true atmospheric point set, then they were flagged. The spectra corresponding to the flagged, excluded points were then refitted with a Gaussian function which had as the first guesses the mean values of the amplitude, radial velocity and spectral widths of the points in the true atmospheric data point set. In this manner the algorithm attempted to search for a peak in the spectrum which had similar characteristics to the other points at the same range within the seven data sets. Figure 3.11 shows spectra at two of the heights in which outliers were present in the profile shown in Figure 3.10. The topmost plot and the plot second from the bottom show the original Gaussian fits to the large spurious peak on the left. The second plot from the top and the bottom plot show the corrected fits to the plots directly above each of them. Note that in the second plot from the bottom, the size of the contamination in the spectra is such that the small atmospheric peak is barely visible.

This standard deviation test was observed to work well for random outliers which fell outside the 2σ limits for both vertical data and off-zenith data. It was also observed to work well for random outliers which made up a minority in being either less than 0.5 ms^{-1}, or in the range between 0.5 ms^{-1} and the 2σ limit for the appropriate off-zenith beam. Figure 3.11 is proof of the effectiveness of this standard deviation test. The use of the average characteristics of spectra that are determined to be good, as the first guesses of the Gaussian fitting function for spectra that are determined to be contaminated, makes it possible to extract true atmospheric peaks from spectra that are heavily contaminated. However, this standard deviation test is not effective at detecting and correcting points which are obvious outliers, yet fall within the limits calculated for true atmospheric data points. Figure 3.12 shows such an outlier in a set of seven profiles of horizontal velocity.

In order to detect these points, the algorithm passed the seven data sets through one final test which uses the derivatives of profiles of radial velocity as a function of height and time to test the smoothness of the data sets. The aim of this test is to identify points in the new parameter sets that are incompatible with the range and time that they belong to, rather than obviously disagreeing with the appropriate thresholds. It is based on the fact that points which an observer would consider to be "bad" have the basic characteristic of being discontinuous with the data set that they

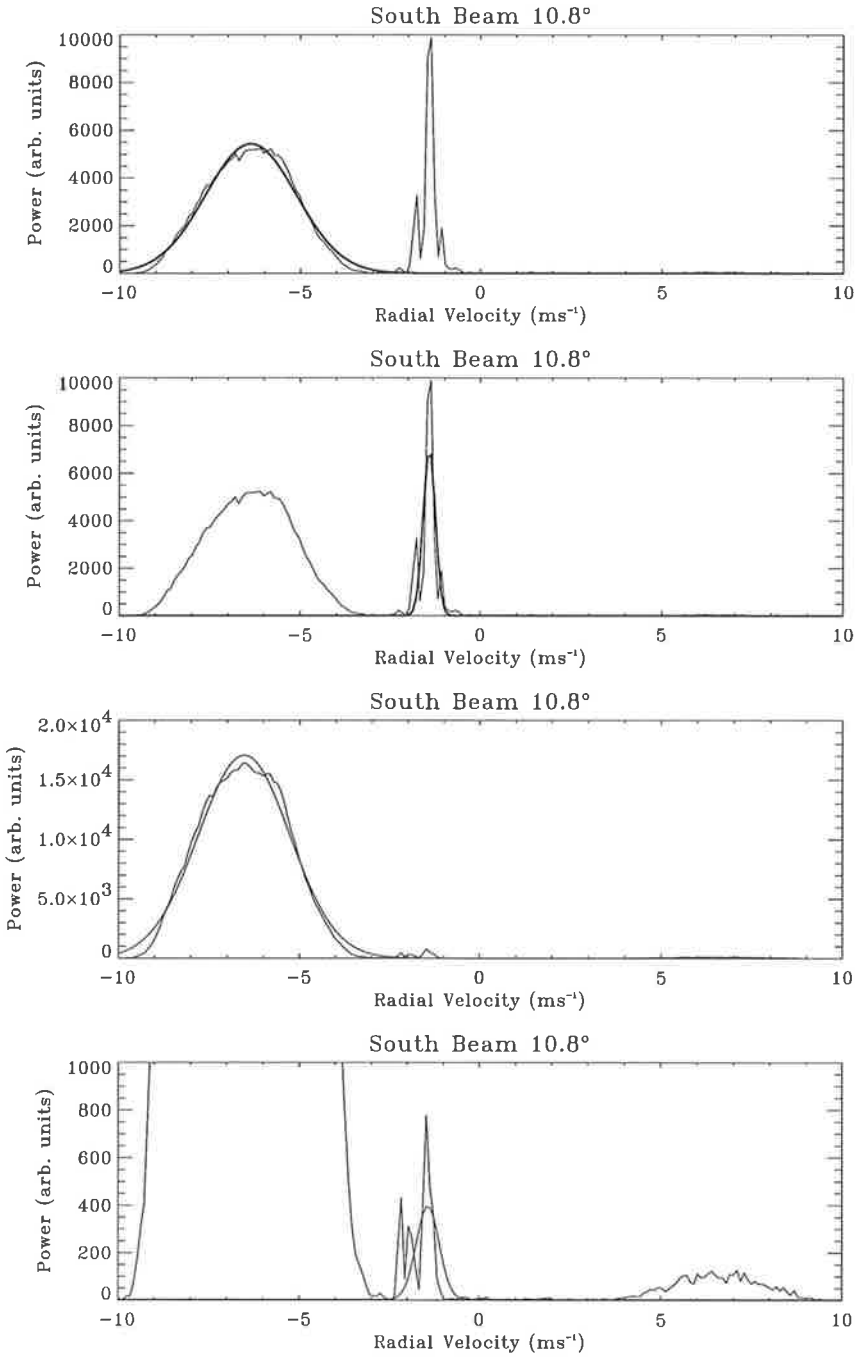

Figure 3.11: Top: Single power spectrum collected with a 10.8° off-zenith south beam. The large spurious peak to the left has been incorrectly identified as the atmospheric peak. Second from top: The same power spectrum as the one directly above this one, but with the correct atmospheric peak identified and fitted. Second from bottom: Single power spectrum, one range bin above the spectrum at the top of the page. Bottom: The same power spectrum as the one directly above this one, but with the correct atmospheric peak identified and fitted. Note the different y-axis scales; the amplitude of the spurious peak in the plot second from bottom is such that the true atmospheric peak is barely visible.

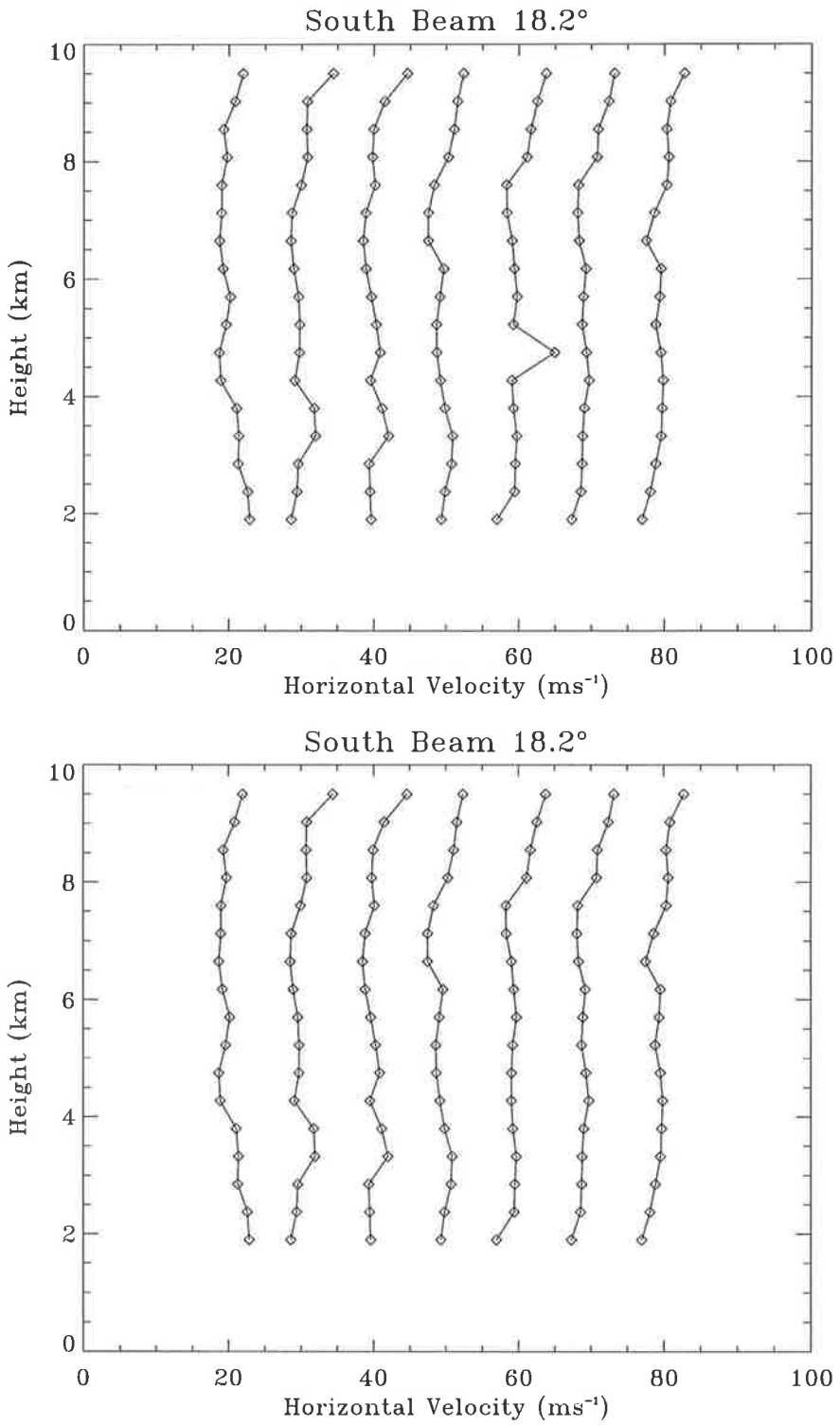

Figure 3.12: Top: Seven successive profiles of horizontal velocity through time with an 18.2° off-zenith south beam. This plot shows an outlier due to a random peak in the spectrum of one of the profiles. Bottom: The same seven profiles - here corrected for the random outlier. Each successive profile is shifted by 10 ms^{-1}.

belong to; their very nature is that they are an abrupt transition between the points before and after them. This is analogous to saying that a data set which has no bad points in it is continuous or smooth, each point being a gradual transition from the points before it to the points following it. The derivative of a data set is a sensitive indicator of the smoothness or regularity of that data set.

In a data set where the maximum absolute value is an abrupt change from the data points around it, the sudden change will cause a disruption in the derivative of the data set around the point where the bad value exists. The effect is a "seesaw" distribution about the position of a bad point which results in the maximum and minimum of the derivative straddling the location of the bad point. If however, the maximum absolute value is a smooth progression from the points around it, the derivative of the data set will not "seesaw" about the location of the bad point in the original data set. The derivative test used here is based on this fact.

Profiles of the radial velocity through both time and range were tested. Each of the seven data sets were differentiated as a function of range and time, and the minimum and maximum absolute values of the data sets and their derivatives were calculated. If the location of the maximum or minimum absolute value in the original data set as a function of time, and the mean of the locations of the maximum and minimum values of the derivative of the data set as a function of time were the same, then the value at that location in time was flagged. If the location of the maximum absolute value in the profile through range, and the mean value of the locations of the maximum and minimum values of its derivative through range were the same, and equal to the location of the point that was flagged in the profile through time, then the point was flagged. The spectrum corresponding to this flagged point was then refitted with a Gaussian function which had as the initial guesses the amplitudes, radial velocities and spectral widths of the other data points at the same range. Figure 3.13 shows the outlier in the fifth data file in Figure 3.12 as a function of time and range, along with the derivative of these profiles. The "seesaw" behaviour of the derivative about the location of the outlier in the original profile can be seen.

This derivative test is iterated over three cycles to catch strings of random outliers. The whole derivative test is repeated as a check that the points that were refitted in

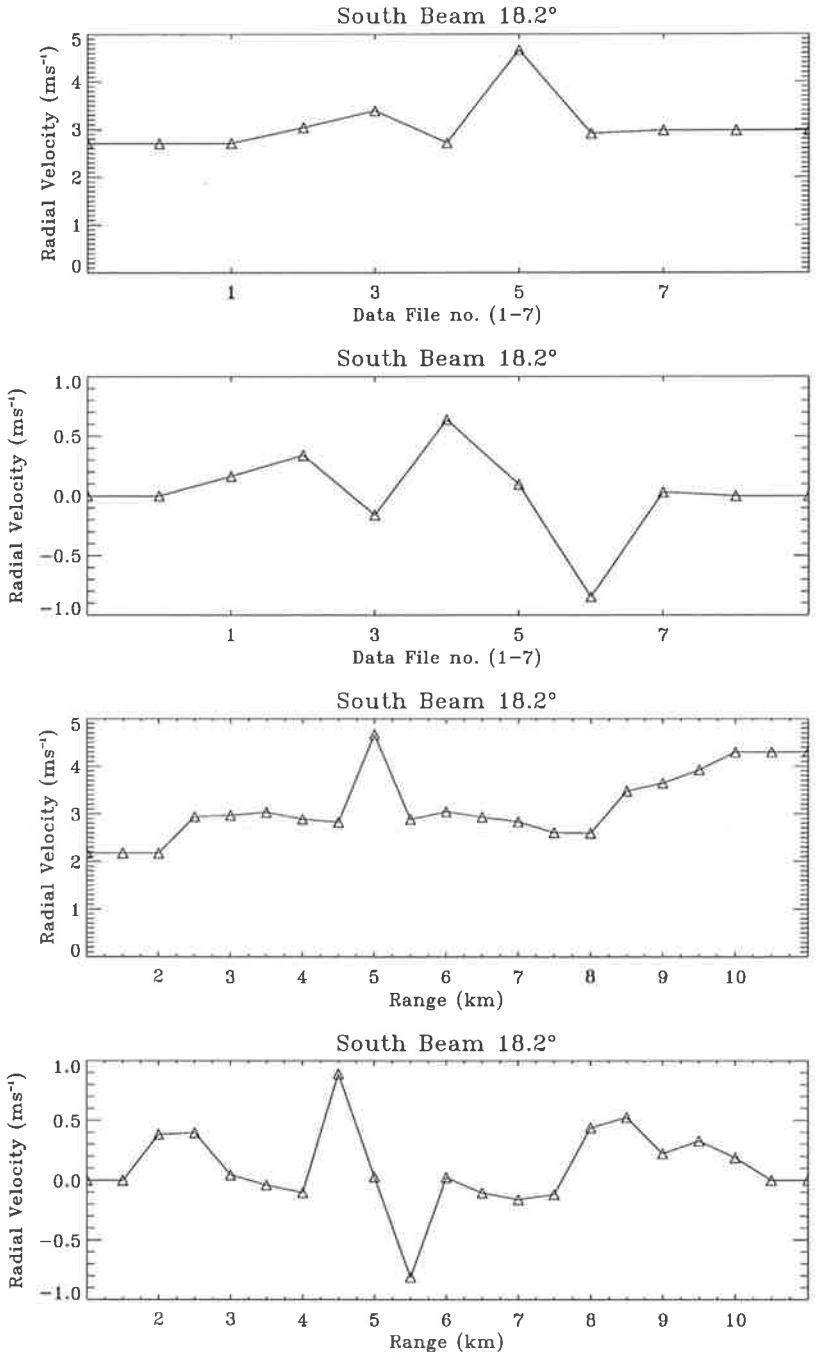

Figure 3.13: Top: Radial velocity as a function of file number for the seven data files shown in Figure 3.11. Second from top: The derivative of the profile directly above this one. Second from bottom: radial velocity as a function of range for the fifth file of the seven shown in Figure 3.11; the one with the outlier. Bottom: The derivative of the profile directly above this one. Note that the original profiles as a function of file number and range, are extended at the ends and contain values equal to the end data values. This is done so that the derivative is well behaved around these end data values.

the first set of iterations of the test are good points in the sense that they make the profiles of the seven data sets smoother as a function of time and range. In the second set of iterations of the derivative test, points which triggered the test were zeroed rather than having their spectra refitted with a Gaussian function - the assumption being that if a fit to a good atmospheric peak could be made, it would have been made in earlier iterations of the derivative test.

The derivative test is a final check that all points that have been refitted throughout have improved the smoothness of the seven data sets as a whole rather than creating more velocity outliers. It is also an effective way of catching random velocity outliers which have escaped the other detection tests in the algorithm by being embedded in the range of points considered to be true atmospheric parameter values Figure 3.14 shows the flow of data as discussed in this section.

3.5.3 Results

The data that were used as examples in this chapter were taken for an experiment that is discussed in Chapter 6. This data was collected over the full range of off-zenith angles from 3.6° to 22.0° off-zenith; six off-zenith directions in all, in all four cardinal azimuths. The large range of beam directions used was useful for testing the algorithm in this chapter, as it resulted in a large range of quality and radial velocities. The data was collected in two campaigns; the first, starting on 24/12/97, in light wind conditions, the second, starting on 21/1/98, in relatively stronger wind conditions. The effectiveness of the algorithm over the first two days of data from these two data sets calculated over the range from 2 - 10 km, over all off-zenith directions for a given azimuth, are presented in Table 3.1.

It can be seen that there is a similar amount of data that is rejected or modified in the western and northern azimuths, but that significantly more data is rejected or modified in the eastern and southern azimuths due to the presence of more contaminants at these two azimuths as a result of fading ground clutter and sea scatter and interference spikes respectively.

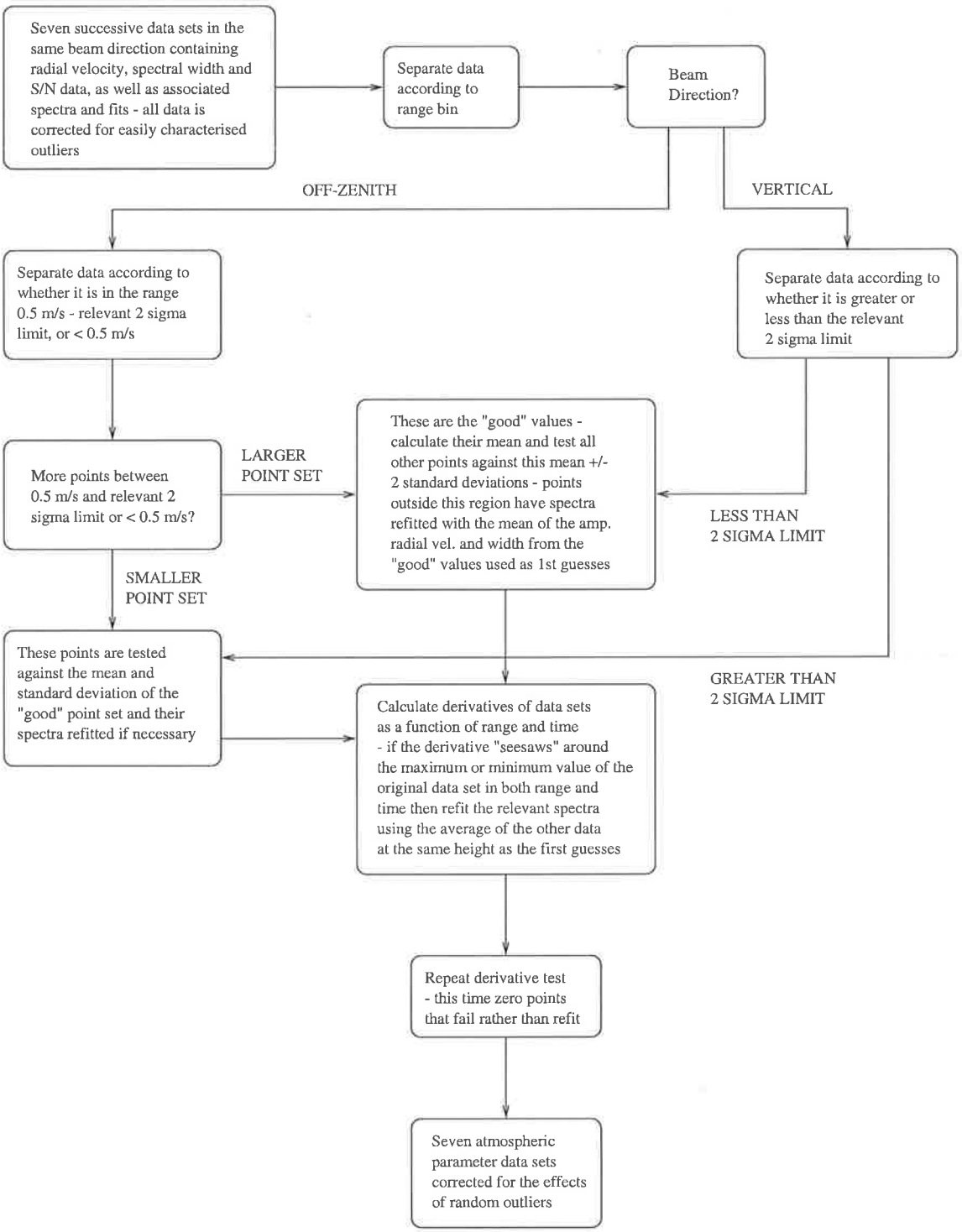

Figure 3.14: Flow chart showing the method of detecting random outliers and correcting for them in the atmospheric parameter data set. This diagram covers the analysis discussed in Section 3.5.2.

Azimuth	24/12/97 Percentage replaced with zero (%)	24/12/97 Percentage replaced with new value (%)
East	0.2	1.3
West	0.2	0.6
North	0.2	0.5
South	0.4	2.0
Azimuth	21/1/98 Percentage replaced with zero (%)	21/1/98 Percentage replaced with new value (%)
East	0.7	7.4
West	0.2	0.8
North	0.1	0.5
South	0.2	1.5

Table 3.1: Statistics on the number of points rejected (replaced by zero) and the number of points for which a new value was found by the algorithm. Data were collected on all off-zenith directions for a given azimuth for two days in each of two data sets, both with different prevailing wind conditions. The data are expressed as percentages of the total number of data points in the data sets; i.e: 0.7% of data in the east direction, from the data set starting on 21/1/98, were rejected.

3.6 Summary

In this chapter, the manner in which raw DBS time series are converted into atmospheric parameters from power spectra and then checked for the presence of outliers is discussed. These methods were developed by the author for use with the new upgraded radar, as the existing Doppler software on the BP VHF system calculated atmospheric parameters in the time domain where it is difficult to remove the effects of contaminants. The main contaminants observed in the data collected with the Buckland Park VHF ST radar are discussed, and then the algorithm which was developed to remove them is examined.

The manner in which the data is checked and corrected for outliers is based on recognizing two different kinds of spectral contaminants; those which produce an easily characterised outlier, and those which produce an essentially random outlier, in profiles of radial velocity as a function of time and height. The algorithm uses predetermined parameters to recognize easily characterised outliers, and a combination of a statistical

test and a smoothness test to detect random outliers. The success of the algorithm in detecting and correcting data over a large range of off-zenith directions, in all four cardinal azimuths is shown through plots of corrected spectra and their associated velocity profiles. The essence of the algorithm is that it returns to the power spectrum which produced a given outlier and looks for the true atmospheric peak. It has been seen in this chapter that this approach is very successful, and true atmospheric peaks are often found in data which is heavily contaminated. These results provide confidence in the accuracy of the atmospheric parameters used in this thesis.

Chapter 4

DBS and FCA measurements

4.1 Introduction

In this chapter a comparison of spaced antenna (SA) full correlation analysis (FCA) data with Doppler beam-swinging (DBS) data is presented. Horizontal velocities and aspect sensitivity via the aspect sensitivity parameter, θ_s, are estimated from the two techniques and compared. This chapter will begin with a discussion of the main findings of θ_s studies in the ST region. The rest of the chapter will focus on the experiment, beginning with a discussion of the set up of the radar and the data analysis that was required, before discussing the results of the comparisons of the two techniques.

4.2 Measurements of aspect sensitivity

The most common parameterisation of radar backscatter is to approximate the polar diagram of the backscatter of the atmosphere received by a vertically pointing beam by the function $exp(-\sin\theta^2/\sin\theta_s^2)$, Equation 1.13 in Chapter 1, where θ_s is the $1/e$ half width of the polar diagram. Given this, various investigators have reported θ_s values using the DBS technique. One of the features of DBS θ_s measurements is that the value of θ_s is dependant on the beam directions used to form the ratio r in Equations 1.15 and 1.17. *Hocking et al.* [1990], *Hooper & Thomas* [1995] and *Jain et al.* [1997] discuss comparisons of θ_s values calculated from various combinations of angles. *Hooper & Thomas* [1995] calculated θ_s values from combinations of the off-zenith angles 0°, 4.2°

and 8.5°, *Hocking et al.* [1990] used angles of 0°, 5°, 7°, 15°, 16° and 20°, while *Jain et al.* [1997] used angles from 0° to 12°, in 2° steps. All of these studies have shown that combinations of angles closer to the zenith generally produce smaller values of θ_s than combinations using off-zenith beam directions further from the vertical.

These differences are caused by the fact that, in essence, DBS power measurements of θ_s via the methods discussed by *Hocking et al.* [1986] and *Hooper & Thomas* [1995], attempt to reproduce the shape of the fall-off of power as a function of off-zenith angle, using only two points on the curve. Physically, θ_s is the $1/e$ half-width of the backscatter polar diagram, which is the -3 dB point on a zenith distribution of power plot such as that shown in Figure 1.2. Given this fact, it can be seen that if measurements of power at large off-zenith angles do not behave as described by Equation 1.7, they will be unable to represent the shape of the curve at a point only 3 dB down on the vertical beam power.

Hocking et al. [1990] has discussed how the scatter appears to flatten off at larger off-zenith angles, and that there appears to be an exponential (linear in dB) drop-off in power from 0° to about 8° - 12°, rather than the Gaussian (parabolic in dB) fall-off predicted by Equation 1.7. This is in agreement with the results of *Tsuda et al.* [1997a], as shown in Figure 1.2, Chapter 1 of this thesis, which shows a fairly linear drop-off in power between off-zenith angles of about 2° - 10°. *Hooper & Thomas* [1995] have noted that, at times, the scattering at off-zenith angles of 4.2°, 6° and 8.5° can be described by a single value of θ_s. While calculations of θ_s using 0° or 12° off-zenith beams produced smaller and larger values respectively.

Hocking et al. [1990] have suggested that different values of θ_s for different off-zenith beam combinations may be interpreted as evidence of the presence of different types of scatterers, with the aspect sensitive ones being more important directly overhead. This interpretation for the *Hooper & Thomas* [1995] results means that the different θ_s values observed using scatter from 0.0°, from off-zenith angles between 4.2° - 8.5°, and from off-zenith angles greater than 12°, are indicative of different scatterers. The differences in θ_s values as a function of off-zenith angle are a result of the fact that the θ_s parameterisation does not account for the different types of scatter that exist. As discussed in Chapter 1, the likely mechanisms for the aspect sensitivity at near vertical

beams are a combination of anisotropic turbulence and specular layers or "sheets" as observed in the temperature soundings of *Dalaudier et al.* [1994]. Beams at large off-zenith angles are less likely to be affected by this scatter and, as a result, the dominant scattering mechanism at these angles is the background isotropic scatter. Despite the limitations of the θ_s parameterisation, it is useful for the purposes of comparison both with other workers, and between the scattering observed with different radar techniques.

Measurements of θ_s in the ST region using VHF radars, include those utilising the power methods of *Hocking et al.* [1986] and *Hooper & Thomas* [1995], the FCA spatial correlation method used by *Vincent & Röttger* [1980] and *Vincent et al.* [1987], and the alternative DBS methods described by *Hocking et al.* [1990]. Together, these measurements provide a good picture of the characteristics and variation in θ_s, over a wide range of conditions and off-zenith beam angles.

In general, conditions in the troposphere have been found to be less aspect sensitive, with associated larger values of θ_s, than in the stratosphere. Although the results from a specific data set seem to depend on the meteorological conditions, and there is evidence of increased isotropy above about 18 km in the stratosphere. *Hocking et al.* [1986] reported increased aspect sensitivity in the lower stratosphere, relative to the troposphere. This was seen in θ_s decreasing from around 4° in the height range from 6 - 10 km to close to 2° above 10 km. Above about 18 km the θ_s values were greater than the values observed in the troposphere, indicating increased isotropy at these heights.

Despite the lack of θ_s information, *Tsuda et al.* [1986] reported similar findings by studying the backscatter over a range of off-zenith angles. Their measurements, over the height range from 6 - 15 km indicated increased aspect sensitivity above about 10 km. More recent multiple-beam DBS studies by *Hocking et al.* [1990] and *Jain et al.* [1997] confirm these results. Both of these studies saw strong aspect sensitivity in the lower stratosphere, above about 10 km, with the maximum aspect sensitivity being observed in the 15 - 18 km region in the *Hocking et al.* [1990] study, and 15 - 21 km in the *Jain et al.* [1997] study. Above these maximum heights, more isotropic scatter was seen in both investigations.

The effects of weather events on this general scattering behaviour have been investigated by *Hooper & Thomas* [1995] and *Yoe et al.* [1994]. *Hooper & Thomas* [1995] have shown that during the passage of a warm front, the scatter in the troposphere became more aspect sensitive, and was similar in nature to the scatter from the stratosphere. Tropospheric θ_s values during this time were approximately 5°. In the same study, a data set collected during calm conditions was also presented, in which less aspect sensitive scatter was observed in the troposphere, relative to the stratosphere, with tropospheric θ_s values of about 10° - 12°.

Yoe et al. [1994] found that in the presence of the jet stream, θ_s values in beams directed normal to the jet showed the expected greater aspect sensitivity in the stratosphere relative to the troposphere. Stratospheric θ_s values were in the range 4° - 8°, and tropospheric θ_s values were in the range 10° - 20°. However, θ_s values in beams directed parallel to the jet stream showed increased aspect sensitivity in the upper troposphere, in the height range from 9 - 12 km, with θ_s values in the range 4° - 8°. This scatter was more similar in nature to the scatter above it, from the stratosphere, then to the scatter below it from the middle troposphere. The work of *Yoe et al.* [1994] and *Hooper & Thomas* [1995] has thus shown that there are times when the troposphere is as aspect sensitive as the stratosphere. Generally, the anisotropy seen by these two studies corresponded to θ_s values less than 10°, while values larger than this were considered to be from less aspect sensitive scatter.

In contrast to the wide usage of the DBS techniques for θ_s measurements in the ST region with VHF radars, there have been relatively few measurements using SA techniques in the ST region. The measurements that have been made are in agreement with the DBS values in both magnitude and behaviour as a function of height. The spatial correlation method θ_s values of *Vincent & Röttger* [1980] are in the same general range as those by authors using the DBS technique. *Vincent & Röttger* [1980] report θ_s values (called σ_A in their paper) over the height range from 2 - 7 km of between 2° - 10°, with occasional values up to 20°. While the spatial correlation method θ_s measurements of *Vincent et al.* [1987] show increased aspect sensitivity in the stratosphere relative to the troposphere, in agreement with various DBS experiments, through histograms of θ_s values which display generally larger values in the

mid-troposphere (5 - 8 km) then in the lower stratosphere (12 - 15 km).

The spatial correlation method has been applied in the mesosphere by, for example, *Lesicar & Hocking* [1992] who compared spatial correlation method θ_s values with those from a spectral width method and a horizontal velocity method. These two latter techniques are similar to the methods used by *Hocking et al.* [1990] in the ST region, who used them along with the DBS power method of *Hocking et al.* [1986]. These techniques rely on estimating the amount by which a given spectral width or horizontal velocity measurement is underestimated due to the presence of aspect sensitive scattering. *Hocking et al.* [1990] used horizontal wind values from far off-zenith beams as the "unaffected" values, and winds from beams nearer to zenith for the "affected" values, while *Lesicar & Hocking* [1992] used the FCA derived horizontal winds and 11.6° DBS winds as the unaffected and affected measurements respectively. In the spectral width method, *Hocking et al.* [1990] compared the spectral width of vertical beam data with the theoretical values expected from isotropic scatter, while *Lesicar & Hocking* [1992] used the FCA fading time, $\tau_{0.5}$, which is inversely proportional to the spectral width, to directly calculate θ_s.

Reid [1988] has compiled mesospheric θ_s measurements made with various techniques by various researchers with the Adelaide MF radar. The results show good general agreement between the data which was collected in several separate experiments published between 1971 - 1988. *Lesicar & Hocking* [1992] have conducted the most extensive θ_s method comparison, using three years of mesospheric MF radar data. Their results showed that the spatial correlation and spectral width methods, which use vertical beams only, gave similar θ_s values with a clear seasonal dependance. However, the method using the 11.6° DBS horizontal winds resulted in different θ_s values, with no clear seasonal dependance. Given that DBS θ_s values are known to be dependant on the off-zenith angles used, the results of *Lesicar & Hocking* [1992] imply that other comparisons are needed between DBS and SA methods, with a range of DBS beams.

The aim of the work presented in this chapter was to compare θ_s as measured by the FCA spatial correlation method with values from the DBS power methods of *Hocking et al.* [1986] and *Hooper & Thomas* [1995]. This is the first such comparison, as *Lesicar*

& Hocking [1992] did not use the DBS power method, and *Hocking et al.* [1990] did not use the FCA spatial correlation method. Furthermore, the DBS power method and the FCA spatial correlation methods are more independant than the three methods used for the comparison of *Hocking et al.* [1990], all of which relied on data from the same Doppler beams, and more independant than those used for the comparisons of *Lesicar & Hocking* [1992], all of which relied on some aspect of the FCA. As such it should be a better test of both methods.

4.3 Experiment description

The FCA part of the experiment dictated the sub-groups of the antenna arrays used on reception, as the FCA requires three non-colinear antenna groups. This meant that FCA measurements were not possible with the older, East-West array, as it can only be split into groups joined by east-west baselines, as shown in Figure 2.13. A first attempt at a DBS/FCA experiment was conducted over the period 24-26/3/98, using the reception antenna groupings shown in Figure 4.1, where the numbers in the sections refer to the receiver number that the antenna group was connected to. The whole array combined was used to produce the transmit beam.

The best antenna arrangement for FCA is an equilateral triangle; the use of non-equilateral triangles has been shown to result in biases in the direction of the true velocity towards the azimuth perpendicular to the longest side of the triangle (e.g. *Briggs* [1984]). The FCA can be applied to four spaced antenna groups, and was, in theory, possible with the antenna configuration shown in Figure 4.1. However, the distances between the two groups on the diagonals in the array was too large and the analysis broke down as a result of the corresponding low correlations between antenna group pairs.

The fact that the analysis broke down is evidenced by the output of the FCA that was used for this experiment. The programs used to obtain FCA were provided by ATRAD[1], and were equipped with a series of data checks which reject results which

[1] Atmospheric Radar Systems, a radar development company which is licensed by the University of Adelaide and closely linked to the Atmospheric Physics Group of the University of Adelaide

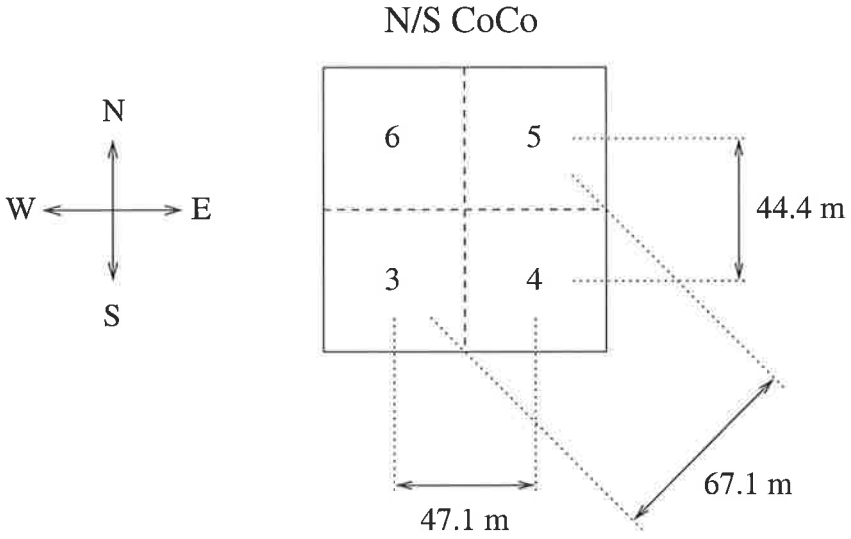

Figure 4.1: Antenna groupings for the experiment run over the period 24-26/3/98. The numbers in each of the sections corresponds to the receiver that the antenna group was connected to.

are physically or mathematically unreasonable. The first test of the FCA analysis is therefore that the analysis "accepts" the calculated results, rather then rejecting them. Analysis on the four antenna groups resulted in essentially no acceptances, as the basic pattern analysis on the groupings broke down due to the low correlations between the antenna groups. Despite the expected biases in the FCA applied to three groups in a right angles triangle, the FCA was attempted on this arrangement also. However, as for the the four antenna group data, due to the large distances between the antenna groups on the diagonal, most of the results were rejected by the FCA. A full description of the FCA rejection criteria is given by *Holdsworth* [1995], while Table B.1 summarising the criteria is shown in Appendix B. *Røyrvik* [1983] had similar problems with antenna spacing during a mesospheric FCA data run. The centres of the antenna groups in the work of *Røyrvik* [1983] were 149 m apart, and the author concluded that a smaller antenna array, preferably with spacings less than 30 m, would have produced better FCA results from the experiment.

A second FCA/DBS experiment was run over the period 12-14/5/98, with the antenna groupings as shown in Figure 4.2. This arrangement was quite close to an equilateral triangle, and the distances along the longest sides were considerably smaller

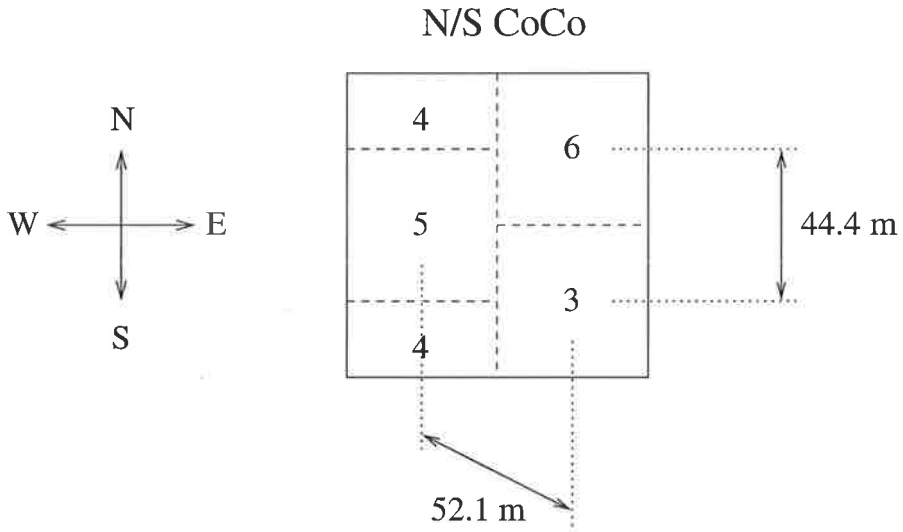

Figure 4.2: Antenna groupings for the experiment run over the period 12-14/5/98. The numbers in each of the sections corresponds to the receiver that the antenna group was connected to.

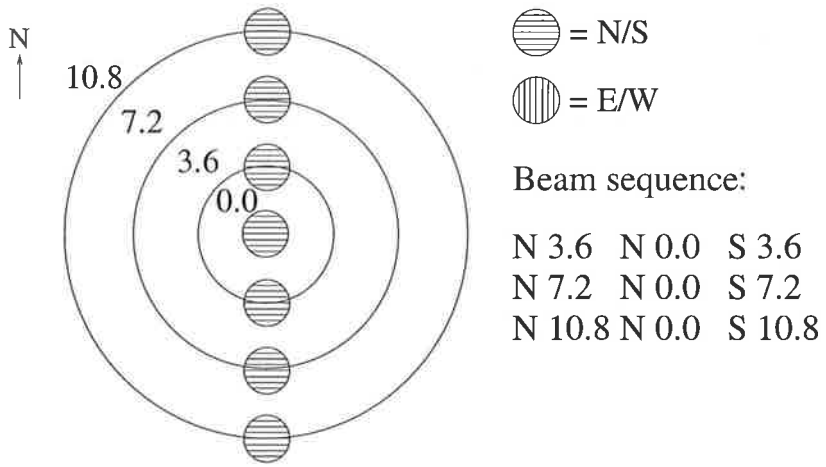

Figure 4.3: Beam sequence and direction for the experiment run over the period 12-14/5/98. The vertical beam data was used for the FCA, while all of the data was used for the DBS analysis.

than the longest distances in the antenna arrangement used for the 24-26/3/98 experiment. The antenna arrangement used for the data collection period 12-14/5/98 resulted in a good number of results being accepted by the FCA.

Figure 4.3 shows the beam sequence and directions that were used in the successful 12-14/5/98 experiment, while Table 4.1 shows the data collection parameters. Figure 4.4 shows the one way polar diagram of one of the square receiving antenna

Collection parameter	Parameter Value
PRF (Hz)	4096
No. coherent integrations	512
Time for one data set (seconds)	56.25
No. of data points	450
Velocity resolution (ms^{-1})	0.05
Max. unaliased velocity (ms^{-1})	11.1
Height range (km)	2.0 - 15.0
Range gate (km)	0.5
Pulse length (km)	1.0

Table 4.1: Data collection parameters for the 12-14/5/98 data set.

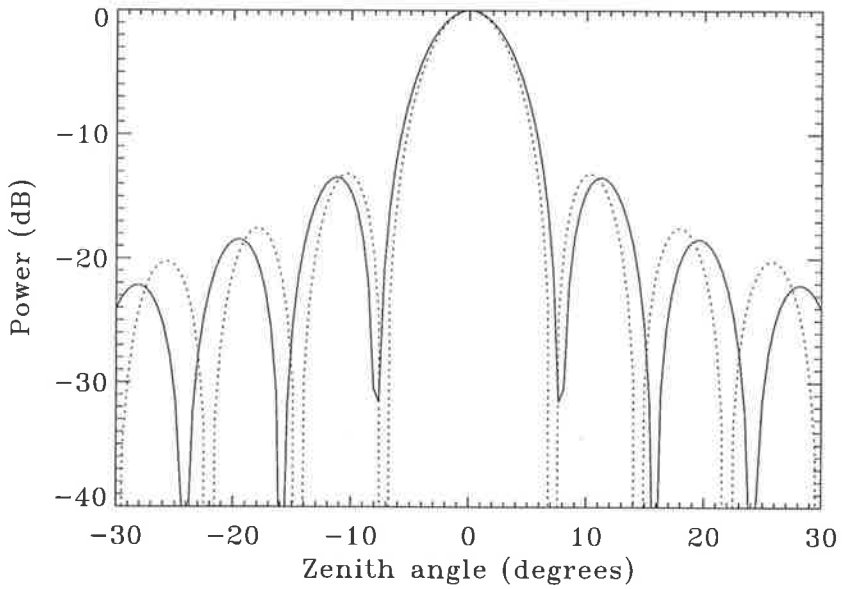

Figure 4.4: Cross-sections through the one way polar diagram of a square of antennas equal to one quarter of the North-South array, for a vertically pointing beam. Solid lines denote the east-west cross-section and dashed lines denote the north-south cross-section. This antenna grouping was used for both the 24-26/3/98 and 11-14/5/98 experiments.

sub-groups shown in Figure 4.2. This diagram has a half-power half-width of approximately 3.2° and 3.5° in the east-west and north-south planes respectively. Due to the fact that only the North-South array could be used for the FCA measurements, no data was taken on the East-West array, resulting in DBS measurements in the north-south or meridional plane only. Once data transfer times were taken into account, the data collection time for each beam direction was almost exactly one minute. A complete beam sequence was therefore collected in nine minutes. Note from Table 4.1 that the pulse length was 1 km while the range gates were 500 m. This is a result of the fact that 1 km is the minimum pulse length available with the BP VHF ST system, so in order to get good height resolution, it was necessary to oversample the pulse. All of the data presented in this thesis were collected with this pulse length/range gate relationship.

4.4 Data analysis

The FCA was applied to the data from receivers 3, 5 and 6, corresponding to the three square groups in Figure 4.2, for vertical beams in the sequence. DBS analysis was carried out on data from the whole array, for all beam directions. Before the DBS analysis could be carried out, the data from all four receivers for any given time series had to be combined to produce a single Doppler reception beam. The DBS analysis described in Chapter 3 was then applied to the single time series that resulted.

As was noted in Chapter 2, there is usually a phase offset between receivers about which the measured phase differences, or angles of arrival, between receivers varies. Figure 2.19 in Chapter 2 shows the phase differences between pairs of receivers as histograms. The offsets of these histograms are an instrumental effect, caused by various phase errors in the system. They must be removed before the real angles of arrival (AOAs) can be determined, and before the time series from various receivers can be combined. *Thorsen et al.* [1997] discuss procedures to remove these phase offsets, in a process commonly called "phase calibration". The assumption is that, on average, the returns will emanate from vertical, and as such, the histograms of the phase differences between receivers should be centred on 0°. *Thorsen et al.* [1997] find

that the best determination of the mean of the histogram is a Gaussian fit, as opposed to a moment calculation. *Thorsen et al.* [1997] also find that the phase offset varies as a function of height. This behaviour has also been seen by *Holdsworth* [1995], as well as being seen for the data presented here.

For the work presented in this thesis, this variation of the phase offset as a function of height was not seen to be of great importance when combining the data from various receivers into one Doppler beam. It was, however, an important effect in AOA measurements because the difference as a function of height was of the same order of magnitude as the AOA measurements themselves. As such, this effect will be discussed in Chapter 5 where the AOA measurements from this thesis are presented. For now, the fact that the effect exists is noted, as well as the fact that the approach of *Thorsen et al.* [1997] was followed here, and the phase offsets were determined from Gaussian fitting of the histograms of the phase differences. The mean of the histograms of data taken over a range of heights was used to remove the phase offset for all heights for which data were collected.

As well as the mean phase differences between receivers, amplitude differences between the time series from different receivers also exist. These differences are due to small differences in the gain between receivers, which persist despite the use of individual receiver gain settings. The amplitude of the time series from a given receiver can be calculated by calculating the amplitude of the auto-correlation function in the time domain, or the area under the spectral peak in the frequency domain, while the phase difference between receivers is calculated from the zero-lag phase of the cross-correlation function. Figure 4.5 shows histograms of the amplitude differences between receivers, expressed as the ratio of the amplitudes on the control receiver, receiver 3, with each of the other receivers, and histograms of the phase differences between receiver 3 and the other receivers. The amplitude correction applied to the data was calculated from the mean of a Gaussian fitted to the histogram, in the same manner as the method of removing the phase offsets.

The first thing that can be noted when comparing Figure 4.5 with Figure 2.19 from Chapter 2 is that the widths of the phase difference histograms are significantly larger in Figure 4.5. These widths are due to real angle of arrival differences in the

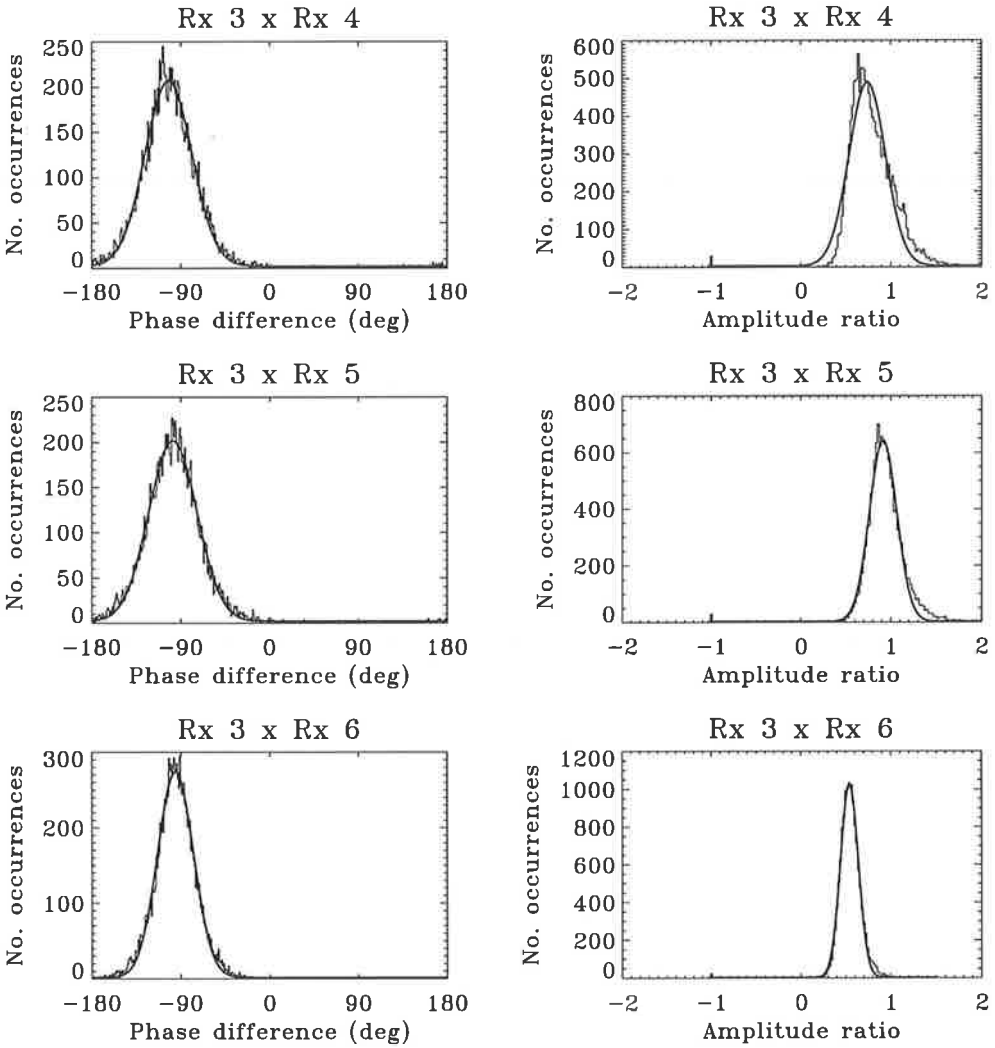

Figure 4.5: Histograms of the phase differences and amplitude ratios of receiver 3 with each of receivers 4, 5 and 6, before time series correction. The histograms were formed with data from the vertical beam on the North-South array, over the height range from 4 - 8 *km*, for the 12-14/5/98 data set. Also shown are Gaussian fits to the histograms. The mean of a Gaussian fit to a histogram for a given receiver with receiver 3 was used as the offset to be subtracted at all heights in data from that receiver.

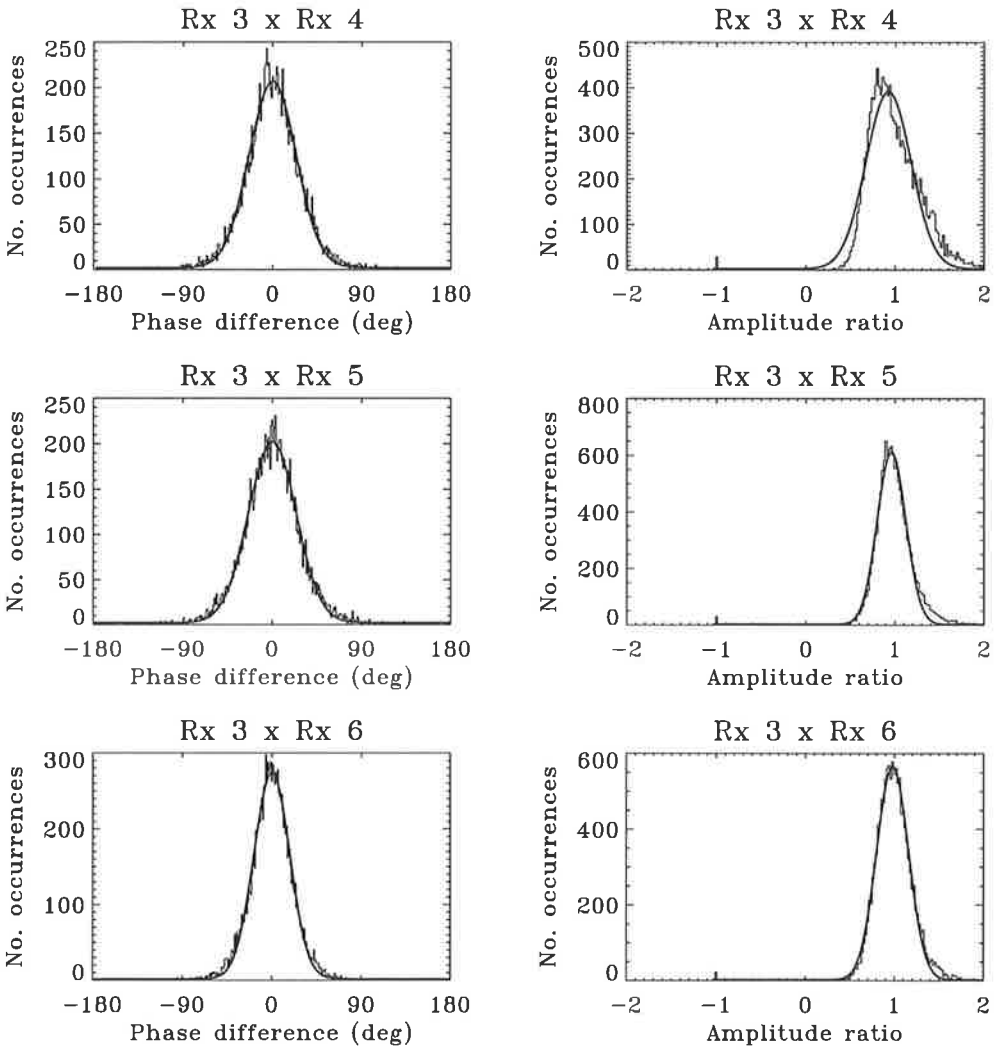

Figure 4.6: Histograms of the phase differences and amplitude ratios of receiver 3 with each of receivers 4, 5 and 6, after time series correction. The histograms were formed with data from the vertical beam on the North-South array, over the height range from 4 - 8 *km*, for the 12-14/5/98 data set. Also shown are Gaussian fits to the histograms. The mean of a Gaussian fit to a histogram for a given receiver with receiver 3 was used as the offset to be subtracted at all heights in data from that receiver.

signals received on a given pair of receivers. The narrow histograms of Figure 2.19 were the result of splitting a single output into four receivers; these were instrumental variations, as opposed to the real variations seen in Figure 4.5. The test data set discussed in Section 2.6, in Chapter 2, revealed that the minimum phase difference between receivers that could be observed with the BP ST system was $\pm 5°$, which corresponds to AOA measurement of $\pm 0.2°$ for the smallest antenna spacings. The width of the histograms in Figure 4.5 prove that the system is measuring real AOAs, far in excess of the errors estimated for the test data set discussed in Chapter 2. A combined time series, ts_{comb}, can be obtained by adding the time series from the receiver 3, ts_3, which was used as the control receiver, and the time series from each of the other receivers, each weighted with the means of the histograms

$$ts_{comb} = ts_3 + \frac{\overline{A}_3}{\overline{A}_4} ts_4 \overline{\phi}_{34} + \frac{\overline{A}_3}{\overline{A}_5} ts_5 \overline{\phi}_{35} + \frac{\overline{A}_3}{\overline{A}_6} ts_6 \overline{\phi}_{36}, \tag{4.1}$$

where, for example, ts_4 is the time series from receiver 4, $\overline{A}_3/\overline{A}_4$ is the mean of the histogram of the amplitude ratios of receivers 3 and 4, and $\overline{\phi}_{34}$ is the mean of the histogram of the phase differences between receivers 3 and 4. Each of the individual terms in Equation 4.1 is the time series from a given receiver, corrected with respect to receiver 3. Figure 4.6 shows the histograms of the phase differences and amplitude ratios, once the time series from individual receivers had been corrected. It can be seen that the histograms are centred on a phase difference of 0.0° and an amplitude ratio of 1, as expected.

4.5 DBS and FCA horizontal velocities

Before comparing the DBS and FCA horizontal velocities, the DBS data that had passed through the analysis discussed in Chapter 3 were first compared for consistency between off-zenith beam angles. Figure 4.7 shows scatter plots of the hourly averaged meridional velocity for the entire two day period from 12-14/5/98, calculated from the northward and southward beams at a given off-zenith angle, for all three combinations of the three off-zenith angles in the beam sequence.

The data shown in Figure 4.7 are from the height ranges 3 - 8 km. The height

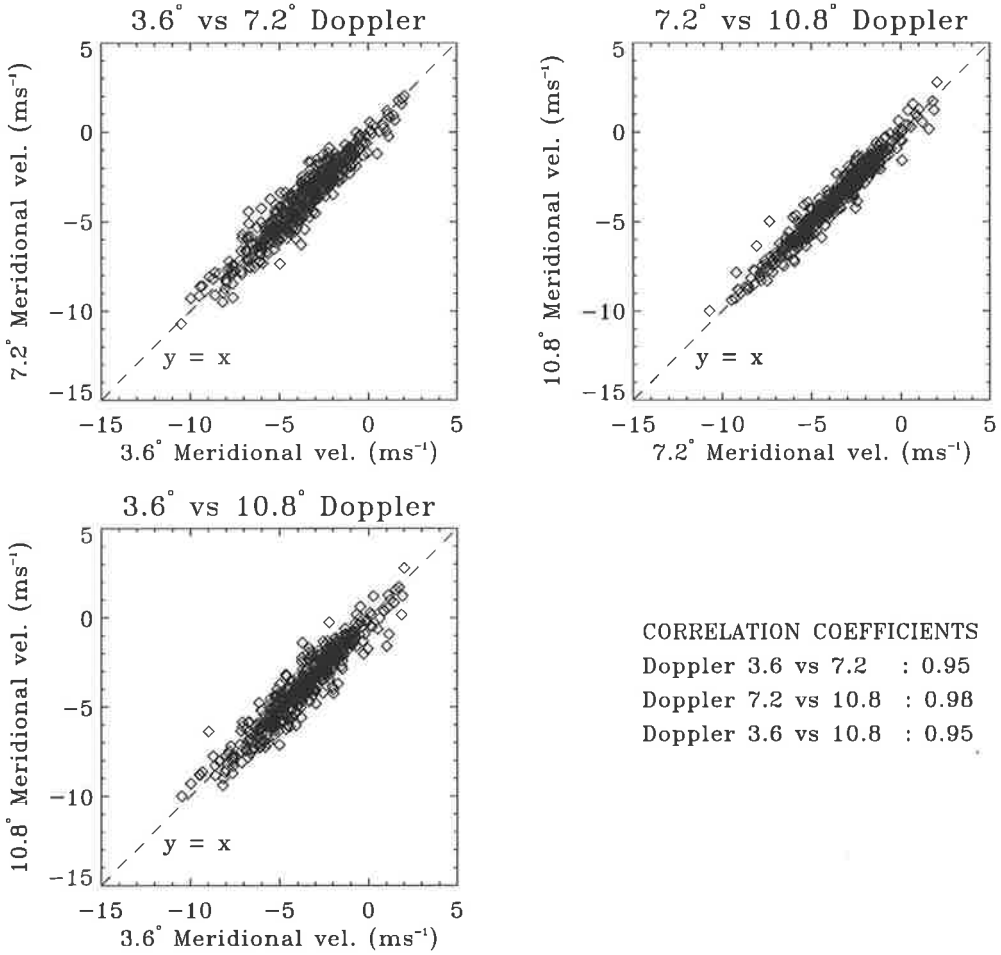

Figure 4.7: Scatter plot of the various combinations of DBS off-zenith beam meridional velocities. The individual velocities are hourly averaged meridional winds at each range gate from 3 - 8 *km*, over the full two day period from 12-14/5/98. Also shown are the lines y = x for each scatter plot, and the correlation coefficient for the data shown in the corresponding scatter plot.

range up to about 8 *km* was used for all of the data in this thesis as it provided the maximum number of results over the full length of the data sets. At times, good results were obtained up to about 12 *km* but data at these ranges were patchy in time and therefore not ideal.

It can be seen from Figure 4.7 that there is excellent agreement between the meridional velocities from the various beam directions. The correlation coefficients shown in Figure 4.7 were calculated from the time series of hourly averaged meridional velocities, and range from 0.95 for the comparisons including the 3.6° beam, to 0.98 for the 7.2°/10.8° combination. These correlation coefficients are reflected in the spread and

positioning relative to the line $y = x$ of the scatter plots. The 7.2°/10.8° combination shows a very tight clustering around the line $y = x$, while the combinations involving the 3.6° beam show slightly more points below the line $y = x$, indicating that the 3.6° velocities are very slightly under-estimating the true meridional velocities with respect to the other beams. This is the expected behaviour for beams affected by aspect sensitivity, and as such is confirmation that these DBS horizontal velocities are correct.

The correlation coefficients for the horizontal velocities at the minimum resolution of nine minutes, due to the time taken to sample all of the beams in the sequence, varied over height from from 0.70 to 0.87 for the 3.6°/7.2° combination, 0.68 to 0.86 for the 3.6°/10.8° combination, and 0.86 to 0.94 for the 7.2°/10.8° combination. This general behaviour is in keeping with the trend for better agreement for the 7.2°, 10.8° combination, due to the reduced affects of aspect sensitivity at these larger angles.

Figure 4.8 shows a scatter plot of the hourly averaged DBS meridional velocities, for each of the three off-zenith beams used, with the hourly averaged FCA off-zenith meridional velocities over the same period. Note here that an individual FCA measurement contributing to a given averaged value, was taken in the time between the corresponding DBS off-zenith beam measurement, as shown in the beam direction sequence description of Figure 4.3. For example, the comparison of hourly averaged FCA with hourly averaged 7.2° DBS, used data which was collected at north 7.2° for one minute, then FCA on a 0.0° beam for one minute, and then south 7.2° for one minute. The north and south beams were then combined to form a meridional velocity, using Equation 1.3 in Chapter 1, so that the DBS meridional velocity spanned the time period including the FCA measurement. This beam sequencing meant that the average of the individual FCA and DBS meridional velocities over one hour, provided essentially coincident FCA/DBS data sets, since the individual FCA/DBS values used to form the hourly average were collected over a period of only three minutes. This means that Figure 4.8 actually shows the results of three, completely independant, FCA/DBS experiments. For this reason, the correlation coefficients of each of these comparisons is shown, one coefficient for each of the three off-zenith beam directions bracketing the corresponding FCA measurements in time. The velocities shown in

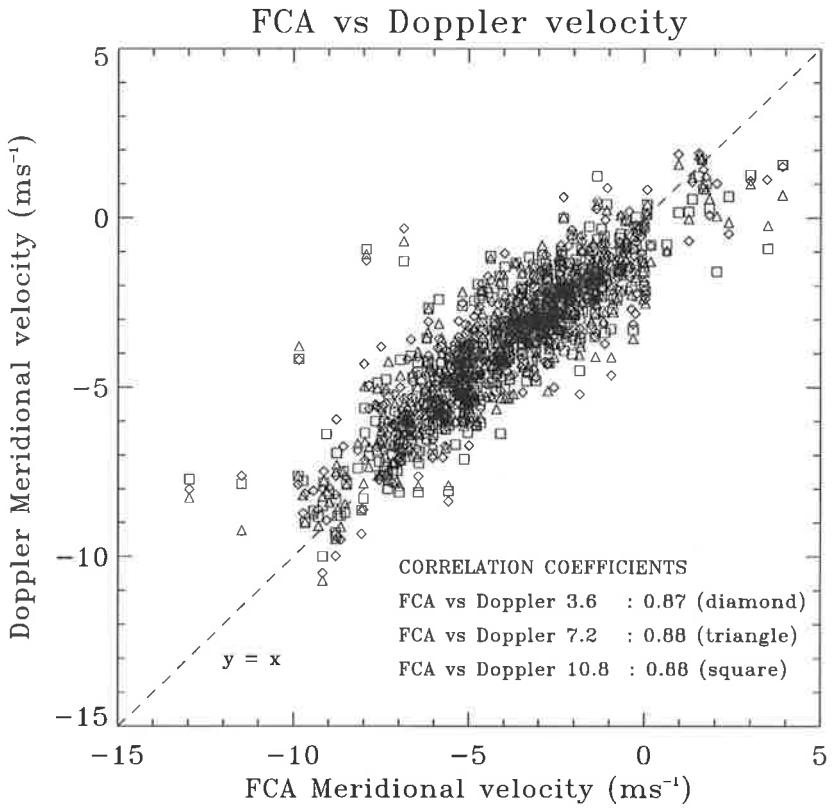

Figure 4.8: Scatter plot of the hourly averaged meridional velocities from DBS and FCA. The individual velocities are hourly averaged meridional winds at each range gare from 3 - 8 *km*, over the full two day period from 12-14/5/98. Also shown is the line y = x, and the correlation coefficient for the FCA with each of the three DBS off-zenith beam meridional velocities used in the experiment.

Figure 4.8 were measured over the height range from 3 - 8 km, for the entire data collection period from 12-14/5/98.

Figure 4.9 shows the individual hourly averaged meridional velocities for the 10.8° DBS data set, and the FCA data set, for each hour of the data set from 12-14/5/98. These results are expressed as a function of time, for a set of ranges within those used for the scatter plot shown in Figure 4.8. Also shown in Figure 4.9 are the meridional wind estimates from the six-hourly radiosondes launched at Adelaide Airport, represented by asterisks. The FCA velocities in Figure 4.9 are shown with error bars corresponding to the standard deviation of the meridional velocities withinthe one hour time bin. For clarity, the error bars for the DBS velocities are not shown on this plot as well. The DBS/FCA velocities shown in Figure 4.8 and Figure 4.9 were not corrected for the 4° rotation of the BP VHF antenna arrays, as shown in Figure 2.1 of Chapter 2. Instead, the radiosonde data shown in Figure 4.9 were rotated by 4° to lie in the same plane as the radar data.

It can be seen from Figure 4.8 and Figure 4.9 that the agreement between the DBS and FCA meridional velocities is very good. In Figure 4.9, the FCA velocity estimates are seen to be nearly always within the error bars of the 10.8° DBS velocity estimates, and at times the point-to-point comparison between the two techniques is excellent, as shown by the two lines joining the points for a particular method being almost coincident. As expected, there are more outliers for the scatter plot shown in Figure 4.8 then for the DBS off-zenith beam intercomparison scatter plots shown in Figure 4.7. However, the scatter in Figure 4.8 is well centred on the line $y = x$, and the spread of the plot is seen to be quite small, as evidence by the high correlation coefficients between the individual FCA/DBS comparisons of 0.87-0.88.

One limitation of this comparison is that the winds during the 12-14/5/98 data set were quite light, so the range over which the velocities were compared is quite restricted. With respect to the comparison between the radar and radiosonde wind values, the good agreement between the two radar techniques, as measured on the same radar, suggests that the times when these two techniques do not agree well with the radiosonde are a result of the spatial variation of the wind field between BP and Adelaide Airport. The last radiosonde shown, and the early sonde velocities at the 3

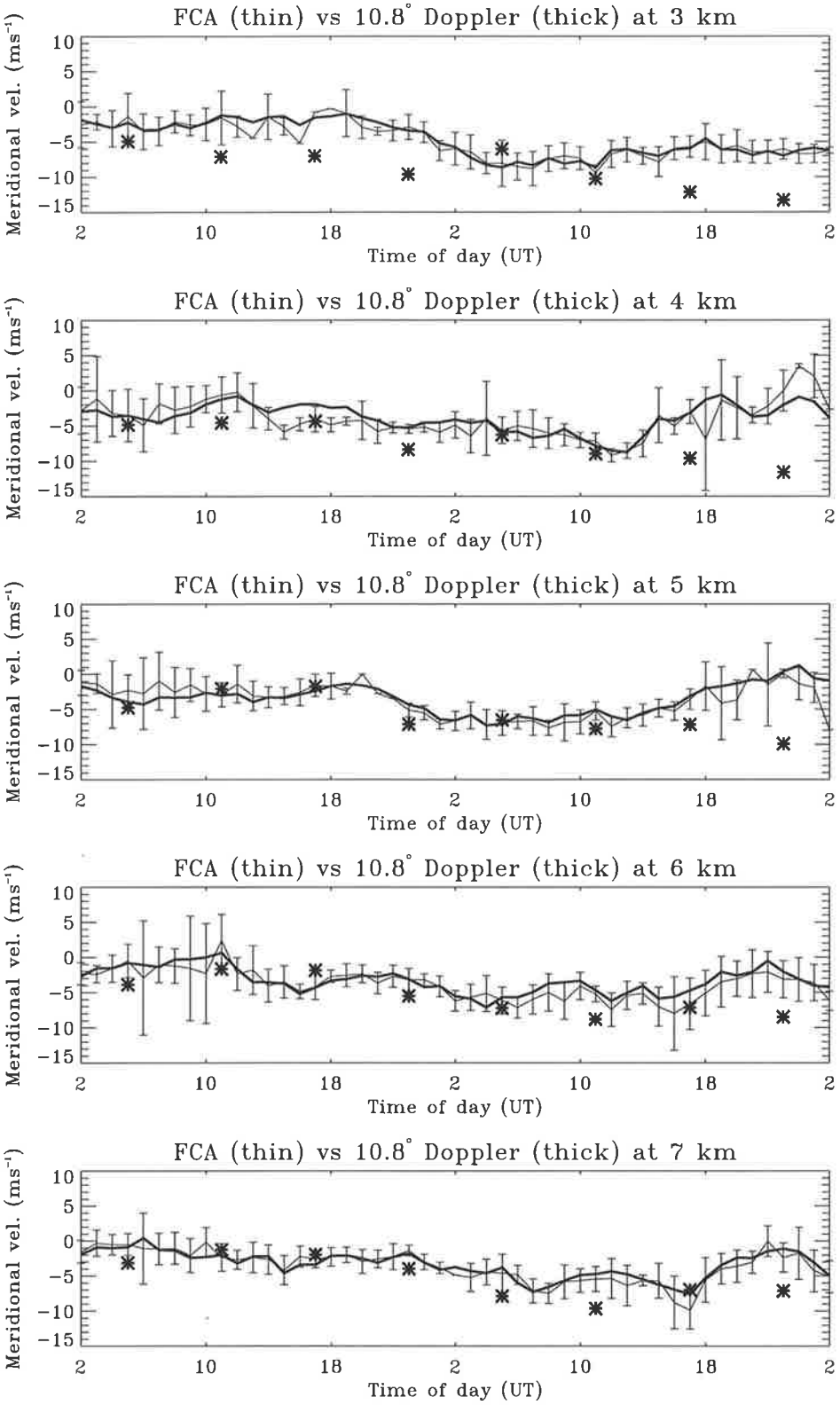

Figure 4.9: Time series plots of the hourly averaged meridional velocities from the 10.8° DBS data set and the FCA data set, at a selection of ranges, for the 12-14/5/98 data set. The meridional wind as measured by six-hourly Adelaide Airport radiosondes is shown as the asterisks.

km range gate, in particular, do not agree very well with the radar wind velocities. Except for these values, the radiosonde velocity estimates are generally within the error bars of the 10.8° DBS velocities.

4.5.1 Discussion

The DBS/FCA horizontal velocity comparison of *Van Baelen et al.* [1990] was from data collected over a $3\frac{1}{2}$ day period, although results were presented for only one data set, with ten 1 minute DBS data sets at 10° off-zenith, being compared with twelve 40 second FCA data sets before and after the DBS data sets. This experiment scheduling meant that the DBS and FCA velocities were spaced in time by roughly nine minutes. The emphasis of the *Van Baelen et al.* [1990] study was to establish the bounds within which the agreement between the two techniques was good or bad. As such, antenna spacing, the effects of the vertical velocity, and comparisons with both the FCA apparent and true velocities were investigated.

The DBS/FCA horizontal velocity comparison of *Vincent et al.* [1987] was based on DBS data collected at off-zenith angles of 4°, 7°, 11° and 15°, with the original BP VHF ST radar. Each DBS data set took between 8-14 minutes to collect, one after the other, over roughly $2\frac{1}{2}$ hours, with the FCA measurements being made in between manually changing the DBS phasing cables. The emphasis of the *Vincent et al.* [1987] work was to compare FCA winds on the BP VHF ST system, which was new at the time, with wind measurement made by radiosondes. The work concentrated on the differences between these two methods in order to verify the correct operation of the radar.

As such, the work of *Vincent et al.* [1987] and *Van Baelen et al.* [1990] do not present a comparison over a period long enough to do time averaging in order to assume that the DBS and FCA are coincident. In contrast, the DBS/FCA comparisons presented here are, firstly, collected closely in time, and secondly, collected over a sufficient time period so that it can be assumed that averaging over an hour for each method will provide a time series of essentially coincident values from the two methods, over the full two day period. By taking this approach it was possible to calculate

correlation coefficients and to show the results in scatter plot formation, both of which give concrete information on the degree of similarity between the two techniques, in a manner which has been used by other researchers to compare radar winds with other techniques such as radiosondes.

Hocking [1997*b*] found a correlation coefficient between DBS and radiosonde wind speeds of 0.92, and a correlation coefficient between DBS and radiosonde wind directions of 0.97. While *Vincent et al.* [1987], found a correlation coefficient of 0.91 between the wind direction measured using the FCA and radiosondes, and a correlation coefficient of 0.85 between the magnitude of the wind speeds measured using the FCA and the radiosondes, over the height range from 2 - 8 *km*. The differences between the comparisons made in these two works can be explained in terms of the fact that the *Hocking* [1997*b*] work used radiosonde data from sondes launched at the radar site, while *Vincent et al.* [1987] used sondes launched at Adelaide Airport; the same launching site as the sonde data used for Figure 4.9. Because of the fact that the radar data collected for the FCA/DBS comparison presented here was restricted to the meridional plane only, the correlation coefficients shown in Figure 4.8 are effectively for the wind speed only. As such, the correlation coefficients shown in Figure 4.8 agree well with the correlations coefficients determined by *Hocking* [1997*b*] and *Vincent et al.* [1987] for their radar/radiosonde wind speed comparisons.

4.6 DBS and FCA aspect sensitivities

Figure 4.10 shows time series of θ_s calculated using the *Hocking et al.* [1986] DBS power method and FCA spatial correlation method, as discussed in Section 1.5 of Chapter 1, over a range of heights. The data points in this plot are the median values of θ_s for each method, over a one hour period, for the full two days of the 12-14/5/98 data set.

Individual FCA θ_s measurements in a given one hour period were calculated from individual one minute FCA time series, from the vertical beams in the sequence shown in Figure 4.3. The median value of these one minute FCA estimates was then calculated for each height. Individual DBS θ_s measurements in a given one hour period were

calculated from the power in the one minute time series in a given off-zenith beam, and the power in the one minute time series in the vertical beam, collected either directly before or directly after the off-zenith beam time series, as shown in the beam sequence of Figure 4.3. This meant that θ_s values using the DBS method for the north and south directions at a given off-zenith angle were not independant as they use the same vertical beam parameters, from the beam directed between them in time. The median value of the individual DBS estimates was calculated for each height, for both the north and south directions. DBS θ_s from the north beam only are shown in Figure 4.10. The results from the south beam were essentially identical and are therefore not included.

The thick unbroken line in this plot represents θ_s values as calculated using the FCA spatial correlation method. The thin unbroken line shows the DBS method using the north 3.6° beams, the dashed line shows the DBS method for the north 7.2° beams, and the dash-dot-dot-dot line shows the DBS method for the north 10.8° beams. As discussed in Chapter 1 the spatial correlation method of measuring θ_s from FCA data utilises pattern scale measurements. As such, it should be noted here that while the limitations of the DBS power method of measuring θ_s are in the assumption about the distribution of backscatter as a function of off-zenith angle, the limitations in the FCA spatial correlation method are in the fact that the particular antenna spacing used in the experiment will dictate to some extent the spatial scales that are observeable. This is a possible source of bias in FCA θ_s values. In the limiting case, if FCA data is collected with radar beams that are too narrow the pattern scale measured with the antenna groups will bear no relationship to the atmosphere scatterers. *Holdsworth* [1995] has studied in detail the various potential biases in the FCA, including this so-called beam-limiting case. However, the beam widths used for the FCA experiment discussed here are not expected to be affected by this problem, and given the fact that the FCA and DBS horizontal velocity values are in very good agreement, it is fair to assume that no significant biases exist in the FCA data set examined here.

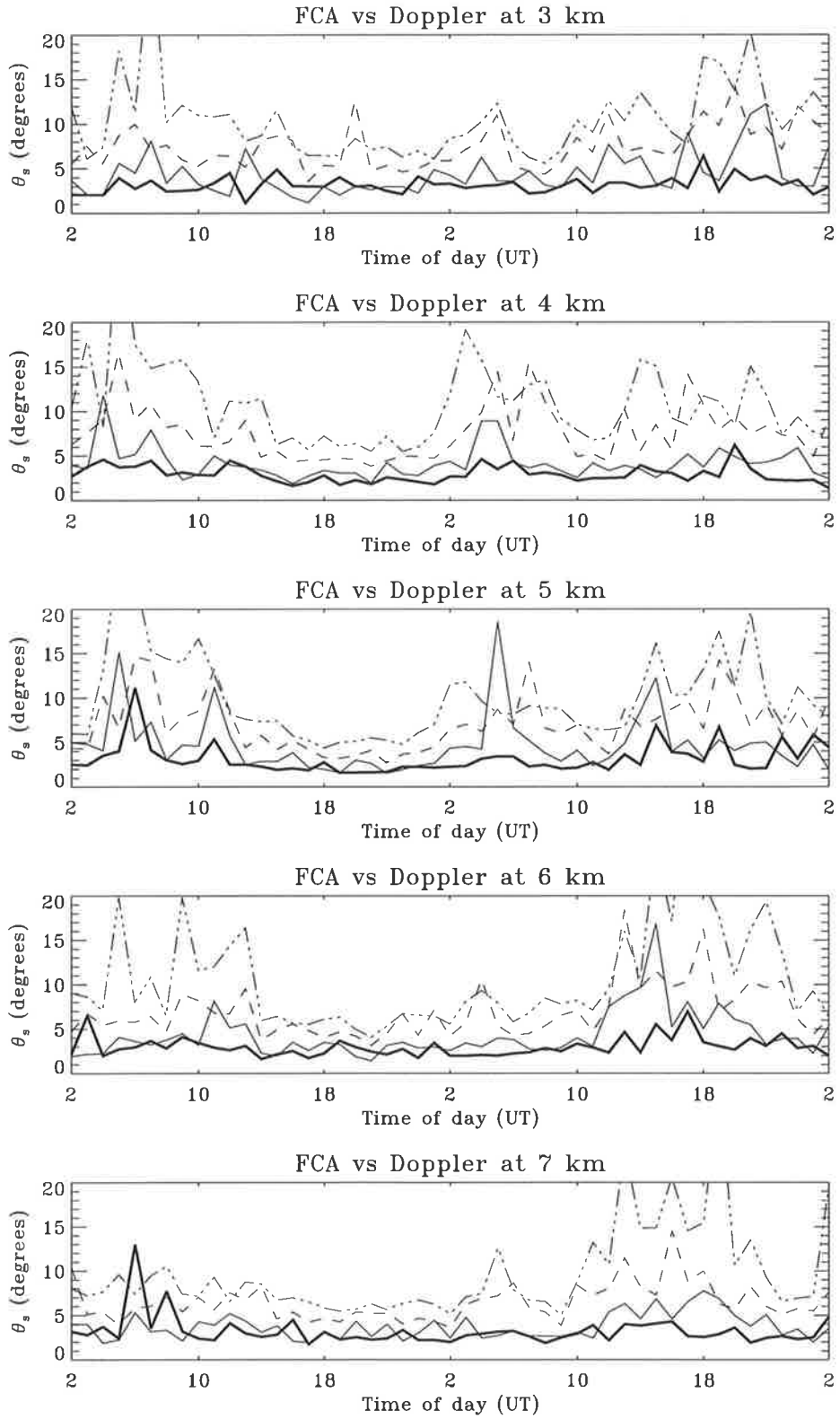

Figure 4.10: Median θ_s values from one hour periods, for the *Hocking et. al.* [1986] DBS method and the FCA spatial correlation method, for selected range gates, over the full two day period of the 12-14/5/98 data set. Thick unbroken line = FCA spatial correlation θ_s, thin unbroken line = DBS using 3.6° and 0.0° beams, dashed = DBS using 7.2° and 0.0° beams and dash-dot-dot-dot = DBS using 10.8° and 0.0° beams.

4.6.1 Discussion

A number of the features of the θ_s behaviour, as a function of time, height and method are obvious from Figure 4.10. The first thing to note is that the values of θ_s as shown in Figure 4.10 are in the same range seen by other workers, as discussed in Section 4.2. Secondly, the magnitude of the DBS method θ_s values increases as a function of the off-zenith beams used, with the largest DBS θ_s values being produced by the 10.8° beam, and the smallest DBS θ_s values resulting from the 3.6° beam. This is also agreement with the results found by other authors. Thirdly, it can be seen that there is more variation as a function of time in the 10.8° and 7.2° DBS θ_s values then in the 3.6° DBS or the FCA θ_s values. And finally, it can be seen that in general the 3.6° DBS θ_s values and the FCA θ_s values have similar magnitudes, in contrast with the other two DBS θ_s estimates at 7.2° and 10.8°.

In order to understand this behaviour, it is necessary to examine the scattering as a function of off-zenith angle that produced the θ_s results shown in Figure 4.10. Figure 4.11 shows the hourly averaged signal power in each of the beams: 0.0° on the North-South array, north 3.6°, north 7.2° and 10.8°, at two of the ranges shown in Figure 4.10. The data in the two plots shown in Figure 4.11 are expressed in linear units in order to make the variation as a function of off-zenith power clearer. These plots show signal power rather than SNR as signal power is used in the *Hocking et al.* [1986] method to calculate the θ_s values.

For comparison with these signal power plots, Figure 4.12 shows the noise power over the same period and range gates as for Figure 4.11. The passage of the galactic centre is evident in the two plots of Figure 4.12 as the two enhancements at roughly 18 UT on 12/5/98 and 13/5/98. The galactic centre moves at a rate of approximately 15° an hour, and since all of the beams used in the 12-14/5/98 data set were within 10.8° of one another, the galactic centre peaks in all of the beam directions within a one hour period. The noise power values shown in Figure 4.12 are the median values in the same hour of data for which the average signal power values were calculated for Figure 4.11. The median was calculated for the data in Figure 4.12 in preference to the mean because of the "spiky" nature of the noise profiles. For Figure 4.11, the median

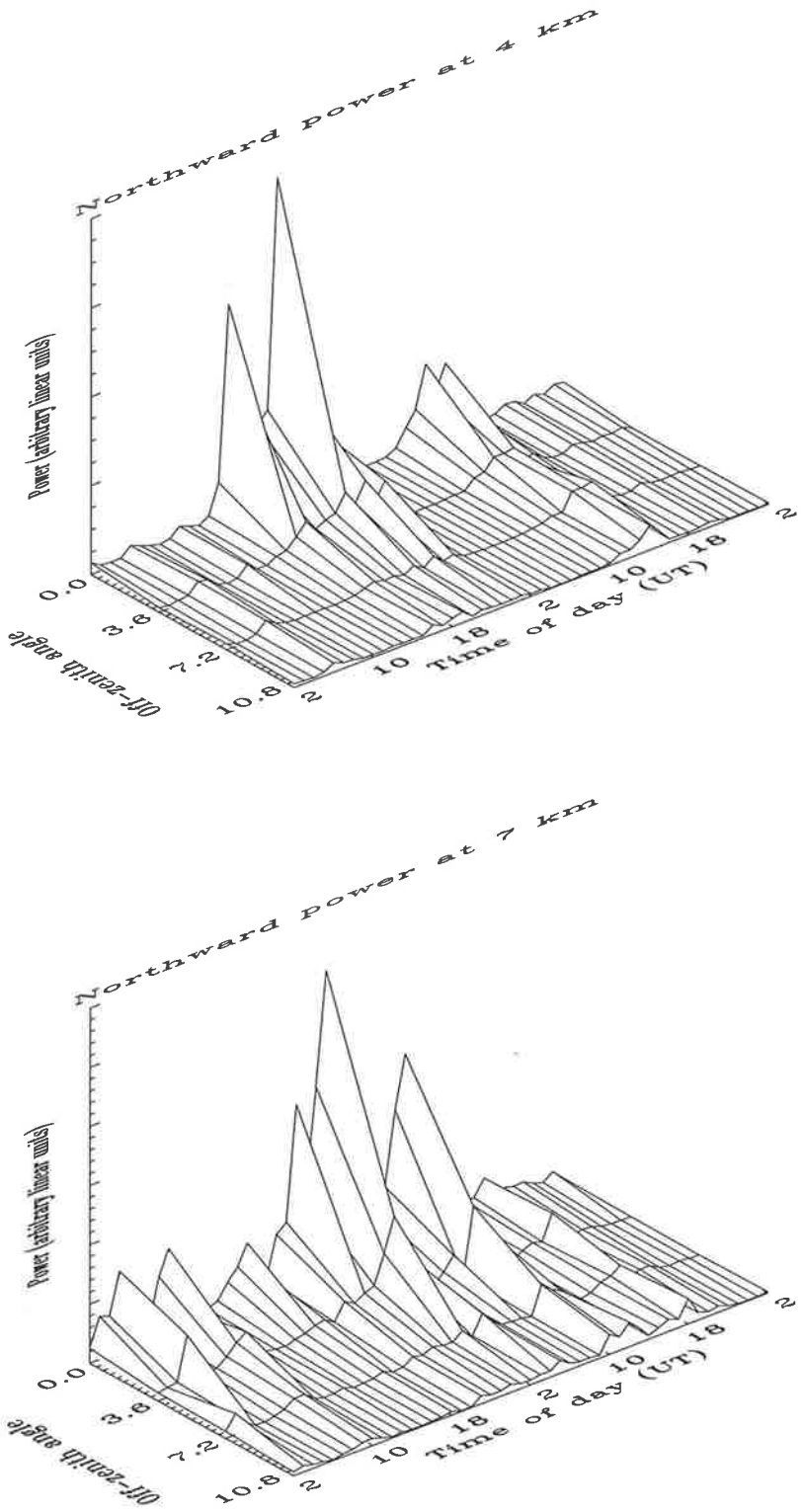

Figure 4.11: Hourly averaged signal power in the northward beams, for the full two day period of the 12-14/5/98 data set, at two selected range gates, in linear units.

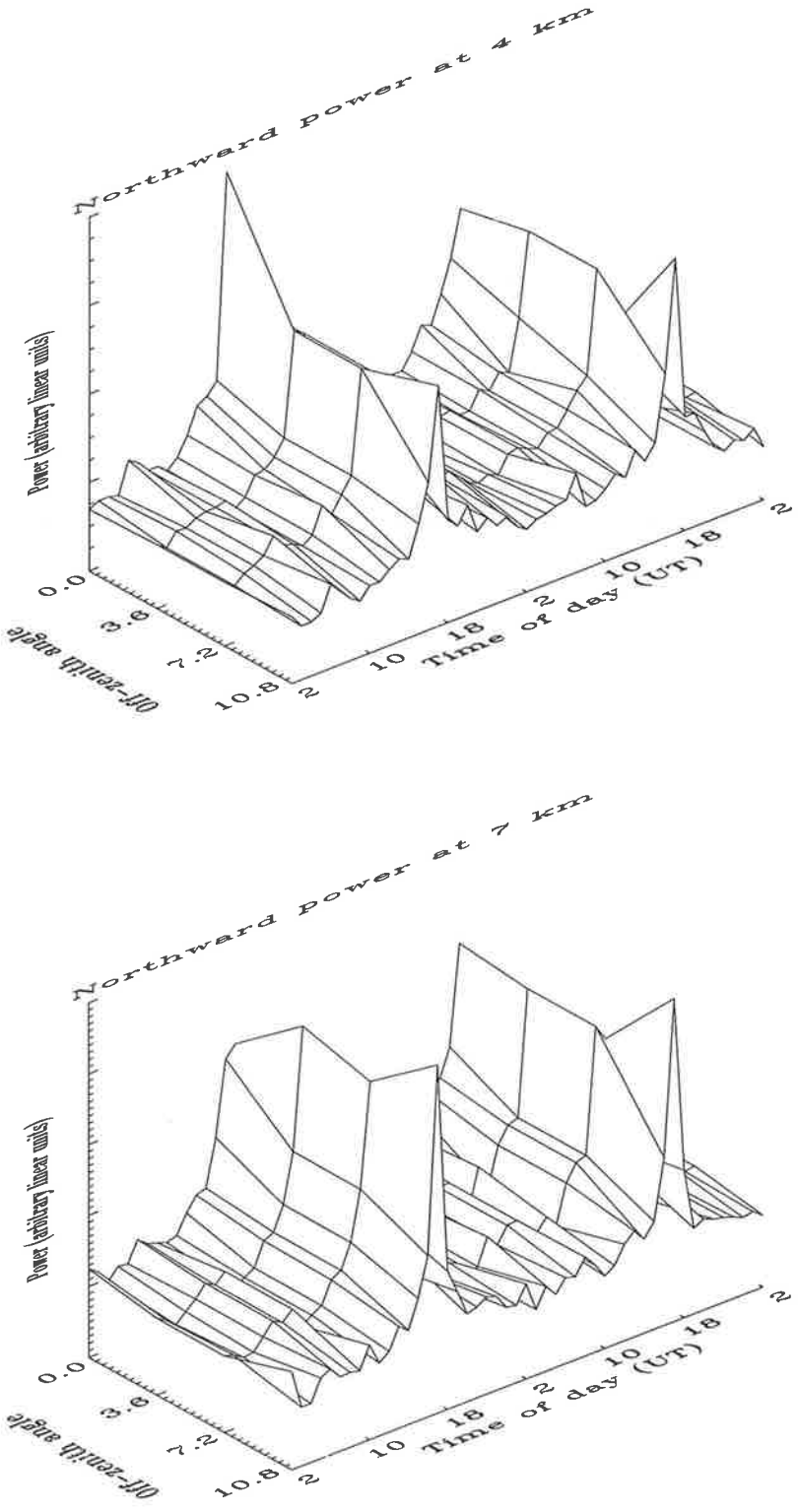

Figure 4.12: Hourly median noise power in the northward beams, for the full two day period of the 12-14/5/98 data set, at two selected range gates, in linear units.

and average values within a one hour period gave almost exactly the same results and as such, the average was used. By comparing Figure 4.11 and Figure 4.12 it can be seen that the enhancements in signal power as a function of off-zenith angle shown in Figure 4.11 appear to be genuine atmospheric enhancements, and not related to the background noise as shown in Figure 4.12. The galactic centre is the main noise feature and it appears to affect all the beams in the same manner, while the enhancements in power seen in Figure 4.11 do not.

The off-zenith power distributions at 4 km and 7 km shown in Figure 4.11 are quite different from one another, as are the corresponding θ_s values for these two heights as shown in Figure 4.10. At 4 km, between the hours of approximately 16 UT on 12/5/98 and 2 UT on 13/5/98, the θ_s values in Figure 4.10 for all methods track each other; they all have the same general behaviour from point to point, despite the offsets between the FCA and 3.6° DBS θ_s values and the 7.2° and 10.8° DBS values. Figure 4.11 shows that in this period there was a large difference in the back-scattered power as a function of off-zenith angle, with the power at 0.0° and 3.6° being greatly enhanced above the power at 7.2° and 10.8°. At 7 km, from the beginning of the data set until about 10 UT on 13/5/98, the θ_s values in Figure 4.10 for all methods have the same general behaviour, again, despite the offsets shown by the 7.2° and 10.8° DBS methods. The backscattered power as a function of off-zenith angle in Figure 4.11 shows enhanced power at 0.0° and 3.6° relative to that at 7.2° and 10.8°.

It therefore appears that when the scatter in the 12-14/5/98 experiment was highly aspect sensitive, that is, when the power observed in a given beam direction was dependant on the pointing angle, all of the DBS θ_s values, at each of the angles used in the experiment from 3.6° to 10.8° show the same general variation as the FCA θ_s value, even though the 7.2° and 10.8° DBS θ_s values were larger. In addition, during these periods of anisotropic scatter, the absolute value of θ_s from the 3.6° DBS and FCA seem to agree very well, as seen in Figure 4.10. The assumption that other researchers have made when θ_s values are the same for different beam directions is that the beams are responding to the same scattering mechanisms. In this instance then, it appears that the vertical and 3.6° beams are receiving backscatter from the same scattering structures, while the beams at 7.2° and 10.8° are receiving different

scatter relative to the beams closer to zenith.

At other times in the data set, for example, at 4 km before 16 UT on 12/5/98 and between 2 UT and 10 UT on the 13/5/98, and at 7 km after 10 UT on 13/5/98, the scatter as seen in Figure 4.11 appears to be quite isotropic, that is, independant of the pointing angle of the beam. At these times, the values of θ_s in Figure 4.10 display more variation as a function of θ_s calculation method. During these isotropic periods, the 7.2° and 10.8° DBS methods show large variability. The categorisation of scatter in terms of θ_s as used by other workers is to ascribe θ_s values of greater than about 10° - 20° to isotropic scatter. It can be seen from Figure 4.10 that the value of θ_s as measured by the 7.2° and 10.8° DBS methods is often above 10° - indicating the isotropic scatter seen in Figure 4.11.

With respect to the FCA 3.6° DBS θ_s calculation methods, these two do not show quite the same consistently good agreement during the isotropic scattering periods. At times during these periods, the 3.6° DBS values of θ_s are larger than the FCA θ_s values, yet not quite as large and variable as the 7.2° and 10.8° DBS θ_s values; for example, the period between 12 UT on 13/5/98 and 0 UT 14/5/98 at 7 km. At other times the agreement appears to be as good as for the aspect sensitive times, for example, the period between abut 7 UT and 10 UT on 13/5/98 at 4 km.

The comparison of the 3.6° DBS θ_s values and the FCA θ_s values provides interesting information on the nature of the off-zenith scattering distribution. During aspect sensitive times, the fact that the 3.6° DBS θ_s and FCA θ_s values agree is suggestive of one and the same scattering mechanism affecting both the 0.0° and 3.6° beam directions. During periods of isotropy, the fact that the good agreement between the 3.6° DBS θ_s and the FCA θ_s is sporadic, is suggestive of competing scattering processes at 3.6°. At times in these isotropic periods, the scattering mechanism present on the vertical beam appears to be present on the 3.6° beam, while at other times, a less aspect sensitive scattering mechanism appears to be at work, as shown by the fact that the 3.6° DBS θ_s values are greater than the FCA θ_s values at these times. The fact that the 3.6° DBS θ_s values are rarely as large as the values produced by the further off-zenith DBS θ_s methods suggests that the scattering mechanism competing with the vertical beam scattering mechanism is not quite the isotropic scatter seen

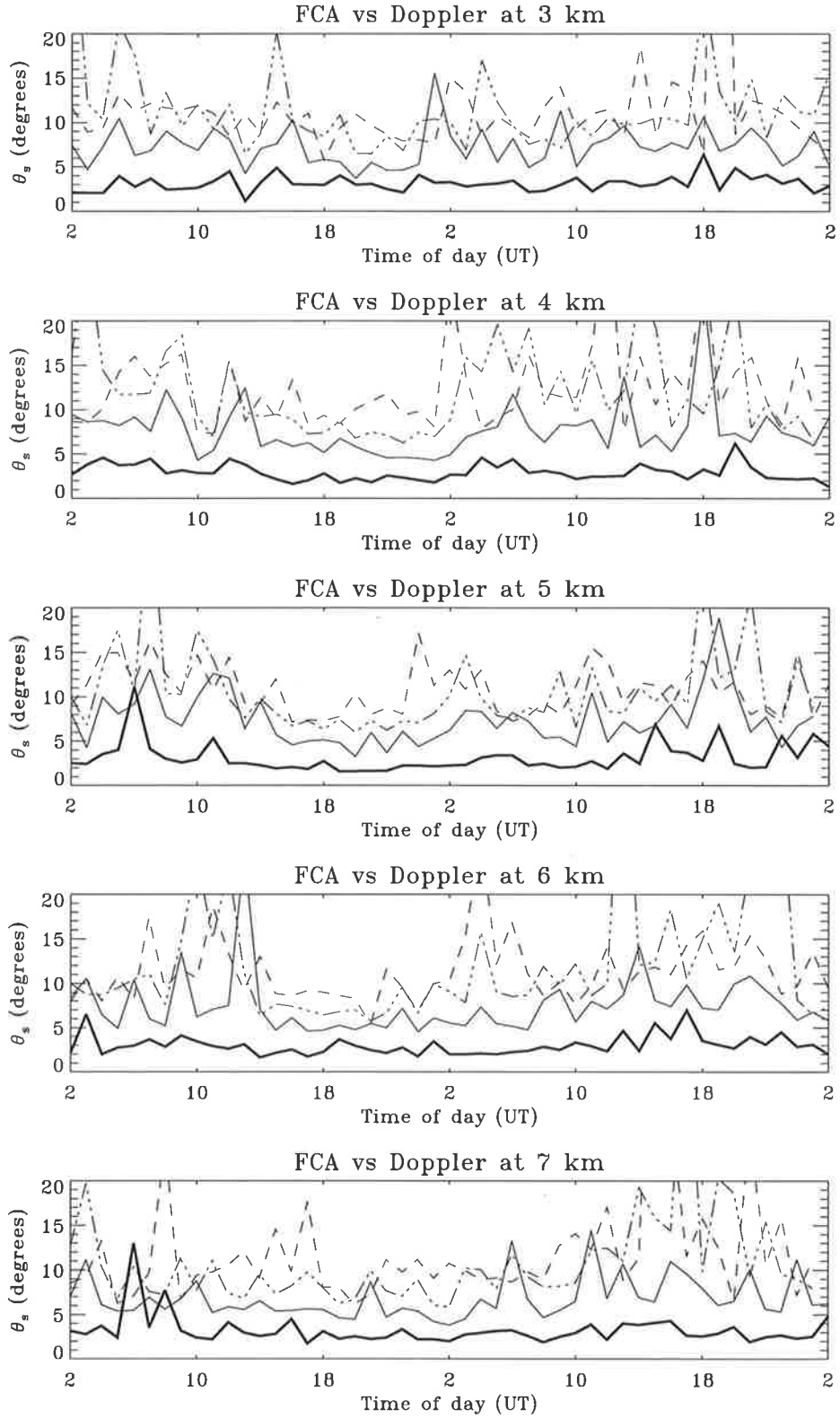

Figure 4.13: Median θ_s values from one hour periods, for the *Hooper & Thomas* [1995] DBS method and the FCA spatial correlation method, for selected range gates, over the full two day period of the 12-14/5/98 data set. Thick unbroken line = FCA spatial correlation θ_s, thin unbroken line = DBS using 3.6° and 7.2° beams, dashed = DBS using 7.2° and 10.8° beams and dash-dot-dot-dot = DBS using 3.6° and 10.8° beams.

on these further off-zenith beams, but instead perhaps a blend of the aspect sensitive scatter seen on the vertical beam and the isotropic scatter seen on the larger off-zenith beams.

Figure 4.13 shows the θ_s values calculated using the DBS power method of *Hooper & Thomas* [1995]. The thick unbroken line in Figure 4.13 shows the FCA θ_s values, the thin unbroken line shows the *Hooper & Thomas* [1995] DBS θ_s method for 3.6°/7.2°, the dashed line for 7.2°/10.8°, and the dash-dot-dot-dot line for 3.6°/10.8°. It can be seen that the general behaviour of the θ_s values as a function of time, height and method, is very similar to that shown in Figure 4.10, with the exceptions that the DBS methods shown in Figure 4.13 seem to be more spiky in nature, and none of the *Hooper & Thomas* [1995] DBS θ_s methods give values in agreement with the FCA method. This is not surprising given that it has already been established that only the 3.6° beam appears to be receiving similar scatter to that seen on the vertical beams of the FCA method. As such, the use of beams further off-zenith in the *Hooper & Thomas* [1995] method, rather than the use of the vertical beam as in the *Hocking et al.* [1986] method, will not produce θ_s values in agreement with the FCA method.

4.7 Summary

In this chapter, SA FCA data have been compared with DBS data at off-zenith angles of 3.6°, 7.2° and 10.8°. To the best of the author's knowledge, this is the first successful application of FCA on a CoCo antenna array. In addition, this is the first comparison of the FCA spatial correlation θ_s method and the DBS power θ_s method. The results of the comparison show excellent agreement between FCA and DBS velocities, with correlation coefficients of between 0.87 and 0.88 depending on the off-zenith DBS beams used. Reasonable agreement between the radar velocities and radiosonde velocities from Adelaide Airport is also found.

Comparisons of θ_s using the FCA spatial correlation method and the DBS power method of *Hocking et al.* [1986] show that in aspect sensitive conditions, θ_s values from the DBS method using an off-zenith angle of 3.6° agree very well with FCA θ_s values, indicating that the 3.6° off-zenith beam is responding to the same scatterers as the

vertical beam. In isotropic scattering conditions, the agreement is sporadic, with the 3.6° DBS θ_s values often being larger. This result can be interpreted as evidence that in the absence of strong aspect sensitivity, the 3.6° off-zenith beam is being influenced by a combination of scatter from the vertical direction, and more isotropic scatter, presumably from larger off-zenith angles.

Chapter 5

Angle of arrival measurements

5.1 Introduction

In this chapter the results of experiments combining the Doppler beam swinging (DBS) and angle of arrival (AOA) measurements are presented. This chapter will begin with a discussion of the AOA results of other researchers, working with VHF radars in the ST region of the atmosphere. The rest of the chapter will focus on the experiments that were conducted, beginning with a discussion of the set up of the radar, and the necessary data analysis, before discussing the results that were obtained using this combination of techniques.

5.2 Angle of arrival measurements

The AOA is a measure of the power-weighted mean position of the radiowave backscatter. The first AOA measurements in the ST region were made by *Vincent & Röttger* [1980]. They found AOA values in the range $\pm 1.5°$, over the height range from approximately 2 - 10 km, in a short data set spanning some minutes. Soon afterwards, *Röttger & Ierkic* [1985] proposed the time domain AOA calculation method shown in Equation 1.12 of Chapter 1. This is the most common method of calculating AOAs, although frequency domain methods are also used (e.g. *VanBaelen et al.* [1991b]). *Chau & Balsley* [1998] discuss a comparison of the time and frequency domain methods and conclude that the frequency domain method is more susceptible to outliers.

For the most part, AOA measurements in the ST region have been made with the purpose of examining their effects on vertical velocities. Evidence of a relationship between AOAs and vertical velocity values was reported by *Röttger et al.* [1990]. In this work, *Röttger et al.* [1990] measured the AOA in both the eastward and northward planes, vertical velocity and power over the height range from approximately 2 - 13 km. The authors noted a periodic variation with altitude of the eastward AOA, which appeared to be related to the radial velocity. A scatter plot of vertical velocity and incidence angle revealed that the vertical velocity and the eastward AOA were correlated, and further analysis revealed a 99% significant correlation coefficient of between 0.25 and 0.31. The measured AOAs corresponded to inclinations of the scattering structures in the direction of the horizontal wind. This fact led to the interpretation that the relationship between the vertical velocities and AOAs was caused by the folding of the horizontal wind into the vertical beam by tilting of scattering layers.

Palmer et al. [1991] further demonstrated the effect of the horizontal wind being folded into vertical beam measurements, by comparing the vertical velocity calculated with an interferometry technique and that using standard DBS measurements. The interferometry technique takes the AOA of the scatter into account, while the DBS does not. The results of *Palmer et al.* [1991] revealed that larger differences between the vertical velocities from the two methods occurred at heights where the AOA was large, where all of the AOAs measured were in the range $\pm 1°$. *Palmer et al.* [1991] also calculated a predicted difference between the DBS and interferometry method vertical velocities by calculating the vertical velocity that would result from the projection of the horizontal wind into the vertical DBS beam for the measured AOA. Their results showed close agreement between the actual differences and the predicted differences, indicating that DBS vertical beam velocities needed to be corrected for the effects of the non-zero AOA within the beam.

The first attempt to do so was made by *Larsen & Röttger* [1991]. These authors found eight minute average AOA values in the range $\pm 2°$, and six hour average values in the range $\pm 1°$. *Larsen & Röttger* [1991] reported corrections to four days of continuous data, and concluded by stating that the corrected vertical velocities were in better agreement with the prevailing meteorological conditions then the original

vertical velocities. Following these studies, *VanBaelen et al.* [1991b], *Larsen et al.* [1992] and *Palmer et al.* [1993] discussed the use of angle of arrival information to calculate wind velocity in the ST region using radar interferometry, or post-statistic wind steering. The most relevant aspect of these studies to the work presented in this chapter, are the AOA values seen by these authors. *VanBaelen et al.* [1991b] reported values in the range $\pm 1°$ over a 12 minute period, while *Palmer et al.* [1993] found 24 hour average AOA values in range $\pm 0.2°$.

The general assumption about the non-zero AOAs that have been measured by various researchers is that they are a result of tilting of the specular layers in the atmosphere that are believed to be at least partly responsible for the observed aspect sensitivity at VHF wavelengths. The AOA is assumed to be the angle corresponding to the peak in the power distribution as a function of off-zenith angle. Recently *Palmer et al.* [1998] have reported results from a DBS/AOA data run over 30 minutes, using the flexible middle and upper (MU) atmosphere radar in Japan, which appear to validate this assumption. The authors used inter-pulse-beamsteering DBS measurements to estimate the power as a function of off-zenith angle for 45 beams within 5° of zenith, at every 30° of azimuth. In addition, they collected AOA data. Using the distribution of power within 5° of zenith they calculated the offset of maximum power from zenith, and compared it with the AOA measurement. Results were obtained for the altitude range 8 - 16 km, and showed good agreement between the AOA and the angular position of the maximum power as seen on the DBS beams, thereby verifying the assumption that the AOA is the angle from which maximum backscattered power originates, as measured in Doppler beams.

Most DBS systems are not capable of AOA measurements, however, DBS radars can measure the power distribution as a function of off-zenith angle and recently *Worthington & Thomas* [1996] and *Tsuda et al.* [1997b] have reported possible evidence of tilted layers in data from off-zenith beam angles. The work of *Worthington & Thomas* [1996] was based around calculating the momentum flux in the ST region. This method of measuring momentum flux was first proposed by *Vincent & Reid* [1983]. The momentum flux in a vertical plane is calculated by taking the difference of radial velocity variances in two symmetrical off-zenith beams. *Worthington & Thomas*

[1996] examined the momentum flux measured using this technique, as well as with the technique of *Fukao et al.* [1988] which uses the vertical beam vertical velocity, and an off-zenith beam horizontal velocity. In addition, *Worthington & Thomas* [1996] proposed a third method using the vertical beam vertical velocity and the horizontal velocity measured with two off-zenith beams. During their investigation, *Worthington & Thomas* [1996] noticed that the difference in power in off-zenith beams, at off-zenith angles of 6° and 12° was often non-zero, and had non-random structure. In the case of isotropic scattering, the difference in powers between off-zenith beams should be zero. As such, *Worthington & Thomas* [1996] suggested that these power differences might be a result of tilted layers.

Further work on this subject was reported by *Worthington & Thomas* [1997] where the power differences were investigated in more detail, with the result that the largest of the power differences were found in conditions of simultaneous high wind shear and high aspect sensitivity. The authors suggest that the effect might result from tilted aspect sensitive layers. The work of *Tsuda et al.* [1997b] involved scanning every 30° of azimuth at a constant off-zenith angle of 6°. These authors found that there was significant azimuthal anisotropy, that is, measureable differences in the power as a function of azimuth. *Tsuda et al.* [1997b] also developed a numerical model for reflection from a corrugated layer, including the effects of vertical displacement of the surface caused by gravity waves. This model was found to be consistent with their results.

Despite the fact that tilted layers are expected to affect off-zenith DBS measurements, and the recent DBS work that appears to prove that they do, there has been no investigation of the link between non-zero AOAs measured on a vertical beam and the DBS off-zenith beam behaviour seen by *Worthington & Thomas* [1996], *Worthington & Thomas* [1997] and *Tsuda et al.* [1997b]. Apart from the work by *Palmer et al.* [1998], which confirms the assumption that AOA measurements are based on, all the AOA work to date has concentrated on the effects of non-zero AOAs on vertical beam data only. Under the assumption that non-zero values of the power differences between symmetrical off-zenith beams, and non-zero values of the AOA measured on a vertical beam are produced by the tilting of specular layers, the experiment discussed in this

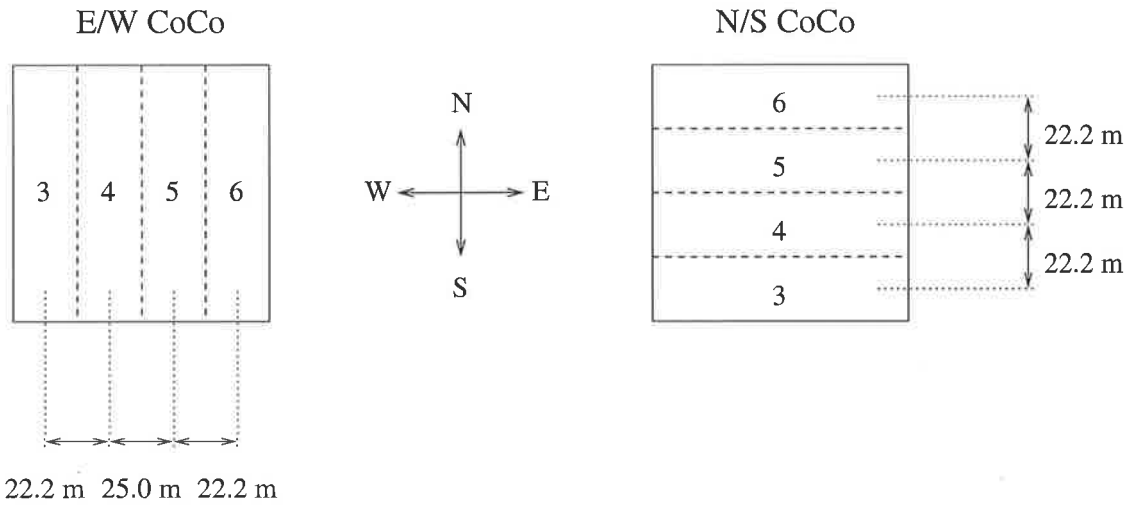

Figure 5.1: Antenna groupings for the experiment run over the period 18-22/2/98. The numbers in each of the sections corresponds to the receiver that the antenna group was connected to.

chapter was designed to use the new dual spaced antenna AOA/DBS capabilities of the BP VHF ST radar to investigate the relationship between these two quantities. In addition, the data in this chapter were also used to calculate the AOAs in off-zenith beams and to examine their effect on measurements of momentum flux, as these measurements are especially sensitive to any differences in the backscatter in symmetrical off-zenith beams.

5.3 Experiment description

As shown in Figure 2.13 of Chapter 2, it is only possible to split the East-West array up into sections joined by east-west baselines. As such, in order to obtain AOA and DBS measurements using both the East-West and North-South arrays, it was necessary to split the arrays up into strips. A DBS/AOA experiment was conducted over the period from 18-22/2/98, with the East-West and North-South arrays split up as in Figure 5.1.

In this antenna arrangement, AOAs are only available in one dimension on each of the East-West and North-South arrays. This was a limitation in the data set, but the benefit of conducting the experiment in this manner was that there was redundancy in the determination of the AOAs on a given array, with two completely independant estimates, and six inter-related estimates of the AOA on each array. Figure 5.2 shows

Collection parameter	Parameter Value
PRF (Hz)	4096
No. coherent integrations (10.8° / 3.6°)	512 / 1024
Time for one data set (seconds)	56.25
No. of data points (10.8° / 3.6°)	450 / 225
Velocity resolution (ms^{-1})	0.05
Max. unaliased velocity (ms^{-1}) (10.8° / 3.6°)	11.1 / 5.5
Height range (km)	2.0 - 15.0
Range gate (km)	0.5
Pulse length (km)	1.0

Table 5.1: Data collection parameters for the 18-22/2/98 data set. Note the different collection parameters for the different off-zenith beam direction data sets. This was done in order to prevent aliasing and maintain the same velocity resolution between data sets.

the beam sequence and directions that were used for the 18-23/2/98 experiment, while Table 5.1 shows the data collection parameters. Note that there are two sets of 'No. of coherent integrations', 'No. of data points' and 'Max. unaliased velocity' values. These two ranges were set to obtain the velocity range most suited to the off-zenith angle being used, 3.6° or 10.8°, such that no aliasing occurred, while also maintaining the same velocity resolution in each of the two data collection regimes. The vertical beam in the sequence between each of the off-zenith coplanar 3.6° or 10.8° beams was collected with the same parameters as the corresponding off-zenith beams, in order to keep as many of the parameters constant between beam directions as possible. A data set in a given beam direction took almost exactly one minute to collect, once data transfer times were taken into account. As such, a complete beam sequence took 12 minutes to collect. Figure 5.3 shows the one way polar diagram of one of the strip receiving antenna groups shown in Figure 5.1. This diagram has a half-power half-width of approximately 6.4° in the widest direction, corresponding to the short side of the strip antenna groups, and approximately 1.6° in the narrowest direction, corresponding to the long side of the strip antenna groups. This approximate figure of 6.4° is that produced by the short side of the strip groups for both the East-West and North-South arrays, although the diagram in Figure 5.3 is for the East-West array only.

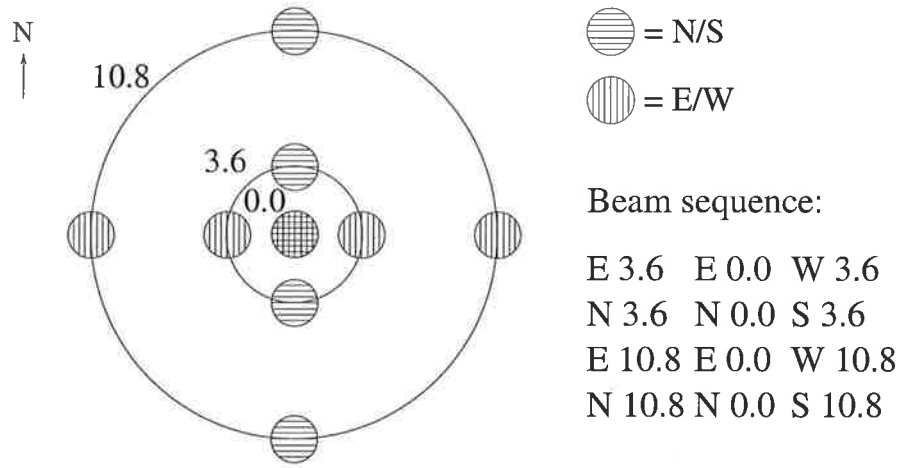

Figure 5.2: Beam sequence and direction for the DBS/AOA experiment run over the period 18-22/2/98.

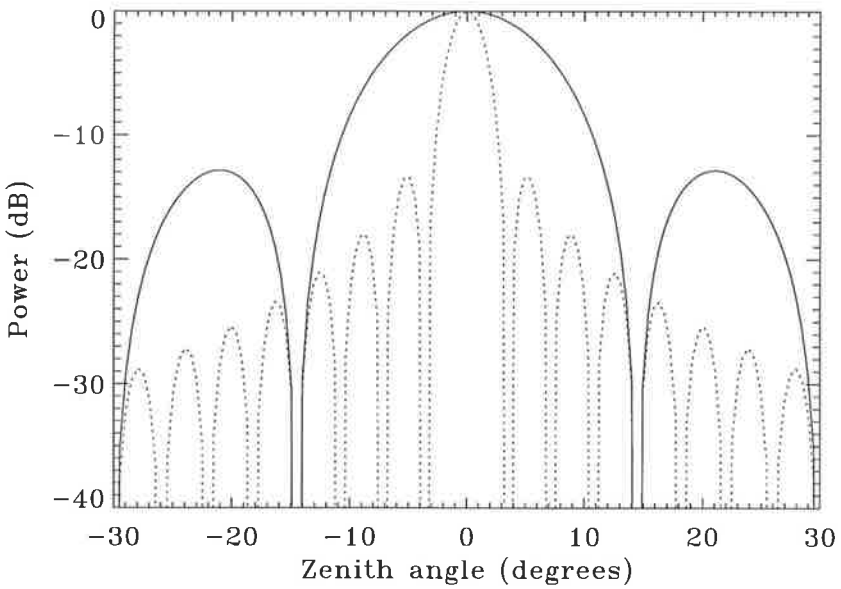

Figure 5.3: Cross-sections through the one way polar diagram of a strip of antennas equal to one quarter of the East-West array, for a vertically pointing beam. Solid lines denote the east-west cross-section and dashed lines denote the north-south cross-section. This antenna grouping was used for the 18-23/2/98 experiment.

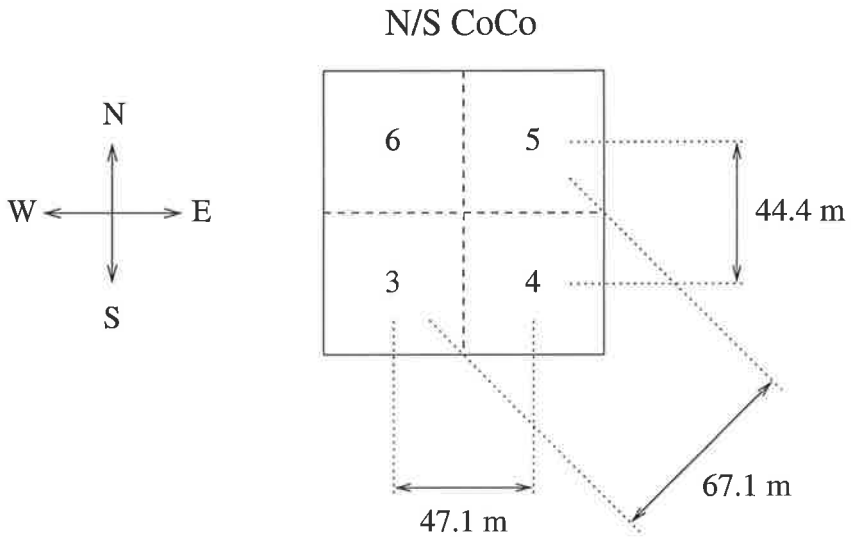

Figure 5.4: Antenna groupings for the experiment run over the period 24-25/3/98. The numbers in each of the sections corresponds to the receiver that the antenna group was connected to.

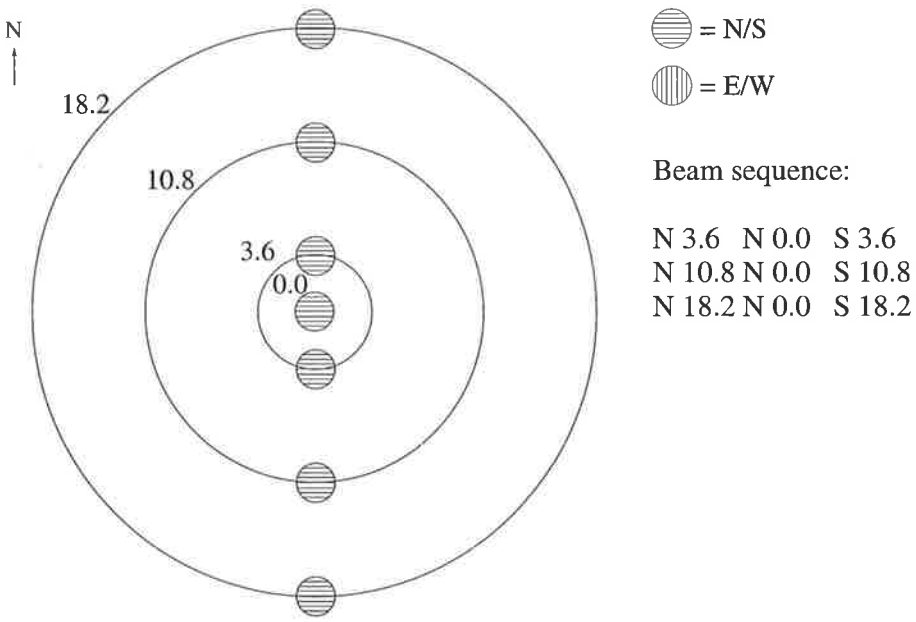

Figure 5.5: Beam sequence and direction for the AOA experiment run over the period 24-25/3/98.

Collection parameter	Parameter Value
PRF (Hz)	4096
No. coherent integrations (18.2° / 10.8° / 3.6°)	256 / 512 / 1024
Time for one data set (seconds)	56.25
No. of data points (18.2° / 10.8° / 3.6°)	900 / 450 / 225
Velocity resolution (ms^{-1})	0.05
Max. unaliased velocity (ms^{-1})(18.2° / 10.8° / 3.6°)	22.2 / 11.1 / 5.5
Height range (km)	2.0 - 15.0
Range gate (km)	0.5
Pulse length (km)	1.0

Table 5.2: Data collection parameters for the 24-25/3/98 data set. Note the different collection parameters for the different off-zenith beam direction data sets. This was done in order to prevent aliasing and maintain the same velocity resolution between data sets.

In addition to this main AOA experiment, the original DBS/FCA dataset which was found to be unsuitable for FCA due to the longest antenna baseline being too large, was also used to calculate AOA values. This experiment uses the North-South array only, with the antenna arrangement shown in Figure 4.1., reproduced in Figure 5.4, over the period 24-25/3/98. The beam sequence and directions used in the 24-25/3/98 experiment are shown in Figure 5.5, while Table 5.2 shows the corresponding data collection parameters. Note that as for the 18-22/2/98 experiment, this 24-25/3/98 experiment uses different combinations of 'No. of coherent integrations', 'No. of data points' and 'Max. unaliased velocity' in order to ensure that the most suitable velocity range for a given off-zenith angle was used, while also maintaining the same velocity resolution. A complete beam sequence was performed in nine minutes, one minute for each beam direction. This antenna arrangement gives two estimates of the AOA in a given plane, which are completely independant. The polar diagram for this antenna arrangement was shown in Chapter 4, in Figure 4.4.

5.4 Data analysis

As for the data discussed in Chapter 4, the data in the 18-23/2/98 and 24-25/3/98 experiments were compiled into single beams for DBS analysis by adding the time series

from a given receiver together, after accounting for the phase offsets and amplitude differences between receivers. The DBS data were then passed through the analysis described in Chapter 3. These phase offsets and amplitude differences were calculated by fitting Gaussian function to the histograms phase differences or amplitudes for a given receiver, with respect to a control receiver, which for this thesis, was receiver three. This procedure was discussed in Section 4.4 of Chapter 4. The phase offsets and amplitude corrections to be applied for a given receiver, in order to add the DBS time series together to form a beam in software, were calculated over a range of heights, and then applied to the data for all heights of interest in the data set. These phase offset and amplitude calculations were therefore implicit height averages. It was found, however, that the phase offset actually varied as a function of height. This effect has been found by other researchers, including *Thorsen et al.* [1997] and *Holdsworth* [1995]. The compilation of the DBS data was not found to be very sensitive to this height variation, and as such, the height averaged corrections were appropriate. This was shown by the fact that slightly different corrections were calculated for the data from the East-West and North-South arrays, yet there was virtually no difference in the DBS results using different corrections on each array or the same corrections for both arrays. These differences were approximately 10° between arrays, meaning that the mean of the histogram from data in the East-West array was up to 10° different from the mean of the histogram of data from the North-South array. The fact that the DBS data was not sensitive to the different correction factors required for the two arrays, and the fact that the difference in phase offset as a function of height was about the same value as the array specific correction differences, meant that the DBS data was also not sensitive to the height variation of the phase offsets.

However, the variation of the phase offset as a function of height did have a noticeable effect on the mean value of the AOA. Figure 5.6 shows the phase offset as a function of height, for all receiver pairs used in the test data set first discussed in Chapter 2. Four receivers were used in this data set, each connected to the same antenna, so that the phase differences that are seen between the receivers are an instrumental effect caused by various phase errors in the system. It can be seen that this test data set shows significant variation as a function of range. Figure 5.7 shows the

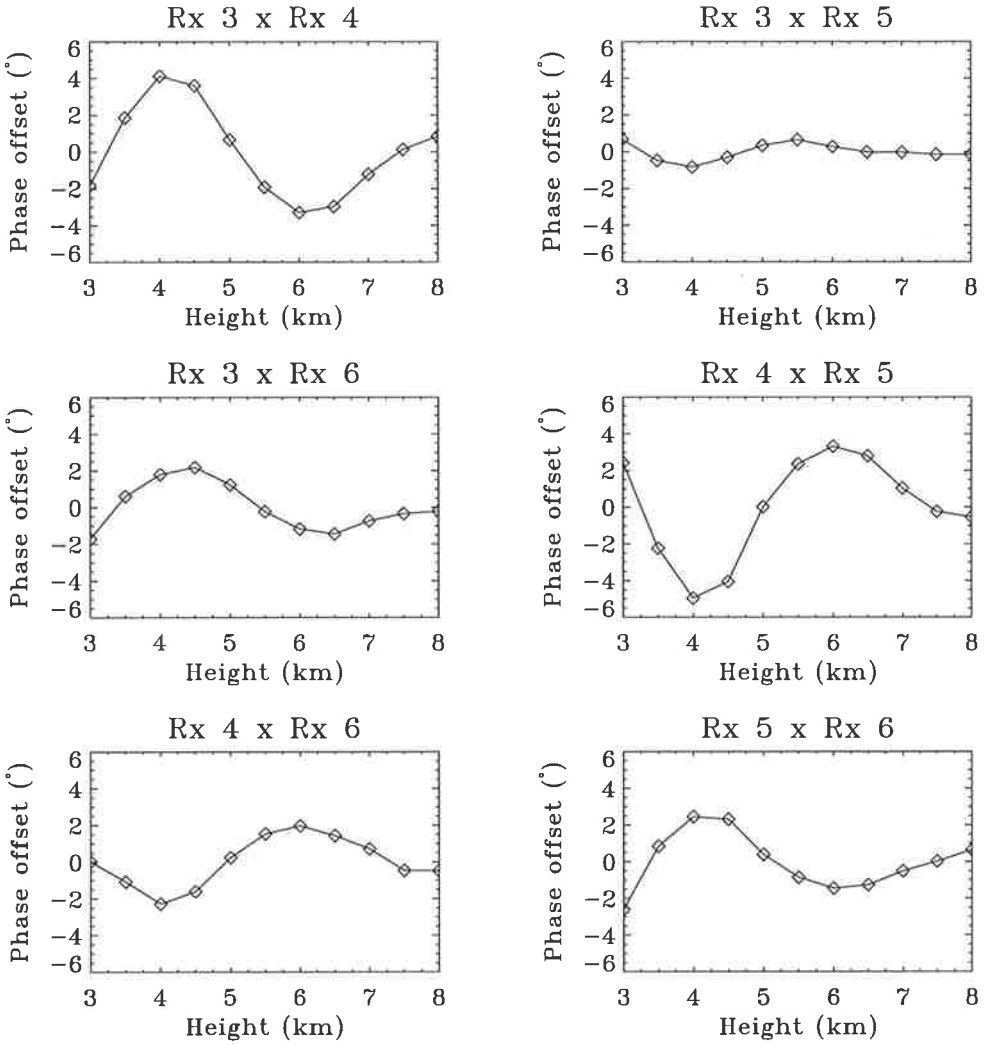

Figure 5.6: Phase offset as a function of range for the test data set in which all receivers were connected to the same antenna. All receiver combinations are shown. This phase offset measurement is the mean of the Gaussian function fitted to the histogram of the phase differences between any two receivers, as a function of time, as discussed in Section 4.4, Chapter 4.

effect on the real data set collected over the period 18-22/2/98. It can be seen that similar variations in this data exist as were seen in the test data. Note that the data in Figure 5.7 are plotted on a larger scale then the data in Figure 5.6. Figure 5.7 shows the variation for a few of the receiver pairs, on both the East-West and North-South arrays, thus showing the phase offset behaviour as a function of height and array.

If the mean offset as a function of height is removed from the time series of AOA at a given height, Figure 5.7 shows that a mean, non-zero AOA would result. The implication of a non-zero mean AOA is that the angle of arrival is consistently centred

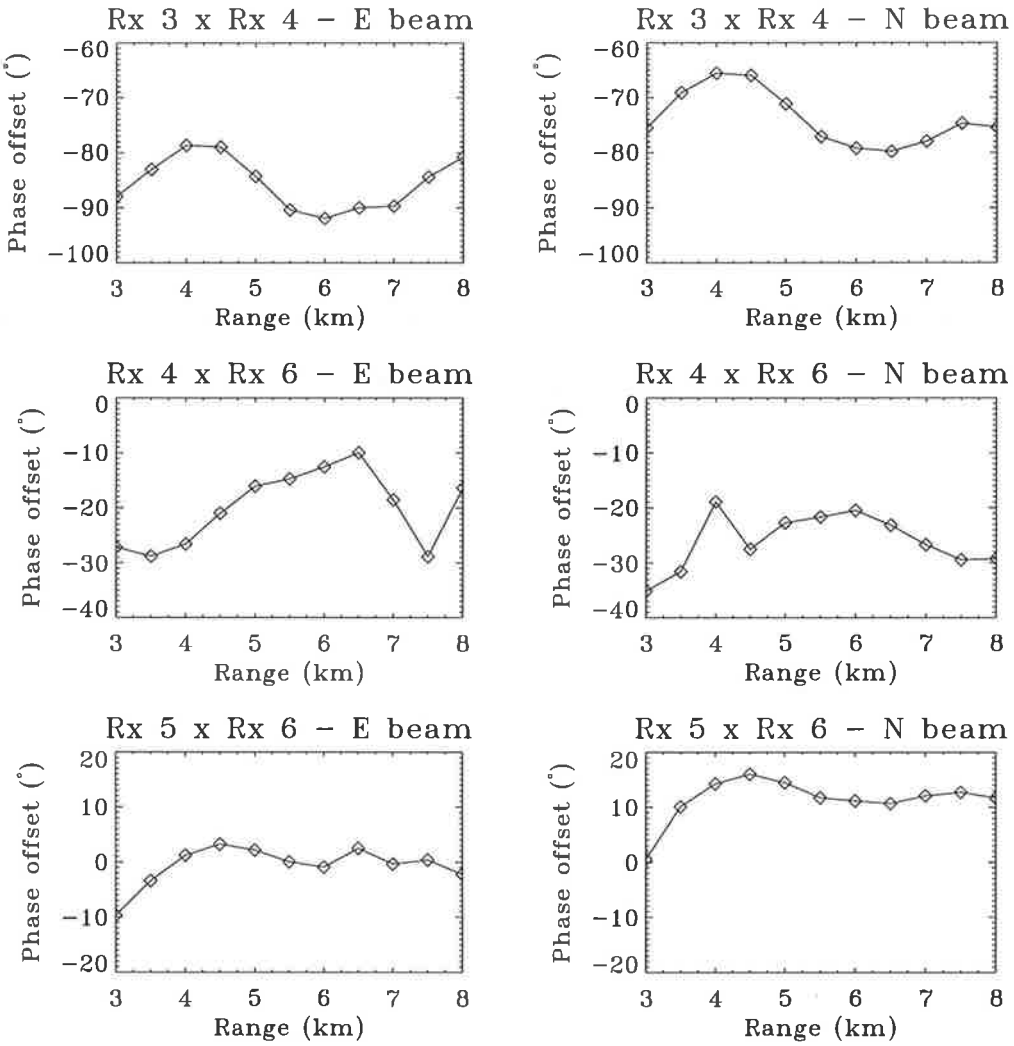

Figure 5.7: Phase offset as a function of range for data from the period 18-23/2/98. Three combinations of receivers are shown, for both the East-West and North-South arrays. This phase offset measurement is the mean of the Gaussian function fitted to the histogram of the phase differences between any two receivers, as a function of time, as discussed in Section 4.4, Chapter 4.

off-zenith. There is no atmospheric reason that this should be the case, especially over a five day data set, and there is obvious proof from Figure 5.6 that the basic effect is instrumental and not related to real AOA behaviour. As a result, the assumption was made for the AOA data in this chapter that on average, the AOA should be 0.0°. As such, the mean of the AOA time series at each height, for both the 18-22/2/98 and 24-25/3/98 data sets, were removed so that no phase offsets existed.

5.5 Angle of arrival results

As mentioned in Section 4.3, the antenna arrangement used for the experiment conducted over the period 18-22/2/98 allowed two independant and six inter-related estimates of the AOA on a given array. If the assumption is made that at any given time, the AOA measured on each of the six possible combinations of antenna groups in either the East-West or North-South array is the same, then the phase differences measured on each of the six possible combinations of antenna groups should be directly proportional to each other, where the difference between the combinations is due to the different distances separating the various antenna groups.

Figure 5.8 shows histograms of the phase differences seen for each of the six possible combinations of antenna groups, for the vertical beam on the North-South array. This figure was compiled using data from the 18-22/2/98 experiment, over the height range from 4 - 8 km, in the same manner as Figure 2.19 in Chapter 2, using test data, and Figure 4.4 in Chapter 4, using data from the period 11-14/5/98. The histograms in Figure 5.8 are shown overplotted with Gaussian functions which were fitted to the histograms. It can be seen in Figure 5.8 that the widths of the histograms from the receiver pairs 3 and 4, 4 and 5, and 5 and 6, are about the same, as expected from the fact that the antenna groups connected to these three sets of receiver pairs are separated by the same distance. For the same reason, the widths of the histograms from the receiver pairs 3 and 5, and 4 and 6, are about the same, and larger than the histograms from the afore-mentioned pairs. This is expected because the distances between the antenna groups for the receiver pairs 3 and 5, and 4 and 6 are larger than the distances between the receiver pairs 3 and 4, 4 and 5, and 5 and 6. Finally, the

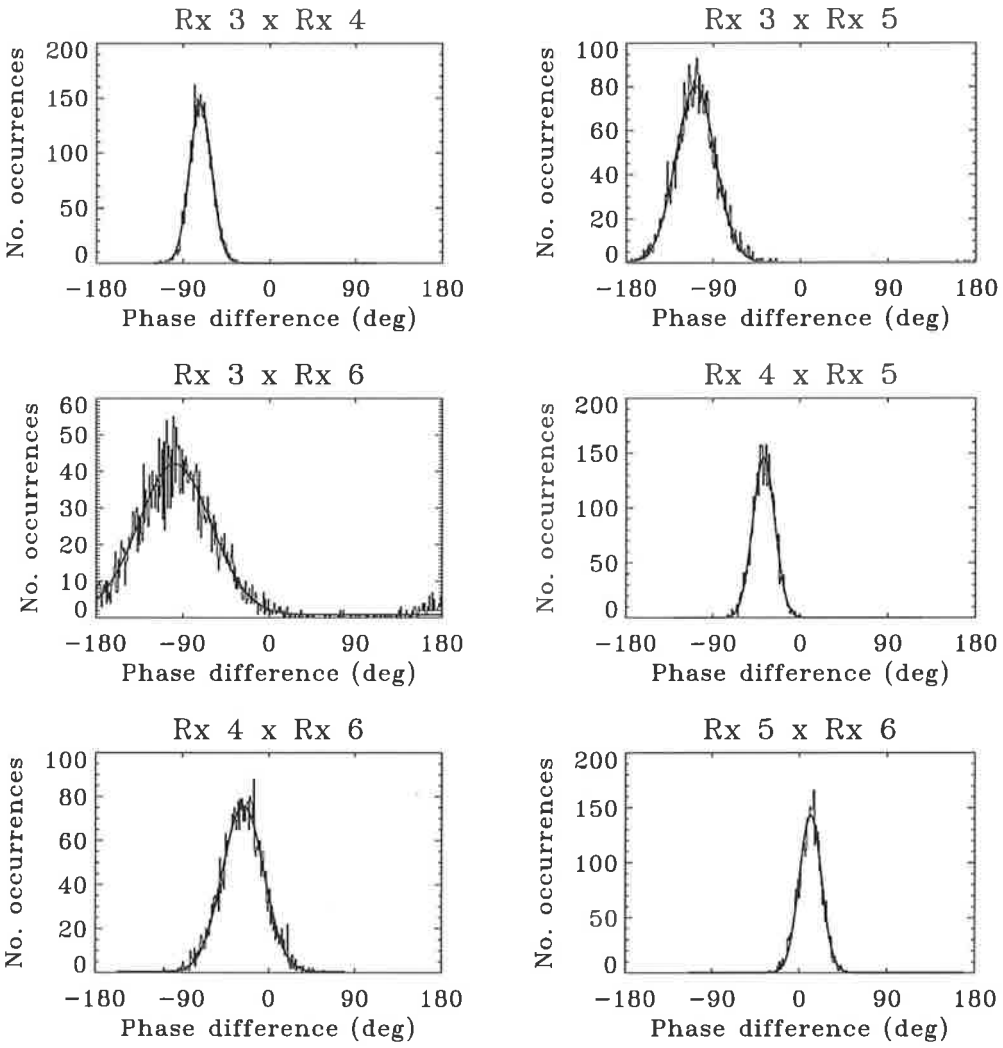

Figure 5.8: Histograms of the phase differences between each of the four receivers before time series correction. The histograms were formed with data from the vertical beam on the North-South array, over the height range from 4 - 8 km, for the 18-22/2/98 data set.

broadest histogram is for the receivers 3 and 6, which are connected to the antenna groups on the ends of the antenna array, and therefore have the largest separation. This behaviour is a good indication that roughly the same AOAs are being observed on each of the possible antenna groups across the array.

Figure 5.9 confirms that the various combinations of antenna groups in a given array measure almost exactly the same AOA. In addition it shows that the individual AOA measurements are in the same range as those seen by other workers, as discussed in Section 5.2, and that the values of the AOA are significantly larger then the minimum

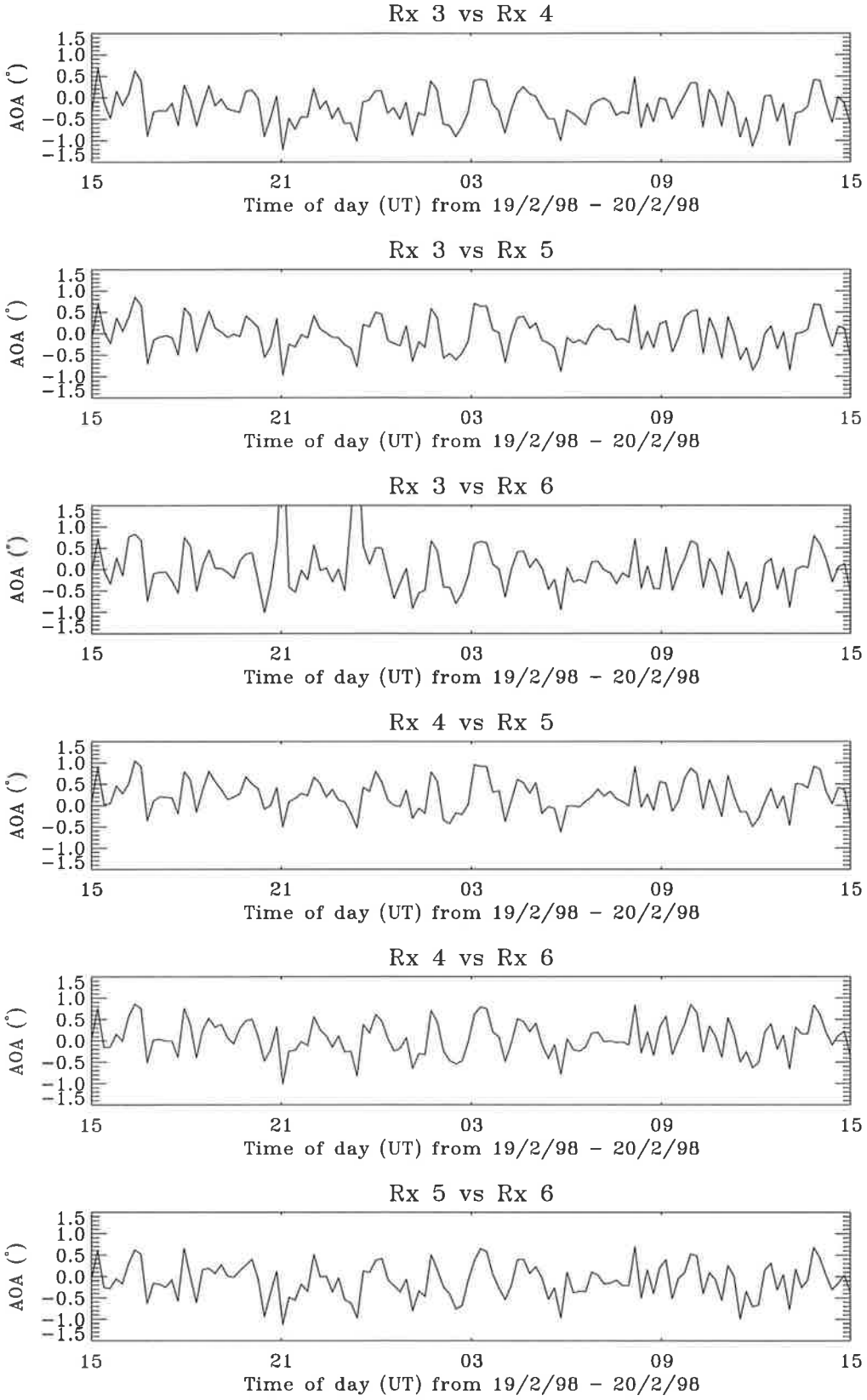

Figure 5.9: Time series of the AOA measured on each of the 6 possible combinations of the 4 antenna groups on the North-South array for the 18-22/2/98 data set. The AOAs shown were measured at a range of 6 km, and are shown for a 24 hour period.

observable AOA of 0.2° due to instrumental effects in the system, as discussed in Chapter 2. Figure 5.9 shows a 24 hour time series of AOA from the 18-22/2/98 data set. The AOA values shown were measured on the vertical beam of the North-South array, at a range of 6 km, with the beam in the beam sequence between the north 3.6° and south 3.6° beams, and are shown at the minimum resolution of 12 minutes. It can be seen that the six profiles are very similar over the 24 hours shown in Figure 5.9. Except for the "spikes" in the profile from the combination of receivers 3 and 6, the agreement of the AOAs measured at any given time, on any given receiver combination is excellent. This good agreement between the AOA values seen with the various combinations of antenna groups was a general feature over the full five days of the 18-22/2/98 data set, for both the East-West North-South arrays, with the exception of the AOA measured with the receiver 3 and 6 combination, which corresponds to the two furthest antenna groups, which often showed spikes such as that shown in Figure 5.9.

The reason for this behaviour is partly explained by the relatively large distance between the two furthest antenna groups, which were connected to receivers 3 and 6 for the 18-22/2/98 data set. As explained in Chapter 1, an individual AOA is calculated from the phase difference, ϕ_{ij}, between a given pair of antennas, i and j, a distance d_{ij} apart, by using the equation

$$\delta_{ij} = sin^{-1}(\frac{\lambda\phi_{ij}}{2\pi d_{ij}}), \tag{5.1}$$

where δ_{ij} denotes the value of the AOA. The distance between the antenna groups dictates the range of AOAs that are observable. This range can be calculated by substituting for the maximum range of the phase difference between receivers, ± 180, into Equation 5.1, for a given antenna separation. For the largest spacing in the 18-22/2/98 experiment of 66.6 m, the observable range of AOAs was $\pm 2.4°$, while for the smallest separation of 22.2 m, the range was $\pm 7.2°$. AOA values outside this range were ambiguous and therefore not good AOA estimates. The vast majority of AOA estimates from both the 18-22/2/98 and 24-25/3/98 experiments were in the range $\pm 1.5°$, which is consistent with the transmitter beam half-power half-width on the whole array for these experiments of between 1.6° and 1.7°. The percentage of

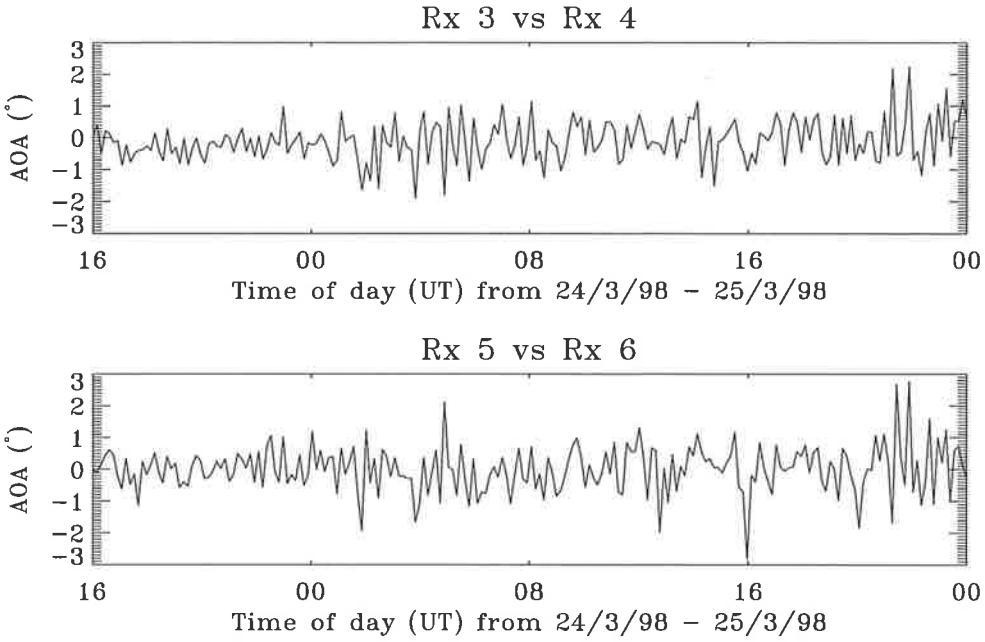

Figure 5.10: Time series of the AOA measured for the 2 possible combinations of the 4 antenna groups on the North-South array that produce AOAs in the east-west plane, for the 24-25/3/98 data set. The AOAs shown were measured at a range of 6 km, and are shown for a 32 hour period.

measured AOAs outside the observable range, for all possible antenna separations, was between 0.6% and 1.7% for the 18-22/2/98 data, over the height range from 3 - 8 km. This range of percentages is from the four separate vertical beams used in this experiment, as shown in the beam sequence in Figure 5.2. The percentage for all possible antenna grouping separations, except that using the two groups furthest apart, over the same height range and for the same 18-23/2/98 vertical beams was between 0.02% and 0.4%; a clear improvement. The antenna group separations for the 24-25/3/98 experiment produce observable AOA ranges of 3.4° for the 47.1 m east-west separation and 3.6° for the 44.4 m north-south separation. The percentages of AOAs which lie outside the observable range for the 24-25/3/98 experiment were of the same magnitude as the 18-22/2/98 values, excluding the largest antenna separation pair.

The two estimates of the AOA as measured in a given plane for the 24-25/3/98 experiment do not show quite the same good point to point agreement as the estimates from the 18-22/2/98 experiment do. This is not surprising given the larger beam

width of the antenna groups of the 18-22/2/98 experiment. The wider cross-section of the polar diagram for the 18-22/2/98 experiment is in the direction between antenna groups, and is approximately double the width of the polar diagram for the 24-25/3/98 experiment, in the direction between antenna groups. This means that the beams for the 18-22/2/98 experiment have greater coverage, and therefore a given antenna group is more likely to sample the same scatterers as the neighbouring antenna group, resulting in very similar measurements of the AOA. Figure 5.10 shows a 32 hour time series of the AOA measured on the receiver pairs 3 and 4, and 5 and 6, for the 24-25/3/98 data set, with a vertical beam on the North-South array. These receiver pairs give AOA values in the east-west plane. The AOA values shown were measured at a range of 6 *km*, and were measured with the beam in the beam sequence between the north 3.6° and south 3.6° beams. The values are shown at the minimum resolution of 9 minutes. It can be seen that there is generally good agreement between the time series of AOA values in Figure 5.10, but not the same striking agreement as for the time series of AOA in Figure 5.9.

Given that the different estimates of the AOA measured in a given plane, at a given time, show good agreement, an average value for the AOA in the plane can be calculated from these individual estimates. Average AOAs were calculated for each instant in time, using both possible combinations of the AOA in a given plane for the 24-25/3/98 data set, and all combinations of the AOA in a given plane for the 18-22/2/98 data set, except that from the antenna groups furthest apart.

Figure 5.11 and Figure 5.12 show the results, for the 18-22/2/98 and 24-25/3/98 data sets respectively. The data is shown in histogram form, where the histograms were compiled over the height range from 3 - 8 *km* in each case. It can be seen that the distributions are very narrow, being less than half the value of the half-power half-widths of the transmit beams used in the experiments, which had half-power half-widths of between 1.6° and 1.7°. Note that the histograms are centred on 0.0° because the phase offsets were removed at each height, as discussed in Section 4.3. The widths of these distributions are similar to those seen in similar histograms plots by *Chau & Balsley* [1998] who used a transmit beam half-power half-width of approximately 2° and a receive beam half-power half-width of approximately 4.1°, and obtained Gaussian

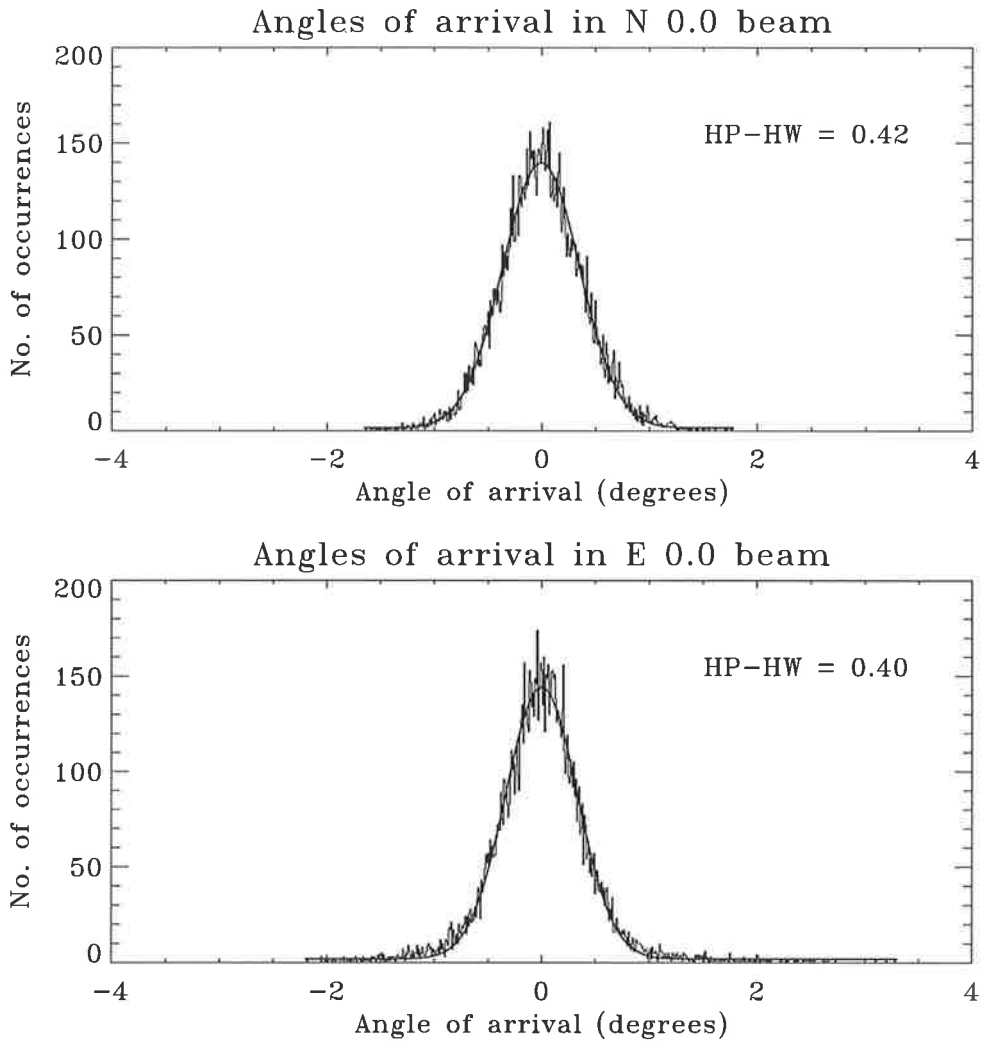

Figure 5.11: Histograms of the average AOAs measured with a vertical beam on the given array, for the 18-22/3/98 data set. The individual average values are the average of the AOAs at a given time, over all of the antenna group combinations except the Rx 3 vs Rx 6 combination, which uses data from the furthest two antenna groups. The histograms were formed with data from the height range from 3 - 8 km, and are shown overplotted with a Gaussian function fitted to the histogram, and the corresponding half-power, half-width value.

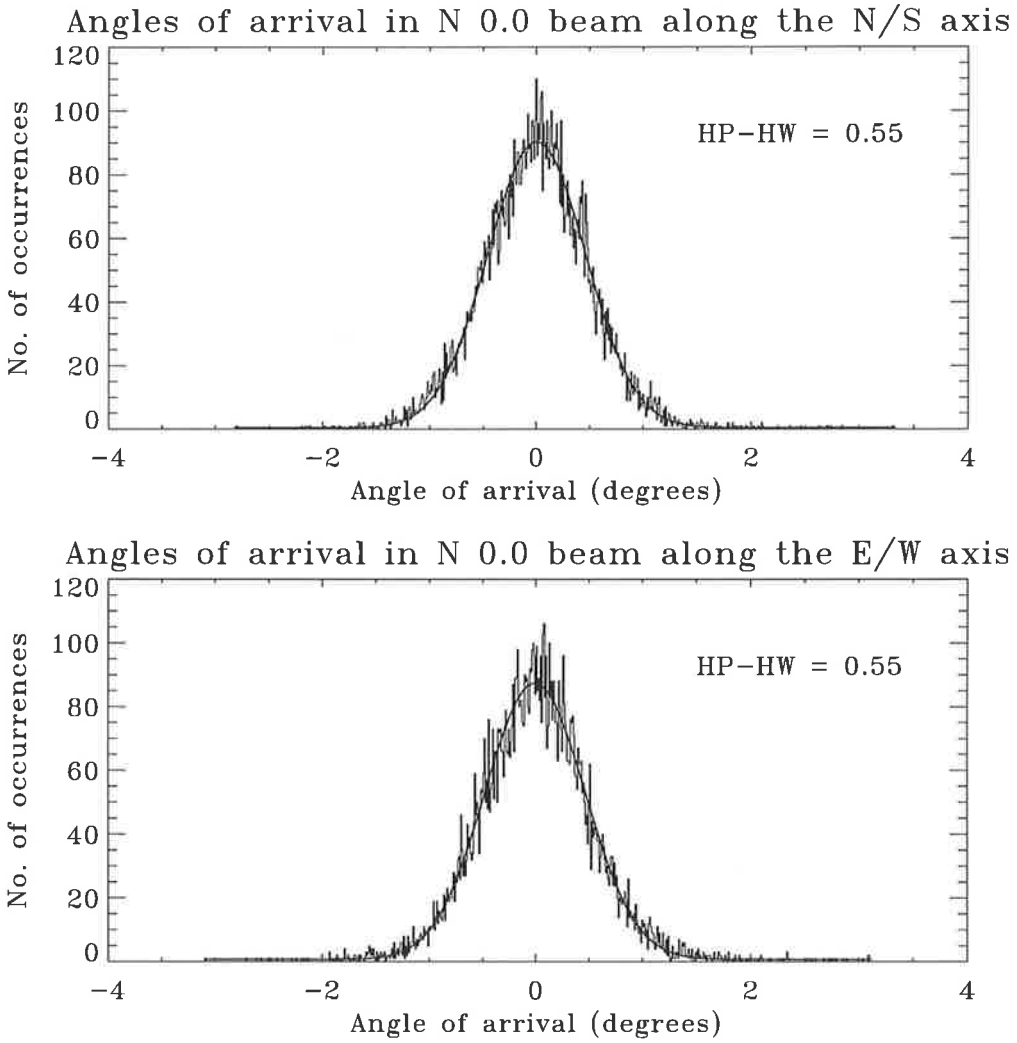

Figure 5.12: Histograms of the average AOAs measured with a vertical beam in the given direction, for the 24-25/3/98 data set. The individual average values are the average of the AOAs at a given time, over the two possible antenna group combinations in a particular direction. The histograms were formed with data from the height range from 3 - 8 *km*, and are shown overplotted with a Gaussian function fitted to the histogram, and the corresponding half-power, half-width value.

half-power half-widths of approximately 0.4°.

5.6 Off-zenith beam SNRs and vertical beam AOAs

In chapter 4 it was shown that in conditions of aspect sensitive scatter, vertical beams and off-zenith beams at 3.6° produce θ_s values in very good agreement, suggesting that the beams are responding to the same type of scatterers. In this section, the possibility that the two beams are responding to the tilting of specular layers is investigated, using SNR (signal to noise ratio) data in off-zenith DBS beams, and AOA data on vertical beams.

The data collection regime used for the work in this chapter was adopted so that in one three minute period, a set of measurements including two symmetric off-zenith beams and a vertical beam were collected in the order; off-zenith beam 1, vertical beam, off-zenith beam 2. In this manner, under the assumption that the atmosphere did not change dramatically over the three minute period, the SNR differences in the symmetric pair of DBS beams were calculated and directly compared with the AOA measured on the vertical beam.

Figure 5.13 shows a schematic of the simplest case of a single totally flat, or smooth, tilted specular layer being observed in a vertical beam, and two off-zenith beams directed at 3.6° to the north and south. The work by *Tsuda et al.* [1997b] suggests that the layers are probably corrugated due to the passage of gravity waves, rather then flat, or smooth, as depicted in Figure 5.13. However, the assumption that the layer is flat is adequate for the present work. In addition, the fact that there is only one layer in Figure 5.13 is not expected to be the case in real data. Any number of layers may be present in the range gate of the radar, but the depiction of only one layer in the range gate as shown in Figure 5.13 is adequate to describe the assumptions about the relationship between the AOA and the SNR in the off-zenith beams. The half-power half-width of the beam on the full arrays of the BP VHF ST radar, of approximately 1.7°, means that the 3.6° off-zenith beams are positioned exactly either side of the vertical beam, neglecting the effects of biases towards the zenith due to aspect sensitivity. The orientation of the layer in the beam as shown in Figure 5.13 is

expected to cause the beam directed to the north to receive slightly more power than the beam directed to the south, due to the fact that the beam directed to the north is more perpendicular to the layer. At the same time, the layer is expected to cause a slightly off-zenith AOA in the vertical beam, with the direction slightly towards the north.

Before presenting the comparison of the SNR differences and AOA data, it is necessary to determine the nature of the scattering affecting the data sets. The top plot in Figure 5.14 shows the SNR profiles for three beams used in the 18-22/2/98 experiment, over the full 5 days of the data set, at a range of 5.5 km. The thick solid line in Figure 5.14 corresponds to the vertical beam on the North-South array, the thin solid line shows the SNR for the 3.6° off-zenith beam, and the dashed line shows the SNR for the 10.8° off-zenith beam. There were six minutes separating the measurements in the three beams. Despite this, it can be clearly seen from this plot that the atmosphere sampled by these three beams is aspect sensitive throughout the data set, with a slight drop in SNR between the 0.0° and 3.6° off-zenith beams, and a large decrease in SNR between these two beams and the 10.8° off-zenith beam. This off-zenith SNR behaviour was a general feature of the backscatter over the full height range of interest in this work, from 3 - 8 km.

The bottom plot in Figure 5.14 shows the SNR of the north and south 3.6° off-zenith beams, also at a range of 5.5 km, over the full 18-22/2/98 data set. The northward beam is shown as the solid line, while the southward beam is shown as the dashed line. It should be noted that in this figure, the time in hours along the x-axis is approximate only as it is rounded to a whole number and as such, the difference between any two labels on the x-axis varies from 6 to 7 hours. It can be seen in the bottom plot of Figure 5.14 that the pair of 3.6° beams track each other fairly well, despite the fact that two minutes separated the measurements in each beam. It can also be seen, however, that there are differences between the two beams. The time series of SNR in Figure 5.14 are shown at the minimum possible resolution of 12 minutes for the data collection in a given beam of the 18-22/2/98 experiment.

As discussed in Chapter 1, the aspect sensitivity of the atmosphere results in underestimation of the horizontal wind speed measured in an affected off-zenith beam.

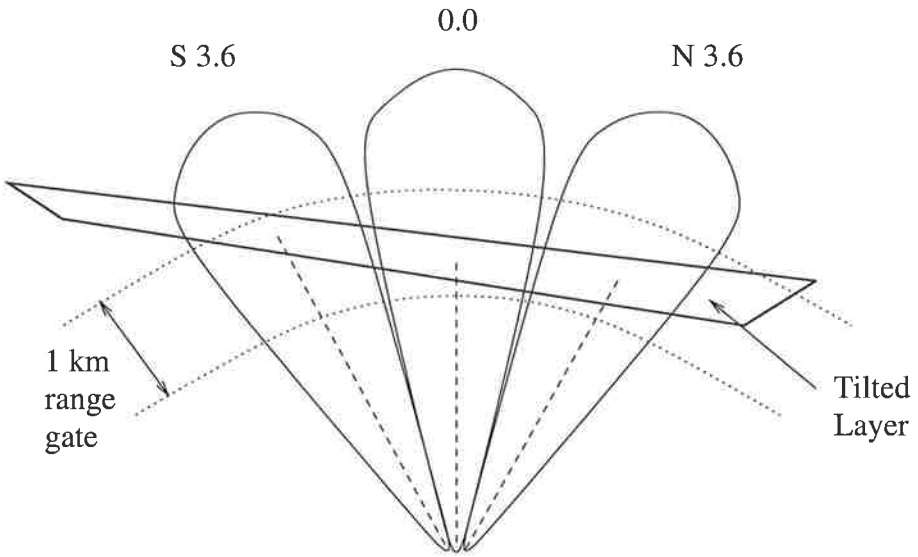

Figure 5.13: Schematic showing the measurement of a tilted specular layer in a vertical beam and two off-zenith beams directed at 3.6° to the vertical, under the assumption that the layer is observed in all three beams, directed one after the other over a three minute period.

The actual beam direction is biased towards vertical by the aspect sensitive scatter, which results in an over-estimation of the bore-sight angle at which a given DBS velocity is measured. As such, since the atmosphere was observed to be fairly aspect sensitive during the 18-22/2/98 data set, there are expected to be under-estimations in the horizontal velocity measured in 3.6° off-zenith beams relative to that measured in 10.8° off-zenith beams. Figure 5.15 shows the meridional velocity measured in various beams, at a range of 5.5 *km* over the full 18-22/2/98 data set. The top plot in Figure 5.15 shows the north 3.6° off-zenith beam as the thin line, and the north 10.8° off-zenith beam as the thick line. The bottom plot in Figure 5.15 shows the corresponding south beams, with the thin line representing the south 3.6° off-zenith beam and the thick line representing the 10.8° off-zenith beam. The velocity time series in Figure 5.14 are shown at the minimum possible resolution of 12 minutes for the data collection in a given beam of the 18-22/2/98 experiment.

It can be seen from Figure 5.15 that the 3.6° measurements of the meridional velocity are highly variable relative to the 10.8° velocity measurements. There were six minutes between a measurement in a 3.6° off-zenith beam and a measurement in the same direction on a 10.8° off-zenith beam. This six minute separation of the

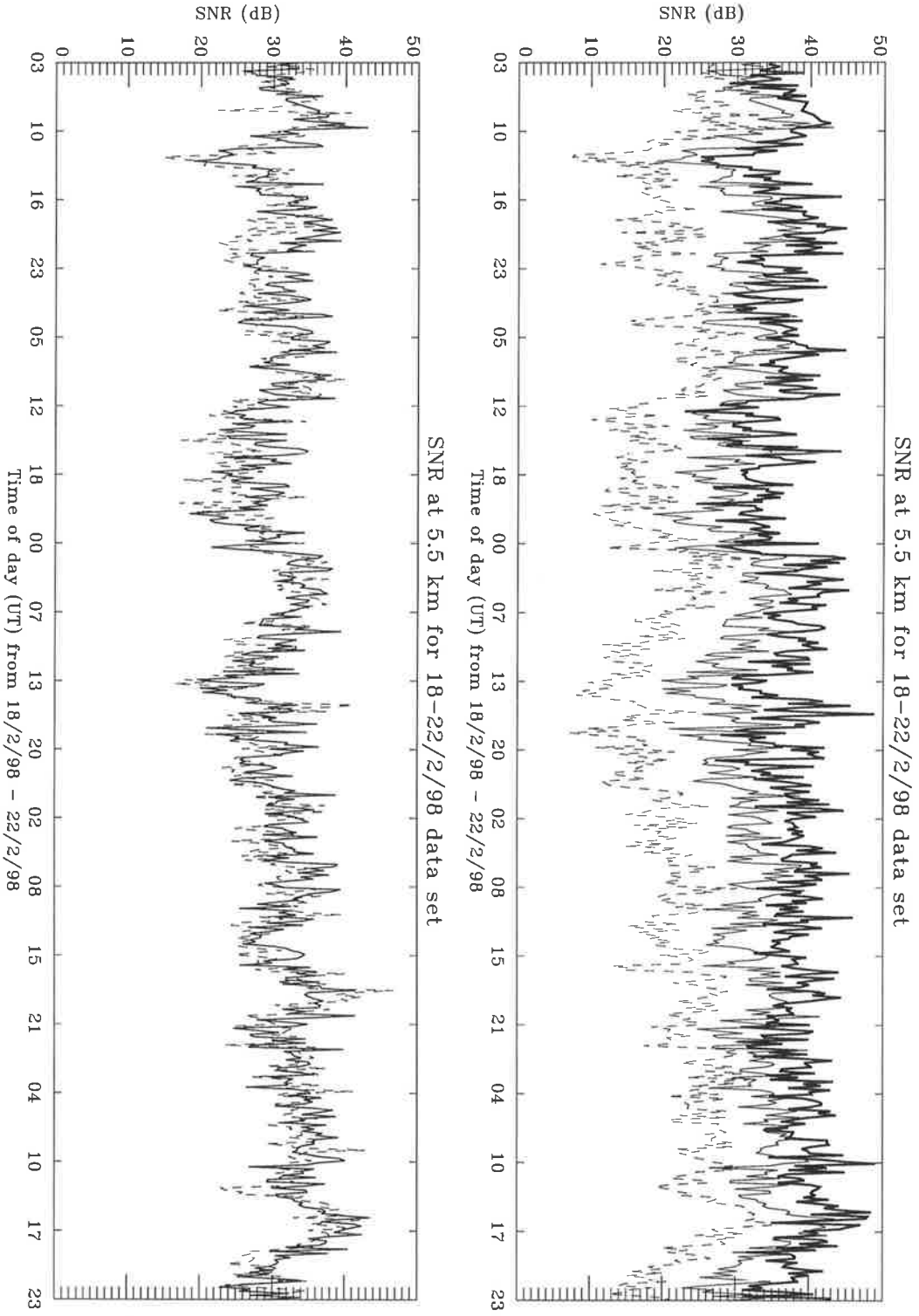

Figure 5.14: Top: SNR in three beams on the North-South array, at 5.5 *km* over the full 18-22/2/98 data set. Thick solid line - 0.0°, thin solid line - north 3.6°, dashed line - north 10.8°. Bottom: SNR in in the same data set and at the same height as above, but for 3.6° beams on the North-South array. Solid line - north beam, dashed line - south beam.

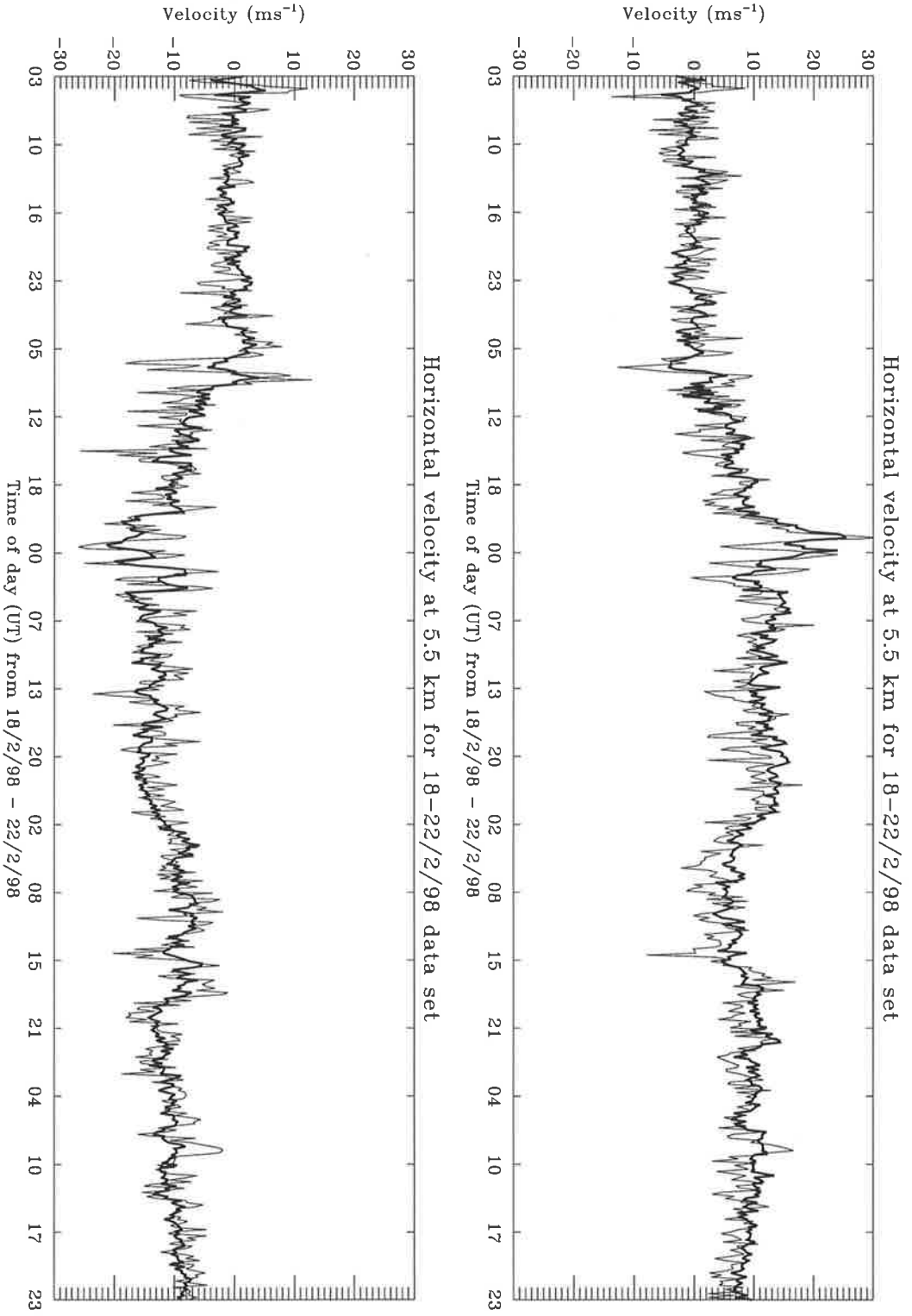

Figure 5.15: Top: Horizontal velocity in the meridional direction for the 18-22/2/98 data set, at 5.5 km, for the north 3.6° beam - thin line, and north 10.8° beam - thick line. Bottom: as above, but for the south 3.6° beam - thin line, and south 10.8° beam.

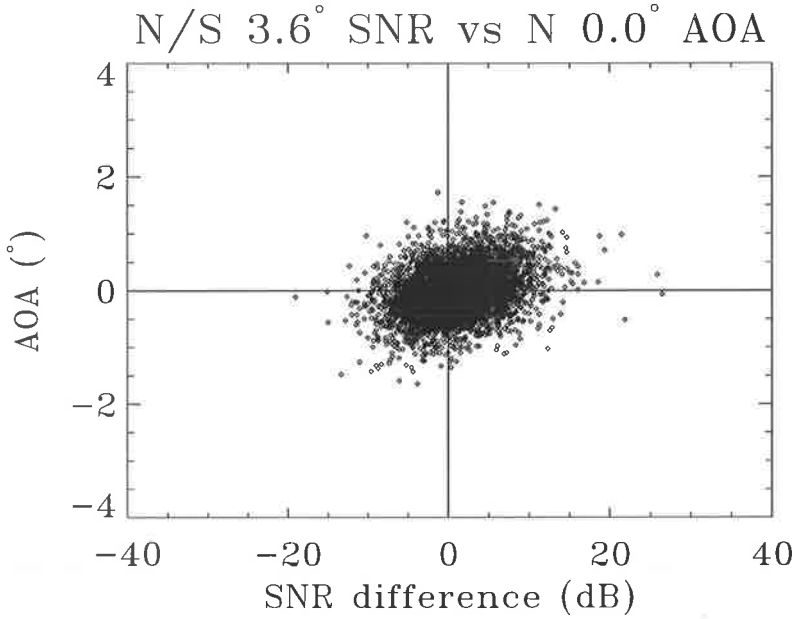

Figure 5.16: Scatter plot of SNR differences seen in the off-zenith beams north 3.6° and south 3.6° versus AOAs seen on the vertical beam directed between the north and south beam in time. Data is from the height range from 3 - 8 km, over the full 18-22/2/98 data set.

sampling will cause a reasonable amount of variation between the two profiles in a given direction. However, it can be seen that, the 3.6° off-zenith values are on average smaller then the 10.8° off-zenith values, once the high variability of the 3.6° off-zenith velocities is taken into account.

The investigation of the relationship between SNR differences in symmetrical off-zenith beams, and AOAs on vertical beams, was undertaken in a similar manner as that used by *Röttger et al.* [1990] who investigated the relationship between AOA and vertical velocities via correlation techniques, as discussed in Section 5.2. The first step in this process was to examine the behaviour of the time series of SNR differences, relative to the corresponding time series of AOAs. The individual measurements of the SNR differences were assumed to be coincident with the corresponding individual measurements of AOA, although in reality the three beams necessary for the measurements were directed sequentially and each took approximately one minute to collect. Note that all the SNR differences in a given pair of symmetrical off-zenith beams were calculated north beam SNR - south beam SNR, and east beam SNR - west beam SNR.

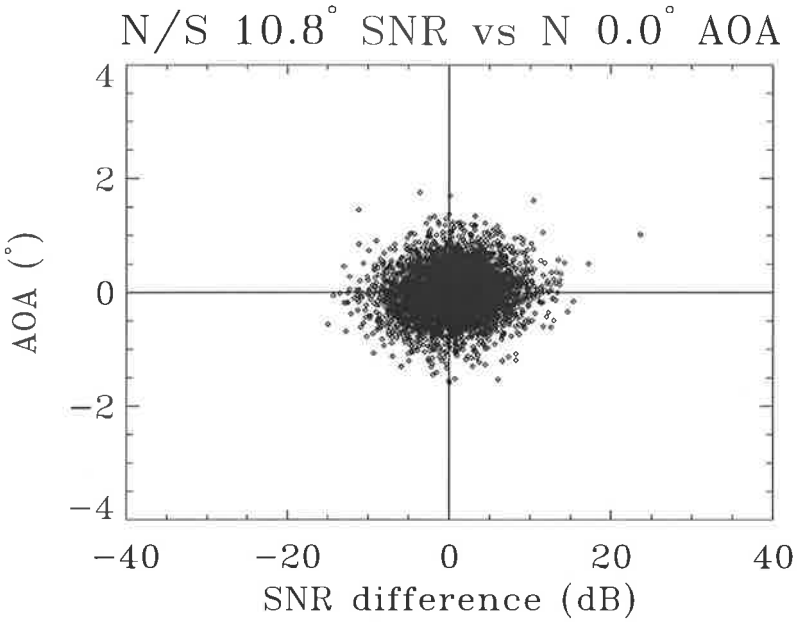

Figure 5.17: Scatter plot of SNR differences seen in the off-zenith beams north 10.8° and south 10.8° versus AOAs seen on the vertical beam directed between the north and south beam in time. Data is from the height range from 3 - 8 km, over the full 18-22/2/98 data set.

Figure 5.16 is a scatter plot of the SNR differences observed in the north and south beams at 3.6° off-zenith, and the AOA measured on the vertical beam directed between them in time. Figure 5.17 is a scatter plot of the SNR differences observed in the north and south beams at 10.8° off-zenith, and the AOA measured on the vertical beam directed between them in time. In both Figure 5.16 and Figure 5.17 the SNR differences are plotted along the x-axis while the corresponding AOAs are plotted along the y-axis. Both scatter plots were compiled from data over the height range from 3 - 8 km, using data at the minimum possible resolution of 12 minutes over the full 18-22/2/98 data set. These two figures are shown overplotted with the lines $x = 0$ and $y = 0$ for reference. The AOAs in these figures are the average AOA values at a given point in time, for all receiver pair combinations except that corresponding to the antennas with the largest separation, as discussed in Section 5.5. This average value of the AOA across the various antenna groups is used throughout the analysis in this section.

When comparing Figure 5.16 and Figure 5.17 it can be seen that the scatter in

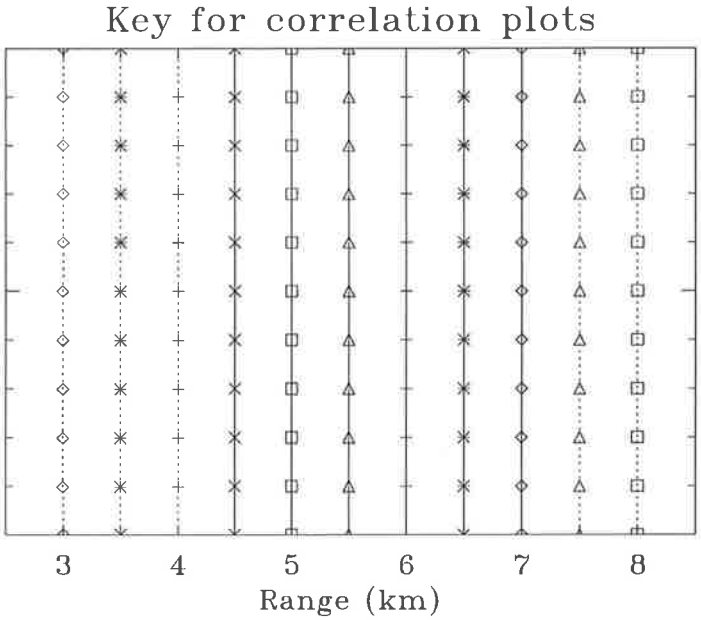

Figure 5.18: Key for the plots on the following pages. The data at a range of 3 *km* is shown using diamonds connected with a dashed line, data at a range of 3.5 *km* is shown with asterisks connected with a dashed line and so on, over the height range from 3 - 8 *km*.

the first figure has a distinct positive slope to it, while the scatter in the second figure shows virtually circular scatter about the origin of the plot. Figure 5.16 is suggestive of a relationship between the SNR differences seen on symmetrical off-zenith beams directed at 3.6° off-zenith, and the AOAs seen on a vertical beam between the two off-zenith beams in time. While Figure 5.17 shows that there is no clear relationship between the SNR differences seen on symmetrical off-zenith beams directed at 10.8° off-zenith, and the AOAs seen on a vertical beam between the two off-zenith beams in time. Before examining this behaviour in more detail, it is necessary to introduce the key to plots on the pages that follow. Figure 5.18 shows the plot symbol that is used for the data at a given height on the following pages.

In order to obtain more detailed information on the relationship between the AOAs and the SNR differences between a given pair of symmetric off-zenith beams, correlation coefficients were calculated. Given the scatter in Figure 5.16, perfect correlations resulting in a correlation coefficient of 1.0 were not expected. As such, it was necessary to determine the significance of any correlation coefficients that were calculated, and

to determine the lower limit of what constituted a "real" correlation coefficient.

If the true linear correlation coefficient, r, between two variables which are Gaussian distributed is zero, then the statistic

$$\frac{r\sqrt{n-2}}{\sqrt{(1-r^2)}} \tag{5.2}$$

has a t-distribution with n - 2 degrees of freedom, where n is the number of samples. Given this, the linear correlation coefficient is significantly different from zero at the α level of confidence if

$$\left|\frac{r\sqrt{n-2}}{\sqrt{(1-r^2)}}\right| \geq t_{\alpha/2,n-2} \tag{5.3}$$

where $t_{\alpha/2,n-2}$ is the t statistic for the appropriate number of samples and confidence level. Both the SNR difference data and the AOA data used here had Gaussian distributions. Correlation coefficients were calculated at each height for each of the five days of the 18-22/2/98 data set. Small data gaps in the DBS data resulted from the rejection of outliers as discussed in Chapter 3 of this thesis. No interpolation over data gaps was performed, as such, the correlation coefficients were calculated for only those points in time where data existed in all three beams. The minimum number of points suitable for correlation at a given height, on a given day in the 18-22/2/98 data set was found to be 100. Using this value of n, correlation coefficients greater than 0.2 were found to be significantly different from 0.0 at the 95% confidence level

As a further test of the validity of the correlation between the SNR differences and AOAs, the non-parametric or rank correlation coefficient was also calculated. Rather than calculating the correlation coefficient of the data, rank correlation calculates the correlation coefficient of the ranks of the data. Each data point is replaced with its rank within the data set and the two sets of ranks are correlated. This kind of correlation assumes nothing about the distribution of the original data and as such is considered to be a more robust measure of correlation than linear correlation, in the same way that the median is more robust than the mean (*Press et al.* [1986]). The Spearman rank-order correlation coefficient, r_s, was used to compare with the linear correlation coefficient. The same significance test as was applied to r can be applied

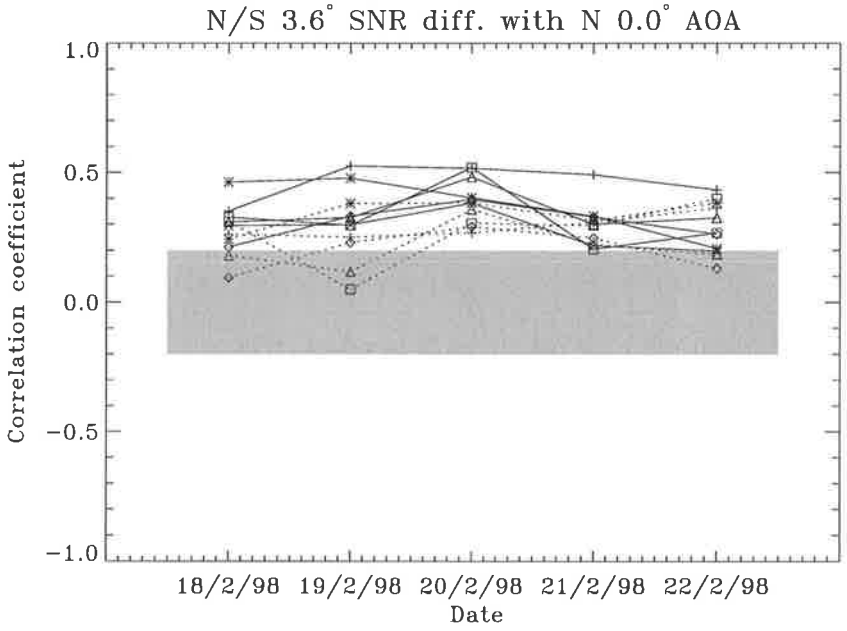

Figure 5.19: Linear correlation coefficients for the SNR differences seen on 3.6° off-zenith DBS beams to the north and south, and the AOAs seen on the vertical beam directed between the DBS beams in time, for the 18-22/2/98 data set. Coefficients are shown as a function of day and height, where data points outside the shaded region are significant at the 95% confidence level.

to r_s, resulting in the same 95% confidence level of significant correlation for r_s larger than 0.2.

In practice, for the variables used here, the difference between the correlation coefficient from linear and rank correlation was minimal, due to the fact that the variables were well described by Gaussian distributions, and as such, were well suited to the linear correlation test. Figure 5.19 shows the linear correlation coefficient between the SNR differences in the north and south beams at 3.6° off-zenith, and the AOA measured on the beam between them in time, for each day of the 18-22/2/98 data set, at all heights from 3 - 8 *km*. The shaded area in this plot shows the area within which a correlation coefficient is not significant. Points outside the shaded area are significant correlations at the 95% level, while points inside the shaded region are not significantly different from a correlation coefficient of 0.0. Figure 5.20 shows the Spearman rank-order correlation coefficient for exactly the same data as in Figure 5.19. It can be seen that the two are very similar. As such, the linear correlation coefficient appears to be a robust measure of the degree of correlation between the two variables and was used

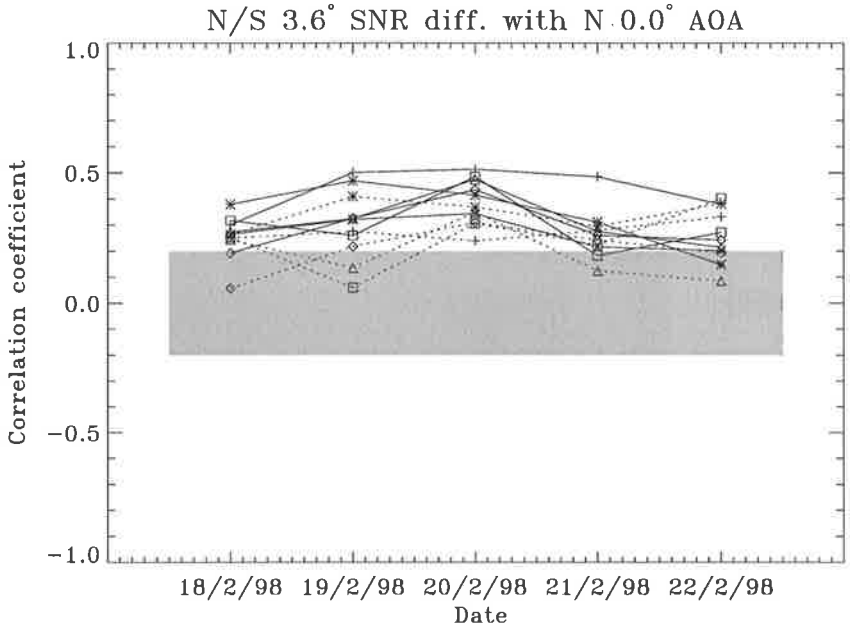

Figure 5.20: Spearman rank-correlation coefficient for the SNR differences seen on 3.6° off-zenith DBS beams to the north and south, and the AOAs seen on the vertical beam directed between the DBS beams in time, for the 18-22/2/98 data set. Coefficients are shown as a function of day and height, where data points outside the shaded region are significant at the 95% confidence level.

for the remainder of the data.

It can be seen from Figure 5.19 that there is significant positive correlation between the SNR differences as seen on DBS beams directed at 3.6° off-zenith to the north and south, and the vertical beam AOA. The variation of the SNR differences, as seen in the two off-zenith beams at 3.6°, is therefore related to the AOA on the vertical beam. Figure 5.21 shows the linear correlation coefficient between the SNR differences as seen on DBS beams directed at 10.8° off-zenith to the north and south, and the AOA as measured on the vertical beam directed between the off-zenith beams in time. It can be seen that in contrast to Figure 5.19, there are hardly any significant points in this figure, which suggests that the SNR differences as seen on the two off-zenith beams at 10.8° are independant of the AOA as seen on the vertical beam.

Figure 5.22 and Figure 5.23 show the linear correlation coefficient diagrams for the data from the East-West array. Figure 5.22 shows the correlation between SNR differences seen on DBS beams directed at 3.6° off-zenith to the east and west, and the AOA measured on a vertical beam directed between the two off-zenith beams in time.

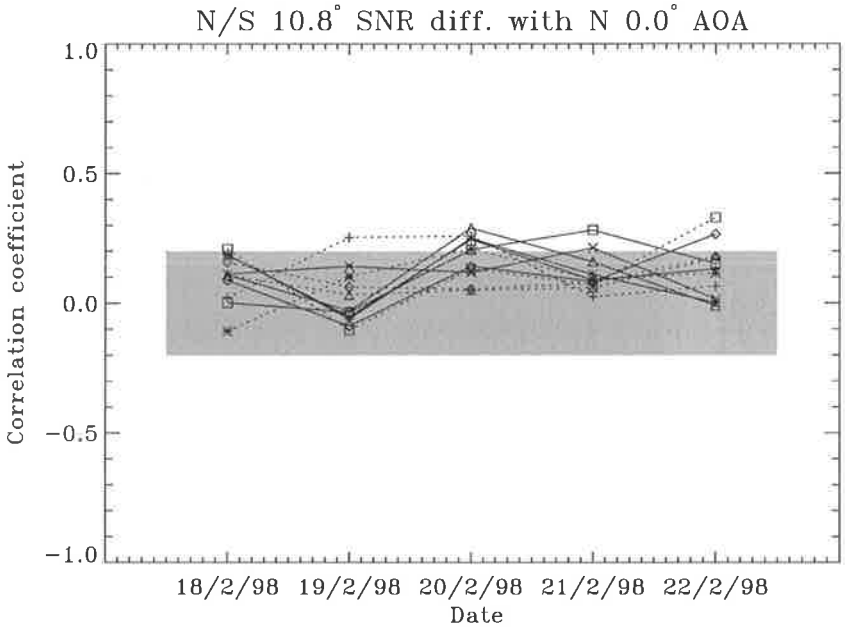

Figure 5.21: Linear correlation coefficient for the SNR differences seen on 10.8° off-zenith DBS beams to the north and south, and the AOAs seen on the vertical beam directed between the DBS beams in time, for the 18-22/2/98 data set. Coefficients are shown as a function of day and height, where data points outside the shaded region are significant at the 95% confidence level.

While Figure 5.23 shows the correlation results for the 10.8° off-zenith DBS beams to the east and west and the AOA for the vertical beam directed between the two off-zenith beams in time. It can be seen that the behaviour for the two angles is very similar to that seen in Figure 5.19 and Figure 5.21, with a high number of significant correlations for the 3.6° off-zenith data, and fewer significant correlations for the 10.8° off-zenith data. Significant correlation coefficients for the 3.6° off-zenith data are in the range from 0.2 - 0.5, while significant correlation coefficients in for the 10.8° are in the range 0.2 - 0.3.

In order to check that the significant correlations for 3.6° off-zenith data shown in Figure 5.19 and Figure 5.22 were meaningful, the correlation coefficient between the SNR differences seen on the north and south 3.6° off-zenith beams and the AOA seen on the vertical beam that was directed between the north and south 10.8° off-zenith beams in time was calculated. This correlation is between an SNR difference measured on 3.6° off-zenith beams at one time, and an AOA measured on the vertical beam on the same array, six minutes later. Figure 5.24 shows the results. It can be seen that the

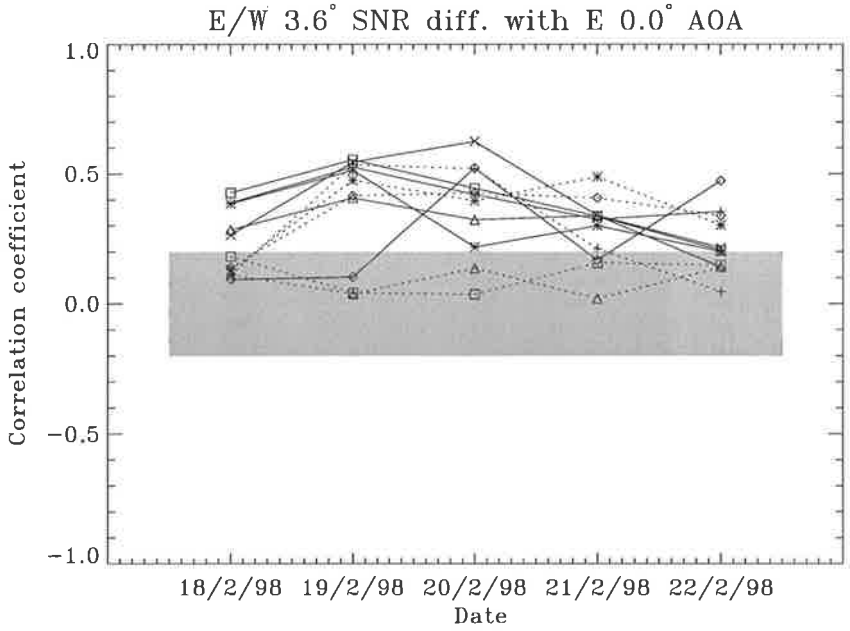

Figure 5.22: Linear correlation coefficient for the SNR differences seen on 3.6° off-zenith DBS beams to the east and west, and the AOAs seen on the vertical beam directed between the DBS beams in time, for the 18-22/2/98 data set. Coefficients are shown as a function of day and height, where data points outside the shaded region are significant at the 95% confidence level.

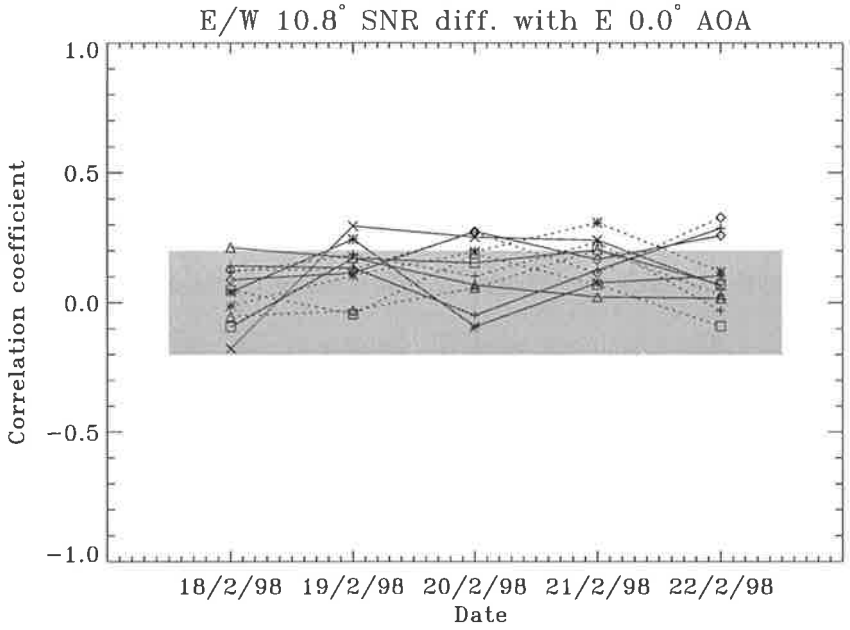

Figure 5.23: Linear correlation coefficient for the SNR differences seen on 10.8° off-zenith DBS beams to the east and west, and the AOAs seen on the vertical beam directed between the DBS beams in time, for the 18-22/2/98 data set. Coefficients are shown as a function of day and height, where data points outside the shaded region are significant at the 95% confidence level.

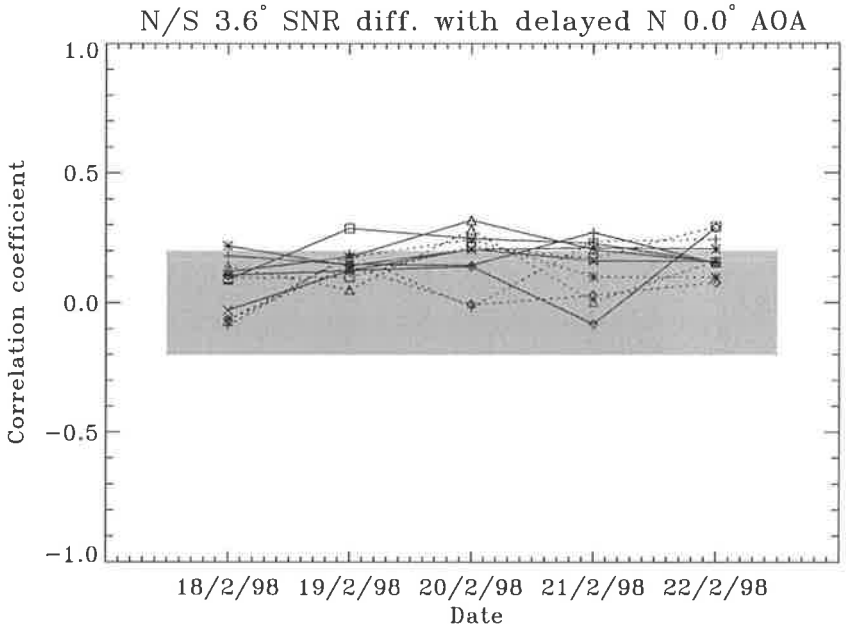

Figure 5.24: Linear correlation coefficient for the SNR differences seen on 3.6° off-zenith DBS beams to the north and south, and the AOAs seen on the vertical beam measured 6 minutes after the DBS beams, for the 18-22/2/98 data set. The AOAs used here were measured on the vertical beam that was directed between the 10.8° off-zenith DBS beams to the north and south.

number of significant correlations has decreased between this figure and Figure 5.19. This suggests that the variation in the atmosphere over the six minutes is such that the vertical beam measuring the AOA, and the 3.6° off-zenith beams measuring SNR differences are not experiencing the same scatter, as they were for the data shown in Figure 5.19. A further check was made by calculating the linear correlation coefficient between the SNR differences seen on DBS beams at 3.6° off-zenith to the north and south, and the AOA measured on the vertical beam that was directed between the east and west 3.6° off-zenith beams in time. This correlation is between the SNR differences measured with 3.6° off-zenith beams on one array, and the AOA measured only three minutes later, on the opposite array. Figure 5.25 shows the results. It can be seen that there are virtually no significant correlations between these two data sets, as expected since the data from the two antenna arrays are completely independant.

The same analysis that was performed for various combinations of SNR differences and AOA for the 18-22/2/98 data set, was also used on the 24-25/3/98 data set. The backscatter in the 24-25/3/98 data set was aspect sensitive throughout, in the same

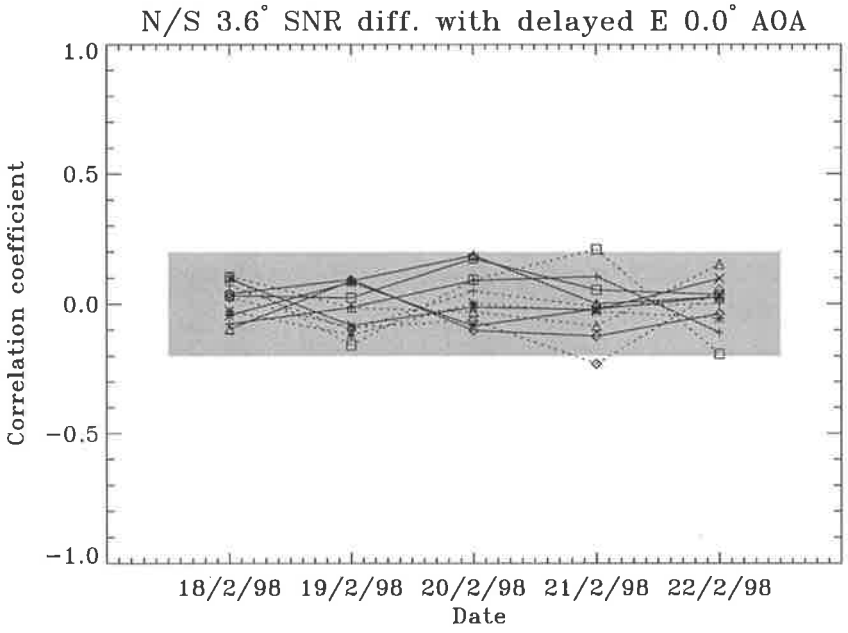

Figure 5.25: Linear correlation coefficient for the SNR differences seen on 3.6° off-zenith DBS beams to the north and south, and the AOAs seen on the vertical beam measured 3 minutes after the DBS beams, for the 18-22/2/98 data set. The AOAs used here were measured on the vertical beam that was directed between the 3.6° off-zenith DBS beams to the east and west.

manner as for the 18-22/2/98 data set, although it is not shown here. Figure 5.26 shows the results for the correlation between the SNR differences of the north and south DBS beams at 3.6° off-zenith, and the AOA measured along the north-south baseline of the vertical beam directed between them in time, for each of the ranges from 3 - 8 km, for the two days of the 24-25/3/98 data set. The AOA here is the average AOA measured using the two pairs of antenna groups along the north-south baseline, as discussed in Section 5.5. Because of the fact that there were less beam directions in this data set relative to the 18-22/2/98 data set, the number of points in the sample to be correlated was higher, which resulted in a decrease in the minimum significant correlation coefficient from 0.2 in the 18-22/2/98 data set to 0.16 in the 24-25/3/98 data set. Figure 5.27 shows the results for the correlation between the SNR differences of the north and south DBS beams at 10.8° off-zenith, and the AOA on the vertical beam directed between the these off-zenith DBS beams in time.

It can be seen that the behaviour of the correlation coefficients shown in Figure 5.26 and Figure 5.27 is very similar to that for the same beam direction combinations in the

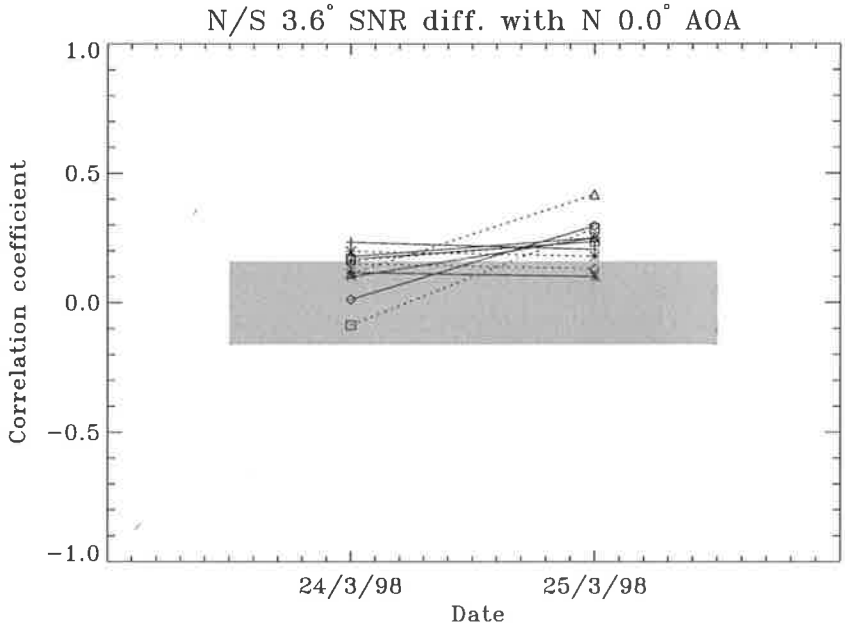

Figure 5.26: Linear correlation coefficient for the SNR differences seen on 3.6° off-zenith DBS beams to the north and south, and the AOAs seen on the vertical beam directed between the DBS beams in time, for the 24-25/3/98 data set. Coefficients are shown as a function of day and height, where data points outside the shaded region are significant at the 95% confidence level.

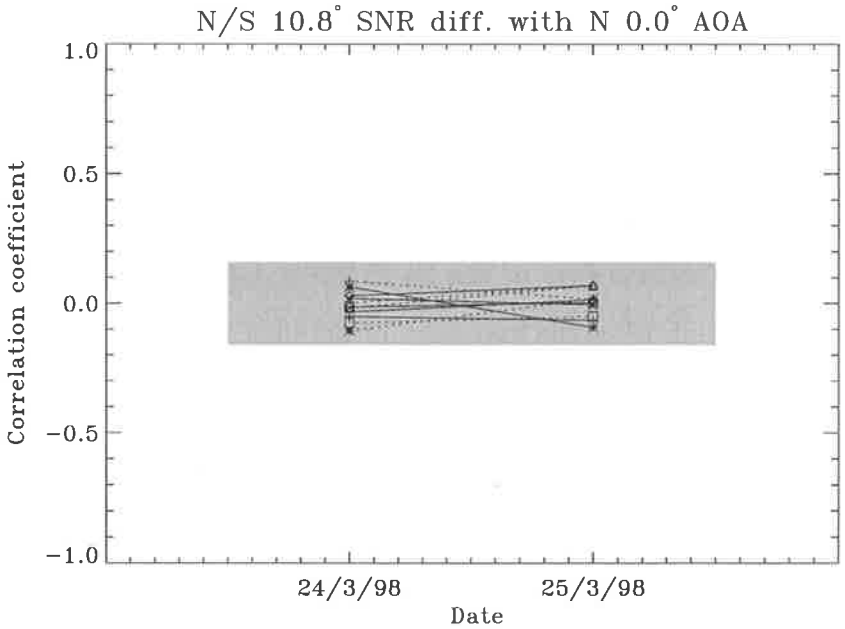

Figure 5.27: Linear correlation coefficient for the SNR differences seen on 10.8° off-zenith DBS beams to the north and south, and the AOAs seen on the vertical beam directed between the DBS beams in time, for the 24-25/3/98 data set. Coefficients are shown as a function of day and height, where data points outside the shaded region are significant at the 95% confidence level.

18-22/2/98 data set, with the exception that the correlation coefficients were generally lower in the 24-25/3/98 data set. As was noted in Section 5.5, the AOA measurements from the 18-22/2/98 data set showed a greater similarity between the various antenna groups along a given baseline then the AOA measurements from the 24-25/3/98 data set. As such, the average AOA for the 18-22/2/98 data set is expected to be a better measure of the actual AOA then the average AOA for the 24-25/3/98 data set. This fact could explain the relatively lower correlations for the 24-25/3/98 data set, as seen in Figure 5.26 and Figure 5.27.

5.6.1 Discussion

In Chapter 4 it was shown that in aspect sensitive conditions the value of θ_s as measured using vertical beams only, with the FCA spatial correlation method, and as measured on a vertical beam and a beam at 3.6° off-zenith, with the DBS method, produced very similar values of θ_s which suggests that the two beams were responding to the same scatterers. In addition, the θ_s values that were calculated for the 0.0° and 3.6° off-zenith beams using the Doppler method in Chapter 4, during aspect sensitive periods, were less than 5°. Recent calculations by *Hocking & Hamza* [1997] suggest that θ_s values less then 5° are the result of specular scatter. These authors claim that anisotropic turbulence is not capable of producing scatter that is aspect sensitive enough to produce θ_s values below 5°. If this is the case, then the scatter which both the 0.0° and 3.6° beams in Chapter 4 are measuring is most likely to be due to specular layers, which may be tilted.

The data sets presented in this chapter, from 18-22/2/98 and 24-25/3/98 were aspect sensitive throughout, and although the θ_s values from the 0.0° and 3.6° off-zenith beams for these data sets are not shown, they were less than 5° in the same manner as the aspect sensitive θ_s values which were calculated for Chapter 4. This fact, coupled with the fact that the SNR differences between symmetrical off-zenith beams, and AOA values on a vertical beam directed between the off-zenith beams in time, were shown to be significantly correlated for most heights throughout the data sets, suggests that the 3.6° off-zenith DBS beams and the vertical beam are receiving

backscatter from tilted specular layers. This behaviour was observed in data from both the zonal and meridional planes, in two different data sets, collected using different antenna arrangements.

Scattering from specular layers, which may be tilted, and anisotropic turbulence are believed to be the mechanisms which cause aspect sensitive scatter. Anisotropic turbulence could be responsible for the non-zero AOA measurements presented in this chapter. But, there is no physical reason why the AOA produced by anisotropic turbulence, as observed in a vertical beam, should be correlated with the differences in SNRs in off-zenith beams at 3.6°. However, tilted layers do provide a sound physical reason for the significant correlations between the 3.6° off-zenith, and vertical beam data that have been shown in this chapter.

In contrast to the 3.6° off-zenith results, there were far fewer significant correlations between the 10.8° off-zenith beams and the corresponding vertical beam AOAs, measured on a beam directed between the off-zenith beams in time. The lower number of significant correlations as a function of height and day for the 10.8° off-zenith comparison was seen in both zonal and meridional data, for both the 18-22/2/98 and 24-25/3/98 data sets. This result suggests that the 10.8° off-zenith DBS beams were not responding to the layers measured in the vertical beam as often as the 3.6° off-zenith beams. Another possible cause could be the difference between the sampling of the 3.6° and 10.8° off-zenith beams. At the highest range used for this work, 8 km, the 3.6° off-zenith range gate is centred on a height of 7.98 km, while the 10.8° off-zenith gate is centred on a height of 7.86 km. The range gates used for this work were 1 km in length, which meant that the 10.8° off-zenith beam samples approximately 86% of the same height range as the vertical beam. In addition, the 10.8° off-zenith beams are approximately 3 km apart at a range of 8 km, while the 3.6° off-zenith beams are approximately 1 km apart at the same range. These spatial differences could contribute in some way to the differences between the relationship between the AOAs and the 3.6° or 10.8° off-zenith beams. In that case, the difference in the correlation behaviour for the two different off-zenith angles might be indicative of the horizontal extent of the layers seen on the vertical beam, and the concentration of layers within a radar range gate.

The fact that there were some significant correlations between the 10.8° off-zenith beam SNR differences and the vertical beam AOAs, for the 18-22/2/98 data set at least, does suggest that there are times when the 10.8° off-zenith beams are affected by the aspect sensitive layers observed with the vertical beam. This is in agreement with the work of *Tsuda et al.* [1997a] which showed that truly isotropic scatter was only consistently measured with beams directed at angles of 18° off-zenith or more. The generally lower correlations between the data for the 24-25/3/98 data set meant that there were no significant correlations at all for the 10.8° off-zenith SNR differences and the AOAs. Because of this, it was not possible to see if there was a difference between this behaviour and that at 18.2° off-zenith for the 24-25/3/98 data, as both sets had no significant correlations.

Correlation coefficients were also calculated between the 3.6° off-zenith beam SNR differences on the north and south beams and the AOAs measured on a vertical beam, on the North-South array, six minutes after the 3.6° off-zenith beams. This was done for the 18-22/2/98 data set only. It was found that the number of significantly correlations reduced markedly, compared to the number when using the essentially coincident vertical beam AOAs. In addition, correlation coefficients for the 3.6° off-zenith beam SNR differences on the north and south beams and AOAs measured on a vertical beam, on the East-West array, three minutes after the 3.6° off-zenith north and south beams were calculated. This was also done for the 18-22/2/98 data set only. The North-South and East-West arrays are totally independant and as such, the measurements were expected to be unrelated. This was seen to be the case with virtually no significant correlations for this pair of variables.

The fact that there were some significant correlations between the pair of off-zenith SNR differences at 3.6° off-zenith and the AOA measured six minutes later on the same array, suggests that while most of the layers have modified enough within the six minutes, such that the number of significant correlations is reduced, there are still a number of layers that are similar enough in their orientation that they are still significantly correlated with the SNR differences recorded six minutes earlier.

The fact that the vertical and off-zenith data presented in this chapter were not collected simultaneously will have an effect on the results discussed here. The results

of *Palmer et al.* [1998] which showed excellent agreement between the direction of maximum backscattered power in off-zenith beams and AOAs on a vertical beam, were collected essentially simultaneously using inter-pulse-beam-steering. It is possible that the actual value of the significant correlation coefficients for the 3.6° off-zenith DBS data would be closer to 1 if the data presented here were collected in a similar manner. Although it is also possible that the layers seen on the 0.0° and 3.6° off-zenith beams have enough "roughness", or corrugations, that the small differences created by sampling different parts of the layer will result in no better agreement between the AOAs and the SNRs on off-zenith beams than what has been seen here, regardless of the data collection regime.

5.7 Off-zenith beam AOAs

The results from the previous section suggested that 10.8° off-zenith beams were for the most part not affected by the tilting of the structures seen on a vertical beam. However, there is some variability in the AOA within any radar beam due to the finite beam width. A number of authors have presented momentum flux measurements in the ST region of the atmosphere in recent years. Because of the manner in which momentum flux measurements are made they are especially sensitive to anything which might cause a difference in the radial velocities in two symmetric off-zenith beams. As such, it is worth examining the role different that varying AOA measurements in off-zenith beams play in measurements of momentum flux. In this section AOA measurements from the off-zenith beams used in the 18-22/2/98 experiment are presented, and the effect of the AOA variation within the symmetric beams required for momentum flux measurements are quantified over the course of a data set.

In Chapter 3 it was noted that the east beam data was affected by ground clutter. In the context of AOA measurements, this fact means that the time series from the east beams may have scatter from the main lobe which gives a certain AOA value, and scatter coming in through sidelobes or even in through the main lobe which corresponds to a different AOA. As discussed in Section 5.5, the distance separating a given pair of receiving antennas determines the range of off-zenith angles that can be

measured. AOAs which are outside this range will alias and are therefore ambiguous. For the 18-22/2/98 data set, it was found that the eastern beam AOA time series, particularly at 10.8°, aliased quite often, indicating that AOAs were being observed outside the main lobe. The fact that it was the east beam time series that had this problem suggested that it might be due to ground clutter, and as such, only the data from beams to the north and south will be discussed here.

Figure 5.28 shows a histogram of the average AOAs measured in the north and south beams at 3.6° off-zenith, for the range from 3 - 8 km, in the 18-22/2/98 data set. The average AOAs were calculated in the same manner as the AOAs for the vertical beam data, discussed in Section 5.5. Figure 5.29 shows the corresponding histogram for the average AOAs in the north and south beams at 10.8° off-zenith, for the same range, in the same data set. Both figures include the Gaussian fits to the histograms and the corresponding half-power half-width (HPHW) value, and are plotted over the same y-axis range. It can be seen from these two figures that there is a noticeable difference between the shape of the AOA histograms of the 3.6° and 10.8° off-zenith beams. The 3.6° off-zenith beam histogram is much wider and flatter then the 10.8° off-zenith histogram. This is consistent with the fact discussed in the last section that the 3.6° off-zenith beams appear to be responding to the changing AOAs caused by the tilting of specular layers, whereas the 10.8° off-zenith beams do not appear to be as affected by this scatter. It should be noted that these histograms have half the number of points in them when compared to the histograms for vertical beam data from the same data set, as shown in Figure 5.11.

Figure 5.30 and Figure 5.31 show image contour plots of the meridional and zonal wind in the 18-22/2/98 data set, over the range from 3 - 8 km. The wind values in these figure are calculated from the pair of beams in the given plane, at the minimum resolution possible for the 18-22/2/98 data set, of 12 minutes.

As noted earlier, *Vincent & Reid* [1983] developed the most commonly used method of determining the momentum flux from the data in two symmetric off-zenith beams, under the assumption that the atmosphere is statistically homogeneous in the two off-zenith radial beams, and that the horizontal velocities are independant of the horizontal position. If $\overline{V_N'^2}$ and $\overline{V_S'^2}$ are the mean square radial velocities in the north and

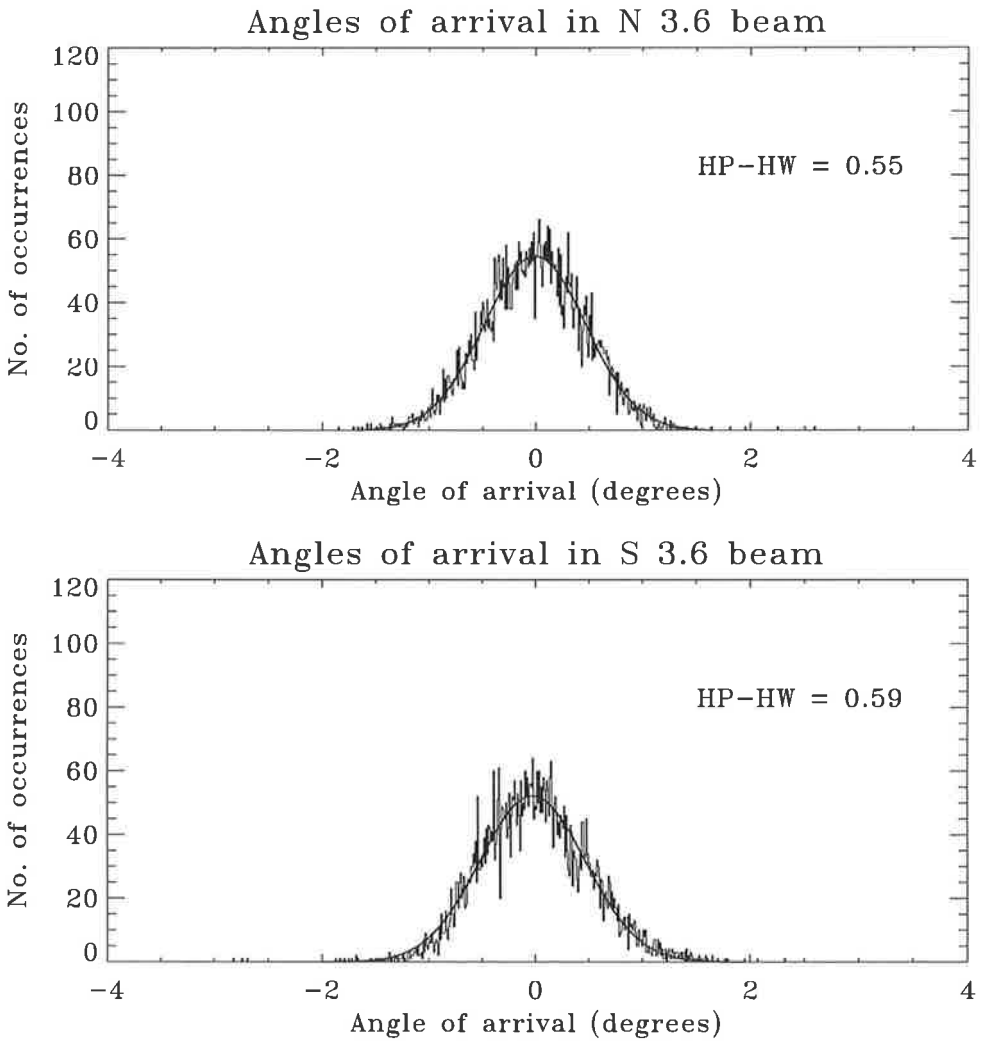

Figure 5.28: Histograms of the average AOAs measured with DBS beams at 3.6° off-zenith to the north and south, for the 18-22/3/98 data set. The individual average values are the average of the AOAs at a given time, over all of the antenna group combinations except the Rx 3 vs Rx 6 combination, which uses data from the furthest two antenna groups. The histograms were formed with data from the height range from 3 - 8 *km*, and are shown overplotted with a Gaussian function fitted to the histogram, and the corresponding half-power, half-width value.

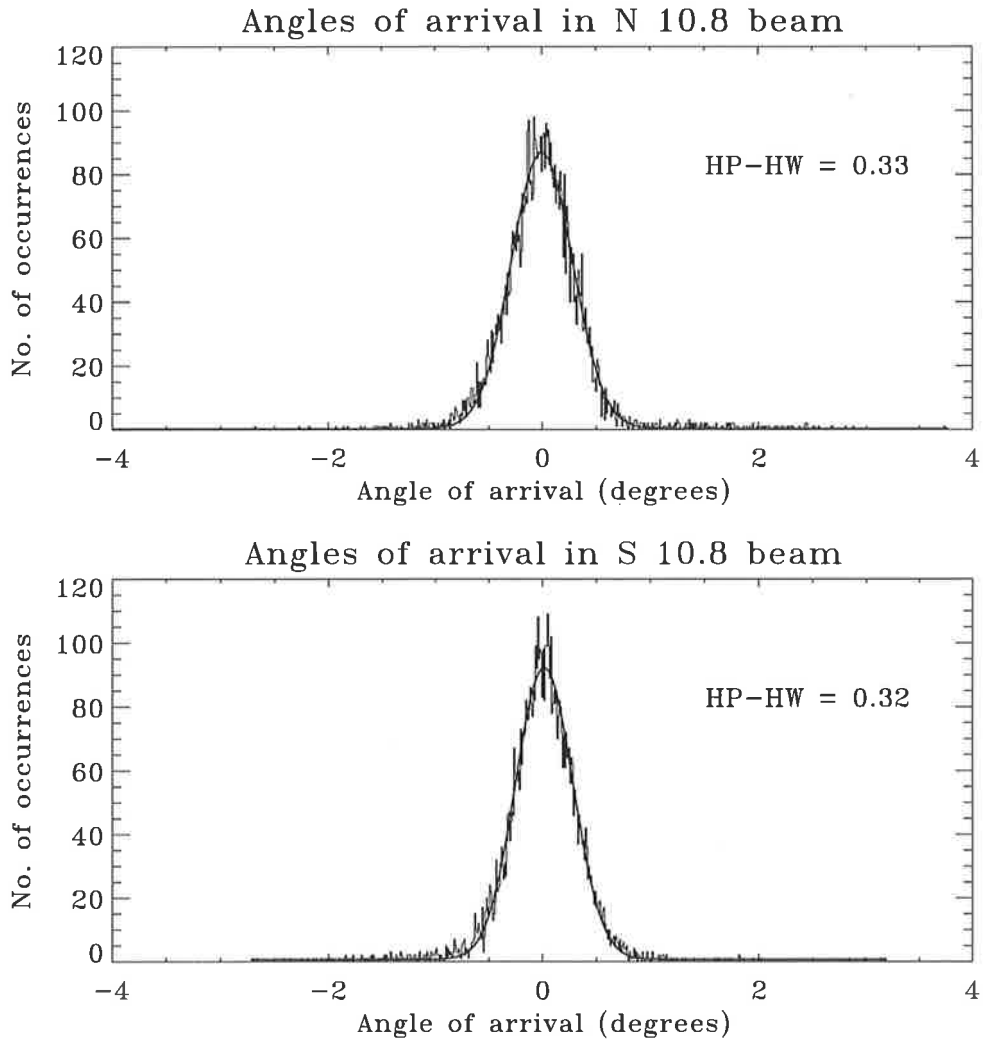

Figure 5.29: Histograms of the average AOAs measured with DBS beams at 10.8° off-zenith to the north and south, for the 18-22/3/98 data set. The individual average values are the average of the AOAs at a given time, over all of the antenna group combinations except the Rx 3 vs Rx 6 combination, which uses data from the furthest two antenna groups. The histograms were formed with data from the height range from 3 - 8 *km*, and are shown overplotted with a Gaussian function fitted to the histogram, and the corresponding half-power, half-width value.

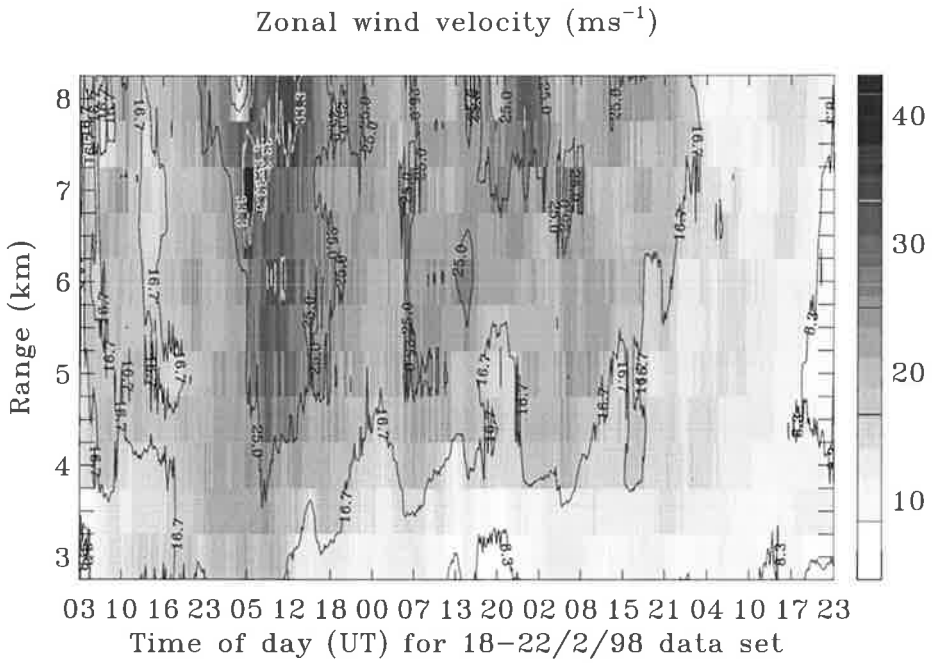

Figure 5.30: Image contour plot of the zonal wind velocity over the height range from 3 - 8 *km* for the 18-22/2/98 data set. Wind velocities were calculated from the 10.8° off-zenith DBS beams directed to the east and west and are shown at the minimum resolution possible for the 18-22/2/98 data set, of 12 minutes.

south beams respectively, and θ is the off-zenith angle, then the meridional momentum flux can be determined, using the following equation

$$\overline{v'w'} = \frac{\overline{V_N'^2} - \overline{V_S'^2}}{2sin2\theta}, \tag{5.4}$$

where $\overline{v'w'}$ is the meridional momentum flux, comprising the perturbation velocities in the meridional (v) and vertical (w) directions. By calculating the mean square radial velocities in the east and west beams, the zonal momentum flux, $\overline{u'w'}$ can also be determined. Measurements of the momentum flux using this method, and other methods which utilise various combinations of vertical and off-vertical perturbation velocities have been made in the ST region by, for example, *Fukao et al.* [1988], *McAfee et al.* [1989], *Fritts et al.* [1990], *Pritchard & Thomas* [1993], *Murayama et al.* [1994], *Worthington & Thomas* [1996] and *Chang et al.* [1997].

Since the momentum flux that is measured is commonly ascribed to the activity of gravity waves, the usual method of calculating momentum flux is to separate the

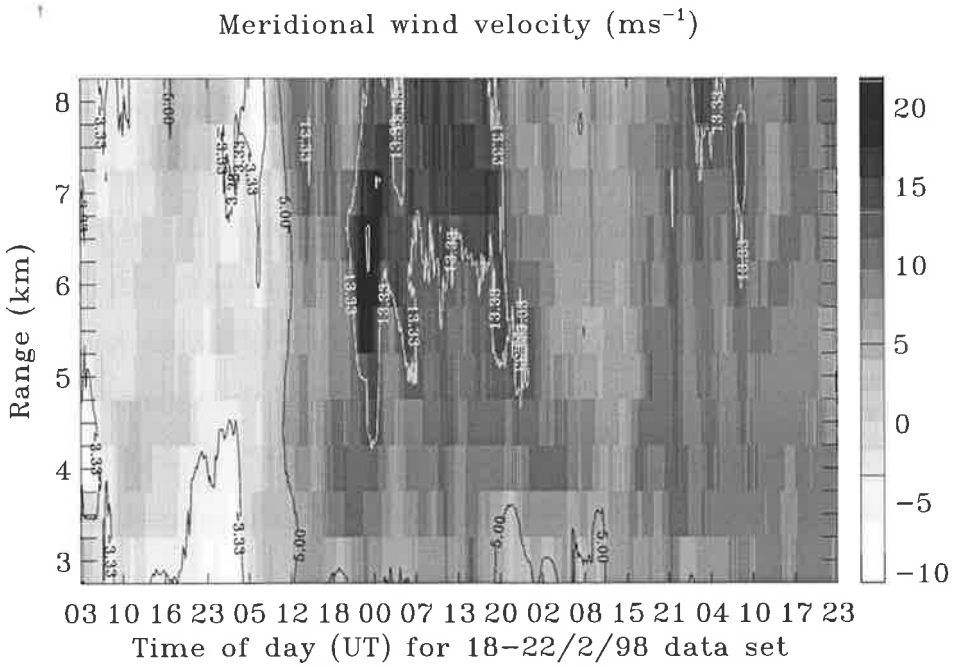

Figure 5.31: Image contour plot of the meridional wind velocity over the height range from 3 - 8 *km* for the 18-22/2/98 data set. Wind velocities were calculated from the 10.8° off-zenith DBS beams directed to the north and south and are shown at the minimum resolution possible for the 18-22/2/98 data set, of 12 minutes.

fluctuating velocities, V', into bands corresponding to the time scales of gravity activity. The high-frequency gravity wave momentum flux is most commonly calculated for data that is filtered to retain periods less than six hours. Since the high frequency measurements are the most susceptible to small differences in the radial velocities, the momentum fluxes calculated here are for periods less than six hours.

The differences in the pointing direction of the radial beams will act to induce a spurious momentum flux. In order to estimate this induced value, the background radial velocity at a given height for the 18-22/2/98 data set was smoothed. The perturbations in radial velocity induced by the varying AOA were then superimposed onto this estimated background wind. The top plot in Figure 5.32 shows the measured radial velocity in the north 10.8° off-zenith beam, at a range of 5 *km*, at the minimum resolution possible for the 18-22/2/98 data set of 12 minutes. The middle plot in Figure 5.32 shows the smoothed north 10.8° off-zenith beam radial velocities which were used as an estimate of the background wind. Finally, the bottom plot in Figure 5.32 shows the simulated radial velocity due to the variation of the AOA in

the 10.8° off-zenith north beam. This simulated north beam radial velocity time series was calculated from the time series of the background wind in the north beam and the time series of the AOA in the north beam. To ensure that the momentum flux values calculated from the simulated radial velocities were due to the AOA variations alone, the same background wind was used for the north and south beam simulated velocities. The simulated radial velocities in the south 10.8° off-zenith beam were therefore calculated from the north beam background wind and the time series of the AOA in the 10.8° off-zenith beam. It can be seen from Figure 5.32 that the variance of the simulated radial velocity is very small compared to the measured radial velocity.

The perturbation velocities, V', were calculated for both the simulated and measured radial velocities over the range 3 - 8 km for the 18-22/2/98 data set. The term $\overline{V'^2}$ was then calculated for a variety of periods. In most of the literature on momentum flux values in the ST region the time average, denoted by the overbar, is made over a few days. The assumption upon which the momentum flux method is based is that the atmosphere is statistically homogeneous in the two radar beams. The different AOAs in the various beams mean that at a given instant the atmosphere is not homogeneous in the two beams. However, over a sufficient averaging time the atmosphere is expected to be approximately homogeneous. As such, in this study, the time average was calculated over three different periods in order to determine the effects of the AOA variations as a function of this time average. The simulated and measured momentum fluxes were calculated over six hour periods, one day periods and the average over the full five day data set.

Figure 5.33 shows the simulated and measured momentum flux values over the height range from 3 - 8 km, for the one day and full five day averaging periods. Note that in this figure the x-axes are five times wider for the measured results than for the simulated results. The magnitudes of the measured momentum fluxes are within the range of values seen by other authors. *Fukao et al.* [1988] measured momentum fluxes averaged over four days, and obtained values in the range ± 1 $m^2 s^{-2}$, *McAfee et al.* [1989] took measurements averaged over eight days and obtained values in the range from -0.6 - 0.0 $m^2 s^{-2}$, and *Fritts et al.* [1990] obtained values from -0.5 - 0.2 $m^2 s^{-2}$, averaged over six days of data. It can be seen from Figure 5.33 that the simulated

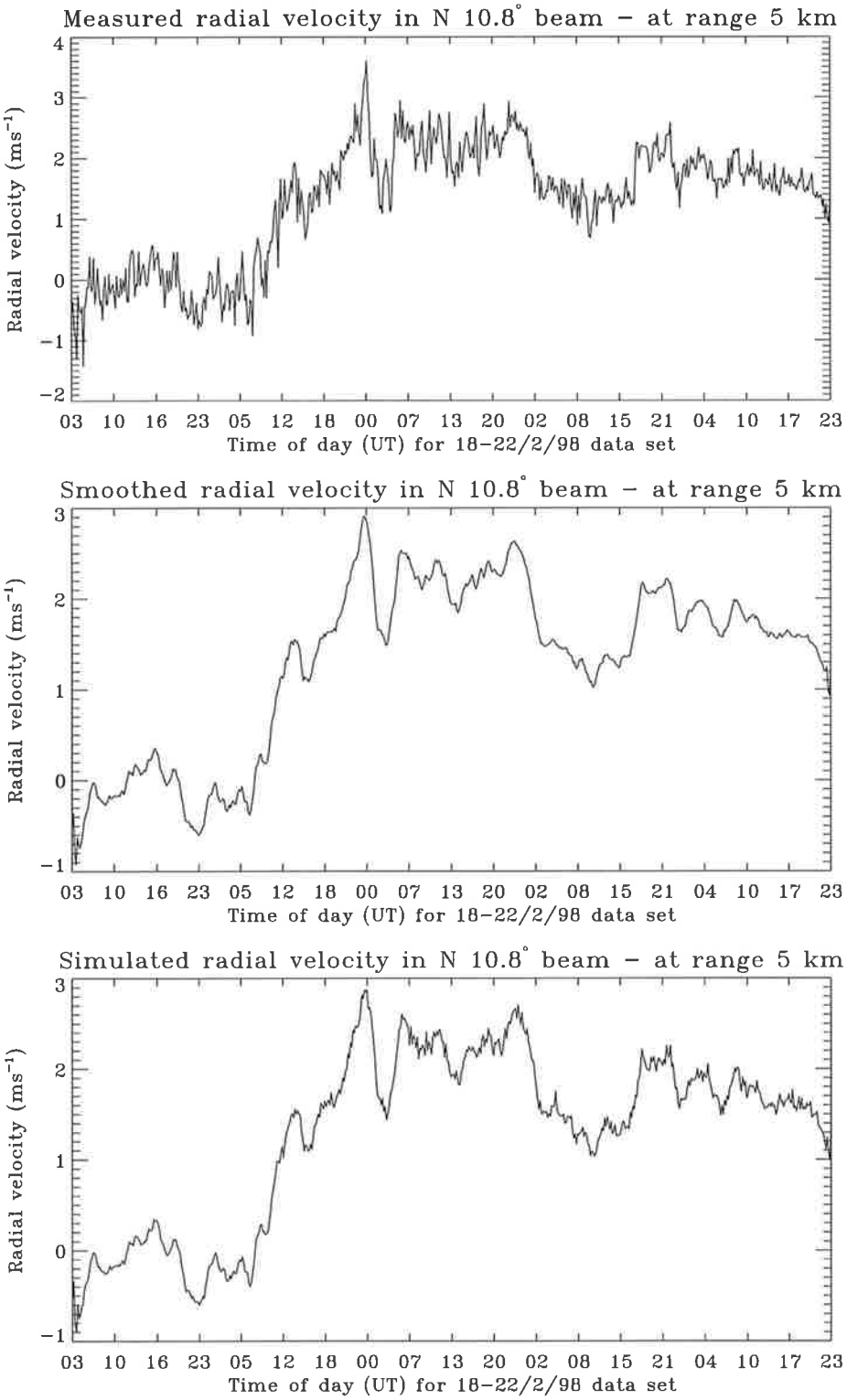

Figure 5.32: Measured, smoothed and simulated radial velocity for the 10.8° off-zenith north DBS beam, at a range of 5 *km*, for the 18-22/2/98 data set. Radial velocity data are shown at the minimum resolution possible for the 18-22/2/98 data set, of 12 minutes.

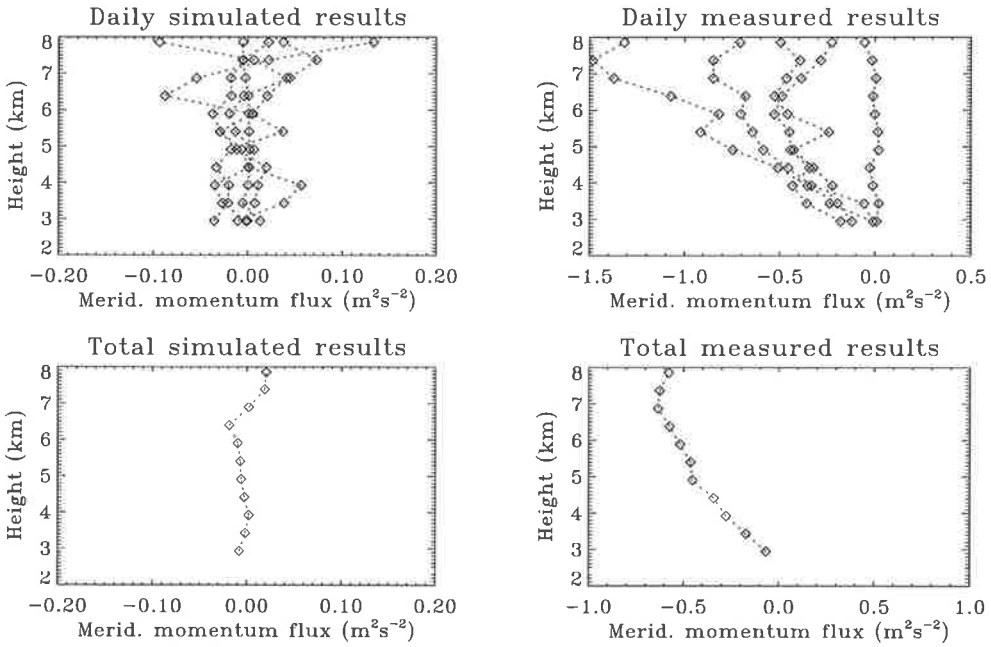

Figure 5.33: Simulated and measured meridional momentum flux for the individual days, and for the entire period of the 18-22/2/98 data set. Note that the x-axes of the plots in this figure are 5 times wider for the measured results than for the simulated results.

momentum flux is generally much smaller than the measured flux, as expected from the relative variation in the radial velocity time series used to calculate the fluxes, as shown in Figure 5.32.

In order to quantify the magnitude of the simulated momentum flux relative to the measured momentum flux, the ratio of simulated momentum flux to measured momentum flux was calculated for each of the averaging periods, at each height in the range from 3 - 8 km. This meant that for the six hour averaging period, there were 20 ratios calculated; four for each of the five days of the data set, for each range gate. For the 24 hour averaging period, there were five ratios, one for each of the five days of the data set, for each height. And for the total five day data set, one ratio at each height. In this manner, the magnitude of the induced spurious momentum flux as a fraction of the measured momentum flux could be calculated and expressed as a percentage. The median value of the ratio at each height was then calculated for the six and 24 hour averaging periods.

Table 5.3 shows the median of the ratios of simulated spurious flux to measured

Range (km)	Median % for 6 hour periods	Median % for 24 hour periods	% for full 5 day period
3.0	19.6	18.2	3.9
3.5	12.2	11.2	0.9
4.0	13.8	5.7	0.8
4.5	10.3	4.3	0.7
5.0	4.4	2.0	1.3
5.5	3.9	5.4	1.4
6.0	7.0	4.2	1.8
6.5	4.7	4.2	3.2
7.0	9.3	9.6	0.3
7.5	13.6	2.2	3.0
8.0	12.8	9.4	3.5

Table 5.3: Simulated meridional momentum flux as a percentage of measured meridional momentum flux, shown over the height range from 3 - 8 km for the 18-22/2/98 data set. For the 6 and 24 hour averaged fluxes, the results are shown as the median value over time for a given height.

flux over the number of periods of a given averaging scheme. So, for example, in the case of the six hour averaging period, the median at each height was calculated over the 20 ratio values at each height over the five day data set. The median was used in preference to the mean due to the highly variable nature of the ratios as a function of time. Table 5.3 shows that for the six hour and 24 hour averaging periods, the spurious momentum flux induced by the changing AOA in the pair of symmetrical off-zenith beams can amount to nearly 20% of the measured value at a given range. The results for the full 5 day data set, however, show that the ratio of the induced momentum flux to the measured momentum flux is very small, being in the range from 0.3 - 3.9%. It is likely, therefore, that the radial velocities in the two symmetric beams, over the five day period approach the required statistical homogeneity, as this range of values is small enough not be a significant problem for the flux measurements. *Murphy* [1990] has modelled the effect of varying pointing angles on momentum flux measurements. The results of *Murphy* [1990] showed that the percentageerror in the momentum flux was of the order of 3% at short periods. This figure is in good agreement with the value found for the percentage of the momentum flux induced by the varying AOA, for the full five day averaged data set discussed in this section. The results of the analysis

in this section suggest that averaging periods in excess of 24 hours should be used to calculate the momentum flux in the ST region, in order to minimise the effects of the varying AOA on momentum flux measurements.

5.8 Summary

In this chapter, results from two dual DBS/AOA experiments with the BP VHF ST radar are presented. The two experiments were run with different antenna configurations in order to fully utilise the flexibility of the system. In both experiments the atmosphere was seen to be aspect sensitive. The AOA values determined with a vertical beam were examined and found to be significantly larger than the minimum observable AOA due to instrumental effects in the system, as discussed in Chapter 2. The AOAs were also found to be comparable between the two different antenna configurations that were employed.

The DBS and AOA data was used to compare SNR differences as seen in symmetrical off-zenith beams, with AOAs as seen on a vertical beam. Independantly, measurements of SNR differences in symmetrical off-zenith beams and non-zero vertical beam AOAs have been attributed by various authors to the effects of tilted specular layers. The comparison of the SNR differences and AOAs presented in this chapter suggests that this is the case for 3.6° off-zenith beams, and that the SNR differences measured on 3.6° off-zenith beams, and the AOAs measured on vertical beams were both responding to the changing tilt of the specular layers. In contrast, the 10.8° off-zenith beam did not appear to be as affected by the tilted layers, evident in AOA measurements on the vertical beam, although there were times and ranges where there did appear to be a relationship between the two. The observed relationship for the 3.6° and 10.8° off-zenith SNR differences and vertical beam AOAs was the same for both of the data sets studied in this chapter.

Finally, AOAs in 3.6° and 10.8° off-zenith beams were examined. The distribution of the AOAs at the two different angles was seen to be quite different, in general agreement with the results from the off-zenith SNR and vertical AOA comparison. Momentum flux measurements are expected to be sensitive to any AOA differences in

pairs of symmetric off-zenith beams, and as such, their effect was quantified. It was found that the spurious momentum flux induced by changes in AOA at a given height, averaged over a 24 hour period can be up to 20% of the measured value at the same height, over the same time period. Averaging over the full five days of the data set reduced this value to 3%.

Chapter 6

Multiple-beam Doppler measurements

6.1 Introduction

In this chapter a study of the backscattered power as a function of off-zenith angle in two, five-day, multiple beam DBS data sets is presented. A simple parameterisation of the variation of power as a function of off-zenith angle is used to gain an understanding of the variation in the decrease of power with increasingly large off-zenith angle, and of the angles at which isotropic scatter occurs. In addition, θ_s, the $1/e$ half-width of the polar diagram of backscatter, is calculated directly from the off-zenith distribution of power and compared with the common DBS method of calculating θ_s, first used by *Hocking et al.* [1986]. This chapter begins with a discussion of the nature of the fall-off in backscattered power that has been observed by other researchers, before the results of the multiple off-zenith beam DBS experiments using the BP VHF ST radar are discussed.

6.2 Multiple-beam Doppler measurements

Attempts to parameterise and understand the angular distribution of backscattered power have generally focussed on the behaviour at small off-zenith angles, which are expected to be heavily influenced by aspect sensitivity. These attempts have resulted

in the θ_s parameterisation of *Hocking et al.* [1986], and as discussed in Chapter 4, there is now a reasonable data base of θ_s values by various authors, spanning various weather conditions, height ranges and experimental setups. However, knowledge of the behaviour of the backscattered power at larger off-zenith angles, and identification of the isotropic scattering level is limited to a handful of studies.

The first high angular resolution measurements of backscattered radar power in the ST region as a function of off-zenith beam angle were made by *Röttger et al.* [1981]. The results from this experiment clearly showed the effects of aspect sensitivity, thereby confirming earlier observations made by *Gage & Green* [1978] and *Röttger & Liu* [1978] with wide antenna beams, and a limited number of off-zenith angles. This first experiment of *Röttger et al.* [1981] utilised beams at eight angles in a single azimuth from 0.0° to 11.9°, at intervals of 1.7°. Measurements were made over two short periods, roughly 3 hours each, on two separate days. Later measurements over one hour and twenty minutes, with the same angles and angular interval as the work of *Röttger et al.* [1981] were made by *Waterman et al.* [1985]. The data of *Tsuda et al.* [1986] consisting of measurements at eight angles in a single azimuth between 0° and 10° in 2° steps, were collected in two short experiments, on two separate days, lasting 4.5 and 8 hours each.

Until recently, these three short experiments formed the basis of the knowledge about the backscattered power as a function off-zenith angle at high angular resolution. The fall-off in power observed in the three experiments showed a sharp decrease in power between 0° and about 4° and 6°, with a more shallow decrease to the extent of the measurements, which for these three studies was always less than 12°. The levelling off of the power as a function of off-zenith angle at angles of roughly 8° to 10° seen in these three experiments has been interpreted as being due to isotropic backscatter at these angles.

However, recent studies using more data and a larger range of off-zenith angles have revealed that the assumption that angles at roughly 10° are at the isotropic scattering level may be incorrect. The work of *Hocking et al.* [1990] used off-zenith angles between 0° and 20° in 4° steps, with the addition of a 28° off-zenith beam. The data were collected over a period of 12 hours. The work of *Tsuda et al.* [1997a] utilised

15 angles in a single azimuth in the range from 0° to 28° in 2° steps, over 25 hours. An example of the angular distribution of backscattered power from the work of *Tsuda et al.* [1997a] is shown in Figure 1.2 of Chapter 1. Finally, the work of *Jain et al.* [1997] employed 11 angles in a given azimuth in the range from 0° to 20° in 2° steps, over four-hour data sets collected on four separate days. The results of all of these studies show that the backscattered power generally continues to decrease at off-zenith angles larger than 10°, and the work of *Tsuda et al.* [1997a] in particular has shown that truly isotropic scatter occurs only at angles larger than approximately 18° off-zenith, as shown in Figure 1.2 of this thesis. That is, that the isotropic scattering level, the constant power level where the backscatter is independant of off-zenith angle, begins at approximately 18° off-zenith.

Another point of interest in the studies discussed here is that only the work of *Jain et al.* [1997] contains data from all four cardinal pointing directions. The main aim of the experiment discussed in this chapter was therefore to use the BP ST radar to measure the off-zenith backscatter over a large range of angles, in all four cardinal directions, over a number of days in order to parameterise and quantify the variation in the decrease of power as a function of off-zenith angle, and identify the isotropic scattering level. Another aim of the experiment was to perform a direct comparison of the measured $1/e$ width of the angular distribution of backscatter, and θ_s values using the *Hocking et al.* [1986] DBS method. This work in this chapter therefore uses the angular distribution of backscattered power to examine two important physical parameters; the width of the polar diagram of backscatter at small off-zenith angles, and the isotropic scattering level at large off-zenith angles.

6.3 Experiment description

The data in this chapter were collected in two periods, from 24-28/12/97 and 21-26/1/98, at 0.0° on both the North-South and East-West arrays, and at off-zenith angles of 3.6°, 7.2°, 10.8°, 14.5°, 18.2° and 22.0° to the north, south, east and west. The data were collected using the normal DBS mode utilising the whole North-South or East-West CoCo arrays combined, and a single receiver. Table 6.1 shows the data

Collection parameter	Parameter Value
PRF (Hz)	4096
No. coherent integrations	256
Time for one data set (seconds)	28.13
No. of data points	450
Velocity resolution (ms^{-1})	0.10
Max. unaliased velocity (ms^{-1})	22.2
Height range (km)	2.0 - 15.0
Range gate (km)	0.5
Pulse length (km)	1.0

Table 6.1: Data collection parameters for the multi beam data sets, from 24-28/12/97 and 21-26/1/98.

collection parameters, while Figure 6.1 shows the beam positions and beam sequence of the two identical data sets. Note from Table 6.1 that an individual data set took approximately 28.13 seconds to collect. The data collection regime was to actually collect 56.25 seconds of data in a given direction, and then split the time series into two 28.125 second time series which were Fourier transformed into two spectra, which were then averaged together. The averaging of successive spectra results in greater definition of the atmospheric peaks in the spectra, as mentioned in Chapter 3. This process makes the process of fitting Gaussian functions less likely to fail for low SNR data. As for the DBS data in the rest of this thesis, the data discussed in this chapter were quality controlled using the algorithms discussed in Chapter 3, over the height range from 3 - 8 km.

From Figure 6.1 it can be seen that there are three times as many vertical beam data sets as off-zenith data sets. This sequence was adopted for two reasons. Firstly, because it resulted in the entire beam sequence lasting 30 minutes instead of 26, which made data averaging into an integral number of hours easier to manage. Secondly, collecting a greater number of vertical beam data sets resulted in more reliable estimates of the vertical beam power, which was important for the analysis in this chapter, as the vertical beam dominates the angular distribution in given azimuth, and as such, any parameterisation of the angular distribution of power is very sensitive to the value of the power at 0°.

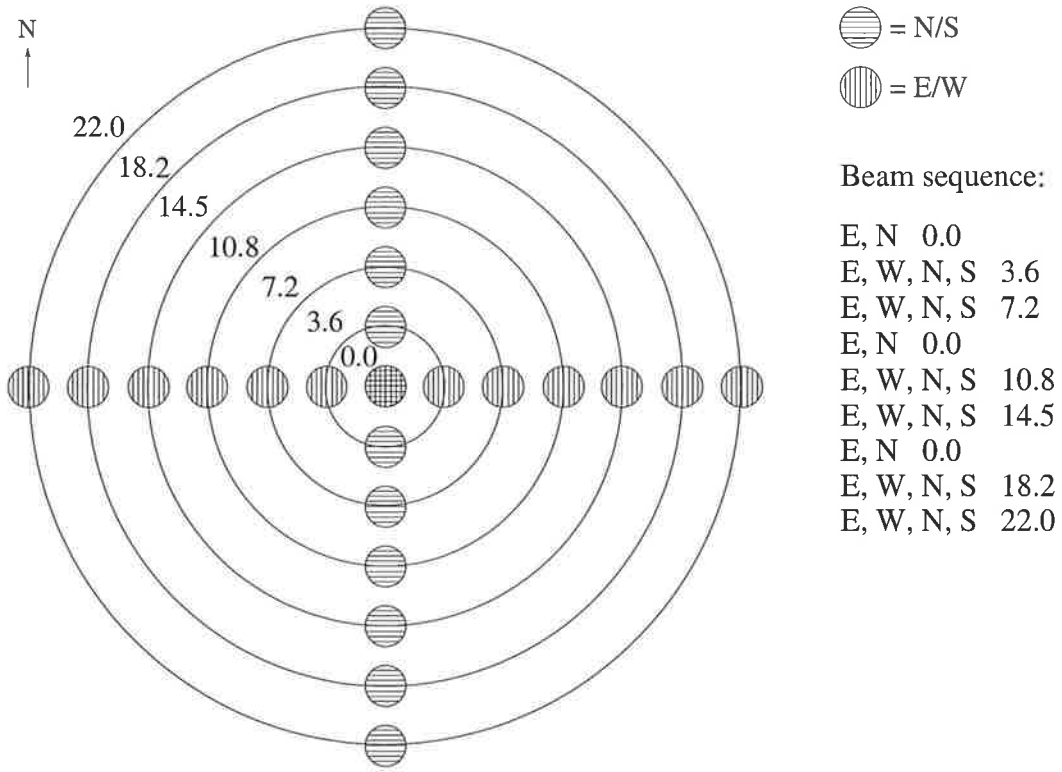

Figure 6.1: Beam sequence and direction for the two multi-beam DBS experiments run over the periods 24-28/12/97 and 21-26/1/98.

6.4 Off-zenith SNR distribution and parameterisation

Because of the relatively large time between two data sets in the same direction, all of the analyses in this chapter were performed on 12 hour averaged data, where the averages were calculated from 00 UT to 12 UT, and 12 UT to 00 UT on a given day. At the 30 minute resolution of the data sets, this resulted in a given point in an averaged angular distribution of power being averaged over 24 data sets in the relevant direction. The 24-28/12/97 data set was exactly five days long, resulting in 10 average angular power profiles, while the 21-26/1/98 data set was five and a half days long, resulting in 11 average angular power profiles. In addition, the SNR at a given off-zenith angle was converted from range to height, using a simple straight line interpolation, and corrected for the effects of the reduction in antenna area for large off-zenith angles, by multiplying the linear SNR at a given off-zenith angle θ by $1/cos^2\theta$ (*Tsuda et al.* [1997a].

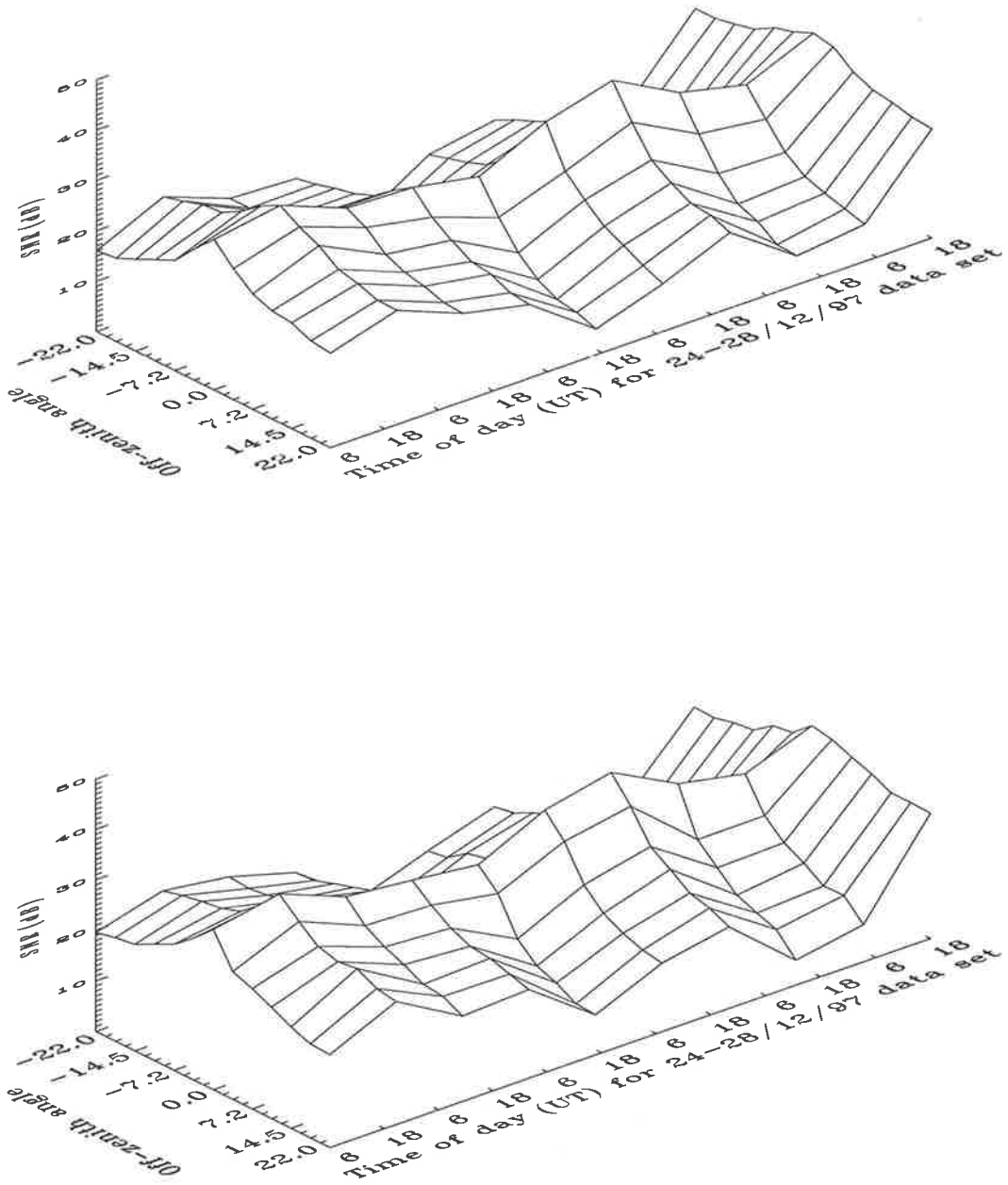

Figure 6.2: 12 hour averaged SNR as a function of off-zenith angle for the 24-28/12/97 data set, at a height of 5 *km*. The top plot shows the SNR for all zonal off-zenith angles, from 22.0° to the east, shown as negative angles, to 22.0° to the west, shown as positive angles. The bottom plot shows the SNR for all meridional off-zenith angles, from 22.0° to the north, shown as negative angles, to 22.0° to the south, shown as positive angles.

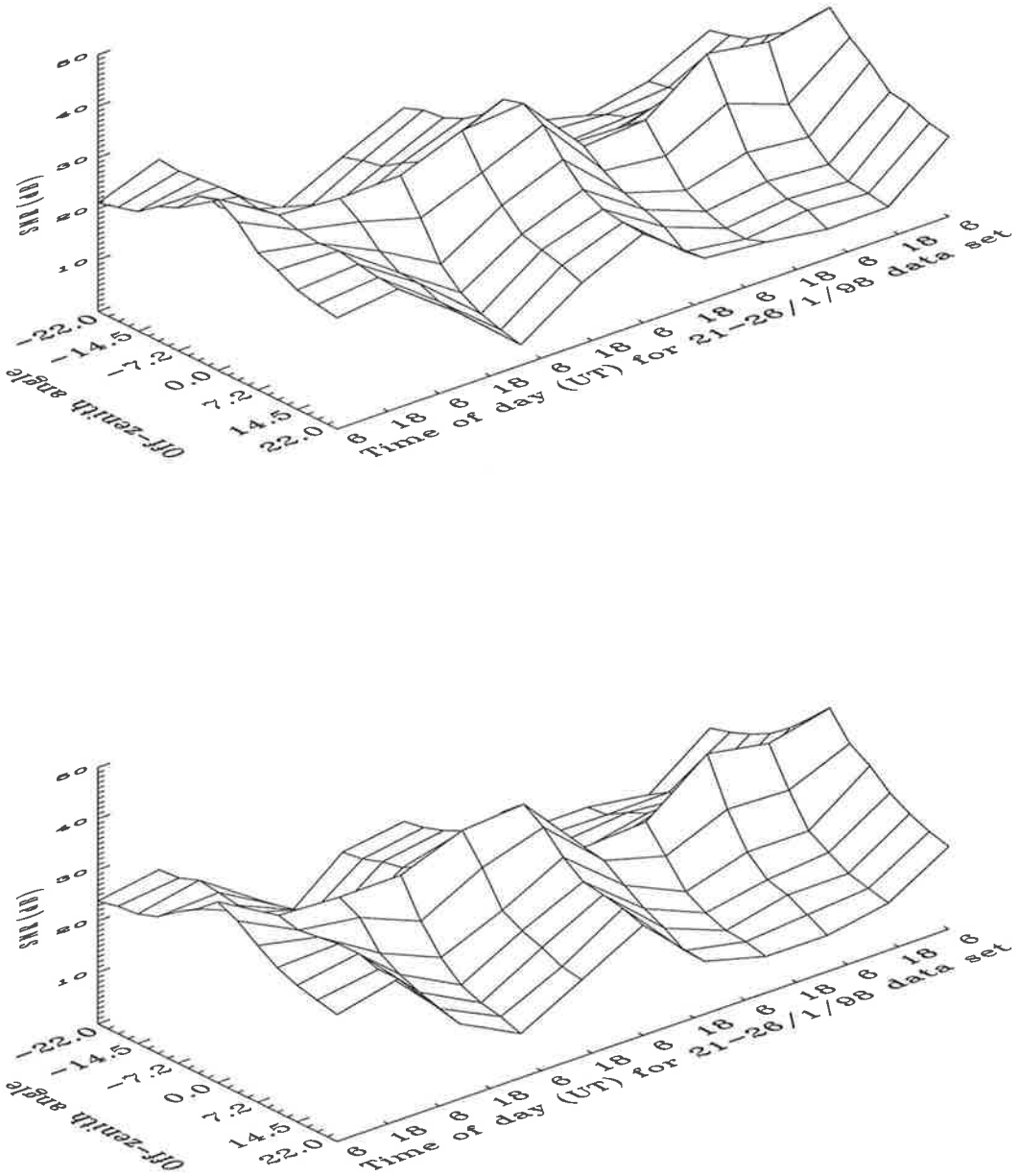

Figure 6.3: 12 hour averaged SNR as a function of off-zenith angle for the 21-26/1/98 data set, at a height of 5 *km*. The top plot shows the SNR for all zonal off-zenith angles, from 22.0° to the east, shown as negative angles, to 22.0° to the west, shown as positive angles. The bottom plot shows the SNR for all meridional off-zenith angles, from 22.0° to the north, shown as negative angles, to 22.0° to the south, shown as positive angles.

Figure 6.2 and Figure 6.3 show surface plots of the 12 hour averaged SNR (in dB) as a function of off-zenith angle for the 24-28/12/97 and 21-26/1/98 data sets respectively, at a height of 5 km. The top plot in each of Figure 6.2 and Figure 6.3 shows the zonal SNR, and the bottom plot in each figure shows the meridional SNR. The time axes in these plots shows labels corresponding to the middle of each 12 hour average. It can be seen from these two plots that there is considerable variation in the angular distribution of power as a function of time and off-zenith angle. Another striking feature of these two figures is the symmetry about 0.0° in both the zonal and meridional direction, and the almost equivalent variation as a function of off-zenith angle in the zonal and meridional directions. This behaviour implies that the scattering structures giving rise to the enhanced backscattered power in the vertical direction and at small off-zenith angles is coherent and the essentially the same in all azimuths.

In order to quantify the observations shown in Figure 6.2 and Figure 6.3 it is useful to identify a parameter that provides some information on the relationship between the power at a given number of off-zenith angles. One important parameter is the slope of the SNR between various off-zenith angles, in $dB/degree$. As noted in the introduction to this chapter, other authors have noted that the decrease of power as a function of off-zenith angle depends on the off-zenith angle at which measurements are made, with larger decreases for small off-zenith angles, and relatively smaller decreases for large off-zenith angles. As such, a piece-wise linear parameterisation is introduced here, where linear fits to the power angular distribution of SNR are made over four angle ranges, from 0.0° to 7.2°, 7.2° to 14.5°, 10.8° to 18.2°, and 14.5° to 22.0°.

Figure 6.4 shows the angular distribution of SNR at a height of 5 km for six of the ten 12 hour average profiles in the 24-28/12/97 data set, for both the zonal and meridional direction. Each plot in Figure 6.4 is shown over the same range of SNR. The error bars in this plot show the standard deviation of the SNR at a given angle for the 12 hour average, and as such represent the variability of the power over the averaging time. Also shown in Figure 6.4 are the piece-wise linear fits to the data between the angles from 0.0° to 7.2°, 7.2° to 14.5°, and 14.5° to 22.0°. The linear fits from 10.8° to 18.2° are omitted for clarity. It can be seen from Figure 6.4 that the

linear fits are a very good parameterisation of the off-zenith behaviour. The thick lines which show the linear fits almost always lie exactly on top of the thin line joining the data points at various angles. It can also be seen that a simple linear fit to the entire range of angles from 0.0° to 22.0° off-zenith at a given azimuth would not be as good. It is the piece-wise nature of the fitting that makes the parameterisation successful. It should be noted that *Hocking et al.* [1990] observed that the fall-off in power in their data between 0° and 8° was often closer to exponential in linear units, or linear in dB, rather than Gaussian in linear units, or parabolic in dB which is assumed by the θ_s parameterisation used in that work. The fact that the linear parameterisation (in dB) is successful between 0.0° and 7.2°, as seen in Figure 6.4 shows that off-zenith behaviour seen here is similar to that seen by *Hocking et al.* [1990].

Figure 6.5 shows the zonal and meridional angular distribution of SNR at the same height as Figure 6.4, but for six of the eleven 12 hour average profiles in the 21-26/1/98 data set. As for Figure 6.4 the data in Figure 6.5 are shown with error bars representing the standard deviations of the 12 hour average values, and all of the piece-wise linear fits, except for the fit from 10.8° to 18.2°. Figure 6.6 shows the same parameters at a height of 3 km for the 24-28/12/97 data set, while Figure 6.7 shows the same parameters at a height of 7 km for the 21-26/1/98 data set. Note that the range of SNR in these latter two plots is different from the range in the former, due to the differences in SNR at the different heights. However, the range of SNR in all four figures showing the angular distribution of SNR is 40 dB so that they can all be easily intercompared. It can be seen from this large number of profiles, that as a function of time, height, and data set, the piece-wise linear parameterisation of power over three adjacent points is a good estimate of the behaviour of the SNR over all relevant angles. It can also be seen that in most of the plots in these figures, the SNR at 0.0° and 3.6° is significantly enhanced relative to the power at all other off-zenith angles, and that the behaviour as a function of off-zenith angle is very similar to that seen by *Tsuda et al.* [1997a], as shown in Figure 1.2.

Given this fact, the behaviour of the various slopes can be investigated. Figure 6.8 shows the slopes from 0.0° to 7.2° for each of the ten 12 hour averages of the 24-28/12/97 data set, for each azimuth, for selected heights in the range from 3 - 8 km.

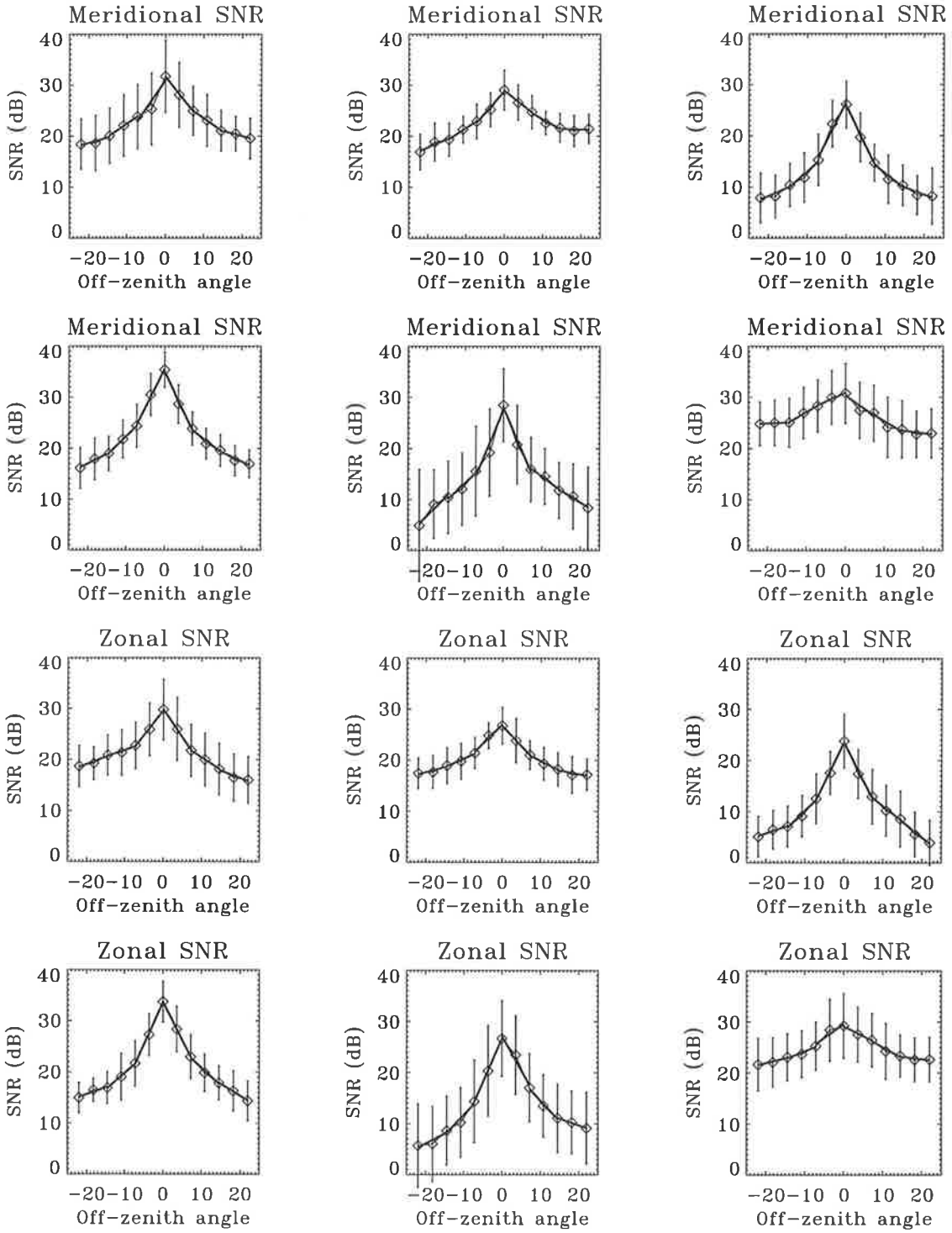

Figure 6.4: 12 hour averaged SNR as a function of off-zenith angle at a height of 5 km, shown for six of the 10 time averages of the 24-28/12/97 data set. The top six plots show the SNR for all meridional off-zenith angles, and the bottom six plots show the SNR for all zonal off-zenith angles, for the same times. Over-plotted on these off-zenith distributions are error bars showing the standard deviations of the averaged SNR, and the piece-wise linear fits over the angles from 0.0° to 7.2°, 7.2° to 14.5°, and 14.5° to 22.0°.

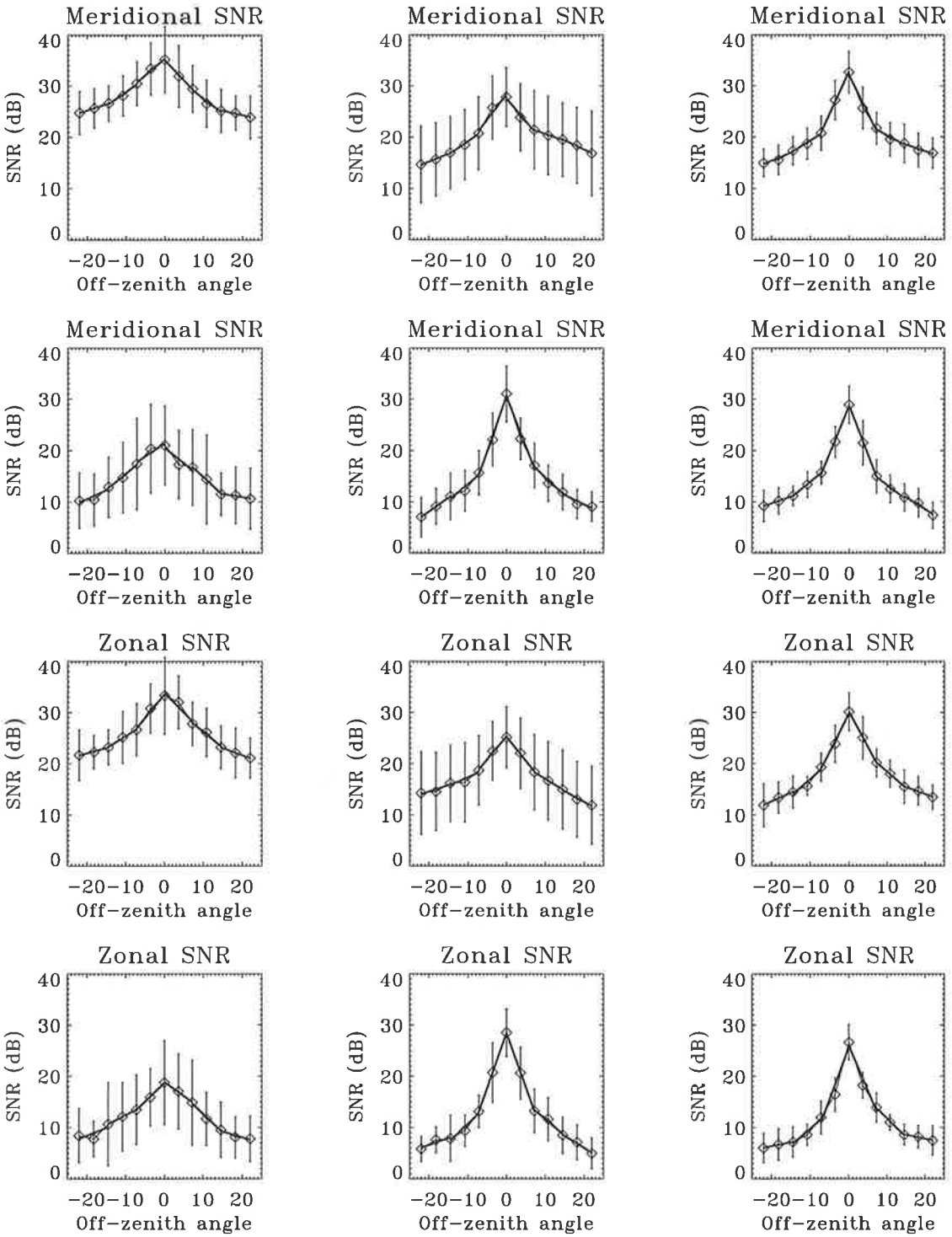

Figure 6.5: 12 hour averaged SNR as a function of off-zenith angle at a height of 5 km, shown for six of the 11 time averages of the 21-26/1/98 data set. The top six plots show the SNR for all meridional off-zenith angles, and the bottom six plots show the SNR for all zonal off-zenith angles, for the same times. Over-plotted on these off-zenith distributions are error bars showing the standard deviations of the averaged SNR, and the piece-wise linear fits over the angles from 0.0° to 7.2°, 7.2° to 14.5°, and 14.5° to 22.0°.

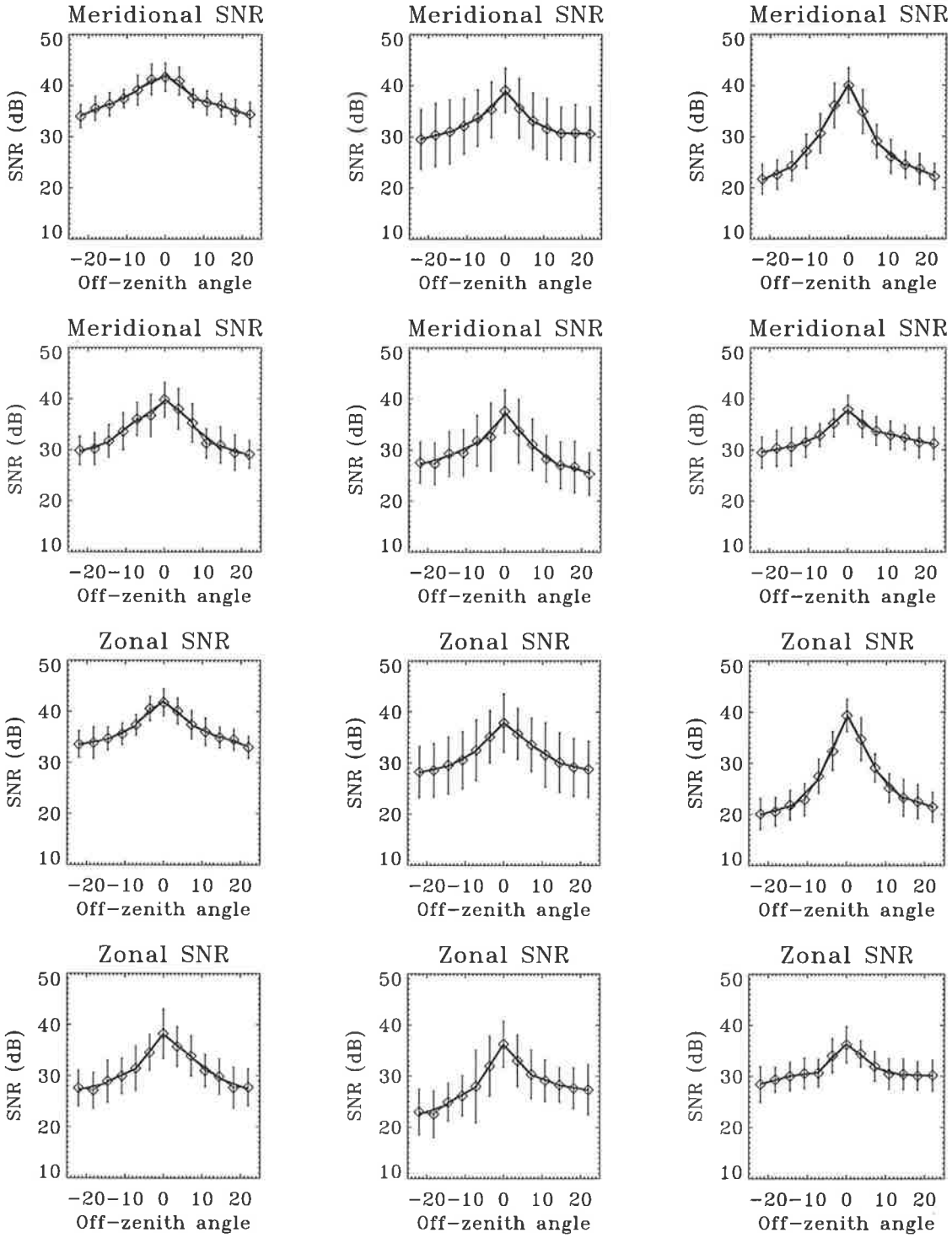

Figure 6.6: 12 hour averaged SNR as a function of off-zenith angle at a height of 3 *km*, shown for six of the 10 time averages of the 24-28/12/97 data set. The top six plots show the SNR for all meridional off-zenith angles, and the bottom six plots show the SNR for all zonal off-zenith angles, for the same times. Over-plotted on these off-zenith distributions are error bars showing the standard deviations of the averaged SNR, and the piece-wise linear fits over the angles from 0.0° to 7.2°, 7.2° to 14.5°, and 14.5° to 22.0°.

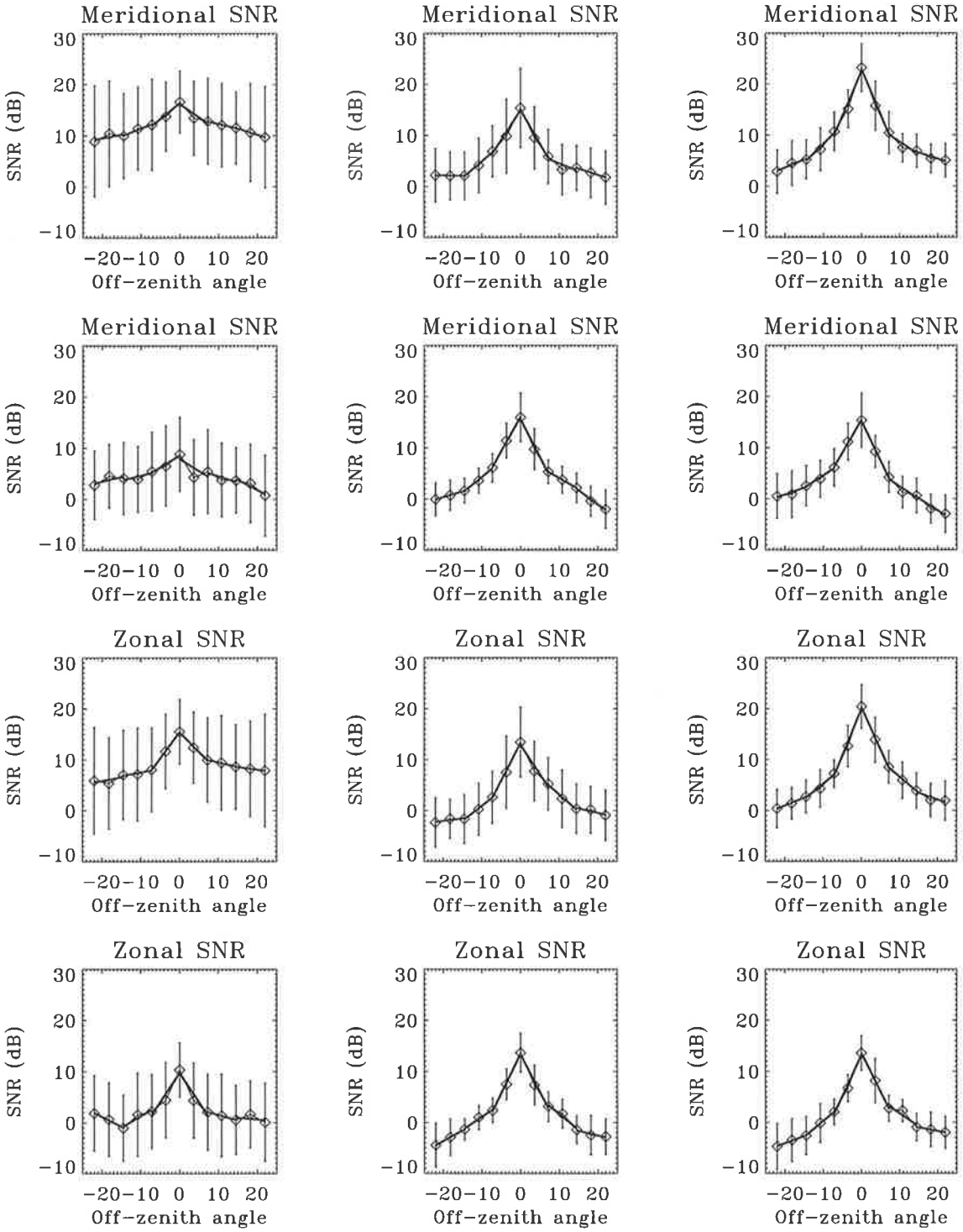

Figure 6.7: 12 hour averaged SNR as a function of off-zenith angle at a height of 7 km, shown for six of the 11 time averages of the 21-26/1/98 data set. The top six plots show the SNR for all meridional off-zenith angles, and the bottom six plots show the SNR for all zonal off-zenith angles, for the same times. Over-plotted on these off-zenith distributions are error bars showing the standard deviations of the averaged SNR, and the piece-wise linear fits over the angles from 0.0° to 7.2°, 7.2° to 14.5°, and 14.5° to 22.0°.

Off-zenith angle range	mean	stan. dev.	range
0.0 - 7.2	-1.2	0.4	-0.1 → -2.2
7.2 - 14.5	-0.5	0.2	-0.02 → -1.1
10.8 - 18.2	-0.3	0.1	0.04 → -0.8
14.5 - 22.0	-0.2	0.1	0.04 → -0.7

Table 6.2: Linear fit slope characteristics for the 24-28/12/97 data set. All analysis was done for the zonal and meridional azimuths combined, over the height range 3 - 8 km. All parameters are in units of degrees/

Note that the slopes for all azimuths in this figure and in the three figures that follow are expressed as negative values, thereby showing the slope power decreasing from small off-zenith angles to larger off-zenith angles, rather than increasing from larger off-zenith angles to small off-zenith angles.

The error bars in Figure 6.8 are the uncertainties in the estimate of the slope, returned by the fitting procedure. They are one standard deviation (or 1σ) errors in the fit. Figure 6.9 shows the slopes from 7.2° to 14.5°, Figure 6.10 shows the slopes from 10.8° to 18.2° and Figure 6.11 shows the slopes from 14.5° to 22.0°, all from the 24-28/12/97 data set, for the same heights as for Figure 6.8. The behaviour as a function of time, particularly for the slopes from 0.0° to 7.2° can be seen to reflect the behaviour of the SNR shown in Figure 6.2, as expected. Table 6.2 shows the mean, standard deviations, maximum and minimum slopes over the height range from 3 - 8 km, over all 12 hour averages of the 24-28/12/97 data set. The corresponding plots and figures for the 21-26/1/98 data set are not shown, although the numbers are very similar for the two data sets. Note that the y-axes in Figure 6.8 to Figure 6.11 are not necessarily the same, as they were chosen in order to best display the various ranges of the data.

A striking difference between the slopes as a function of time from 0.0° to 7.2° and the slopes at the other three ranges of angles, is that there is a high degree of similarity between the 0.0° to 7.2° slopes at the various azimuths compared to the similarity observed between the slopes at various azimuths for the other ranges of angles. It can be seen that this should be the case given the symmetry about the vertical direction of most of the angular power plots in Figure 6.4 to Figure 6.7. This

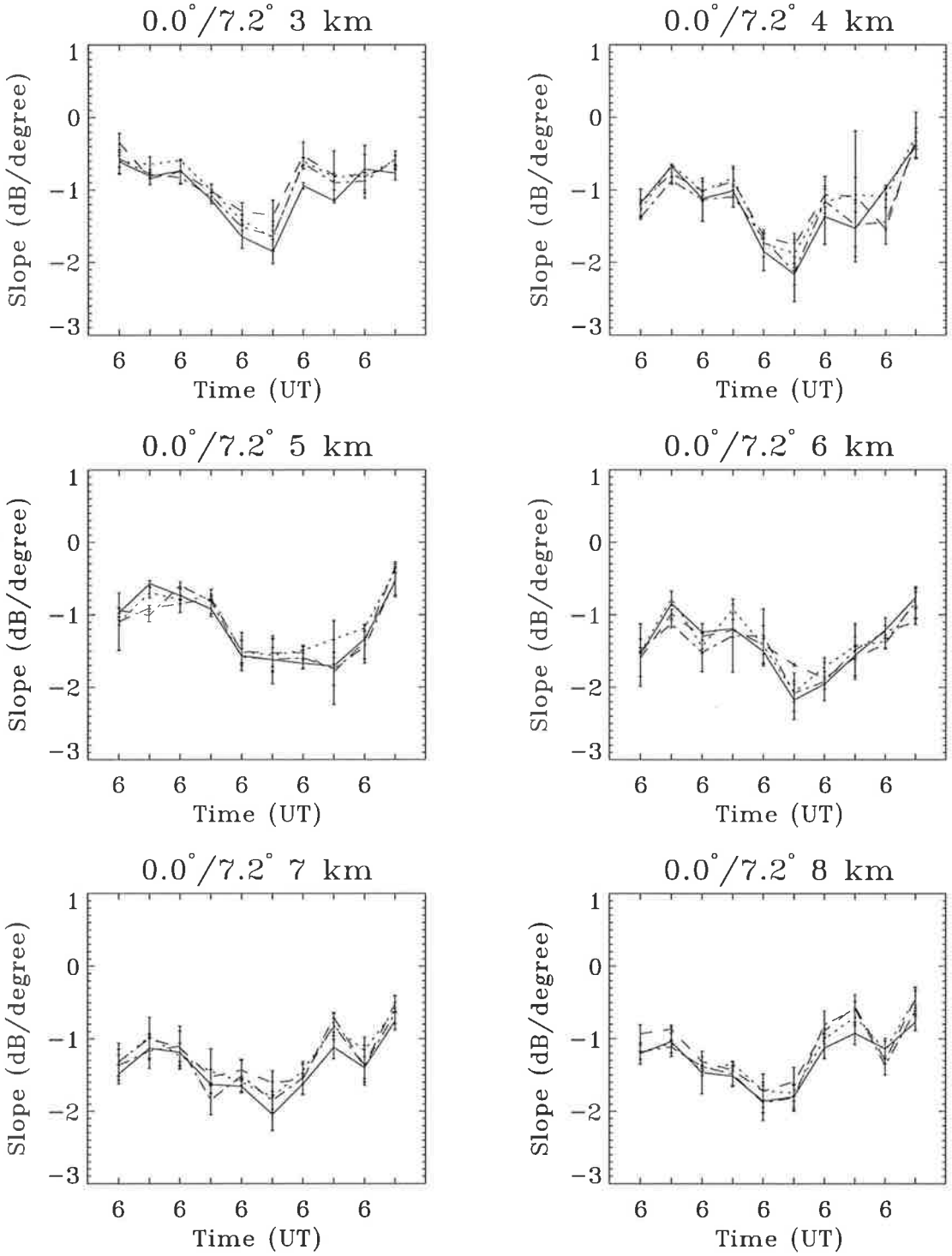

Figure 6.8: Time series of the slopes fitted to the 12 hour averaged SNR as a function of off-zenith angle, between the off-zenith angles of 0.0° and 7.2° for all azimuths, for the 24-28/12/92 data set. The solid line shows the eastern azimuth data, dotted line shows the western azimuth data, dashed line shows the northern azimuth data, and dash-dot line shows the southern azimuth data.

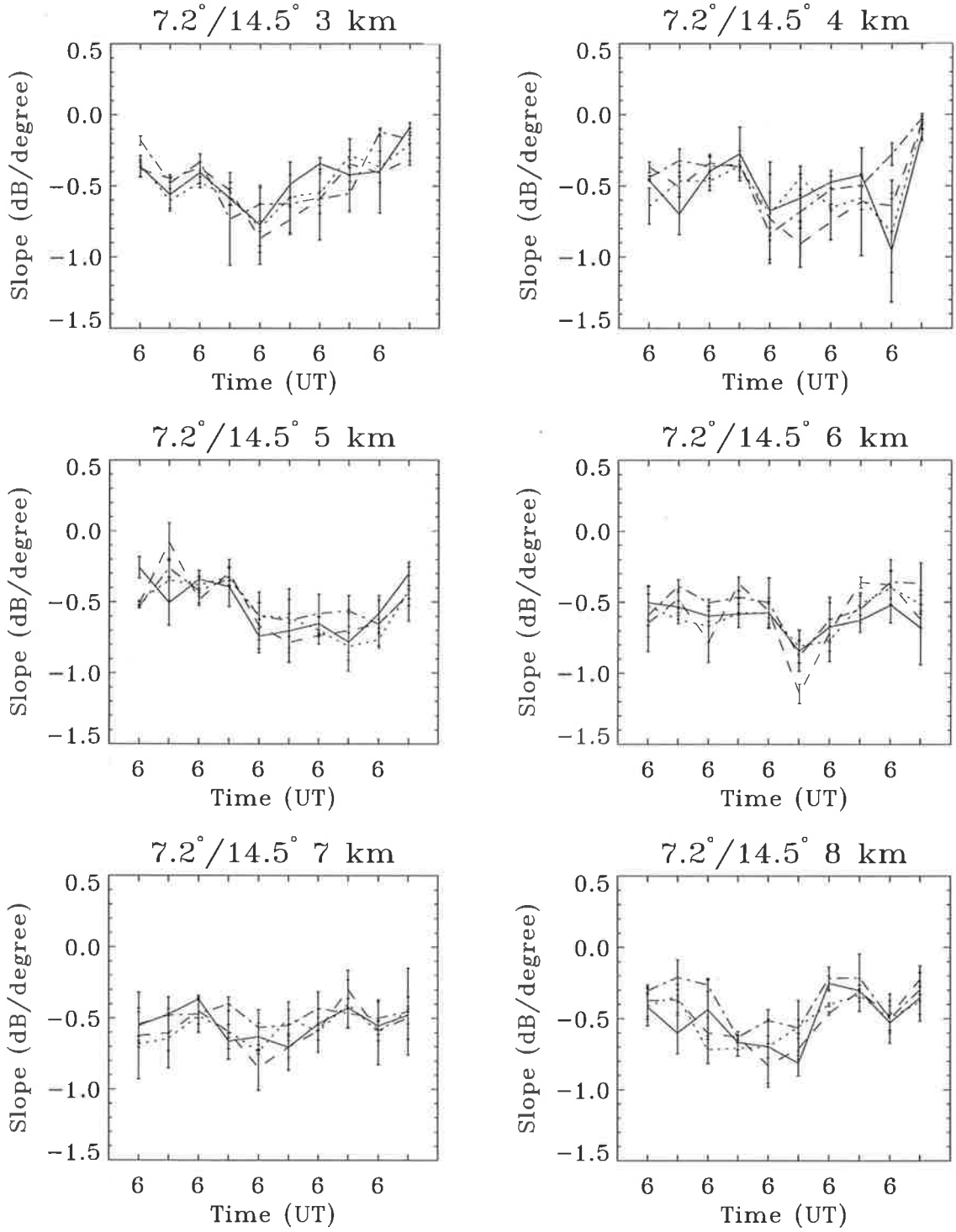

Figure 6.9: Time series of the slopes fitted to the 12 hour averaged SNR as a function of off-zenith angle between the off-zenith angles of 7.2° and 14.5° for all azimuths, for the 24-28/12/92 data set. The solid line shows the eastern azimuth data, dotted line shows the western azimuth data, dashed line shows the northern azimuth data, and dash-dot line shows the southern azimuth data.

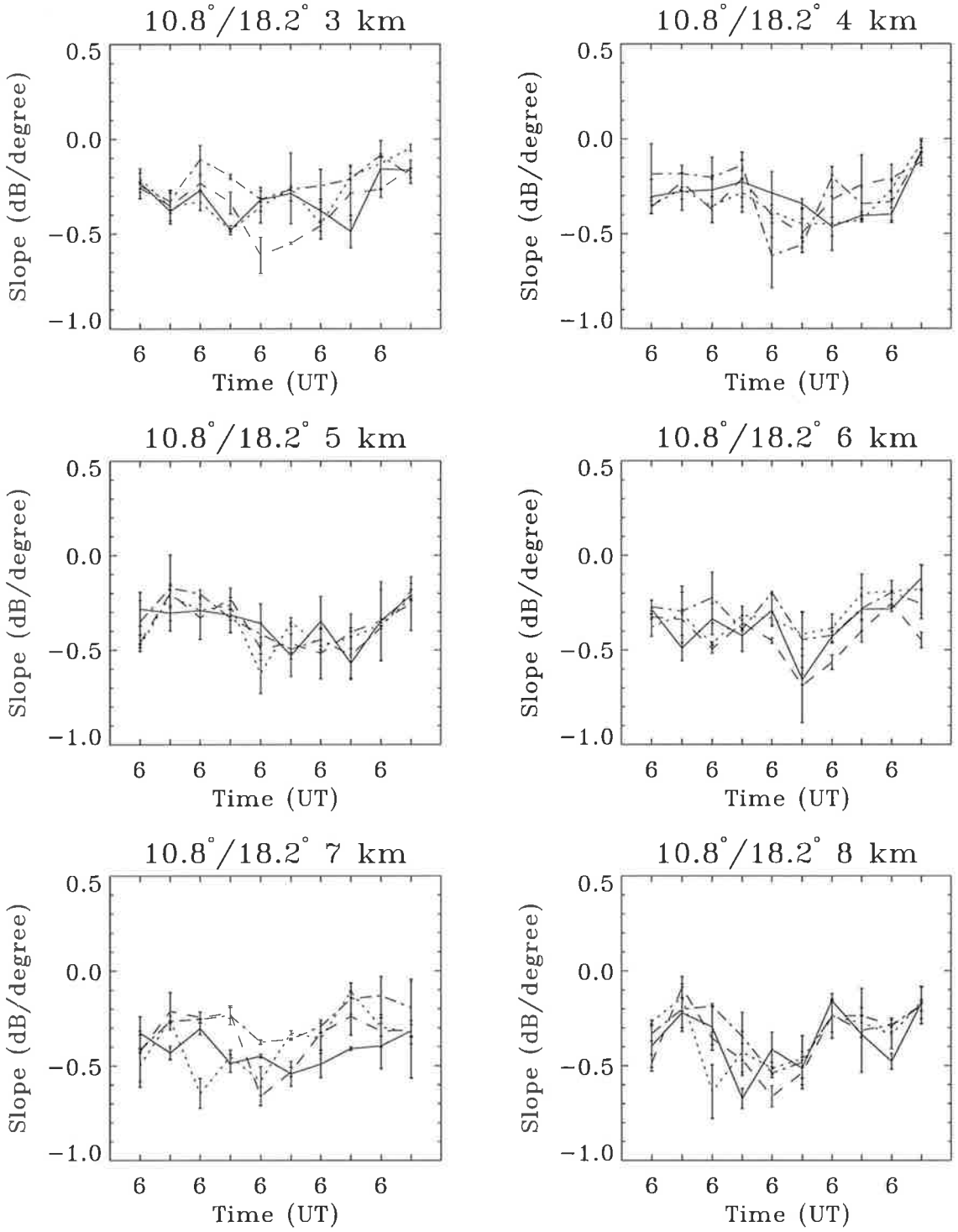

Figure 6.10: Time series of the slopes fitted to the 12 hour averaged SNR as a function of off-zenith angle between the off-zenith angles of 10.8° and 18.2° for all azimuths, for the 24-28/12/92 data set. The solid line shows the eastern azimuth data, dotted line shows the western azimuth data, dashed line shows the northern azimuth data, and dash-dot line shows the southern azimuth data.

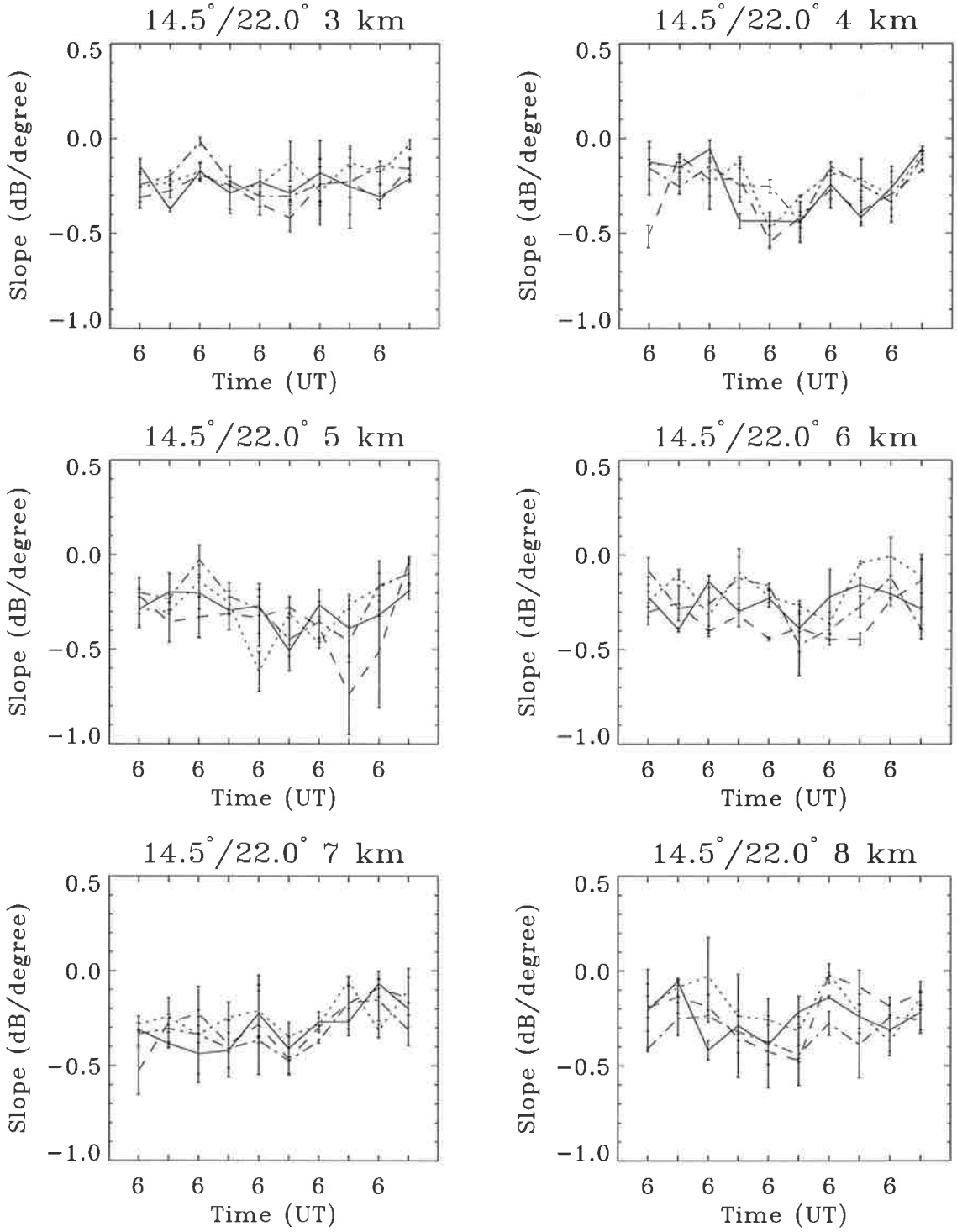

Figure 6.11: Time series of the slopes fitted to the 12 hour averaged SNR as a function of off-zenith angle between the off-zenith angles of 14.5° and 22.0° for all azimuths, for the 24-28/12/92 data set. The solid line shows the eastern azimuth data, dotted line shows the western azimuth data, dashed line shows the northern azimuth data, and dash-dot line shows the southern azimuth data.

fact suggests that the aspect sensitivity is largely independant of azimuth angle, at least over the 12 hour time averages used in this data analysis, and that the aspect sensitive scatterers at small off-zenith angles are coherent in all azimuths at a given off-zenith angle. Given that the degree of aspect sensitivity has been seen to be due to the prevailing weather conditions in studies of θ_s, such as those by *Yoe et al.* [1994] and *Hooper & Thomas* [1995], the day-to-day variability in the slopes shown in Figure 6.8 and the SNR surfaces in Figure 6.2 is probably due to the weather conditions during the data sets. However, rather than pursuing this line of enquiry, the different behaviour as a function of off-zenith angle will be studied further. As such, the large day-to-day variability in the slopes will serve to generalise the results which follow, as the results are not specific to any particular value of the slopes, and by inference, any particular prevailing weather conditions.

If the aspect sensitivity at small off-zenith angles is caused by specular layers, as the work in Chapter 5 suggests, then it makes sense that the scatter is symmetric about the zenith for small off-zenith beam directions. This is because, on small time scales, the scatter at a range of azimuths at a given small off-zenith angle is from the same scattering structures. Over a time average, the small differences between the same layers seen in symmetric off-zenith beams should average out, leaving essentially the same scattering power in all azimuths at a given aspect sensitive off-zenith angle. In the previous chapter it was seen that differences in SNR between symmetric off-zenith beams, at the small, aspect sensitive, off-zenith angle of 3.6° are related to changes in the angle of arrival, and are therefore suggestive of tilted layers affecting the off-zenith beams. In addition, *Tsuda et al.* [1997b] has shown that differences in the SNR at a fixed off-zenith angle in the aspect sensitive range (6°), for a range of azimuths, seem to be related to the effects of gravity waves perturbing layers in refractive index. However, any differences in power as a function of azimuth between a given pair of symmetric off-zenith beams are expected to be insignificant for the 12 hour averages used in this analysis. As such, it is expected that the angular distribution of power should be symmetric about the vertical in a given plane, for aspect sensitive angles. If this is the case, then scatter at larger, less aspect-sensitive angles should be increasingly less similar over the range of azimuths, as random isotropic scatter begins to dominate.

In the case of true isotropic scatter, there should be no correspondence between the scatter in the various azimuths at a fixed off-zenith angle as the scattering power in each beam is expected to be determined by the random filling of the beam volume by isotropic turbulence, and is independant of the off-zenith beam angle. Essentially the scatter in large off-zenith beams at various azimuths is from different, isotropic scattering structures, while the scatter at small, aspect sensitive off-zenith angles is from the same coherent structures.

When comparing Figure 6.8 with Figure 6.9, Figure 6.10, and Figure 6.11 it can be seen that at successively larger off-zenith angle ranges, there is less similarity between the scatter in the various azimuths. In order to quantify this fact, Figure 6.12 shows scatter plots of the zonal and meridional slopes from 0.0° to 7.2°, and from 7.2° to 14.5°, while Figure 6.13 shows scatter plots of the zonal and meridional slopes from 10.8° to 18.2°, and from 14.5° to 22.0°, all for the height range from 3 - 8 km for the 24-28/12/97 data set. The results for the 21-26/1/98 data set, not shown, look very similar. An error bar is shown in each of the scatter plots which corresponds to the average error in the fit over all of the slopes in the plot. The size of the error bar relative to the extent of the scatter shows that the variation in the scatter in each plot is significant. Note that the x and y axes in Figure 6.12 and Figure 6.13 are not necessarily the same, as they were chosen to best suit the various ranges of the data.

It can be seen from Figure 6.12 that, as expected, the correlation between the slopes of the scatter in pairs of azimuths in a given plane is very good in the off-zenith angle range from 0.0° to 7.2°. It can also be seen that there is a definite correlation between the slopes of the scatter in pairs of azimuths in a given plane in the off-zenith angle range from 7.2° to 14.5°, which suggests that aspect sensitive structures are influencing the scatter in this angle range. The top two plots in Figure 6.13 show that there is still a degree of correlation between the slopes of the scatter in the range of relatively large off-zenith angles from 10.8° to 18.2°. Despite the increased width of the scatter in these two plots relative to the plots in Figure 6.12 for the angle range from 0.0° to 7.2°, there is a definite slope of the 10.8° to 18.2° off-zenith scatter in the $y = x$ direction, indicating a degree of correlation between the behaviour in the pairs of azimuths in a given plane. The bottom two plots in Figure 6.13 show that there

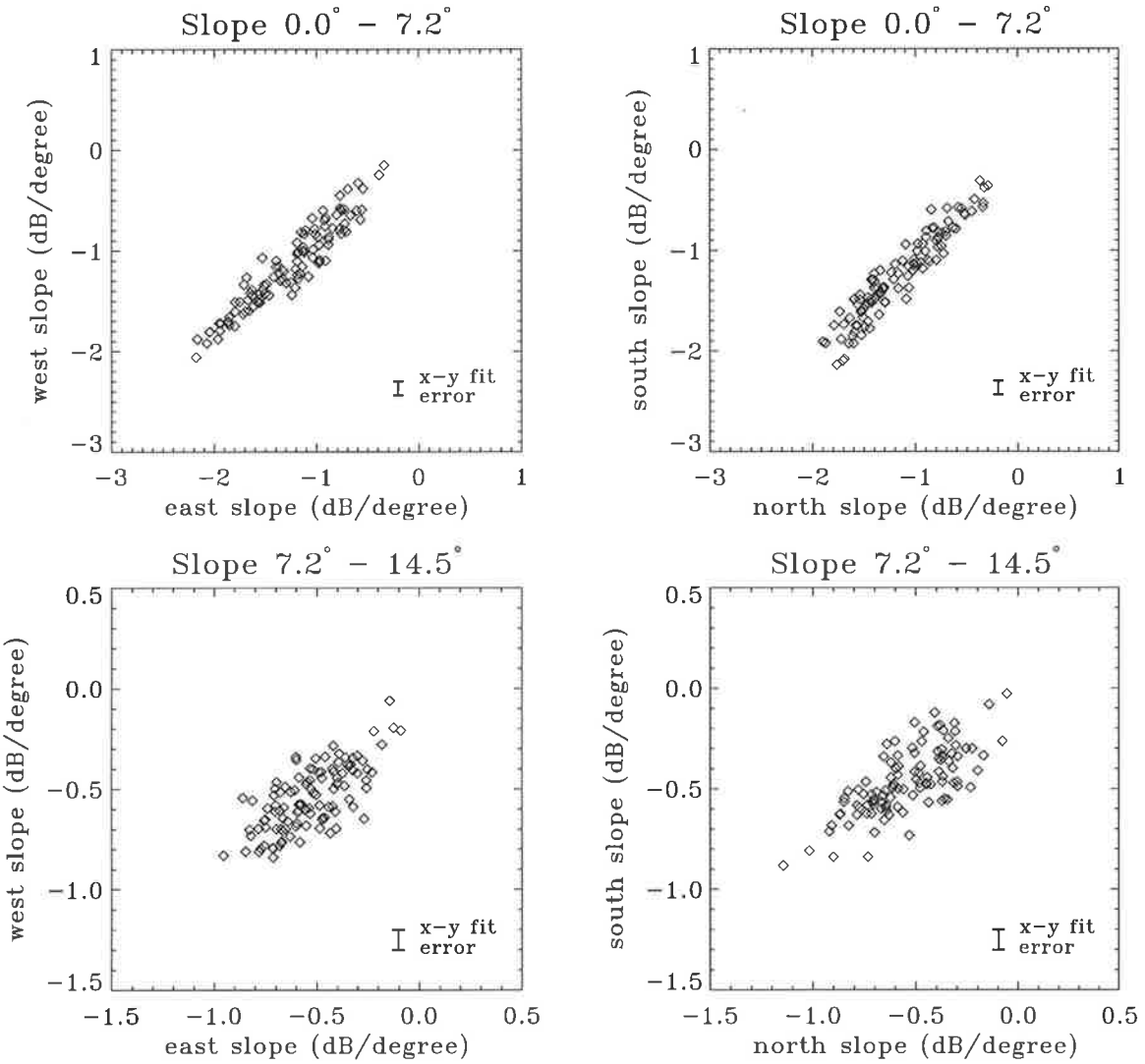

Figure 6.12: Scatter plots of the slopes fitted between the off-zenith angles of 0.0° and 7.2°, and 7.2° and 14.5°, for the east-west and north-south directions. Data are shown for all slopes over the height range from 3 - 8 *km* for the 24-28/12/97 data set. Also shown on these plots is the average error in the slope of the linear fit to the corresponding data. The average error for the slopes from 0.0° to 7.2° is 0.14 *dB/degree*, and from 7.2° to 14.5° is 0.1 *dB/degree*.

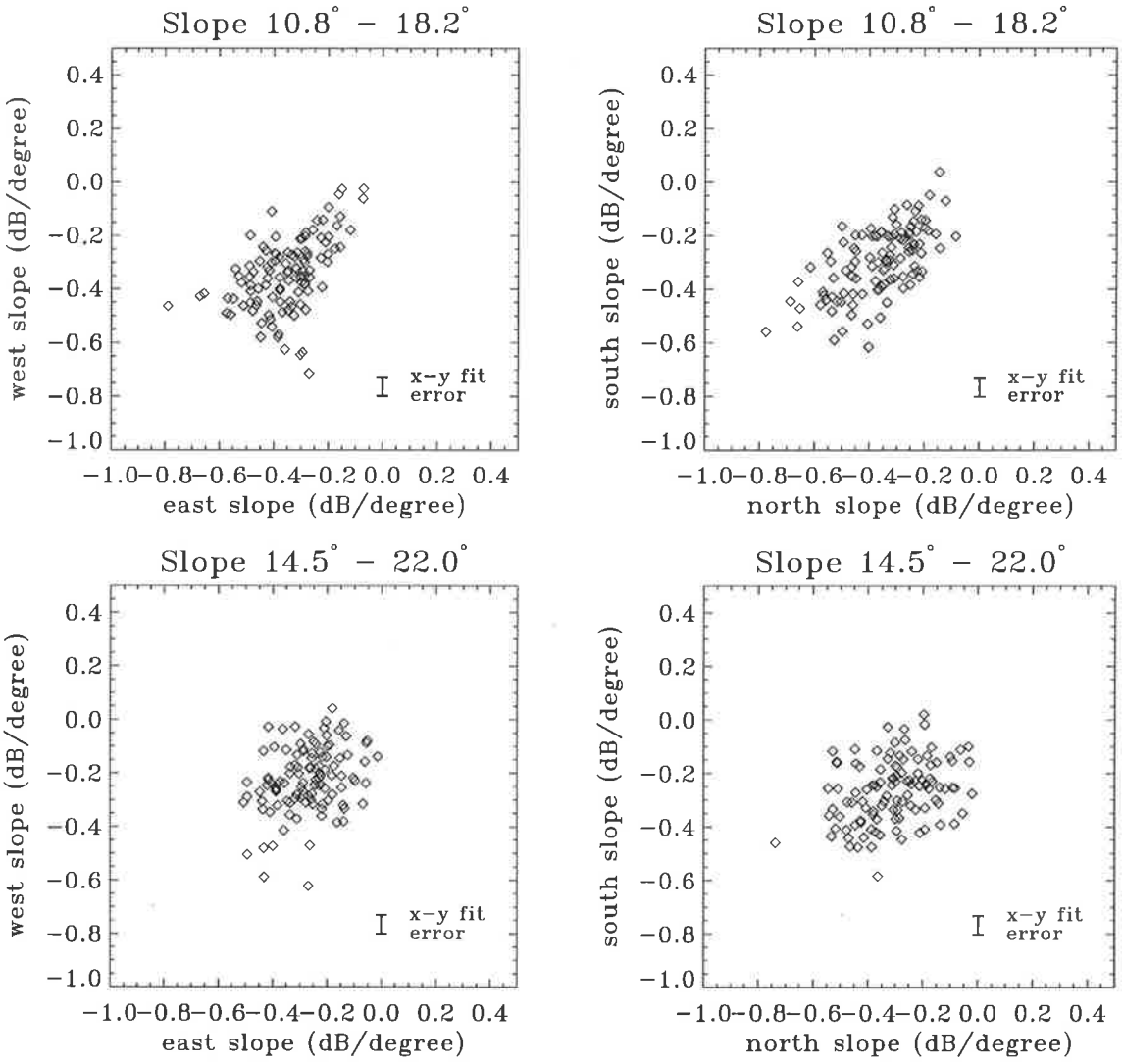

Figure 6.13: Scatter plots of the slopes fitted between the off-zenith angles of 10.8° and 18.2°, and 14.5° and 22.0°, for the east-west and north-south directions. Data are shown for all slopes over the height range from 3 - 8 *km* for the 24-28/12/97 data set. Also shown on these plots is the average error in the slope of the linear fit to the corresponding data. The average error for the slopes from 10.8° to 18.2°, and from 14.5° to 22.0° is 0.07 *dB/degree*.

is essentially no correlation between the slopes of the scatter in the various azimuths in the off-zenith angle range from 14.5° to 22.0°. This suggests that at this range of angles, the scatter is from isotropic structures alone and there is no scatter from coherent, aspect sensitive structures, as appears to be the case in the other angle ranges. The fact that the range of slopes and the average errors in the slopes for the two angle ranges of 10.8° to 18.2° and 14.5° to 22.0° is the same, yet the behaviour of the two angle ranges is different, provides confidence in interpreting the difference in behaviour as being due to different scattering processes and not due to a lack of real variation, or a large error. Therefore, Figure 6.12 suggests that the isotropic scattering level, the constant power level where the scatter is independant of off-zenith angle, lies in the range of angles from 14.5° to 22.0°.

In addition to the fact that scatter from off-zenith angles at the isotropic scattering level should be uncorrelated, the slope of the scatter at these angles should not be significantly different from zero. From Table 6.2 it can be seen that the average slope of the backscatter in the angle range from 14.5° to 22.0° is more than one standard deviation away from 0.0°. A possible explanation for the average non-zero slope in the backscatter between 14.5° and 22.0° is the coherent integration weighting function discussed by *Rastogi* [1983]. *Rastogi* [1983] has shown that the frequency weighting function introduced by coherently averaging data is a maximum at zero Doppler shift in the power spectrum, and a minimum at the largest frequencies in the power spectrum. This means that the actual power received at a relatively large off-zenith angle is reduced with respect to the power at smaller off-zenith angles, irrespective of aspect sensitivity, because of the fact that the scatter corresponds to a larger Doppler shift in the power spectrum. This factor could account for the small slope observed between 14.5° and 22.0°, which coupled with the fact that the scatter plots of the slopes in this range were observed to be isotropic, would suggest that the scattering at off-zenith angles larger than 14.5° is isotropic, despite the fact that the slope is non-zero.

As one final check of the slopes in the largest off-zenith angles range, the average slope of the scatter between the two adjacent off-zenith angles 18.2° and 22.0° was calculated for the 12 hour averaged data, over the height range from 3 - 8 km of both the 24-29/12/97 and 21-26/1/98 data sets. The results of this reduced angle

fit produced average slopes over the height range from 3 - 8 km, for both zonal and meridional data, for both data sets of 0.2 $\pm$0.2 $dB/degree$, which is not significantly different from zero. This fact is in good agreement with the work of *Tsuda et al.* [1997a] who estimated the isotropic scattering level minimum at approximately 18°. With respect to the next lowest off-zenith angle range of 10.8° to 18.2°, the results in Chapter 5 showed that there were some significant correlations between off-zenith SNRs in symmetric beams and the angle of arrival in a vertical beam, in beams that were directed at 10.8° off-zenith. This fact suggests that there are some times and heights where aspect sensitive scatter is present in 10.8° off-zenith beams, which agrees with the fact that there appears to be some correlation between the scatter slopes in the off-zenith angle range between 10.8° and 18.2° in Figure 6.13.

6.5 Angular power distribution half-width estimation

Despite the fact that the *Hocking et al.* [1986] θ_s parameterisation is in common use, there has been no direct comparison of this parameter with the exact parameter that it represents; the $1/e$ half-width of the polar diagram of the backscatter. As discussed and shown in Chapter 4, the choice of off-zenith angles has a large effect on the absolute value of θ_s. This is because the parameterisation assumes that the power at a given off-zenith angle, θ is of the form $exp(-sin^2\theta/sin^2\theta_s)$, which in practice is only accurate at small off-zenith angles.

It is interesting therefore to directly calculate the $1/e$ half-width of the angular distribution of scatter to determine θ_s exactly. The above parameterisation is Gaussian in linear units and parabolic in log units of dB, and the most common DBS θ_s calculation method uses the power at a given off-zenith angle, $P(\theta)$, relative to that measured on a vertical beam

$$\theta_s = arcsin[(-sin^2\theta_A/lnr - sin^2\theta_0)^{\frac{1}{2}}], \tag{6.1}$$

where θ_A is the apparent off-zenith beam direction, θ_0 is the beam width and r

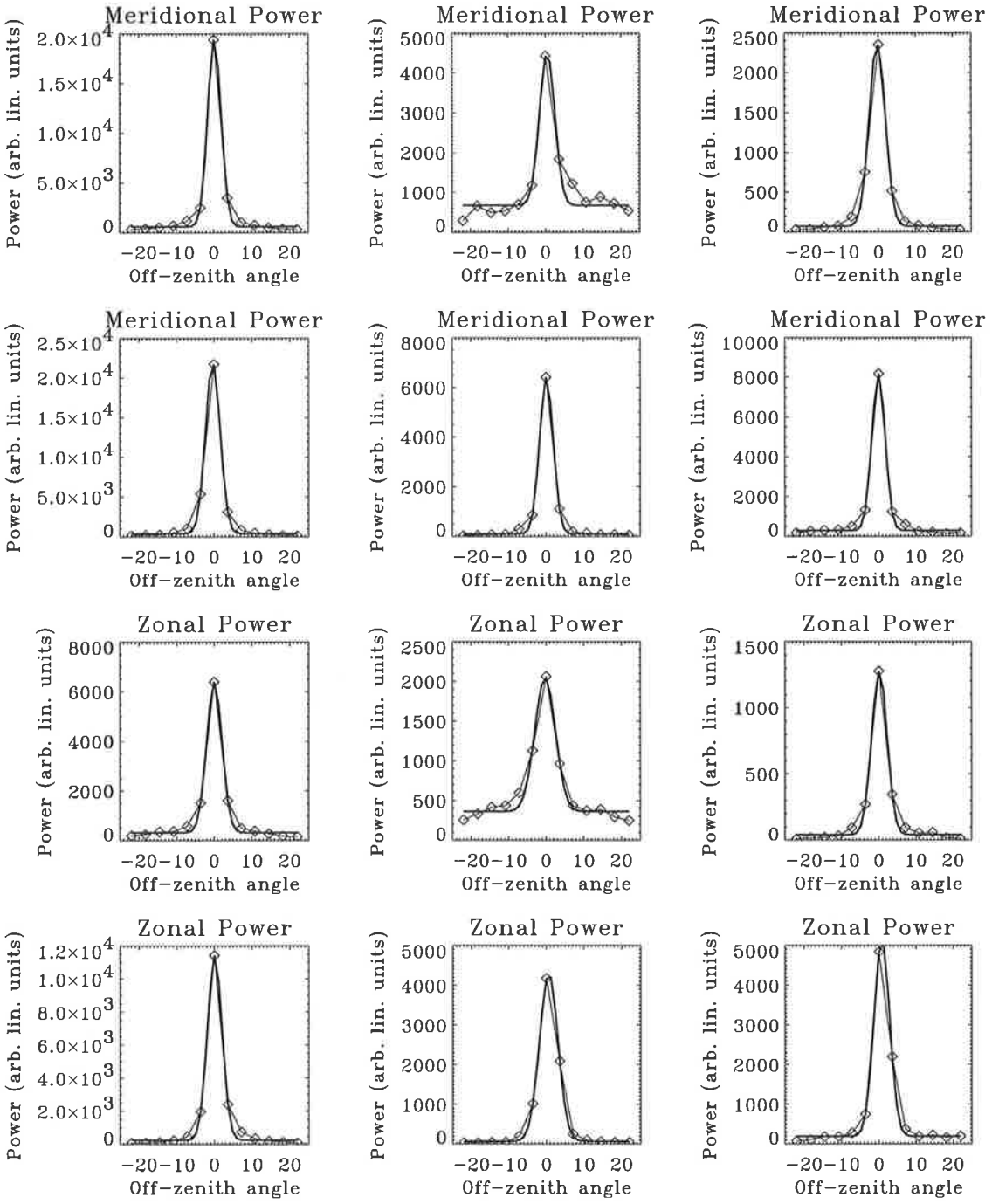

Figure 6.14: 12 hour averaged linear power as a function of off-zenith angle at a height of 5 km, shown for six of the 10 time averages of the 24-28/12/97 data set. The top six plots show the power for all meridional off-zenith angles, and the bottom six plots show the power for all zonal off-zenith angles, for the same times as the top six plots. Over-plotted on these off-zenith distributions are Gaussian fits to the data.

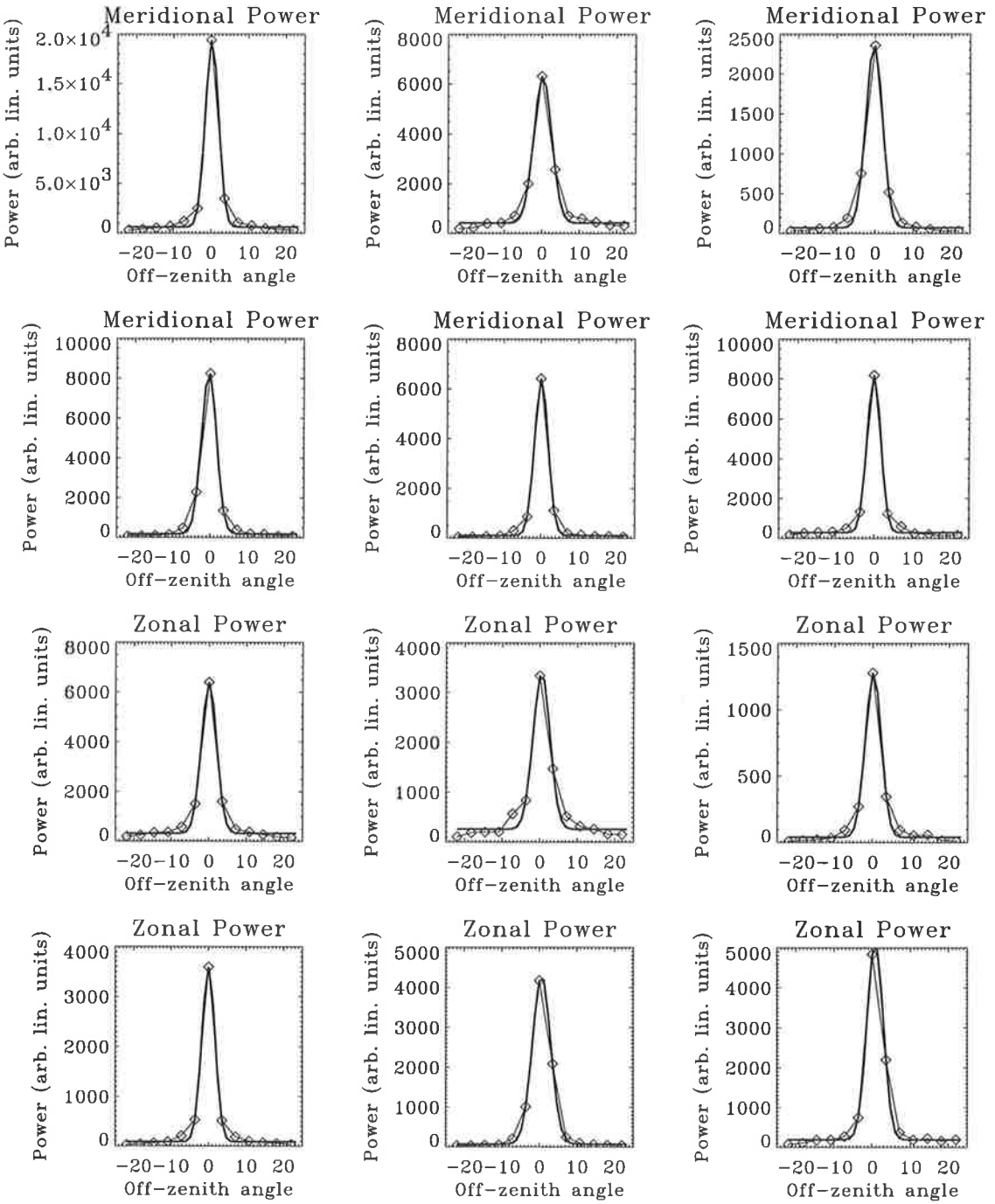

Figure 6.15: 12 hour averaged linear power as a function of off-zenith angle at a height of 5 km, shown for six of the 11 time averages of the 21-26/1/98 data set. The top six plots show the power for all meridional off-zenith angles, and the bottom six plots show the power for all zonal off-zenith angles, for the same times as the top six plots. Over-plotted on these off-zenith distributions are Gaussian fits to the data.

$= P(0)/P(\theta_A)$. As such, in order to keep the power measurements the same in both the direct estimation of the half width and the θ_s calculation method, they were both calculated on exactly the same data. Twelve hour averaged angular linear power profiles were compiled (note that the angular profiles such as Figure 6.4 were in log units of dB) for both the 24-28/12/97 and 21-26/1/98 data sets. Figure 6.14 shows the 12 hour averaged linear power profiles as a function of off-zenith angle for six of the 10 time averages of the 24-28/12/97 data set, at a height of 5 km, for both the zonal and meridional direction. Figure 6.15, shows the same parameters at the same height, but for six of the 11 time averages of the 21-26/1/98 data set. The $1/e$ half-width was calculated from these profiles by fitting a Gaussian function, which is shown overplotted on each angular profile in Figure 6.14 and Figure 6.15, and θ_s was calculated from the data selected off-zenith angles shown in these figures. It can be seen from these figures that in most cases only the 3.6° off-zenith angle data contributes to the width of the Gaussian fit.

Figure 6.16 shows the comparison of the $1/e$ half-widths as the thick solid line, with DBS θ_s values using off-zenith angles of 3.6° as the thin solid line, 7.2° as the dotted line, and 10.8° as the dashed line, at various heights, over all average times of the 24-28/12/97 data set. The half-widths in this figure are the half-widths in the zonal direction, and the θ_s values are the average of the θ_s values in the eastern and western directions, at a given off-zenith angle. Figure 6.17 shows the comparison of the $1/e$ half-widths measured in the meridional direction with average θ_s in the northern and southern directions, for the off-zenith beam angles of 3.6°, 7.2° and 10.8°. These plots are shown in the same format as Figure 4.10 and Figure 4.13 of Chapter 4 so that the similarity of the behaviour as a function of time can be clearly seen as well as the differences in the magnitudes due to the various off-zenith beams. The results for the 21-26/1/98 data set are were very similar, but are not shown.

It can be seen from Figure 6.16 and Figure 6.17 that the DBS θ_s method using a 3.6° off-zenith beam, and a vertical beam, is the best estimate of the actual half-width of the angular distribution of power. The point-to-point variation of the profiles as a function of time between the 3.6° off-zenith beam θ_s values and the actual $1/e$ half-width agrees very well, and the magnitude of the two values are almost identical.

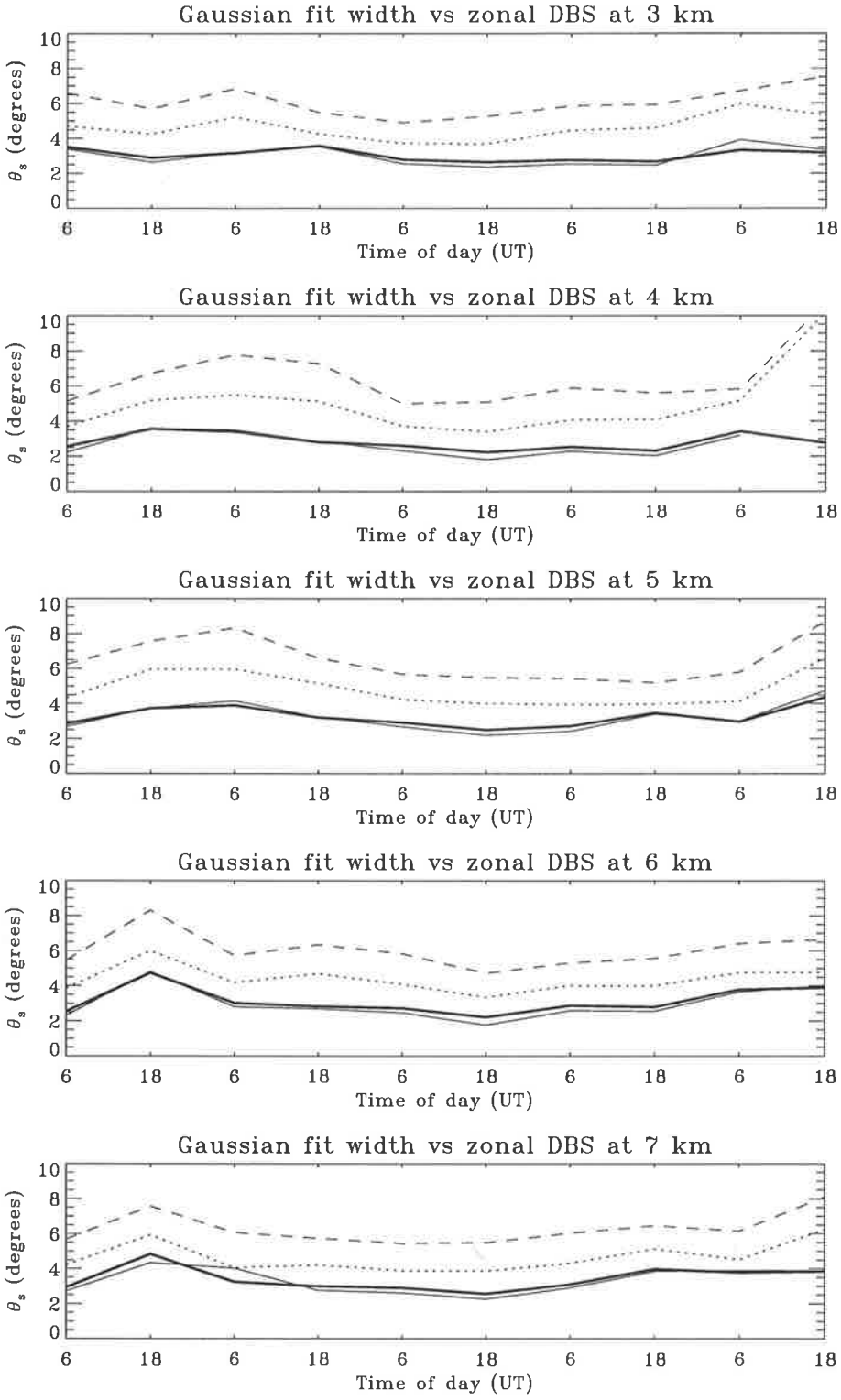

Figure 6.16: Time series of the zonal DBS θ_s values, and the $1/e$ width of the Gaussian fit to the zonal off-zenith distribution of data, for the 24-28/12/97 data set. Both the θ_s and Gaussian $1/e$ values were calculated from 12 hour averaged data at the relevant off-zenith angles. Thick solid line shows the Gaussian fit values, thin solid line shows the 0.0°/3.6° off-zenith θ_s values, dotted line shows the 0.0°/7.2° off-zenith θ_s values and dashed line shows the 0.0°/10.8° off-zenith θ_s values.

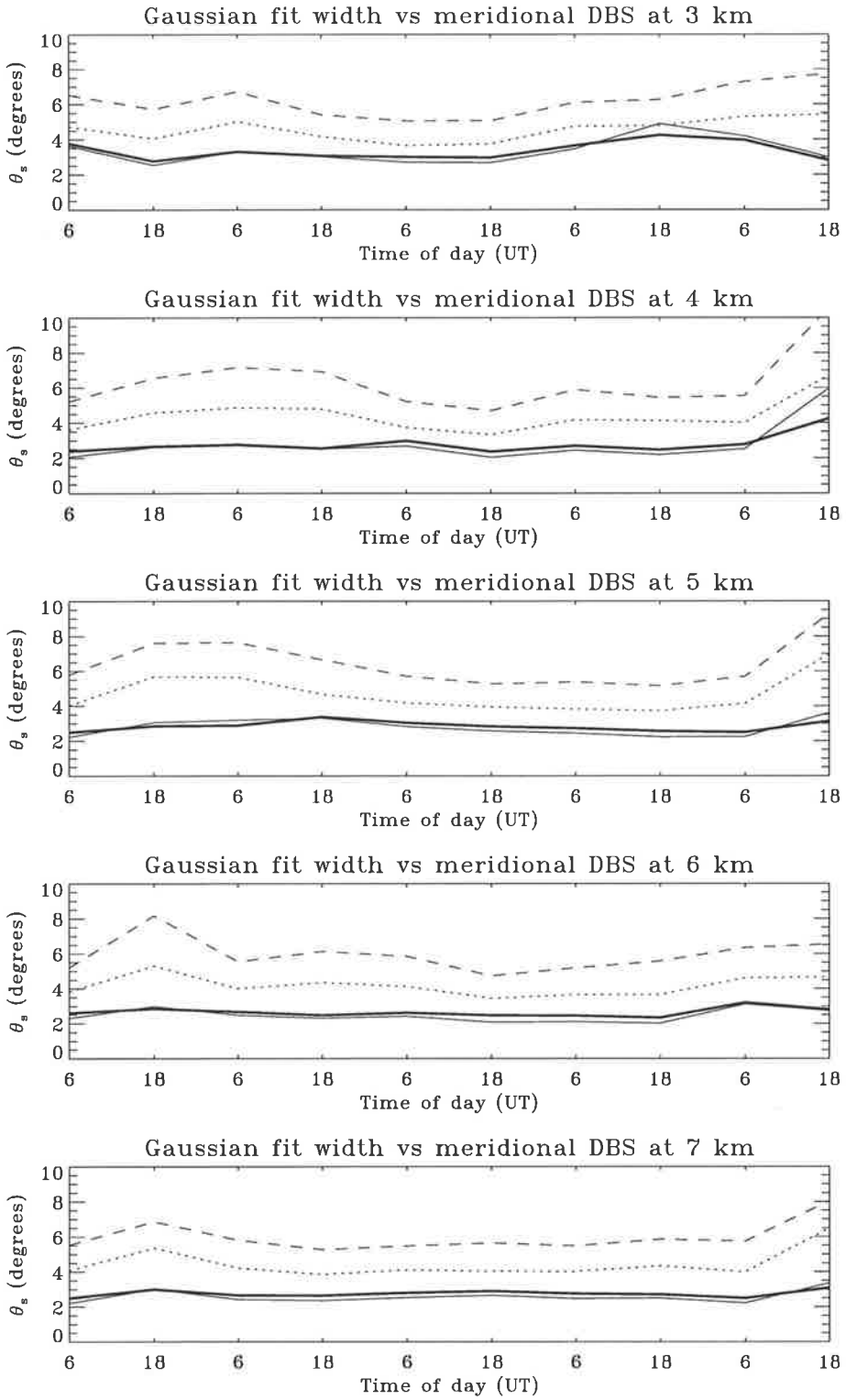

Figure 6.17: Time series of the meridional DBS θ_s values, and the $1/e$ width of the Gaussian fit to the off-zenith distribution of data, for the 24-28/12/97 data set. Both the θ_s and Gaussian $1/e$ values were calculated from 12 hour averaged data at the relevant off-zenith angles. Thick solid line shows the Gaussian fit values, thin solid line shows the 0.0°/3.6° off-zenith θ_s values, dotted line shows the 0.0°/7.2° off-zenith θ_s values and dashed line shows the 0.0°/10.8° off-zenith DBS θ_s values.

The DBS θ_s method using 7.2° and 10.8° off-zenith beams show larger magnitudes, as expected, and although the variation from point-to-point with these methods usually tracks the variation of the 3.6° and $1/e$ half-width values, this is not always the case.

This result is essentially confirmation of the fact discussed in Chapter 4 that the θ_s parameterisation assumed by the DBS θ_s calculation method is only a good representation of the power at small off-zenith angles. Because of the fact that small off-zenith angles influence the Gaussian fit more than comparatively larger off-zenith angles, the 3.6° off-zenith beam DBS θ_s values are the best approximation. If other small off-zenith angles were available, such as 2°, these would also probably produce θ_s values in good agreement with the value obtained with a direct Gaussian fit. It can therefore be seen that in order to obtain the best values of θ_s it is necessary to use small off-zenith angles, of approximately 2° - 4°, where the assumed Gaussian drop-off of power as a function of off-zenith angle (in linear units) is accurate. It should be noted here that this result is also confirmation of the good agreement between the FCA θ_s values and the 3.6° off-zenith and 0.0° DBS values. This is because the angular polar diagram of the backscatter is the Fourier transform of the ground diffraction pattern sampled by the spaced antennas used in the FCA. The spacing of the antennas used in the FCA acts to spatially filter the ground diffraction pattern, making the measured value of θ_s more sensitive to the scatter within a small range of off-zenith angles, in the same way that the direct fit to the distribution as a function of off-zenith angle is more sensitive to the power observed at 3.6° off-zenith.

6.6 Summary

In this chapter an experiment comprising DBS data in the vertical direction and at a number of off-zenith beam angles, in all four cardinal directions has been discussed. The experiment was run over two five-day periods, and the analysis was performed on data which had been averaged for 12 hours.

The off-zenith distribution of power was analysed by introducing a simple piecewise linear parameterisation so that the slope of the decrease in power as a function of off-zenith angle could be quantified. By comparing the slopes at pairs of azimuths

in a single plane, the contribution of aspect sensitive scatter to the scatter in various ranges of off-zenith angle was determined. The results of this analysis showed that truly isotropic scatter, scatter where there was no contribution from coherent aspect sensitive structures, occurred between the off-zenith angles of 14.5° and 22.0°. Calculation of the average slopes in the reduced range from 18.2° to 22.0° resulted in a slope not significantly different from zero, suggesting that the scattering at these two angles lies at the isotropic scattering level, in agreement with the estimation of *Tsuda et al.* [1997a]. Interestingly, for the data in this chapter, non-zero average slopes were observed over the angle range from 14.5° to 22.0°. However, when the results of the coherent averaging simulations of *Rastogi* [1983] are taken into account, it is probable that the small slope between the these three off-zenith angles is not is not real. This fact, coupled with the observed isotropic scatter in the angle range from 14.5° to 22.0° shown in Figure 6.12, suggests that the isotropic scattering level begins at approximately 14.5°.

Finally, the parameterisation that is commonly applied to the off-zenith distribution of data in order to calculate θ_s values using the DBS method is compared with the actual $1/e$ half-width of the angular distribution of backscatter. It is found that the best estimate of the half-width is from the smallest off-zenith angle available with the BP VHF ST radar of 3.6°. This result suggests that small off-zenith angles less then 4° should be used to calculate θ_s if a true representation of the half-width of the scatter is required.

Chapter 7

Summary, conclusions and further work

The work in this thesis has covered the testing and installation of new radar equipment, the development of new data analysis algorithms, and the presentation of new experimental results from the upgraded Buckland Park VHF ST (stratosphere-troposphere) radar. As such, the thesis is essentially in two parts. Chapters 2 and 3 are concerned with the verification of the radar hardware, and data respectively. While Chapters 4, 5 and 6 are concerned with the results of new experiments conducted with the radar. Each chapter has a summary which discusses the main results of the chapter, and as such, this chapter is brief and serves to bring the main results of the thesis together and make suggestions for further experiments that might be conducted with the system.

In Chapter 2 the various tests that were conducted on the new hardware to be added to the system were discussed. The emphasis of these tests was to measure the various phase errors in the new hardware and their effects on the pointing accuracy of the radar beam, and to verify the DBS (Doppler beam swinging) capabilities of the system. By measuring the phase at the centre feeds of each of the antenna rows of the new North-South array it was found that the array has a slight tilt of approximately 0.24° to the west. Tests of the phases introduced by the beam-steering cards showed that the small errors in the values on individual cards resulted in an off-zenith angle error of 0.05° across the full antenna arrays. The magnitude of the variation in the

phase between receivers connected to a single antenna, was measured to be 0.2° of zenith. This value is the minimum AOA (angle of arrival) that is measureable with the system; a limitation due to small phase variations throughout the system. Finally the full DBS capabilities of the system were verified by observing the passage of the galactic centre through the full range of beam positions.

Chapter 3 discusses the data analysis algorithm that was developed for the new DBS data from the upgraded system. The existing DBS analysis software for the old BP ST radar was conducted in the time domain, using the so-called "pulse-pair" technique, where it is difficult to account for various contaminants. To improve this approach, programs were written to perform the analysis in the frequency domain by fitting Gaussian functions to power spectra. In addition, various procedures were developed to ensure the accuracy of the DBS results that these programs produced. The algorithm that encompasses all the DBS analysis and verification programs aims initially to reduce effects of contaminants in the data at the time series level, with a filter window, and then at the power spectrum level, with interpolations over the common ground clutter contaminated frequency range. Finally, the algorithm aims to identify outliers in the atmospheric parameters that are caused by contaminants in the power spectra being incorrectly analysed as atmospheric peaks. The identification of outliers is based on two different types of contaminants; well-characterised contaminants such as ground clutter, sea scatter and noise spikes, and more random contaminants such as backscatter from aircraft and other unidentified sources. Once an outlier is identified, the algorithm aims to return to the power spectrum that caused a given outlier and locate the true atmospheric peak instead. This process was seen to be very successful at retrieving atmospheric parameters from the true atmospheric peak in heavily contaminated power spectra.

The aim of the experiments conducted with the upgraded multiple-beam, multiple-receiver radar were to be able to firstly, combine both SA (spaced antenna) and DBS experiments in order to obtain information about the relationship between the measurements seen by various authors using only one of these techniques, and secondly to conduct multiple beam experiments to study the variation of off-zenith backscattered power that has been seen by various other authors, with the emphasis on the behaviour

at large off-zenith angles.

Chapter 4 discusses a comparison of DBS and SA FCA (full correlation analysis) data. Because of the antenna arrangement necessary for this experiment, it was only possible to obtain data in the meridional direction. Meridional velocities between DBS beams at off-zenith angles of 3.6°, 7.2° and 10.8° were seen to be in excellent agreement, with correlation coefficients of between 0.95 and 0.98. This result is further verification of the success of the analysis algorithms discussed in Chapter 3. Comparison of the meridional velocities at the various off-zenith beam directions and FCA meridional velocities showed excellent agreement, with correlation coefficients between 0.87 and 0.88, and no discernible bias in the magnitude of the velocities as seen in a scatter plot. The DBS and FCA data were used to compare θ_s as measured using the FCA spatial correlation method and the DBS power method using vertical beams and each of the off-zenith angles 3.6°, 7.2° and 10.8°. It was found that in aspect sensitive conditions, the DBS power method utilising 0.0° and 3.6° off-zenith beams produced θ_s values in good agreement with the values produced by the FCA which utilises vertical beams only. This result indicates that the 0.0° beam and 3.6° off-zenith beams were responding to the same scatterers.

Chapter 5 discusses a comparison of DBS and SA AOA data in two separate experiments, the first utilising four parallel antenna strips and the second utilising four squares. The data from these two experiments was used to examine two separate issues in VHF ST radar studies. The first set of analysis was performed to examine the relationship between the AOA seen on a vertical beam, and power measurements in off-zenith DBS beams, under the assumption that the two parameters were varying in response to small changes in the tilt of specular layers. Significant correlations were found between the variation of the power differences between DBS beams at 3.6° off-zenith and the AOA measured on a vertical beam directed between the DBS beams in time, in both the zonal and meridional directions, in data from both experiments. This result suggests that the aspect sensitive scatter observed at 3.6° was due to specular layers. In contrast to this result, fewer significant correlations were observed between power differences in DBS beams at 10.8° off-zenith and AOA measurements made on a vertical beam between the DBS beams in time. This result suggests that the layers

did not affect the 10.8° off-zenith beams to the degree that they affected the 3.6° off-zenith beams. The second set of analysis performed on the AOA/DBS data set was aimed at estimating the effect of small variations in the AOA in off-zenith beams on measurements of momentum flux at 10.8° off-zenith. It was found that the variation of the beam direction resulted in a spurious momentum flux averaged over five days of less than 4% of the measured value. In contrast, measurements over 24 hours showed that the spurious flux could be up to approximately 20% of the measured value.

Chapter 6 discusses a study of DBS data at multiple off-zenith angles, in two five-day data sets. The primary aim of this study was to characterise the decrease in power as a function of off-zenith angle, and identify the angular range where purely isotropic scattering occurs. This was achieved by applying a piece-wise parameterisation to the decrease in backscattered power at increasingly large off-zenith angles, in 12 hour averaged data. This parametrisation gave the slope of the power in $dB/degree$ over various three angle ranges of off-zenith angle, from 0.0° - 7.2°, 7.2° - 10.8°, 10.8° - 18.2° and 14.5° - 22.0°. The variation in the slopes in various angle ranges was found to be quite significant over the duration of the data sets, with the variation in the 0.0° - 7.2° range from -0.1 - -2.2 $dB/degree$, and the variation in the 14.5° from 0.4 - -0.7 $dB/degree$. The fact that aspect sensitive scattering appeared to be coherent across all azimuths at a given off-zenith angle was utilised to identify the range where purely isotropic scattering occurred. Scatter plots of the slopes seen on either side of vertical in a given plane revealed that the scatter in the angle ranges from 0.0° - 7.2°, 7.2° - 14.5° and 10.8° - 18.2° showed some degree of correlation, indicating coherent structures in the beams on either side of vertical. However, the scatter in the angle range from 14.5° - 22.0° was seen to show no correlation. This fact, when coupled with the fact that the slope in this angle range was not considered to be significantly different from zero when the effects of the coherent averaging weighting function are taken into account, suggests that the isotropic scattering level started at around 14.5° off-zenith. Using the same data, a comparison of the DBS power method with direct estimation of the half-width of the polar diagram of backscatter showed that the best estimate of the true θ_s value was produced by the combination of DBS beams at 0.0° and 3.6° off-zenith.

Taken as a whole, the experiments discussed in this thesis have provided important information on the nature of the scattering in the troposphere seen in both small and large off-zenith angle DBS beams, and the link between this scattering and the scattering observed in various SA arrangements. In addition, these experiments have fully utilised the capabilities of the upgraded VHF BP ST radar by using three different antenna arrangements and a large range of off-zenith angles. As such, they have been a good verification of the use of the system for a range of experiments.

In terms of future work with the system, there are a number of extensions of the work that has been discussed in this thesis. It would be useful to install the DBS data analysis algorithm discussed in Chapter 3 so that it acts on DBS data in real time. For the data that were presented in this thesis, the algorithm was applied after data collection of an entire data set, due to the fact that it was in the developmental stage. However, it would be useful to run the algorithm in real time at the BP field site so that verified DBS velocities are available at the site during a given data run. It is also possible that with some optimisation of the hardware and the peak detection algorithm discussed in Chapter 3, the height coverage of the radar could be extended.

The FCA experiment discussed in Chapter 4 should be repeated over a longer data set in order to further verify the application of the FCA on the North-South CoCo array. The experiment described in Chapter 4 spans a few days, which were characterised by light winds. As such it would be good to repeat the experiment in a range of weather conditions. Also concerning the FCA, the six receivers of the new system would allow a comparison of the FCA on the CoCo array, as discussed in Chapter 4, and FCA on the Yagi arrays which stand beside the CoCo arrays, as shown in Figure 2.1. This would be worthwhile experiment as the two sets of measurements would be simultaneous, and completely independant except for the use of the same transmitting beam. The Yagi arrays are spaced by 50 m, which is similar to the spacing used for the experiment in Chapter 4. As such, the effects of the spacing, as well as various other issues associated with FCA could be investigated.

The momentum flux study discussed in Chapter 5 has provided an important insight into the effect of changing AOA in off-zenith DBS beams on this very sensitive

measurement. As such, it would be interesting to conduct further momentum flux experiments given that the errors induced by the changing AOA can now be accounted for in the results.

In both Chapters 4 and 6 a large variation in the aspect sensitive behaviour of the atmosphere was observed from day to day. This point was not addressed in this thesis, and it would be instructive to investigate this behaviour and the reasons for it by gathering a large database. In a large set of data over time, including DBS measurements over the range of angles discussed in Chapter 6 and AOA measurements on a vertical beam as discussed in Chapter 5, the variation of θ_s, the slopes over the various angle ranges, and the correlation between off-zenith DBS powers and AOAs could be examined in detail, and the reasons for the variation as a function of time could be fully investigated both in terms of season and prevailing weather conditions. This would provide valuable insights into the scattering dynamics of the ST region.

Appendix A

Beam steering circuitry

The following page contains a circuit diagram of the beam steering cards in the BP VHF ST radar.

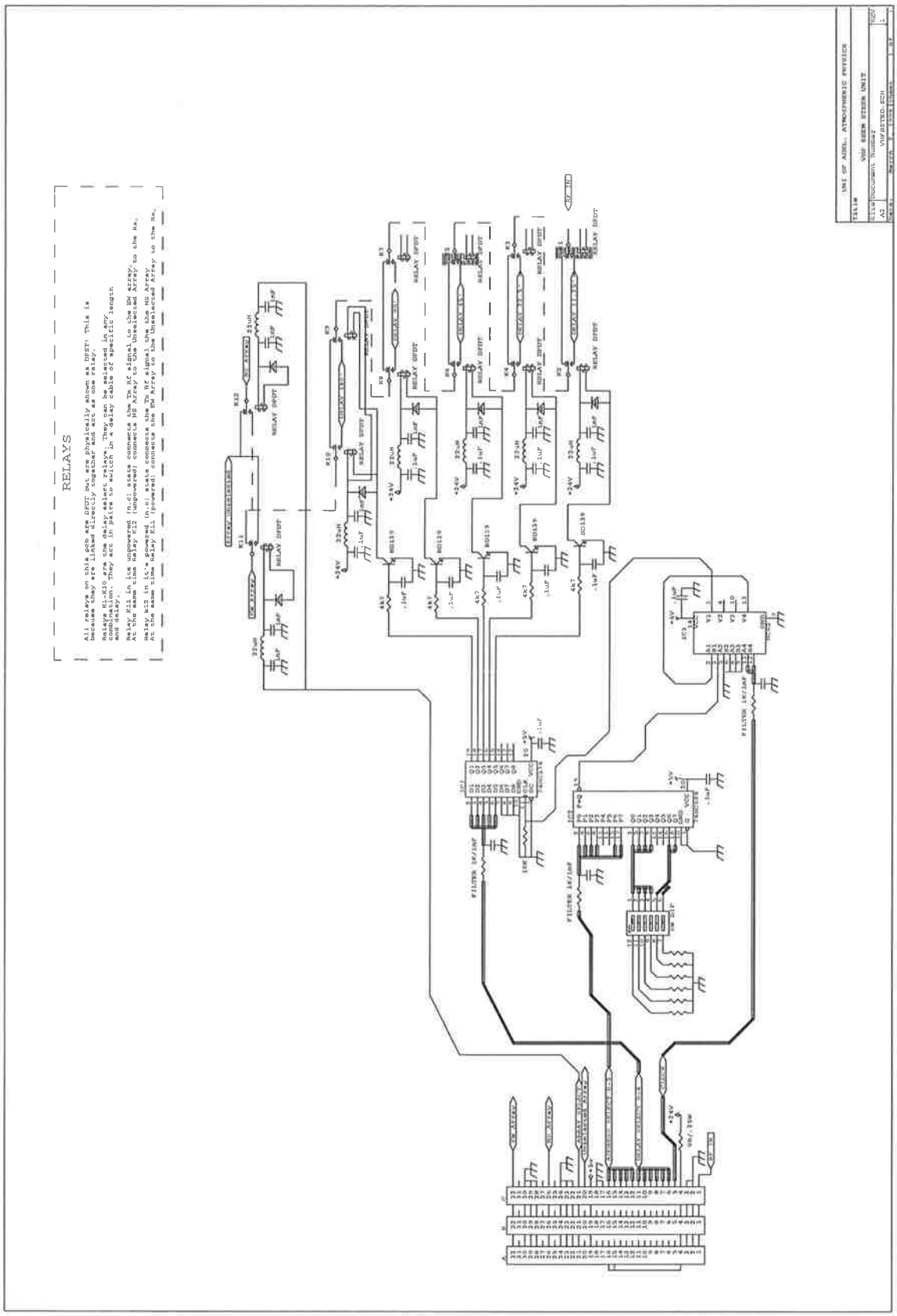

Figure A.1: Circuit diagram of the beam steering cards. The upgraded BP VHF ST radar comprises 64 such cards, see Chapter 2 for a full description of the radar hardware.

Appendix B

FCA rejection criteria

This appendix details the reasons that the FCA code employed in Chapter 4 of this thesis rejects a given analysed result. David Holdsworth developed the FCA code used in Chapter 4, and as such, the content of this appendix is essentially identical to Appendix D of *Holdsworth* [1995].

The error codes for the rejection criteria are shown in Table B.1. The error code zero indicates the analysis has passed all the rejection criteria and obtained a set of results. The rejection of a record can be put down to at least one of three causes:

B.1 Record unsuitable for analysis

The error codes 1 and 2 result from the record being unsuitable for analysis. Such records are rejected prior to the application of the FCA.

• Error code 1 is employed to prevent the analysis of records with low signal level. In such instances the coarse digitization can result in the true velocity magnitude V_t being significantly underestimated.

• Error code 2 is employed to prevent the analysis of records with low SNR; values $<$ -6 dB. This correction is used because the FCA applies noise corrections to the data, and these corrections become difficult when the amplitudes of the signal and noise components are comparable.

Code	Explanation
0	Record accepted
1	Low signal amplitude
2	SNR < -6 dB
3	$\tau_{0.5} > 6$ seconds
4	Slow fading
5	NTD > 0.5
6	$K < 0$
7	Breakdown in pattern analysis
8	$V_a > 250\ ms^{-1}$
9	$\mid \theta_t - \theta_a \mid > 40°$
10	$V_a > 4V_t$
11	$V_t > 1.5V_a$
12	Poor fit to cross-correlation function
13	$\rho_{0ij} < 0.2$
14	Poor zero-lag auto-correlation interpolation
15	Maths error
16	Poor fit to mean auto-correlation function
17	Second peak in auto-correlation function greater than 0.5
18	Fading time larger than maximum lag

Table B.1: The FCA rejection criteria.

B.2 Unsuccessful correlation parameter estimation

The unsuccessful estimation of the correlation parameters can be attributed to a number of causes. It may be due to deficiencies in the correlation functions themselves, or due to errors in the fitting procedures used to estimate the correlation functions.

- Error code 3 results when the estimated half-width $\tau_{0.5}$ of the mean auto-correlation function exceeds 6 seconds. Large fading times are generally indicative of specular scatter rather than volume scatter assumed by the FCA. Error codes 17 and 18 are related to error code 3. Specular scatter generally produces time-series with a small number of dominant frequency components resulting in oscillatory time-series and correlation functions. Error code 17 results where there is a second auto-correlation function maxima exceeding 0.5, indicating an oscillatory correlation function. Error code 18 indicates that the fading time exceeds the duration that the correlation functions are calculated out to, and can indicate that the FCA is not being

calculated over the necessary number of lags.

• Error code 4 results when at least one of the cross-correlation maxima delays τ'_{ij} lies outside the calculated range of the cross-correlation functions. This usually indicates that the main peak of the corresponding cross-correlation function is subdued. This effect can occur if the pattern scale is less than the antenna spacing such that the correlation between the time-series recorded by the antennas is small.

• Error code 5 results if the normalised time discrepancy, defined as:

$$NTD = \frac{\mid \sum \tau'_{ij} \mid}{\sum \mid \tau'_{ij} \mid}, \tag{B.1}$$

exceeds 0.5. The sum of the τ'_{ij} values around a closed loop of antennas should theoretically sum to zero. In practice, statistical variations and noise can result in the sum being non-zero, and as such, this criteria is relaxed to reject those results with NTD > 0.5.

• Error codes 12 to 16 result from the failure of the fitting routines to successfully estimate the correlation parameters. Error code 12 results if any of the τ'_{ij} estimates are nonsensical, indicating that the Gaussian fit to the cross-correlation function has failed. Error code 13 results if any of the ρ_{0ij} estimates are less than 0.2, suggesting that either the fit has failed or that the correlation is too small to be able to provide accurate FCA output. Error code 14 results if any of the interpolated zero-lag auto-covariances are less than zero. This effect can occur if the auto-correlation function has a "jagged" appearance, as is sometimes the case for low SNRs. Error code 15 results when mathematical errors occur within the fitting routines.

B.3 Failure to satisfy the theory of the FCA

The error codes 6 to 11 result from the failure of the data to satisy the assumptions of the FCA.

• Error code 6 is employed to reject data where $K < 0$, where K describes the magnitude of the random changes in the ground diffraction pattern. If there are few random changes in the pattern, K will ideally be close to zero, however, statistical variations may result in K being less than zero.

• Error code 7 is employed to reject data which produces negative values of the ellipsoid parameters, suggesting that the FCA failed to successfully parametrise the spatio-temporal correlation function.

• Error code 8 results if the magnitude of the apparent velocity V_a exceeds 250 ms^{-1}. This suggests that the random changes in the ground diffraction pattern are significantly larger than those expected in practice.

• Error codes 9 and 10 are employed to reject records where the correction for the effects of random changes and pattern anisometry, respectively, are inconceivably large. Error code 9 is employed to reject records where the direction of the true and apparent velocities, θ_t and θ_a respectively, differ by 40°, while error code 10 rejects records where the apparent and true velocity, V_a and V_t respectively, behave as $V_a > 4V_t$.

• Error code 11 is employed because random changes should produce apparent velocity magnitudes V_a larger than true velocity magnitudes V_t. The situation where V_t is significantly larger than V_a suggests tha the FCA failed to successfully parametrise the form of the spatio-temporal correlation function. The record is rejected for $V_t > 1.5V_a$.

Appendix C

Mesospheric rotational temperatures determined from the OH(6-2) emission above Adelaide, Australia

This is a reprint of a paper by B. G. Hobbs, I. M. Reid and P. A. Greet, published in the *Journal of Atmospheric and Terrestrial Physics*. This paper is based on data collected during the Honours year of B. G. Hobbs, with analysis conducted in the first year of the Ph.D. candidature of B. G. Hobbs, prior to the commencement of the work with the BP VHF ST radar that is discussed in this thesis.

Hobbs, B.G., Reid, I.M. & Greet, P.A. (1996) Mesospheric rotational temperatures determined from the OH(6-2) emission above Adelaide, Australia.
Journal of Atmospheric and Terrestrial Physics, v. 58(12), pp. 1337-1344

References

Balsley, B. B. & Ecklund, W. L. (1972), 'A portable coaxial colinear antenna', *IEEE Transactions on Antennas and Propagation* **20**(4), 513–516.

Balsley, B. B. & Gage, K. S. (1980), 'The MST radar technique: Potential for middle atmospheric studies', *Pure and Applied Geophysics* **118**, 452–493.

Balsley, B. B., Riddle, A. C., Ecklund, W. L. & Carter, D. A. (1987), 'Sea surface currents in the equatorial Pacific from VHF radar backscatter observations', *Journal of Atmospheric and Oceanic Technology* **4**(3), 530–535.

Brewster, K. A. & Schlatter, T. W. (1986), Automated quality control of wind profiler data, *in* '11th Conference on Weather Forecasting and Analysis, Kansas City, 17-20 June, 1986', American Meteorological Society.

Brewster, K. A. & Schlatter, T. W. (1988), Recent progress in automated quality control of wind profiler data, *in* '8th Conference on Numerical Weather Prediction, Baltimore, 22-26 February, 1988', American Meteorological Society.

Briggs, B. H. (1984), The analysis of spaced sensor records by correlation techniques, *in* 'Handbook for the Middle Atmosphere Program', Vol. 13, Special Committee for Solar-Terrestrial Physics Secretariat, pp. 166–186.

Briggs, B. H., Phillips, G. J. & Shinn, D. H. (1950), 'The analysis of observations on spaced receivers of the fading of radio signals', **63B**, 106–121.

Broche, P., Forget, P., de Maistre, J. C., Devenon, J. L. & Crochet, M. (1987), 'VHF radar for ocean surface current and sea state remote sensing', *Radio Science* **22**(1), 69–75.

Bufton, J. L. (1973), 'Correlation of microthermal turbulence with meteorological soundings in the troposphere using high-power pulsed Doppler radar', *Journal of the Atmospheric Sciences* **30**, 83–87.

Cervera, M. A. (1996), Meteor observations with a narrow beam VHF radar, PhD thesis, University of Adelaide, Adel., Australia.

Cervera, M. A. & Reid, I. M. (1995), 'Comparison of simultaneous wind measurements using colocated VHF meteor radar and MF spaced antenna radar systems', *Radio Science* **20**, 1245–1261.

Chang, J. L., Avery, S. K., Riddle, A. C., Palo, S. E. & Gage, K. S. (1997), 'First results of tropospheric gravity wave momentum flux measurements over Christmas Island', *Radio Science* **32**(2), 727–748.

Chau, J. L. & Balsley, B. B. (1998), 'Interpretation of angle-of-arrival (AOA) measurements in the lower atmosphere using spaced antenna radar systems', *Radio Science* **33**(3), 517–534.

Clothiaux, E., Penc, R., Thomson, D., Ackerman, T. & Williams, S. (1994), 'Contamination of wind profiler data by migrating birds: Characteristics of corrupted data and potential solutions', *Journal of Atmospheric and Oceanic Technology* **11**, 888–908.

Dalaudier, F., Sidi, C., Crochet, M. & Vernin, J. (1994), 'Direct evidence of "sheets" in the atmospheric temperature field', *Journal of the Atmospheric Sciences* **51**(2), 237–248.

Doviak, R. J. & Zrnić, D. S. (1984), 'Reflection and scatter formula for anisotropically turbulent air', *Radio Science* **19**(1), 523–336.

Eckermann, S. D. & Vincent, R. A. (1993), 'VHF radar observations of gravity-wave production by cold fronts over southern Australia', *Journal of the Atmospheric Sciences* **50**, 785–806.

Elford, W. G. & Taylor, A. D. (1997), 'Measurement of Faraday rotation of radar meteor echoes for the modelling of electron densities in the lower ionosphere', *Journal of Atmospheric and Terrestrial Physics* **59**, 1021–1024.

Fischler, M. A. & Bolles, R. C. (1981), 'Random sample consensus: A paradigm for model fitting with applications to image analysis and automated cartography', *Commu. Assoc. Comput. Mach.* **24**, 381–395.

Fritts, D. C., Tsuda, T., VanZandt, T. E., Smith, S. A., Sato, T., Fukao, S. & Kato, S. (1990), 'Studies of velocity fluctuations in the lower atmosphere using the MU radar. Part II: Momentum fluxes and energy densities', *Journal of the Atmospheric Sciences* **47**, 51–66.

Fritts, D. C. & Vincent, R. A. (1987), 'Mesospheric momentum flux studies at Adelaide, Australia: Observations and a gravity wave–tidal interaction model', *Journal of the Atmospheric Sciences* **44**(3), 605–619.

Fukao, S., Sato, T., Tsuda, T., Kato, S., Inaba, M. & Kimura, I. (1988), 'VHF Doppler radar determination of the momentum flux in the upper troposphere and lower stratosphere: Comparison between the three– and four–beam methods', *Journal of Atmospheric and Oceanic Technology* **5**, 57–69.

Gage, K. S. & Balsley, B. B. (1980), 'On the scattering and reflection mechanisms contributing to clear air radar echoes from the troposphere, stratosphere, and mesosphere', *Radio Science* **15**, 243–257.

Gage, K. S. & Green, J. L. (1978), 'Evidence for specular reflection from monostatic VHF radar observations of the stratosphere', *Radio Science* **13**(6), 991–1001.

Gossard, E. E., Gaynor, J. E., Zamora, R. J. & Nell, W. D. (1985), 'Fine structure of elevated stable layers observed by sounder and in situ tower sensors', *Journal of the Atmospheric Sciences* **42**, 2156–2169.

Green, J. L. & Gage, K. S. (1980), 'Observations of stable layers in the troposphere and stratosphere using VHF radar', *Radio Science* **15**(2), 395–405.

Harris, F. J. (1978), 'On the use of windows for harmonic analysis with the discrete fourier transform', *Proceedings of the IEEE* **66**(1), 51–83.

Headrick, J. M. & Skolnik, M. I. (1974), 'Over-the-horizon radar in the HF band', *Proceedings of the IEEE* **62**(6), 664–673.

Hocking, W. (1997*a*), 'Recent advances in radar instrumentation and techniques for studies of the mesosphere, stratosphere, and troposphere', *Radio Science* **32**(6), 2241–2270.

Hocking, W. K. (1979), 'Angular and temporal characteristics of partial reflections from the D–region of the ionosphere', *Journal of Geophysical Research* **84**, 845–851.

Hocking, W. K. (1997*b*), 'System design, signal-processing procedures, and preliminary results for the Canadian (London, Ontario) VHF atmospheric radar', *Radio Science* **32**(2), 687–706.

Hocking, W. K., Fukao, S., Tsuda, T., Yamamoto, M., Sato, T. & Kato, S. (1990), 'Aspect sensitivity of stratospheric VHF radio wave scatterers, particularly above 15-km altitude', *Radio Science* **25**, 613–627.

Hocking, W. K., Fukao, S., Yamamoto, M., Tsuda, T. & Kato, S. (1991), 'Viscosity waves and thermal–conduction waves as a cause of "specular" reflectors in radar studies of the atmosphere', *Radio Science* **26**(5), 1281–1303.

Hocking, W. K. & Hamza, A. M. (1997), 'A quantitative measure of the degree of anisotropy of turbulence in terms of atmospheric parameters, with particular relevance to radar studies', *Journal of Atmospheric and Solar-Terrestrial Physics* **59**(9), 1011–1020.

Hocking, W. K. & Mu, P. K. L. (1997), 'Upper and middle tropospheric kinetic energy dissipation rates from measurement of C_n^2 - review of theories, in-situ investigations, and experimental studies using the Buckland Park atmospheric radar in Australia', *Journal of Atmospheric and Solar-Terrestrial Physics* **59**(14), 1779–1803.

Hocking, W. K., Rüster, R. & Czechowsky, P. (1986), 'Absolute reflectivities and aspect sensitivities of VHF radio wave scatterers measured with the SOUSY radar', *Journal of Atmospheric and Terrestrial Physics* **48**(2), 131–144.

Holdsworth, D. A. (1995), Signal analysis with applications to atmospheric radars, PhD thesis, University of Adelaide, Adel., Australia.

Hooper, D. & Thomas, L. (1995), 'Aspect sensitivity of VHF scatterers in the troposphere and stratosphere from comparisons of powers in off–vertical beams', *Journal of Atmospheric and Terrestrial Physics* **57**(6), 655–663.

Jain, A. R., Rao, Y. J. & Rao, P. B. (1997), 'Aspect sensitivity of the received radar backscatter at VHF: Preliminary observations using the Indian MST radar', *Radio Science* **32**(3), 1249–1260.

Jordan, J. R., Lataitis, R. J. & Carter, D. A. (1997), 'Removing ground and intermittent clutter contamination from wind profiler signals using wavelet transforms', *Journal of Atmospheric and Oceanic Technology* **14**(6), 1280–1297.

Judasz, T. J. (1983), The coaxial colinear antenna: Theoretical and experimental models, PhD thesis, University of Colorado, Colorado, U.S.A.

Lane, J. A. (1964), Some measurements of the structure of elevated layers in the troposphere, *in* 'Preprints Eleventh Weather Radar Conference, Boulder, CO', American Meteorological Society, pp. 248–251.

Lane, J. A. (1968), Small-scale variations of radio refractive index in the troposphere: Part 1, Relationship to meteorological conditions, *in* 'Proceedings of the IEEE', Vol. 115, pp. 1227–1232.

Larsen, M. F., Palmer, R. D., Fukao, S., Woodman, R. F., Yamamoto, M., Tsuda, T. & Kato, S. (1992), 'An analysis technique for deriving vector winds and in–beam incidence angles from radar interferometer measurements', *Journal of Atmospheric and Oceanic Technology* **9**(1), 3–14.

Larsen, M. F. & Röttger, J. (1991), 'VHF radar measurements of in–beam incidence angles and associated vertical–beam radial velocity corrections', *Journal of Atmospheric and Oceanic Technology* **8**(4), 477–490.

Lesicar, D. & Hocking, W. K. (1992), 'Studies of seasonal behaviour of the shape of mesospheric scatterers using a 1.98 MHz radar', *Journal of Atmospheric and Terrestrial Physics* **54**(3/4), 295–309.

Lindner, B. C. (1975a), 'The nature of D–region scattering of vertical incidence radio waves. I-Generalized statistical theory of diversity effects between spaced receiving antennas', *Australian Journal of Physics* **28**, 163–170.

Lindner, B. C. (1975b), 'The nature of D–region scattering of vertical incidence radio waves. II-Experimental observations using spaced antenna reception', *Australian Journal of Physics* **28**, 171–184.

Low, D. J. (1996), Studies of the lower atmosphere with a VHF wind profiler, PhD thesis, University of Adelaide, Adel., Australia.

Luce, H., Crochet, M., Dalaudier, F. & Sidi, C. (1995), 'Interpretation of VHF ST radar vertical echoes from in-situ temperature sheet observations', *Radio Science* **30**(4), 1003–1025.

Luce, H., Dalaudier, F., Crochet, M. & Sidi, C. (1996), 'Direct comparison between in-situ and VHF oblique radar measurements of refractive index spectra: A new successful attempt', *Radio Science* **31**(6), 1487–1500.

Martin, R. J. & Kearney, M. J. (1997), 'Remote sea current sensing using HF radar: An autoregressive approach', *IEEE Journal of Oceanic Engineering* **22**(1), 151–155.

May, P. & Strauch, R. G. (1998), 'Reducing the effect of ground clutter on wind profiler velocity measurements', *Journal of Atmospheric and Oceanic Technology* **15**, 579–586.

May, P. T. (1986), VHF radar studies of the troposphere, PhD thesis, University of Adelaide, Adel., Australia.

McAfee, J. R., Balsley, B. B. & Gage, K. S. (1989), 'Momentum flux measurements over mountains: problems associated with the symmetrical two–beam radar technique', *Journal of Atmospheric and Oceanic Technology* **6**, 500–508.

Merritt, D. (1995), 'A statistical averaging method for wind profiler Doppler spectra', *Journal of Atmospheric and Oceanic Technology* **12**, 985–995.

Miller, P. A., Barth, M. F., van de Kamp, D. W., Schlatter, T. W., Weber, B. L., Wuertz, D. B. & Brewster, K. A. (1994), 'An evaluation of two automated quality control methods designed for use with hourly wind profiler data', *Annales Geophysicae* **12**.

Murayama, Y., Tsuda, T. & Fukao, S. (1994), 'Seasonal variation of gravity wave activity in the lower atmosphere observed with the MU radar', *Journal of Geophysical Research* **99**, 23057–23069.

Murphy, D. J. (1990), Measurements of Energy and Momentum in the Mesosphere, PhD thesis, University of Adelaide, Adel., Australia.

Palmer, R. D., Larsen, M. F., Fukao, S. & Yamamoto, M. (1998), 'On the relationship between aspect sensitivity and spatial interferometric in-beam incidence angles', *Journal of Atmospheric and Solar-Terrestrial Physics* **60**(1), 37–48.

Palmer, R. D., Larsen, M. F. & Sheppard, E. L. (1993), 'Poststatistic steering wind estimation in the troposphere and lower stratosphere', *Radio Science* **28**(3), 261–271.

Palmer, R. D., Larsen, M. F., Woodman, R. F., Fukao, S., Yamamoto, M., Tsuda, T. & Kato, S. (1991), 'VHF radar interferometry measurements of vertical velocity and the effect of tilted refractivity surfaces on standard Doppler measurements', *Radio Science* **26**(2), 417–427.

Press, W. H., Flannery, B. P., Teukolsky, S. A. & Vetterling, W. T. (1986), *Numerical Recipes*, Cambridge University Press.

Pritchard, I. T. & Thomas, L. (1993), 'Radar observations of gravity–wave momentum fluxes in the troposphere and lower stratosphere', *Annales Geophysicae* **11**, 1075–1083.

Ralph, F. M. (1995), 'Using radar–measured radial vertical velocities to distinguish precipitation scattering from clear-air scattering', *Journal of Atmospheric and Oceanic Technology* **12**, 257–267.

Ralph, F. M., Neiman, P. J. & Ruffieux, D. (1996), 'Precipitation identification from radar wind profiler spectral moment data: Velocity histograms, velocity variance and signal power–vertical velocity correlations', *Journal of Atmospheric and Oceanic Technology* **13**, 545–559.

Rastogi, P. K. (1983), 'A note on the use of coherent integration in periodogram analysis of MST radar signals', *Handbook for the Middle Atmosphere Program* **9**, 509–512.

Reid, I. M. (1988), 'MF Doppler and spaced antenna radar measurements of upper middle atmosphere winds', *Journal of Atmospheric and Terrestrial Physics* **50**(2), 117–134.

Röttger, J. (1981), 'Investigations of lower and middle atmosphere dynamics with spaced antenna drifts radars', *Journal of Atmospheric and Terrestrial Physics* **43**(4), 277–292.

Röttger, J., Czechowsky, P. & Schmidt, G. (1981), 'First low-power VHF radar observations of tropospheric, stratospheric and mesospheric winds and turbulence at the Arecibo Observatory', *Journal of Atmospheric and Terrestrial Physics* **43**(8), 789–800.

Röttger, J. & Ierkic, H. M. (1985), 'Postset beam steering and interferometer applications of VHF radars to study winds, waves and turbulence in the lower and middle atmosphere', *Radio Science* **20**(6), 1461–1480.

Röttger, J. & Liu, C. H. (1978), 'Partial reflection and scattering of VHF radar signals from the clear atmosphere', *Geophysical Research Letters* **5**, 357–360.

Röttger, J., Liu, C. H., Chao, J. K., Chen, A. J., Pan, C. J. & Fu, I. J. (1990), 'Spatial interferometer measurements with the Chung–Li VHF radar', *Radio Science* **25**(4), 503–515.

Röttger, J. & Vincent, R. A. (1978), 'VHF radar studies of tropospheric velocities and irregularities using spaced antenna techniques', *Geophysical Research Letters* **5**(11), 917–920.

Røyrvik, O. (1983), 'Spaced antenna drift at Jicamarca, mesospheric measurements', *Radio Science* **18**(3), 461–476.

Sato, K. & Woodman, R. (1982), 'Spectral parameter estimation of CAT radar echoes in the presence of fading clutter', *Radio Science* **17**, 817–826.

Thomas, L., Astin, I. & Worthington, R. M. (1997), 'A statistical study of underestimates of wind speeds by VHF radar', **15**, 805–812.

Thorsen, D., Franke, S. J. & Kudeki, E. (1997), 'A new approach to MF radar interferometry for estimating mean winds and momentum flux', *Radio Science* **32**(2), 707–726.

Tsuda, T., Gordon, W. E. & Saito, H. (1997b), 'Azimuth angle variations of specular reflection echoes in the lower atmosphere observed with the MU radar', *Journal of Atmospheric and Solar-Terrestrial Physics* **59**(7), 777–784.

Tsuda, T., Sato, T., Hirose, K., Fukao, S. & Kato, S. (1986), 'MU radar observations of the aspect sensitivity of backscattered VHF echo power in the troposphere and lower stratosphere', *Radio Science* **21**(6), 971–980.

Tsuda, T., VanZandt, T. E. & Saito, H. (1997a), 'Zenith–angle dependance of VHF specular reflection echoes in the lower atmosphere', *Journal of Atmospheric and Solar-Terrestrial Physics* **59**(7), 761–775.

Van Baelen, J. S., Tsuda, T., Richmond, A. D., Avery, S. K., Kato, S., Fukao, S. & Yamamoto, M. (1990), 'Comparison of VHF Doppler beam swinging and spaced antenna observations with the MU radar: First results', *Radio Science* **25**, 629–640.

VanBaelen, J. S., Richmond, A. D., Tsuda, T., Avery, S. K., Kato, S., Fukao, S. & Yamamoto, M. (1991b), 'Radar interferometry technique and anisotropy of the echo power distribution: First results', *Radio Science* **26**, 1315–1326.

Vandepeer, B. G. W. (1993), A new Doppler radar for upper atmospheric research, PhD thesis, University of Adelaide, Adel., Australia.

Vandepeer, B. G. W. & Reid, I. M. (1995), 'Some preliminary results obtained with the new Adelaide MF Doppler radar', *Radio Science* **32**(5), 1191–1203.

Vincent, R. A., May, P. T., Hocking, W. K., Elford, W. G., Candy, B. H. & Briggs, B. H. (1987), 'First results with the Adelaide VHF radar: Spaced antenna studies of tropospheric winds', *Journal of Atmospheric and Terrestrial Physics* **49**, 353–366.

Vincent, R. A. & Reid, I. M. (1983), 'HF Doppler measurements of mesospheric gravity wave momentum fluxes', *Journal of the Atmospheric Sciences* **40**, 1321–1333.

Vincent, R. A. & Röttger, J. (1980), 'Spaced antenna VHF radar observations of tropospheric velocities and irregularities', *Radio Science* **15**, 319–335.

Vincent, R. A., Stubbs, T. J., Pearson, P. H. O., Lloyd, K. H. & Low, C. H. (1977), 'A comparison of partial reflection drifts with winds determined by rocket techniques–1', *Journal of Atmospheric and Terrestrial Physics* **39**, 813–821.

Waterman, A. T., Hu, T. Z., Czechowsky, P. & Röttger, J. (1985), 'Measurement of anisotropic permittivity structure of upper troposphere with clear-air radar', *Radio Science* **20**(6), 1580–1592.

Weber, B., Wuertz, D., Welsh, D. & McPeek, R. (1993), 'Quality controls for profiler measurements of winds and RASS temperatures', *Journal of Atmospheric and Oceanic Technology* **10**, 452–464.

Wilczak, J. M., Strauch, R. G., Ralph, F. M., Weber, B. B., Merritt, D. A., Jordan, J. R., Wolfe, D. E., Lewis, L. K., Wuertz, D. B., Gaynor, J. E., McLaughlin, S. A., Rogers, R. R., Riddle, A. C. & Dye, T. S. (1995), 'Contamination of wind profiler data by migrating birds: Characteristics of corrupted data and potential solutions', *Journal of Atmospheric and Oceanic Technology* **12**, 449–467.

Woodman, R. F. & Guillén, A. (1974), 'Radar observations of winds and turbulence in the stratosphere and mesosphere', *Journal of the Atmospheric Sciences* **31**, 493 505.

Worthington, R. M. & Thomas, L. (1996), 'The measurements of gravity wave momentum flux in the lower atmosphere using VHF radar', *Radio Science* **31**(6), 1501–1517.

Worthington, R. M. & Thomas, L. (1997), 'Long-period unstable gravity-waves and associated VHF radar echoes', *Annales Geophysicae* **15**, 813–822.

Yoe, J. G., Czechowsky, P., Rüster, R. & Schmidt, G. (1994), 'Spatial variability of the aspect sensitivity of VHF radar echoes in the troposphere and lower stratosphere during jet stream passages', *Annales Geophysicae* **12**, 733–745.